DTU Library

Bidirectional electrostatic tunable MEMS VCSELs

Simonsen, Arnhold

Publication date:
2023

Document Version
Publisher's PDF, also known as Version of record

DTU Electro
Department of Electrical and Photonics Engineering

Bidirectional electrostatic tunable MEMS VC-SELs

PhD Dissertation

Preface

This dissertation has been submitted as a part of the requirement for the degree of Doctor in Philosophy (PhD) at DTU Electro, Department of Electrical and Photonics Engineering at the Technical University of Denmark.

The main supervisor has been Professor Kresten Yvind, and the co-supervisors have been Professor Emeritus Ole Hansen, and for a brief duration, senior researcher Dr. Gyeong Cheol Park.

I would first and foremost acknowledge the Independent Research Fund Denmark (DFF STEPS 8022-00110A) for supporting this project.

Secondly, I would like to thank my main and co-supervisor for their impeccable guidance throughout the project.

I have been associated with DTU for around 8 years, whereas for the last 5 years, I have been affiliated with the former DTU Fotonik, which is now called DTU Electro. I would like to acknowledge the amazing people and great work atmosphere present here.

In particular, I would like to acknowledge the small MEMS VCSEL team in the research group ”Nanophotonic Devices”, led by Professor Kresten Yvind, that has been formed by PhD students in recent years, namely Masoud Payandeh, Esteban Andres Proano Grijalva, and briefly, Haris Ashraf. As well as senior staff Dr. Hitesh Kumar Sahoo and senior researcher Dr. Elizaveta Semenova. Thank you all for the fruitful discussions.

I would also acknowledge the great collaboration with Octlight ApS, particularly the CEO Dr. Thor Ersted Ansbæk, especially concerning the co-invented patent application.

Lastly, and most importantly, I would acknowledge the unwavering support of my wife, especially at critical deadlines.

Arnhold Simonsen - s144064

Arnhold Simonsen

Arnhold Simonsen

Signature

11.04.2023

Date

Abstract

This thesis deals with the design and characterization of robust high-speed MEMS VCSELs.
These lasers are predominantly used as swept light sources in optical coherence tomography, an imaging modality mainly used within ophthalmology. Due to the lasers' high sweep rate, they allow imaging of the whole eye without motion blur caused by involuntary eye movement. This allows for clear depiction of the eye leading to a more accurate diagnosis.

A result of the thesis is the predicted reduction in optoelectromechanical noise resulting from the use of a robust 2D photonic crystal instead of a high contrast grating conventionally used as the movable mirror in the optical cavity. The increased mechanical stability of the photonic crystal elevates the resonant frequency of higher-order mechanical modes, reducing the risk of unwanted excitation of higher-order modes by a broadband signal. This leads to a possible reduction of the dynamic laser linewidth, resulting in a longer imaging depth.

The thesis also presents a bidirectional electromechanical model. A fabricated bidirectional electromechanical laser experimentally supports the model. The bidirectional electromechanical device allows for linear wavelength tuning, as well as paving a way to actuate ultra-stiff MEMS close to the instability points without the need to amplify the driving signal. The bidirectional laser demonstrates a fractional bandwidth of 3.44% around a center wavelength of 1585 nm at a drive frequency of 2.73 MHz.

Finally, the dissertation presents a new application area for MEMS VCSELs, namely ultrashort pulse generation, enabled by the highly coherent ultra-fast and broad-banded bidirectional electromechanical laser coupled together with a semiconductor optical amplifier and a highly dispersive medium.

Danish Resumé

Denne afhandling belyser design og karakterisering af robuste høj hastigheds MEMS VCSELs.
Disse bølgelængde justerbare lasere bliver hovedsageligt anvendt til optisk kohærens tomografi inden for oftalmologi. Denne type laser, med dets høje repetitionsrate og justerbare bølgelængde, gør det muligt at tage skarpe billeder af øjets opbygning på trods af ufrivillige øjenbevægelser. Dette kan sikre en bedre diagnostik og deraf bedre behandling.

Der er to hovedresultater i afhandlingen. Et af resultaterne er brugen af en robust 2D fotonisk krystal i stedet for det konventionelt brugte høj kontrast gitter som det justerbare kavitetsspejl. Den øgede mekaniske stabilitet af den fotoniske krystal, hæver mekaniske resonanser af højere orden længere op i frekvenspektret. Dette mindsker risikoen for en højere ordens mekanisk stimulering forårsaget af et bredbåndet drivsignal. Dette kan føre til en smallere dynamisk linjebredde som muliggør en dybere afbildning af vævet.

Et andet afhandlingsresultat er en tovejs elektromekanisk model. Denne model understøttes af en eksperimentelt fremstillet tovejs aktueret laser. Den tovejs aktuerede laser muliggør lineært justerbar bølgelængdeændring, samt baner vejen til aktivering af ultra stive MEMS tæt på ustabilitetspunkterne. Dette uden behov for at forstærke drivsignalet. Med den eksperimentelt fremstillede laser demonstreres en relativt båndbredde på 3.44% omkring en centerbølgelængde på 1585 nm, ved en aktueringfrekvens på 2.73 MHz.

Endeligt præsenteres en ny metode hvor førnævnte MEMS VCSELs, koblet sammen med en optisk forstærker samt et medie med høj dispersion, der kan danne ultra korte pulser. Disse korte pulser kan bruges til blandt andet laserskæring af tynde materialer.

Contents

List of Tables

List of Figures

List of Acronyms

AlAs alluminum arsenide. 6

AR anti-reflection coating. 11

AWG arbitrary waveform generator. 10

BOX buried oxide layer. 8

DBR distributed bragg reflector. 5–8, 10

DCF dispersion compensating fibre. xiii, 10, 11, 71, 73–76, 78–80

EC extended cavity. 11

EEL edge emitting laser. 2, 3

FBW fractional bandwidth. 9

FDML Fourier domain mode locking. 10

FFT fast Fourier transform. 9

FSR free spectral range. 3, 8, 11

GaAs gallium arsenide. 6, 11, 81

HCG high contrast grating. x, 5–9, 11, 13, 14, 21, 22, 26, 31

InP indium phosphide. 8, 11, 47

LiDAR light detection and ranging. 3, 9, 29, 81

MEMS microelectromechanical systems. ix–xiii, 4–7, 9–11, 13–15, 20, 22, 25–29, 31, 32, 34, 35, 38–56, 59, 64–66, 68, 71–74, 77–79, 81, 82

OAWG optical arbitrary waveform generator. 10, 11

OCT optical coherence tomography. 4, 5, 9, 13, 27, 29, 31, 81

PhC photonic crystal. x, xi, 11, 13–18, 20–22, 25–29, 71, 81, 82

RCWA rigorous coupled wave analysis. 13–16, 20

RoC radius of curvature. x, 13, 18–20, 27

SCD semiconductor cavity dominant design. 11

Si silicone. 7, 8

SOA semiconductor optical amplifier. xiii, 10, 11, 72, 73, 78, 79

SOI silicon-on-insulator. 11, 47

SS swept source. 4, 9, 13, 29, 31, 81

VCSEL vertical cavity surface emitting laser. x, xi, xiii, 2–7, 9–11, 13–15, 20, 26–29, 31, 32, 40, 47, 54, 56, 59, 68, 71–74, 79, 81, 82

1 Introduction

This chapter serves as an introduction to the vast and ever-evolving field of research that has inspired and provided a foundation for the work presented in this Ph.D. dissertation. By providing a background, current state-of-the-art, the research landscape that has shaped the investigation is presented. In doing so, key motivations and factors that have driven the research are presented to highlight the unique contributions that the work brings to the field.

1.1 Lasers

Lasers (Light Amplification by Stimulated Emission of Radiation) are devices that produce a narrow, coherent, and monochromatic beam of light. The concept of stimulated emission, which forms the basis of laser technology, was introduced by Albert Einstein in 1917[1]. However, it was not until 1960 that Theodore H. Maiman invented the first laser at Hughes Research Laboratories[2], based on theoretical work by Charles H. Townes and Arthur Leonard Schawlow[3].

Since the invention of the laser, considerable effort and resources have been dedicated to advancing laser technology. This has resulted in various medical, defense, communication, and manufacturing applications. The range of applications is due to the various lasers available, each with specific properties and capabilities.

Lasers are classified into four categories: solid-state (and fiber), gas, semiconductor, and dye lasers. Solid-state lasers use a solid material as the lasing medium, and examples include ruby and Nd:YAG lasers[4]. Gas lasers use gas as the lasing medium; examples include helium-neon[5] and CO_2 lasers[6]. Semiconductor lasers use a p-n junction as the lasing medium[7], and examples include laser diodes used in optical communication. Dye lasers use a dye solution as the lasing medium[8], and they are known for their tunable output wavelength.

Each type of laser has its advantages and disadvantages, and the choice of laser depends on application-specific requirements.

Lasers have a broad range of applications, including but not limited to:

Communication: Lasers are used in fiber optic communication systems to transmit information over long distances.

Medicine: Lasers are used in various medical procedures, such as eye surgery, and cancer treatment.

Industry: Lasers are used in manufacturing processes, such as cutting and welding, and in quality control.

Defense: Lasers are used in various military applications, such as missile defense and target designation.

Research: Lasers are used in various scientific applications, such as spectroscopy and imaging.

Regardless of the laser type, the lasing system has to be optically or electrically pumped to achieve lasing. This is due to the needed presence of population inversion, which is when the majority of atoms in the gain material are in an excited state. At thermal equilibrium, most of the atoms in the gain material are in the lower-energy states. However, some atoms are excited to higher energy states when energy is pumped into the system through optical or electrical excitation. The upper-state lifetime is relatively short, and when an excited electron decays back down to a lower energy state, a photon is emitted by spontaneous emission.

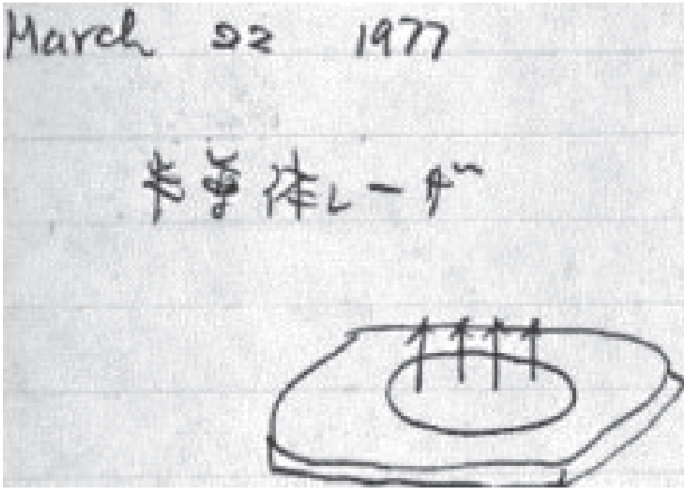

Figure 1.1: Initial sketch of a vertical cavity surface emitting laser.

If an incident photon matches the bandgap, i.e., the difference between the lower and upper state, it can stimulate the decay of an excited electron, which generates a second photon that is identical in energy, phase, and direction of the incident photon. This process is referred to as stimulated emission. The number of photons produced by this process can be greatly amplified if there are more excited atoms than atoms in the lower energy levels, i.e., a population inversion. A cascade of stimulated emission can occur if population inversion is present, leading to light amplification inside the laser cavity.
For lasing to occur, i.e., the laser output is predominantly stimulated emission rather than spontaneous emission, regardless of the laser type, the gain has to surpass the loss in the cavity; this occurs at the threshold gain defined by[9]:

$$g_{\text{th}} = \alpha_0 - \frac{1}{2L_g} \ln \left(R_1 R_2\right) \tag{1.1}$$

where, g_{th} is the gain threshold, α_0 is the assumed constant internal optical loss, L_g is the length of the gain medium, and R_1 and R_2 are the two cavity mirror reflectivities.
Semiconductor lasers have gained much attention due to their small size, low cost, and high efficiency. Since the wafer growth and subsequent processing are done in parallel, mass production of devices is possible, contributing to the low unit cost.
Traditional semiconductor or diode lasers are edge emitting laser (EEL) with light emission in the wafer plane. EELs must be diced out before characterization because their end facets are mirrors that define the optical cavity. These lasers feature a double heterostructure that guides the optical beam and confines light and carrier generation. The end facet reflectivities are around 35%, which is sufficient to support lasing due to relatively long cavity (gain) lengths of tens of μm and upwards, as seen in Eq. (1.1). Due to the broad gain spectrum of diode lasers, they are an ideal choice as wavelength-tunable lasers.

1.2 Vertical cavity surface emitting lasers

Vertical cavity surface emitting lasers (VCSEL) are a highly versatile type of semiconductor laser that has undergone extensive research since its inception. The first VCSEL was invented by Kenichi Iga in 1977[10] and has since seen significant advancements in design and application. Figure 1.1[10] shows the initial conceptual drawing of the VCSEL. As the name suggests, instead of the optical cavity being confined in the horizontal

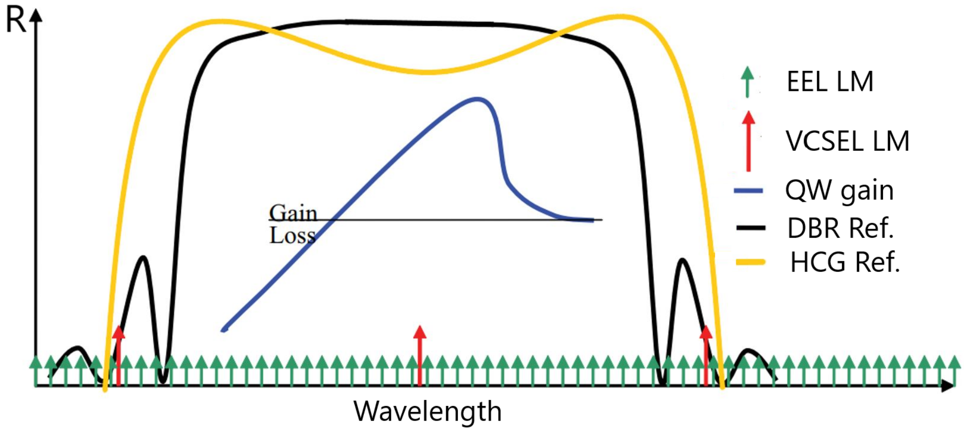

Figure 1.2: Illustration of DBR and HCG reflectivity and gain as a function of wavelength and longitudinal resonator modes for an EEL and a VCSEL.

wafer plane, e.g., by the end mirror facet, as is the case for the EEL, the VCSEL cavity is confined vertically, perpendicular to the wafer plane. This makes the VCSEL quite distinct compared to EEL. The gain length is significantly reduced, necessitating much higher mirror reflectivities as indicated by Eq.(1.1). To support lasing in a VCSEL, the mirror reflectivities must approach 100%.
Two flat mirror laser cavities, also called Fabry-Peròt resonators, support specific wavelengths inside the resonator, i.e., only certain standing waves are sustained. The remaining wavelengths are suppressed due to destructive interference. The wavelengths of the Fabry-Peròt resonator modes are expressed as[11]:

$$\lambda_m = \frac{2nL_m}{m} \tag{1.2}$$

where λ_m is the wavelength corresponding to the maximum transmission in the resonator, n is the refractive index, L_m is the length of the resonator, and m is the mode number.
The length between adjacent resonator modes is referred to as the free spectral range (FSR), and it is defined as[11]:

$$\text{FSR} = \frac{\lambda_\text{m}^2}{2\text{L}_\text{eff}} \tag{1.3}$$

where λ_m is the Fabry-Peròt resonator wavelength, L_eff is the effective cavity length. The added benefit of the VCSEL having short cavity length is the wide FSR, given by Eq. (1.3). This results in only a single longitudinal mode overlapping with the gain spectrum, which results in a single longitudinal mode device. In contrast, the resonator modes in EEL are closely spaced, which results in mode hopping when the temperature of the laser changes due to the peak gain shift with temperature. An illustration of the difference in mode spacing can be seen in Fig. 1.2[12].

The shorter cavity also enables a lower threshold current due to the decreased mode volume[13], which results in low power consumption and high conversion efficiency[14]. In addition, the output is circular, as indicated by Fig 1.1, which eases out-coupling to optical fibers. By virtue of the vertical cavity, it is possible to grow large 2D VCSEL arrays monolithically, which makes characterization prior to cleaving possible, drastically lowering manufacturing costs. For all of the prior mentioned reasons, VCSELs have a lot of application areas indicated by Fig. 1.3. In smartphones a variety of VCSELs are used for auto-focusing, distance measurement in light detection and ranging (LiDAR), and face recognition[15].

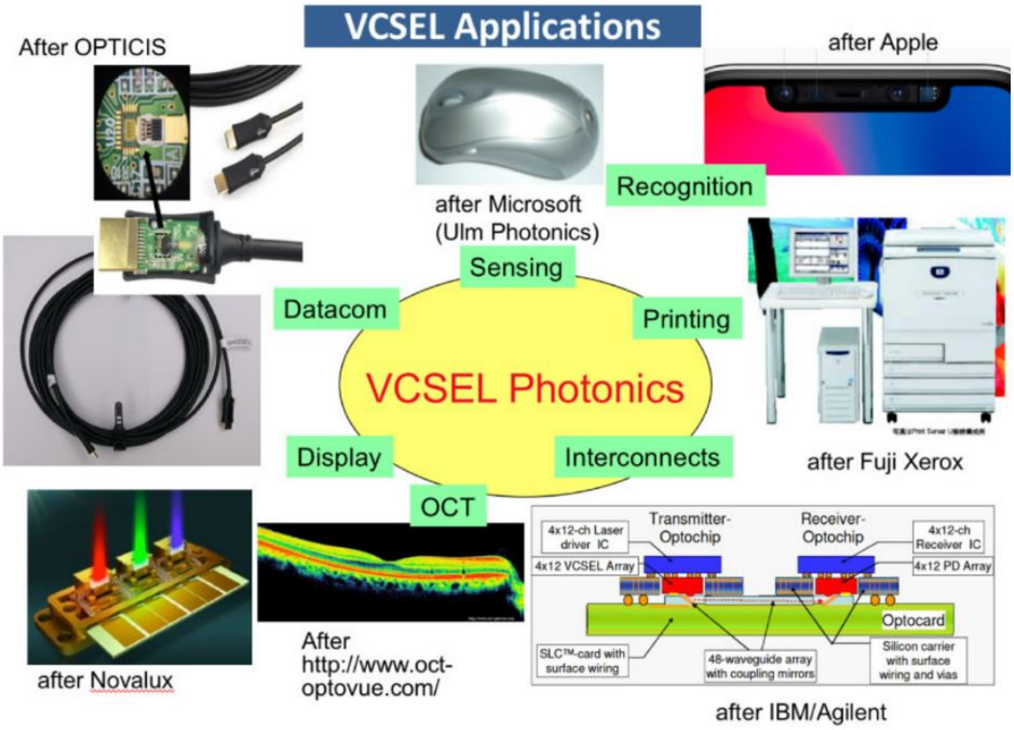

Figure 1.3: Some of the many applications of vertical cavity surface emitting lasers.

In medical imaging, a wavelength tunable VCSEL is employed, where the length of the optical cavity is altered, resulting in a change of the emission wavelength, given by Eq. (1.2).

1.3 Microelectromechanical vertical cavity surface emitting lasers

Microelectromechanical system (MEMS) vertical cavity surface emitting lasers (VCSELs) are semiconductor wavelength tunable lasers mainly used within swept source (SS) optical coherence tomography (OCT). OCT is an in vivo medical imaging modality mainly used in ophthalmology to take submicrometer[16] images of the retina, allowing doctors to assess the eye's health condition. OCT can detect glaucoma[17], macular degeneration[18], and other diseases showing ocular signs, e.g., diabetic macular edema[19]. OCT is finding applications in other medical fields, including cancer research[20].
Two SS-OCT images can be seen in Fig. 1.4, a full eye (a) and the back of the eye (b)[21].

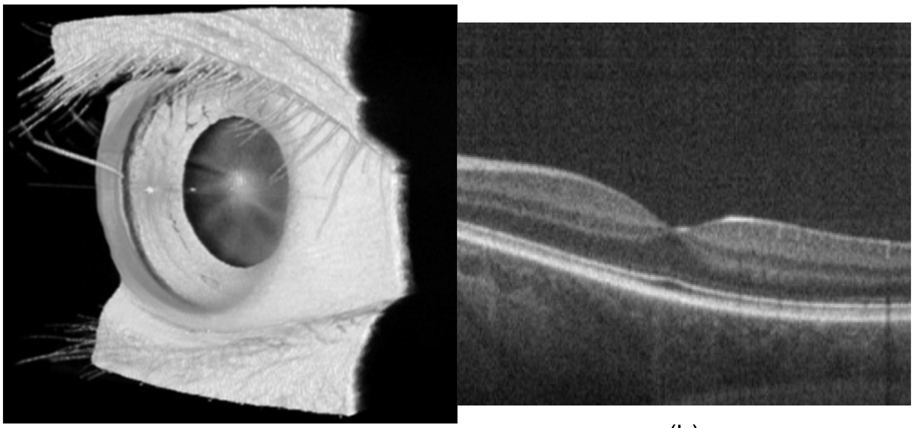

(a) (b)

Figure 1.4: (a) Full image of the eye (front) (b) Image of the back of the eye.

The axial OCT resolution is related to the tuning bandwidth of the laser source[22] (assuming Gaussian spectral distribution):

$$\Delta z = 2\ln 2/\pi \left(\frac{\lambda_0^2}{\Delta\lambda}\right) \tag{1.4}$$

where λ_0 is the centre wavelength, and $\Delta\lambda$ is the tuning bandwidth of the swept source. As indicated, the larger the tuning bandwidth is, the smaller features can be resolved in the light propagating direction.
The driving voltage waveform can control the scanning speed of the laser. However, to generate a large wavelength sweep, it is customary to excite the MEMS close to resonance to generate a large mechanical response. Faster scanning speeds allow for averaging and minimizing motion blur caused by, e.g., involuntary eye movement. For diagnostic purposes, it is, therefore, advantageous to realize a broad and fast-tunable MEMS VCSEL.
There are several ways to wavelength sweep the laser; thermal[23], piezoelectric[24], and liquid crystal[25] tuning. However, the current fastest tuning mechanism is electromechanical tuning.
In electromechanical tuning, a bias is applied to the MEMS above an air gap, which acts as a capacitor storing charges on the surface. On the other side of the air gap, charges of opposite polarity accumulate, resulting in an electric field between the two sides. The magnitude of the electric field is proportional to the potential difference. As a consequence of Coulumb's law, an electrostatic force acts on the movable mirror, causing displacement. The final displacement results from a balance between the electrostatic and restoring spring forces.
There are two types of MEMS VCSELs, those who rely on a DBR mirror and those who rely on a high contrast grating (HCG) as the movable mirror.
The DBR consists of a repeated two-layered structure, as shown in Fig. 1.5[26]. Figure 1.5 depicts a Bragg grating consisting of two alternating materials with different refractive indices (n_1 and n_2) and lengths (L_1 and L_2), forming a repeated period of length Λ. Each interface in the periodic structure partially reflects the incident light. The reflectivity spectra of three Bragg gratings are shown in the figure. The blue and red curves correspond to gratings with 50 and 30 periods, respectively, and both have a refractive index difference (Δn) of 0.36. The green curve represents a grating with 50 periods and a Δn of 0.45.
To achieve constructive interference of partially reflected waves, the optical path length in

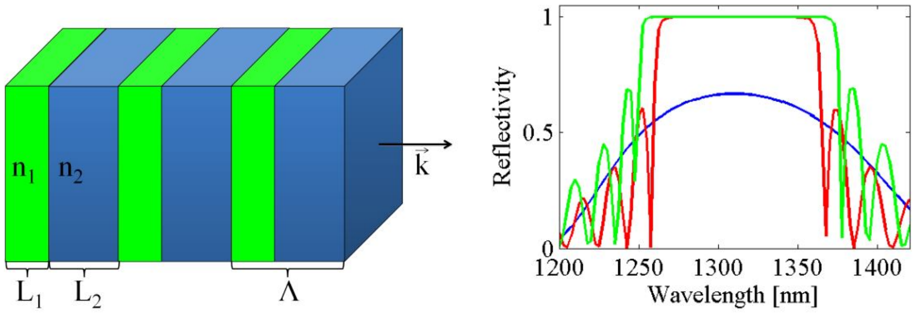

Figure 1.5: 1D bragg grating with alternating refractive indices n_1 and n_2 of lengths L_1 and L_2 summing to a period Λ. Three reflectivity spectra, blue (50 periods) and red (30 periods) with a refractive index contrast of 0.36, and green (50 periods), with a refractive index contrast of 0.45.

each layer needs to be equal. This condition can be expressed as $L_1 n_1 = L_2 n_2$, where n_1 and n_2 denote the refractive indices of the alternating materials, and L_1 and L_2 represent the lengths of the materials in the direction of periodicity. The center frequency of the broad reflectivity band is given by[27],:

$$\omega_B = \frac{n_1 + n_2}{4 n_1 n_2} \cdot \frac{2\pi c}{\Lambda}, \quad \omega_B = \frac{2\pi c}{\lambda_B} \tag{1.5}$$

where the Bragg wavelength λ_B refers to the vacuum wavelength at the middle of the broad reflectivity band, and c is the speed of light. The lengths of the alternating layers are:

$$L_1 = \frac{\lambda_B}{4 n_1} \quad \text{and} \quad L_2 = \frac{\lambda_B}{4 n_2} \tag{1.6}$$

Hence, DBRs are sometimes called quarter wave stacks due to the relationship between the Bragg wavelength and the lengths of the layers.

Figure 1.5 illustrates the stop-band behavior of a DBR, showcasing the decrease in reflectivity as the wavelength approaches the stop-band edge. The reflectivity of a DBR can be increased by increasing the number of grating periods, assuming perfect interfaces and no loss. A higher refractive index contrast ($\Delta n = n_2 - n_1$) also results in a broader stop band for the same number of grating periods. The gallium arsenide (GaAs) system is commonly employed for emission around 1060 nm, with the alluminum arsenide (AlAs)/GaAs Bragg reflector being the usual choice due to the refractive indices of n(GaAs) = 3.49 and n(AlAs) = 2.95. However, a significant number of periods is needed to achieve the required reflectivity for a VCSEL, which poses challenges for wafer growth and thermal management, given the long stack length of several micrometers. An alternative approach is to use dielectric DBR mirrors, which can achieve a higher refractive index contrast and thus reduce the required layers.

The MEMS system can be modeled as a simple harmonic oscillator; the resonant frequency is given by:

$$\omega = \sqrt{\frac{k}{m}} \tag{1.7}$$

where k is the spring constant, and m is the mass. As the resonant frequency is directly proportional to the spring constant, increasing the spring constant would increase the tuning frequency if resonant excitation is used.

A conceptual image of the first realized HCG MEMS VCSEL can be seen in Fig. 1.6[28].

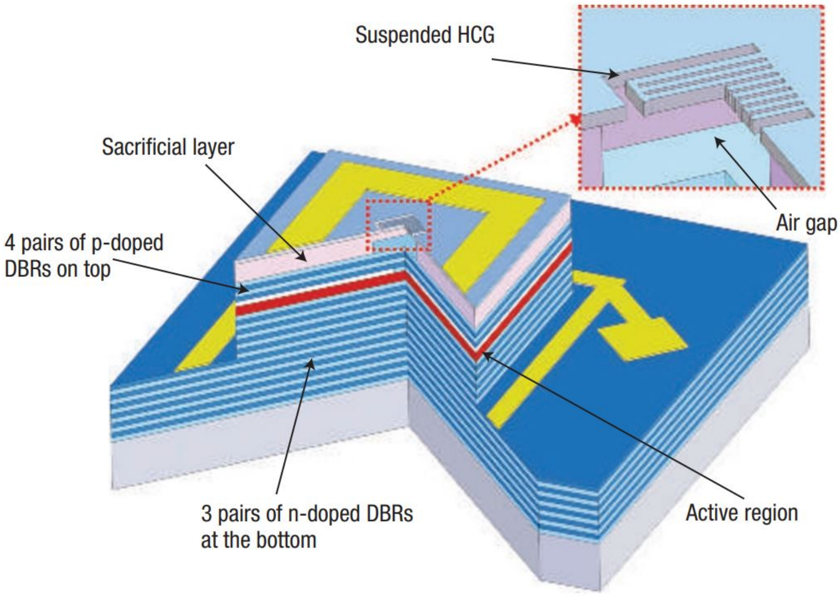

Figure 1.6: First demonstration of a HCG MEMS VCSEL.

According to Eq. (1.7), the resonance frequency is proportional to the inverse of the effective mass m. Therefore, utilizing high contrast gratings with lower effective masses can be a promising alternative to achieve a high resonance frequency and overcome the drawbacks of long DBR stacks.

1.4 Bidirectional microelectromechanical vertical cavity surface emitting lasers

Classical HCG MEMS VCSELs are monolithically grown, relying on III-V materials for the active region and the movable MEMS part. III-V materials are used by virtue of their ability to engineer the band structure in order to achieve high gain at desired wavelengths; however, they are expensive, fragile, and challenging to work with. Therefore, a shift has been made toward utilizing the more established silicone (Si) platform. Si substrates are cheaper and mechanically more robust, and there is a wealth of established knowledge on Si processing. Dielectric DBRs and HCGs can be used with a Si substrate as top and bottom mirrors, respectively.
The bidirectional MEMS VCSEL is based on work done previously in the research group[29], Fig. 1.7 shows an illustration of the device[30].

The device in Fig. 1.7 is a Si substrate-based MEMS VCSEL, with a HCG mirror as the bottom mirror and a dielectric DBR as the top mirror. The actuating part is Si, which sits in a sealed cavity. Encapsulating the actuating part gives the designer control over the operating atmosphere of the MEMS, which is crucial for achieving the desired damping. Furthermore, the actuating part is in Si, which is much better than III-V materials in terms of robustness and reliability. The design offers many advantages over traditional approaches, including a modular design approach where all the elements can be designed and fabricated independently. This modular approach allows for faster design modification to accommodate changes in emission wavelength based on the application area. The HCG can be modified to achieve wide-band reflectivity close to 100% over the desired wavelength range, and the thickness of dielectric DBR layers and the number of pairs can similarly be adapted to achieve the desired reflectivity spectrum. The active material, which is grown independently, can also be changed following the wavelength. The

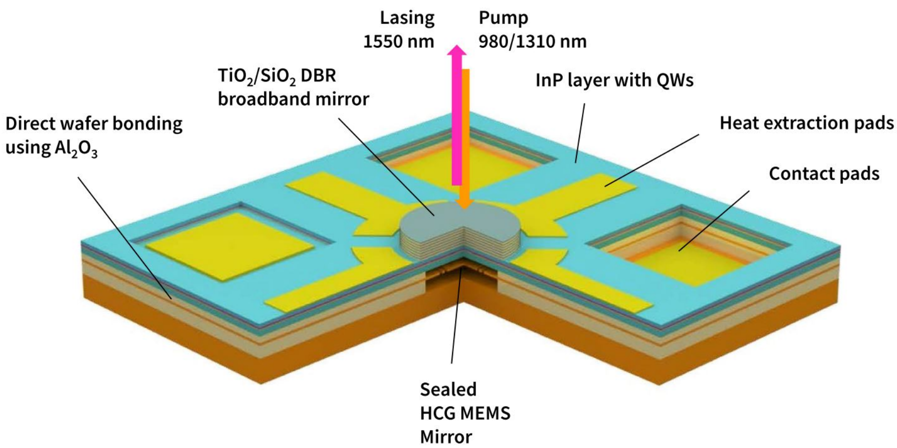

Figure 1.7: Optically pumped bidirectional MEMS VCSEL. The InP wafer is wafer-bonded to a silicon-on-insulator substrate, encapsulating the HCG MEMS.

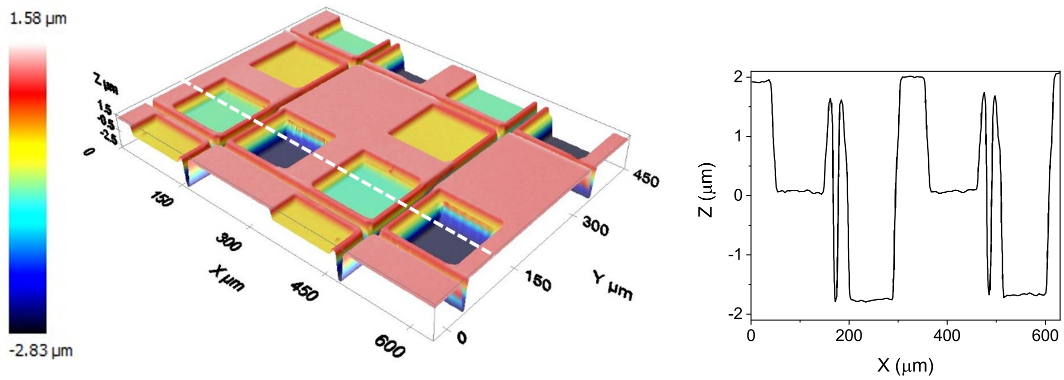

(a) (b)

Figure 1.8: Device height profile, (a) 3D top view and (b) 2D height profile a long the dotted white line shown in (a).

device can also do bidirectional tuning, which is crucial for increasing the tuning range. The design also allows for a smaller cavity by reducing the top air-gap and only tuning the bottom air-gap, if bandwidth limitations are FSR related.

The difference between the current batch and the last run is that the indium phosphide (InP) contact has a two-step metallization to realize an ohmic contact. The gain medium consists of two types of quantum wells totaling eight, realizing a broader gain compared to the eight identical quantum wells used in the previous batch.

Top emission is desirable, resulting in lower target HCG reflectivity than DBR, unlike the example in Fig. 1.2. At the center of the stop band, the HCG reflectivity is below the reflectivity of the DBR mirror, resulting in the outcoupling of laser light on the side of the HCG mirror.

The height profile of the device prior to metalization and top DBR deposition can be seen in Fig. 1.8. As indicated by Fig. 1.8 the III-V epitaxial structure is around, ≈ 1.2 μm, the spacer layer is ≈ 0.94 μm, the Si device layer is ≈ 0.4 μm and the buried oxide layer (BOX) is ≈ 1.0 μm, resulting in a total thickness of ≈ 3.54 μm. The sidewalls of the contact depressions are exposed during metalization, a suggested improvement is mentioned in Chapter 4.

Linearization of the MEMS movement is advantageous for both SS-OCT and LiDAR; Linearity is k-space enables fast Fourier transform (FFT) without resampling. Chapter 3 shows the mirror movement in the bidirectional MEMS VCSEL is linear, indicating immense potential as a laser source for SS-OCT and LiDAR.

1.5 State of the art

There are two figures of merit for MEMS VCSELs, the tuning speed, how fast the MEMS is actuated, and the tuning bandwidth, how broad the laser can be tuned.
State-of-the-art results include > 150 nm around 1310 nm at 480 kHz using an optically pumped device from Praevium Research[31], and electrically pumped 64 nm at 400 kHz[32] and 73 nm achieved by the group of Chang-Hasnain at UC Berkeley[33]. The HCG VCSEL, invented by Chang-Hasnain[28], features low mirror mass for fast tuning and has shown a 7.9 MHz tuning rate, albeit at a narrow optical bandwidth[34]. The group of the late Amann at TU München and Meissner at TU Darmstadt demonstrated 74 nm around 1550 nm at 200 kHz from an electrically pumped device using a more complicated design[35].
Fig. 1.9 shows the state-of-the-art of MEMS VCSELs (the figure is a result of merging two graphs from [36], with some additions[37, 31, 38, 39]). The graph shows both electrically and optically pumped MEMS VCSELs. To direct the viewer's attention a black line is

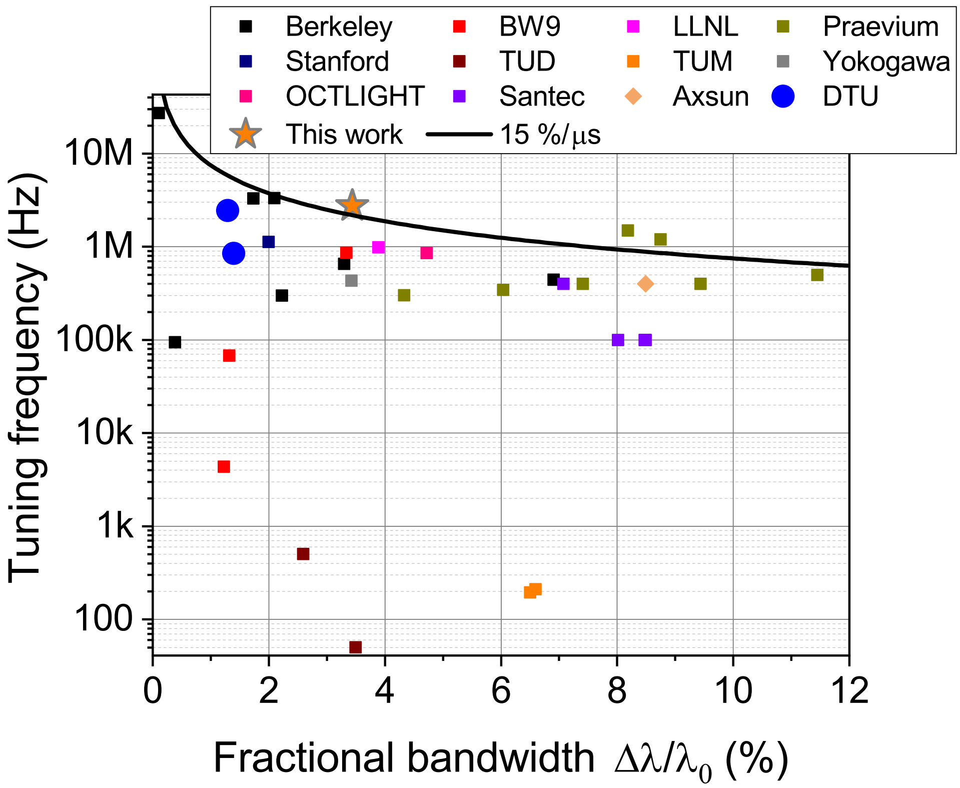

Figure 1.9: Tuning frequency as a function of fractional bandwidth.

added, representing a 15% fractional bandwidth (FBW) pr. microsecond. A general trend is seen in Fig. 1.9, where broad tuning (high FBW) corresponds to relatively slow tuning and vice versa. This is due to the electrostatic nature by which the MEMS is moved; very stiff MEMS require higher electrostatic force to actuate.
"This work"[40], fabricated in-house[41], highlighted in Fig. 1.9 uniquely utilizes bidirectional actuation. As shown in Chapter 3, this can potentially avoid the trade-off between

either fast MEMS with limited bandwidth or slow MEMS with a larger bandwidth. In addition, the design seals the MEMS, protecting it from local environmental changes, contrary to state-of-the-art, where the MEMS is exposed at the top of the wafer. This makes the MEMS more reliable and resilient to condensation.

1.6 Optical arbitrary waveform generators

Today, the options for measuring or controlling the temporal change of a system are typically limited to either cheap but slow electrical methods or ultra-fast optical techniques that require a larger set of equipment and specialized operators, often only found in universities. An alternative approach is presented in the last chapter, which combines a compact optical system with direct electrical control, potentially bringing time-resolved tools into medical clinics and factories. This innovative approach is based on a MEMS VCSEL, which can continuously change the emission wavelength, ensuring that the phase of the light over the entire adjustment interval has a well-defined value. Normally, temporal coherence over a wide bandwidth is only seen in pulsed lasers, but this can now be controlled directly electrically by manipulating a micro-mechanical element within the laser. Relying on the unique coherence properties of MEMS VCSELs coupled with a semiconductor optical amplifier (SOA), and dispersion compensating fibre (DCF) a way of generating optical arbitrary waveform generator (OAWG) is presented. Due to the parallel processing of the components involved, the possibility of producing OAWG at scale can potentially minimize production costs and, thereby, the overall cost of the generator.

Although still in its infancy, the field of OAWG is rapidly expanding in the realm of ultrafast science. Its electrical counterpart, the electronic arbitrary waveform generator (AWG), has been around for several decades, with many applications such as signal testing and characterizations, medical imaging (ultrasound)[42], radar and sonar, to name a few.

The applications of OAWG are still uncertain, as it is a relatively new field. However, its advanced features are expected to enhance the applications of conventional pulse shaping, particularly in areas such as quantum control of fast chemical reactions, manipulation of high-field laser-matter interactions, and generation and processing of ultra-broadband radiofrequency signals using photonic techniques. Additionally, the unique features of OAWG may lead to the discovery of new and previously unknown applications.

There are generally two categories of OAWG, static and dynamic OAWG. Static OAWG refers to line-by-line shaping of a frequency comb source, in which the pulse waveform cannot be updated after every pulse. And dynamic or true OAWG, where the waveform can be changed pulse-by-pulse basis[43].

Low repetition rate lasers with high peak power are better suited for certain applications such as materials processing and temporal characterization of materials[44]. These lasers are currently limited to mode-locked solid-state or fiber lasers, as small and cheap electrically controlled semiconductor lasers have limitations in peak power due to two-photon absorption and the upper state lifetime, which restricts repetition rate to above $\approx$1 GHz.

MEMS VCSELs can potentially fill this semiconductor gap. Since they offer a unique feature, the tuning can be achieved using a continuous Doppler shift, ensuring coherence is maintained across the total bandwidth of the device[45]. Other wavelength tunable semiconductor lasers exist, e.g., tunable edge-emitting DBR lasers. However, they exhibit discontinuities in the wavelength sweep, which prevents them from being used as tunable light sources for OAWG. The only present contender to MEMS VCSELs in the realm of OAWG is the Fourier domain mode locking (FDML) laser. FDML laser is a fiber ring cavity laser with a tunable filter matching the round-trip time in the fiber cavity. However, only partial coherence has been reported[46, 47].

1.7 Coherence

Fast and broad tuning of the MEMS VCSEL is needed to realize highly chirped output. As previously stated, to realize OAWG, the tuning bandwidth of the MEMS VCSEL has to be coherent. In order to have a Doppler-assisted tuning, where lasing does not build up from spontaneous emission at each wavelength, the ”two mirror” cavity implementation is necessary, also referred to as extended cavity (EC). This is achieved by applying an anti-reflection coating (AR) at the interface between the air gap at the active layer. This results in the semiconductor and the air cavity being perfectly coupled and enable a relatively large tuning slope or tuning efficiency, i.e., wavelength change pr. gap change[48]. The fabricated MEMS VCSELs in the project did not have an AR, which results in a ”three mirror” cavity, or semiconductor cavity dominant design (SCD)[48].
The Doppler-assisted tuning enabled by EC is highlighted in Chapter 5.
Decoherence within the wavelength sweep can result in less optimal pulse width. In Chapter 2, a stiffer MEMS mirror is investigated to reduce the wavelength noise associated with mixing MEMS mechanical modes.
The wide FSR enabled by VCSELs (Eq. (1.3)) results in no mode hopping when the cavity length is tuned. If mode hopping occurs, the coherence is broken, as lasing needs to be reestablished initiated by spontaneous emission.

1.8 Thesis outline

Chapter 2 is based on a submitted Optics Express article; see Appendix A.2. It highlights the effect of using a 2D photonic crystal (PhC) instead of the conventional HCG as the MEMS mirror in a unidirectional GaAs VCSEL, with an emission wavelength around 1060 nm. The work was done in collaboration with OCTLIGHT[49] and has resulted in a US patent application filed by the Technical University of Denmark.

Chapter 3 is based on a draft manuscript; see Appendix A.2 and A.3. In the Chapter, the bidirectional equation of motion is derived and compared with experimental results. The InP silicon-on-insulator (SOI) MEMS VCSEL has an emission wavelength of around 1550 nm. A comparison between the unidirectional and bidirectional MEMS VCSEL is presented.

Chapter 4 presents the experimental challenges faced in the project and suggests improvements for the next fabrication iteration.

Chapter 5 outlines how a tailorable pulse source can be set up based on MEMS VCSEL coupled with an SOA and a DCF.

2 Photonic crystal microelectromechanical system vertical cavity surface emitting laser

This chapter is based on the submitted manuscript to Optics Express. See appendix for the submitted manuscript A.1.

The main results of this chapter are the effect the rounded corners have on the reflection of the 2D PhC, the added mechanical stability of the PhC MEMS, as well as the high index volume fraction that ensures high broadbanded reflection.

2.1 Introduction

1D photonic crystal (PhC), or high contrast grating (HCG), employed as the movable cavity mirror in a microelectromechanical systems (MEMS) vertical cavity surface emitting laser (VCSEL), have enabled very fast swept source SS OCT[28, 50]. This is by virtue of their extremely small mass, leading to very high resonant frequencies. The movable mirror is anchored to spring arms situated above an air gap on top of the half VCSEL, containing the laser gain material and the fixed mirror. The MEMS is tuned by electrostatics, i.e., by applying a bias on the contacts, creating an electrostatic force, which is balanced by the spring force leading to a steady-state MEMS position.
Figure 2.1 (a)[51] shows a SEM image (top view) of a fabricated HCG, and Fig 2.1 (b)[51] shows the epitaxial structure of a MEMS VCSEL, and Fig. 2.1 (c)[52] shows a 3D model of the HCG.
As is evident in Fig. 2.1 for a HCG the periodicity is only one (x) direction. The plane of incidence is defined in the $z - x$ plane, Fig 2.1 (c) shows the electric field polarized in the plane of incidence, i.e., the magnetic field is polarized orthogonal to the plane of incidence. This is referred to as a transverse magnetic (TM) mode. If the electric field is polarized along the grating bars, i.e., in the y direction, the electric field is now orthogonal to the plane of incidence, i.e., transverse electric (TE) mode. The unit cell of the HCG consists of the period (Λ), bar width (w), and thickness (t_g).
Figure 2.2[40] shows a 2D PhC MEMS.
Fig. 2.2 (a) shows, similar to Fig. 2.1 (a), the suspended mirror above an air gap and the active laser material, however as can be seen in Fig. 2.2 (b), which is a zoom-in of Fig. 2.2 (a), the periodicity of the PhC is in two orthogonal (x and y) directions. The in-plane parameters of the unit-cell of the PhC are shown in Fig. 2.2 (c). The out-of-plane parameter is the thickness t_g. In addition to the expected periods (Λ_x, Λ_y) and widths (w_x, w_y) in the x and y directions, an additional in-plane parameter appears in the unit cell of the PhC, namely the radius of curvature (RoC) of the rounded corners of the cross. The RoC is a consequence of fabrication, i.e., regardless of the chosen type of fabrication and etching, when designing a cross with 90 degree edges, after fabrication, the edges will always be rounded - therefore, the RoC is included in the simulated unit-cell.

2.2 Rigorous coupled wave analysis

Rigorous Coupled Wave Analysis RCWA[53] is a method used to analyze the behavior of light when it interacts with a periodic structure. It is often used to study the optical properties of diffraction gratings and photonic crystal devices. RCWA involves expressing the

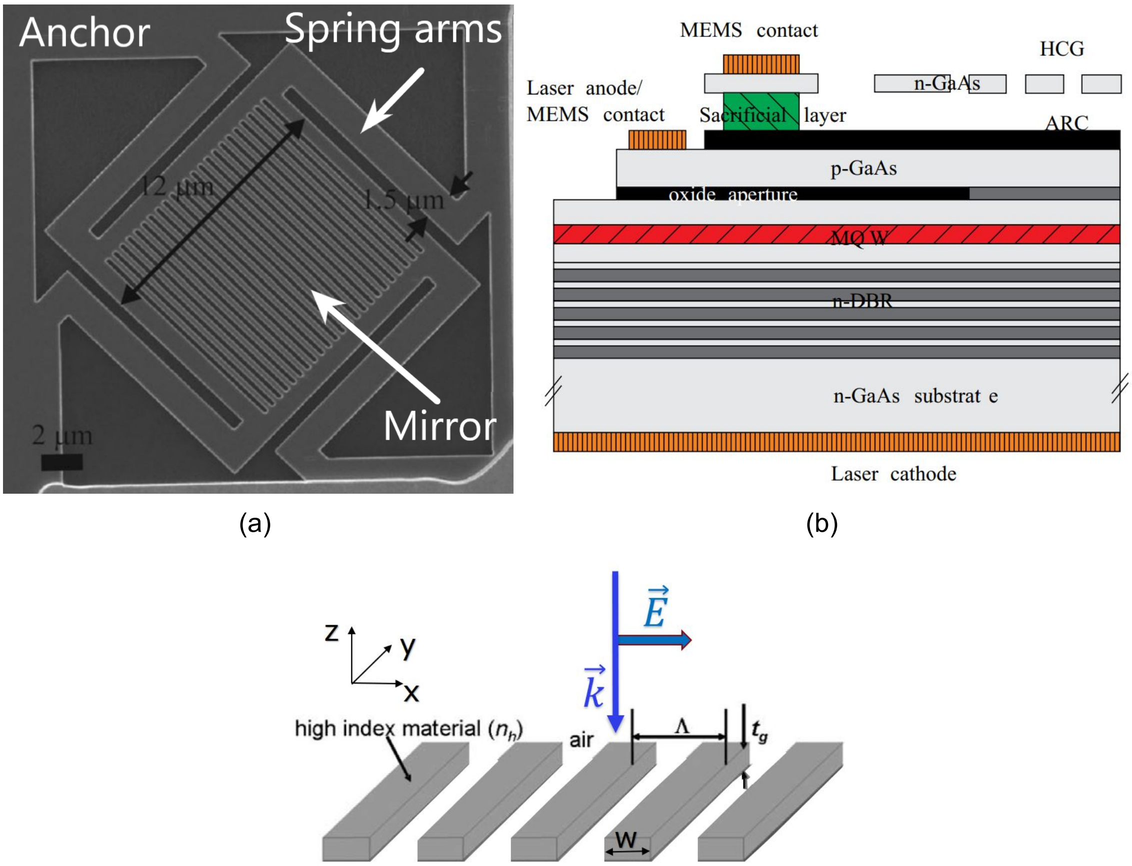

(a) (b)

(c)

Figure 2.1: (a) shows a SEM image of a HCG (top view) over an airgap on top of the VCSEL structure. (b) shows the epitaxial structure of the MEMS VCSEL[51]. (c) shows a model of the HCG with incident (TM) light.

optical field as a sum of plane waves and then using the wave equation to calculate each wave component's complex reflection and transmission coefficients. These coefficients are then used to calculate the system's overall response, including the diffraction efficiency, spectral reflectance, and transmittance. RCWA provides a highly accurate and efficient way to study the optical properties of periodic structures.

A unit cell, e.g., Fig. 2.2 (c), is defined with a periodic boundary condition in the $x-y$ plane, i.e., it is assumed that the layers orthogonal to the propagation direction (assuming normal incidence) are infinite.

The coupled wave equations are then solved for specified diffraction orders. Due to the sub-wavelength nature of the PhC, no diffraction occurs; only the zeroth order is transmitted and reflected. However, increasing the number of diffraction orders solved will lead to higher convergence of the zeroth order reflection (transmission) values. It is, therefore, imperative to perform a convergence test to ensure that the resulting reflection values are within a preset tolerance.

Additionally, for the 2D PhC, it is important to resolve the rounded feature using a high-resolution real-space grid, as seen in Fig. 2.3. The same PhC can be expressed with two different unit cells, Fig. 2.3 (c) represents the same PhC as Fig. 2.2 (c) - the center of the unit cell is just translated by $(\Lambda_x/2, \Lambda_y/2)$. The staircase approximation to the rounded corner is evident in Fig. 2.3 (a), as the real-space grid is too coarse to define the rounded

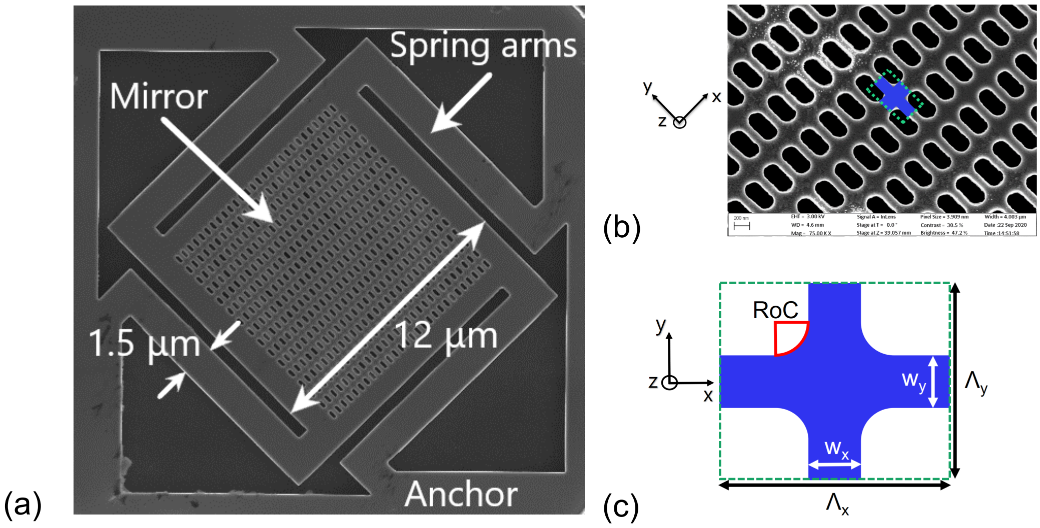

Figure 2.2: 2D PhC MEMS mirror. (a) Top view SEM image of the MEMS VCSEL showing the PhC mirror supported by four springs above an air-gap and the active laser material[51]. (b) Zoom in SEM image of the 2D grating of the MEMS mirror. The unit cell is highlighted in blue. (c) In-plane model of the unit cell showing all in-plane parameters.

feature properly. However, in Fig. 2.3 (c), the resolution is adequate in order to express the rounded feature smoothly. The convolution matrices in Fig. 2.3 (b) and (c) represent the coarse and high-density grid, respectively. The components in the off-diagonal will have more accurate values when the rounded corners are resolved.
The relative permittivity of a 2D periodic structure can be expressed through a Fourier series as follows:

$$\epsilon_r(x, y) = \sum_{m=-\infty}^{\infty} \sum_{n=-\infty}^{\infty} a_{m,n} \mathrm{e}^{\mathrm{j}2\pi\left(\mathrm{mx}/\Lambda_\mathrm{x} + \mathrm{ny}/\Lambda_\mathrm{y}\right)} \tag{2.1}$$

where $j^2 = -1$ is the imaginary unit and $a_{m,n}$ represents the m, n^{th} Fourier component of the relative permittivity. It is calculated as follows:

$$a_{m,n} = \frac{1}{\Lambda_x \Lambda_y} \int_{-\Lambda_y/2}^{\Lambda_y/2} \int_{-\Lambda_x/2}^{\Lambda_x/2} \epsilon_r(x, y) \mathrm{e}^{-\mathrm{j}2\pi\left(\mathrm{mx}/\Lambda_\mathrm{x} + \mathrm{ny}/\Lambda_\mathrm{y}\right)} \mathrm{dxdy} \tag{2.2}$$

A similar approach is followed for the calculation of relative permeability, which is equal to 1 in this case.

To obtain accurate results using the RCWA method for the rounded corners, it is important to calculate the Fourier expansion coefficients with high precision. This is done by discretizing the real-space grid into a very high-density grid, such as 1024 $\times$ 1024 grid points. The Fourier harmonic components of the permittivity and permeability are then calculated using a discrete Fourier transform function, which is rearranged using MATLAB's fftshift. To ensure converged reflection values, it is important to use a large number of harmonic components and a fine discretized space. Finally, the Fourier harmonic components are arranged in convolution matrices for relative permittivity and relative permeability.

In order to simulate a 1D PhC, a 2D simulation domain can be used. However, in order to simulate a 2D PhC, a 3D simulation domain is required. This drastically increases the

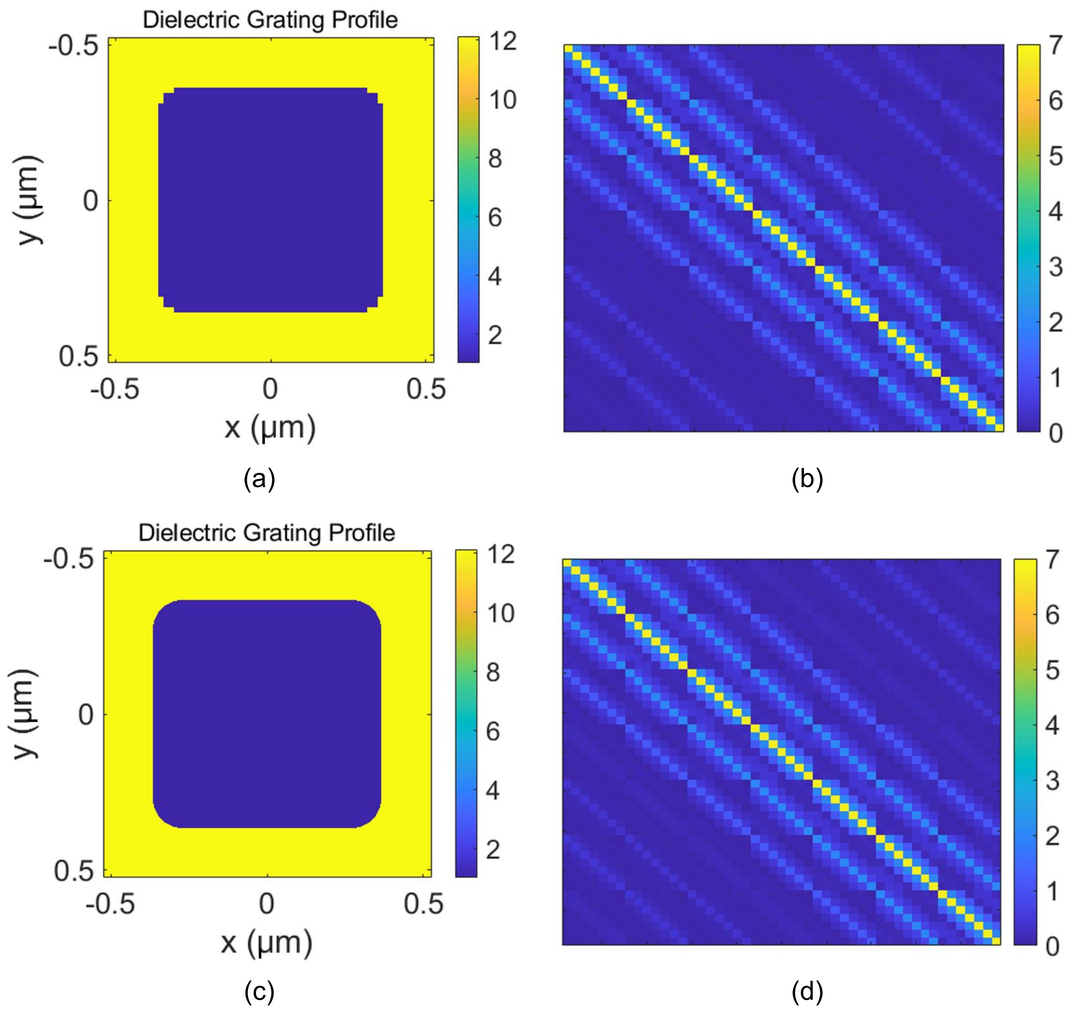

Figure 2.3: Dielectric grating profile of a 2D PhC with a grid resolution of 64×64 (a) and 1024×1024 (c). Corresponding convolution matrices for a grid resolution of 64×64 (b) and 1024×1024 (d).

computational load, i.e., computation time and memory. In Fig. 2.4, the convergence of a 1D and 2D PhC are shown. The y-axis shows the absolute difference in reflection values (% points) between the calculated reflection value using the number of harmonics (N), ($N_x = N_y$) for the 2D PhC, and the reflection value calculated with the highest number of harmonics. The inset in Fig. 2.4 shows a zoom-in, and it is clearly seen that in order to reach an absolute difference of 0.001% points, one needs a far greater number of harmonics for a 2D PhC (37) compared to a 1D PhC (15), i.e., the 2D simulation converges faster than the 3D simulation. The convergence result for the 1D PhC was generated using rigorous optical diffraction software (RODIS)[54], developed by Bart Dhoedt during his Ph.D. at Ghent University, while the 2D PhC was simulated with an in-house developed RCWA code.
A snippet of the 2D PhC RCWA code can be seen in Listing 2.1.

```
%% Device parameters
Lx = 311*nm; % Period in the x-direction
Ly = 634*nm; % Period in the y-direction
w = 168*nm; % Width in the x-direction
```

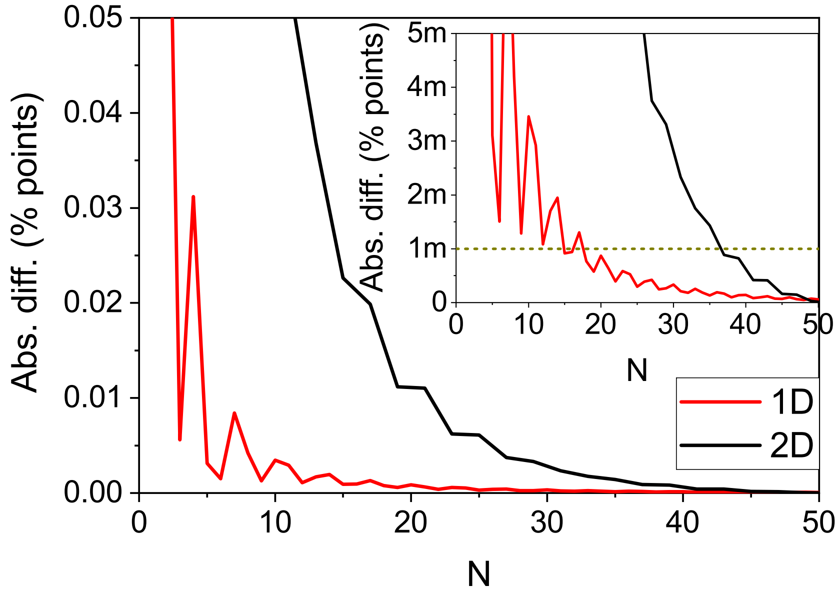

Figure 2.4: Absolute difference between calculated reflection values for different number of harmonics (N), ($N_x = N_y$) for 2D PhC, compared to the highest number of harmonics, for a 1D and 2D PhC.

```
cw = 241*nm; % Width in the y-direction

%% RCWA parameters
Px = 1024;  % Number of points along x in real-space grid
% Number of points along y in real-space grid
Py = round(Px*Ly/Lx);
if mod(Py,2) == 1
    Py = Py + 1;
end
dx = Lx/Px; % Grid resolution along x
dy = Ly/Py; % Grid resolution along y
xa = (0:Px-1)*dx; % x axis array
xa = xa - mean(xa); % Center x axis at zero
ya = (0:Py-1)*dy; % y axis array
ya = ya - mean(ya); % Center x axis at zero

for ii = 1:leng_RoC_vec
     RoC = RoC_vec(ii); % Sets the radius of curvature
     parfor jj = 1:leng_wave_vec
        wave0 = wave_vec(jj); % Sets the wavelength
        k0=2*pi/wave0; % Wavenumber
        n = Si(wave0); % Silicon dispersion function
        erd = n^2; % Permittivity of device
        er1 = 1.0; % Permittivity of air

        Nx = 21; % Number of harmonics in the x direction
        Ny = 21; % Number of harmonics in the y direction
```

```
32
33          Shape = 'Rounded_Cross';
34          % Generate the \acrshort{PhC} in permittivity space
35          ER(:,:,1) = permittivity_function(Shape,erd,er1,Px,Py,xa
               ,ya,dx,dy);
36
37          % Constructs convolution matrices from real space grid
38          ERC(:,:,1) = convmat(ER(:,:,1),Nx,Ny);
39
40          % Calculates reflectivity and transmission values
41          [R,T] = \acrshort{PhC}_2D_function(wave0,Lx,Ly,ERC,Nx,Ny
               ,k0);
42
43          REF(ii,jj) = R; % Generates reflectivity matrix
44          TRN(ii,jj) = T; % Generates transmission matrix
45
46      end
47  end
```

Listing 2.1: Example of parfor loop used in reflectivity matrix calculations.

In Listing 2.1, it is assumed that a vector containing the different RoC values and a vector for the different wavelengths is defined. The number of points in the real-space grid in the x direction is defined as $P_x = 1024$, and subsequently, the number of points along the y direction is defined so that the grid resolution becomes roughly the same in both directions, see lines 10 to 13. Inside the two nested loops, the number of harmonics, N_x and N_y (x-axis in Fig. 2.4) are set in the x and y directions, respectively. Thereafter the unit cell is defined, and a convolution matrix is formed. Finally, the reflection and transmission are calculated.
The convergence difference between 1D and 2D PhC is exacerbated when one calculates a reflection matrix by independently changing two variables, as is done later in this chapter. This is because the number of calculations in a matrix scales as n^2, where n is the number of calculations, as seen in Listing 2.1. Even with access to high-performance computing, one has to accept a higher degree of inaccuracy when modeling 2D PhC compared to 1D. For PhC lasing, a typically required mirror reflection is 99.5%[55], however in order to not meet the maximum allowed memory (512 GB) of the available cluster, when calculating the reflectivity matrices, the reflectivity requirement is lowered to 99.4%, in order not to underestimate the reflection of the simulated mirrors.

If one designs a 2D PhC crystal with rectangular air holes, i.e., with an RoC $=$ 0 nm, irrespective of the lithography and etching used, the corners of the rectangle will become rounded. For this reason, the RoC becomes a design parameter rather than a being a consequence of fabrication imperfection.
Table 2.1 presents the design parameters for two polarization-dependent designs that are optimized for high reflectivity for the electric field polarized along the x-direction. The designs, designated as A and B, have different radii of curvature, with design A having an ideal zero radius of curvature and design B having a more manufacturable radius of curvature of 54 nm. Both designs are modeled as GaAs[56] suspended in air and have in-plane parameters optimized for a large reflectivity bandwidth, with a requirement of more than 99.4% reflectivity. The high index footprints of the two designs are 0.151 μm^2 and 0.143 μm^2 for designs A and B, respectively. The rounded corners are included in the

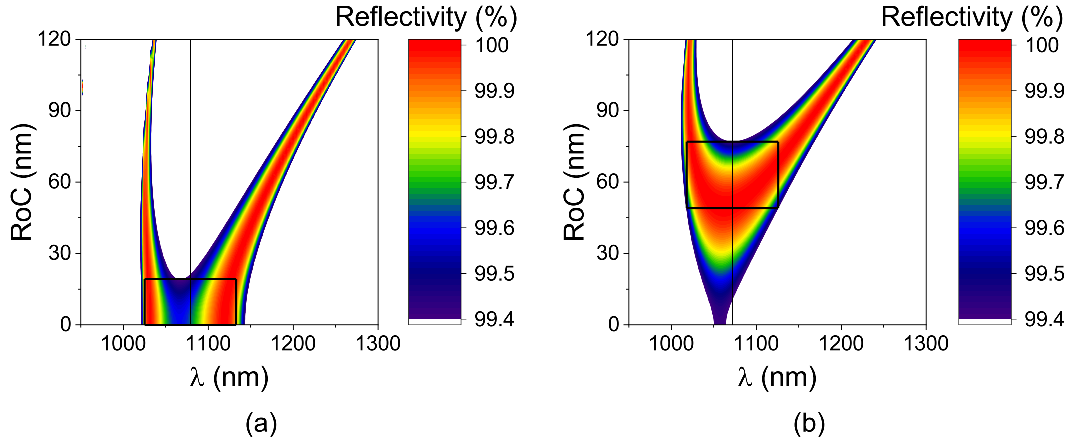

Figure 2.5: Reflectivity matrices as a function of RoC and wavelength for design A (a) and design B (b).

high index area of design B.

In Fig. 2.5, a rectangle highlights the region in which the reflectivity is above 99.4% within

Table 2.1: Design parameters for design A and B.

Design	t_g (nm)	Λ_x/Λ_y (nm)/(nm)	w_x/w_y (nm)/(nm)	RoC (nm)	Materials
A	280	334/618	180/259	0	GaAs/air
B	280	311/634	168/241	54	GaAs/air

a 10% fractional bandwidth (FBW, $\Delta\lambda/\lambda_c$) around the center wavelength λ_c.

Design A in Fig. 2.5 (a) meets the 10% FBW criterion with a RoC between 0 and 19 nm, while design B in Fig. 2.5 (b) meets the criterion between 49 and 76 nm. The impact of rounded corners on the reflectivity spectrum is significant, as they add to the high index footprint. Typically, increasing the RoC leads to an initial increase in the high reflectivity bandwidth on the long wavelength side. However, a further increase will cause the reflectivity dip in the center to drop below the high reflectivity criterion of 99.4%. In the case of design B, which has a small high index footprint (excluding RoC), the RoC must be included in the design to meet the broadband reflectivity criterion. This highlights the existence of a high index footprint window for broadband reflection.

The RoC has the interesting property that it incrementally adds/subtracts high index footprint area in infinitesimal steps. The RoC reveals that there exists a high index footprint window (minimum and maximum) where there is high broadband reflection. Since design B is optimized for a RoC of 54 nm, decreasing the RoC decreases the high reflection bandwidth. When a fractional bandwidth criterion is set (10%), decreasing RoC will eventually lead to a fractional bandwidth below the criterion. This will set a general minimum high index footprint value. On the other side of the high index window, we have design A optimized for RoC of 0 nm, where the addition of RoC will eventually lead to fractional bandwidth below the criterion. This will set a maximum high index footprint value.

Fig. 2.6 shows how the center wavelength is defined. The FBW shown in Fig. 2.6 is 11.4%, i.e., higher than the FBW requirement of 10% because the design lies within the rectangle on Fig. 2.5. The bottom horizontal line on Fig. 2.5 defines where the FBW criterion is initially met and also fixes the center wavelength λ_c.

By scaling designs A and B, it is possible to wavelength scale the designs in order to find

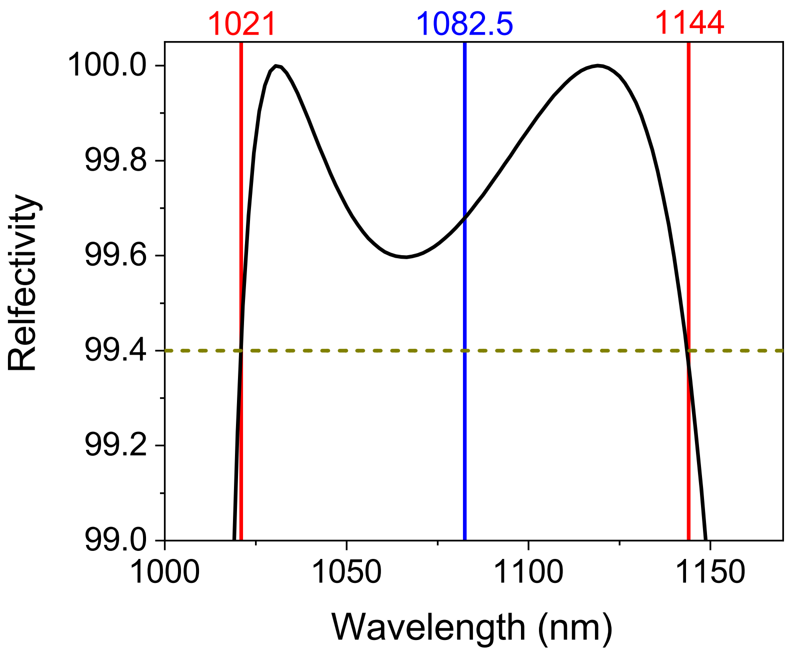

Figure 2.6: Reflectivity as a function of wavelength. The red vertical lines highlight the wavelengths where the reflectivity crosses the 99.4% dashed line. The center wavelength (blue line) λ_c is then the wavelength located between the two red lines.

the high index footprint window at other wavelengths as well. In addition, by normalizing the wavelength with the refractive index[56], one gets the wavelength inside the medium:

$$\lambda_m = \frac{\lambda_0}{n(\lambda_0)} \tag{2.3}$$

where λ_0 is the free space wavelength and n is the wavelength dependant refractive index. Finally, the volume (including the four rounded corners) of the 2D PhC high index material is normalized to the center medium wavelength $\lambda_{c,m}^3$. The result can be seen in Fig. 2.7. The results span from $\lambda_{c,m}$ from 250 nm to 500 nm, which translates to a free space wavelength λ_0 from 950 nm to 1550 nm. The lines in Fig. 2.7 are fitted to the maximum and minimum 2D PhC high index volumes/$\lambda_{\mathrm{c,m}}^3$. The lines represent an upper and lower limit enforced by the 10% FBW criterion. Thus, in order to fabricate broadband functional 2D PhC mirrors for VCSELs, rounded corners must be incorporated into the design. In addition, the high index volume/$\lambda_{\mathrm{c,m}}^3$ must lie between the lines in Fig. 2.7, in order to have a FBW $\geq$ 10%. The figure can be a guideline for high index volume when designing high broadband reflection 2D PhC MEMS at a desired center wavelength.

When modeling with RCWA an incident plane wave is assumed, i.e. no curvature of the wavefront. In addition, since a periodic boundary condition is assumed, the mode size is infinite. However, the fundamental mode in VCSEL is approximately Gaussian, with curvature and a finite mode or spot size. In order to avoid reflectivity trenches and accommodate the finiteness of the mode, plane wave reflectivity maps of tilted incidence is recommended[57]. Fig. 2.8 shows the reflectivity bandwidth of design A (a) and design (b) for different incidence angles (θ).

As indicated, design B in Fig. 2.8 (b), with a RoC of 54 nm, maintains broadband reflection for higher incidence angles, compared to design A in Fig. 2.8 (a), with an unrealistic RoC of 0 nm.

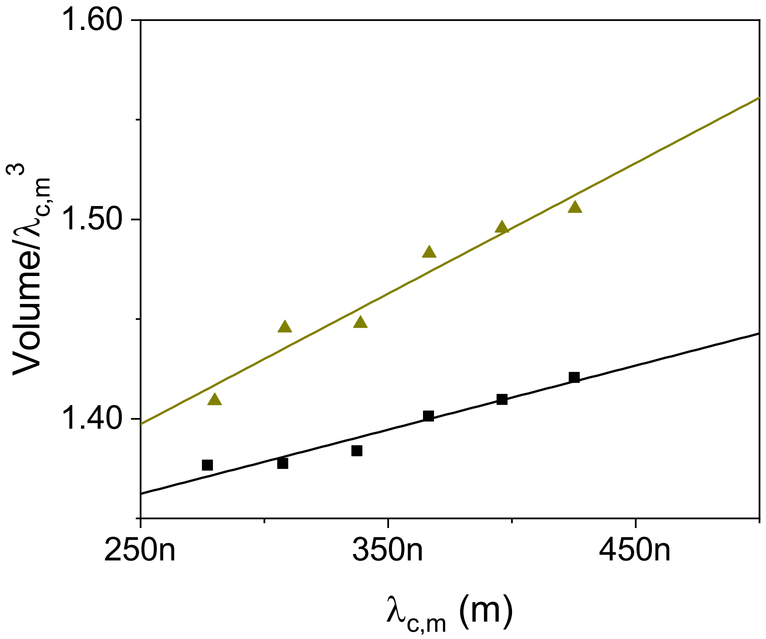

Figure 2.7: Volume of the PhC high index material normalized to $\lambda_{c,m}^3$ as a function of $\lambda_{c,m}$.

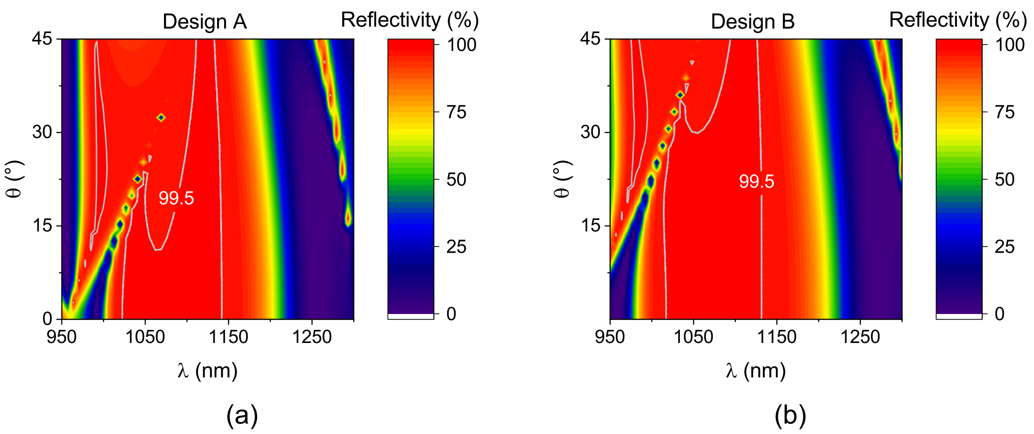

Figure 2.8: Reflectivity matrices as a function of incidence angle and wavelength for design A (a) and design B (b).

The equivalent angular spectral width of the Gaussian mode is given by[57]:

$$\theta_{\text{eq}} = \text{arcsin}\left(\frac{1}{\sqrt{2\pi}}\frac{\lambda}{2w}\right) \tag{2.4}$$

where $\lambda = 1060$ nm is the wavelength, $w = 8$ μm (single mode[29]) is the width of the Gaussian mode, resulting in an equivalent angular spectral width of $\theta_{\text{eq}} = 1.5°$, which is far beneath the limit of design A and B shown in Fig. 2.8.

It has been demonstrated[58] that HCG designs exhibiting high incident angular behavior, meaning that reflectivity decreases with increasing incidence angles, can effectively suppress higher-order transverse modes. This is because higher-order modes tend to emit at larger angles. Mode control in the HCG is advantageous compared to oxide aperture

mode control since the location of the anti-node of the standing wave changes when the mirror is tuned, i.e., the position of the electric field anti-node relative to the oxide aperture changes during wavelength tuning, resulting in wavelength dependant mode control. In contrast, if the mode control is confined to the movable mirror, the mode control would not be wavelength dependant. However, relying on mirror parameters for mode control would require great control of the fabricated parameters. Design A and B would not be suitable candidates for mode control since their bandwidths are maintained for considerable high incidence angles.
In order to ensure that the duty cycle in the x-direction is not at the edge of a reflectivity trench, the reflectivity matrix is calculated for a variety of widths in the x-direction as a function of wavelength for several incident angles, see Fig. 2.9 for design A, and 2.10 for design B.
As shown in Fig. 2.9, design A maintains the bandwidth $\leq 10°$, cutting the bandwidth in two halves. A reflectivity trench approaches the lower end of the bandwidth at high incidence angles $\theta = 20°$.
As shown in Fig. 2.10, design B maintains the same bandwidth up to an incident angle of 30 degrees, which makes design B more resilient to reflectivity trenches compared to design A.

2.3 Finite element method

The finite element method (FEM)[59] is a numerical technique used to solve partial differential equations that describe physical problems. It involves dividing the problem domain into smaller elements, called "finite elements," and then finding approximations of the solution within each element. The global solution to the problem is obtained by assembling the individual element solutions. The main advantage of FEM is its versatility and ability to handle complex geometries, material properties, and boundary conditions. An example mesh of a 2D PhC can be seen in Fig. 2.11.

The FEM tool used in this thesis is COMSOL Multiphysics[60], more specifically, the structural mechanic's module, using solid mechanics physics. An eigenfrequency solver was used in order to find the resonant frequency of the system using fixed boundary conditions at the mirror anchoring positions; see Fig. 2.2 (a).
The most critical meshing parameter is the maximum mesh element size. In order to ensure converged resonant frequencies values, a convergence test has to be performed; see Fig. 2.12. In Fig. 2.12 $f_{\text{res}}^{\text{d}}$ refers to the resonant frequency calculated for the densest mesh (maximum mesh element size of 140 nm), and $f_{\text{res}}^{\text{mesh}}$ refers to the calculated resonance frequency for all the different mesh sizes shown. As evident in Fig. 2.12, in order to ensure below 1% deviation in resonant frequency value, the maximum element size must be below 900 nm for both the fundamental, shown in Fig. 2.13 (b), and fifth mechanical mode, shown in Fig. 2.15 (b).

The resonant frequency of the fundamental mode is slightly lower for the 2D PhC MEMS compared to the HCG MEMS, as is evident in Fig. 2.13. The reason for this is that due to the presence of the crossbars, the mass of the MEMS is slightly larger for the PhC compared to the HCG, which decreases the resonance frequency, as indicated by Eq. (1.7).
The MEMS has multiple mechanical modes of operation, with the most commonly desired one being the fundamental mode, also known as the piston mode, where the spring arms bend out of the plane, and the mirror stays flat, shown in Fig. 2.13. Other modes, such as the anti-symmetric mode where the mirror membrane is twisted, see Fig. 2.14 and

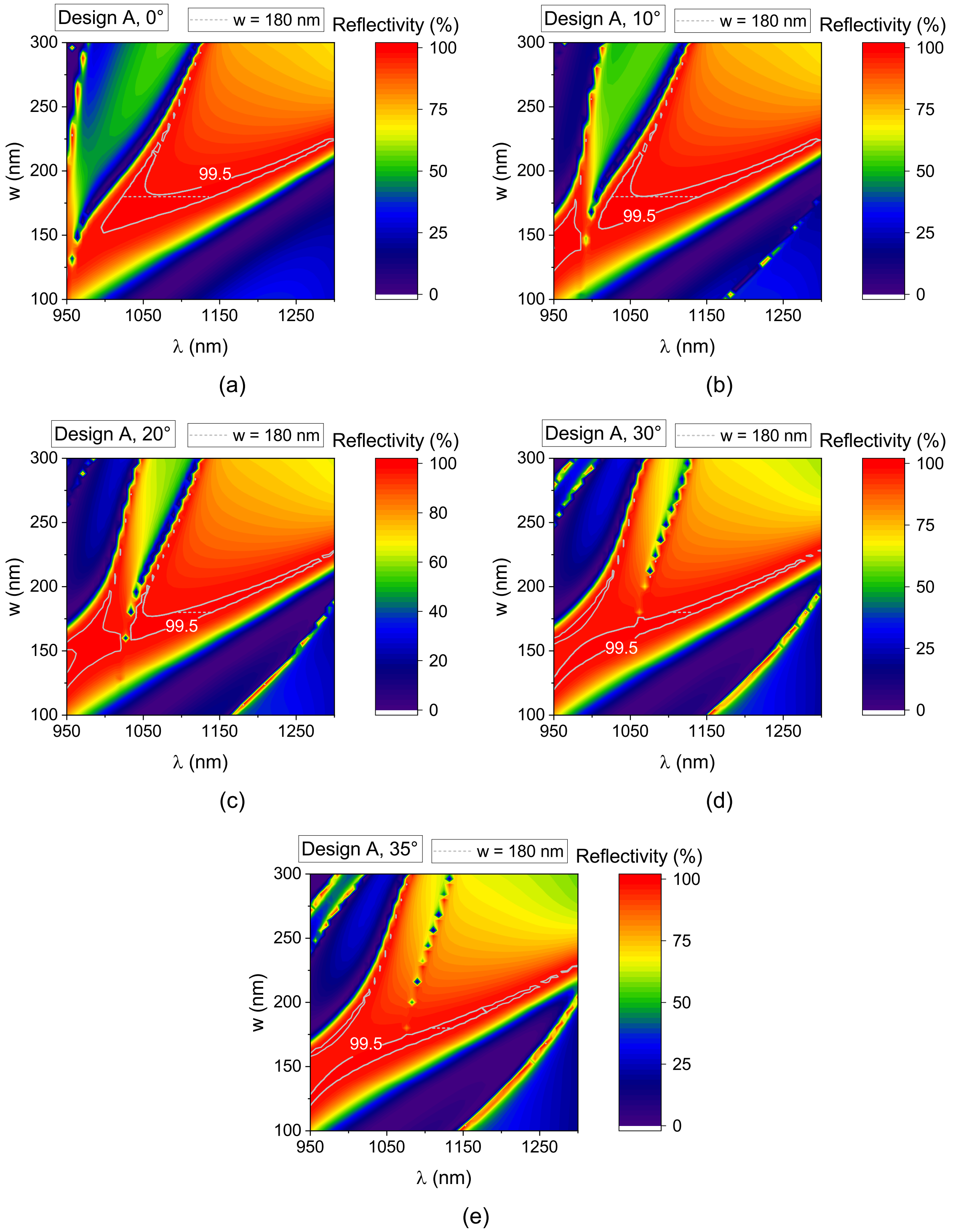

Figure 2.9: Reflectivity matrices for different widths as a function of wavelength for incidence angles of 0, 10, 20, 30, and 35 degrees, for (a), (b), (c), (d), and (e), respectively. The contour lines highlight reflectivity of 99.5%, and the dashed line indicate design A $w_x = 180$ nm.

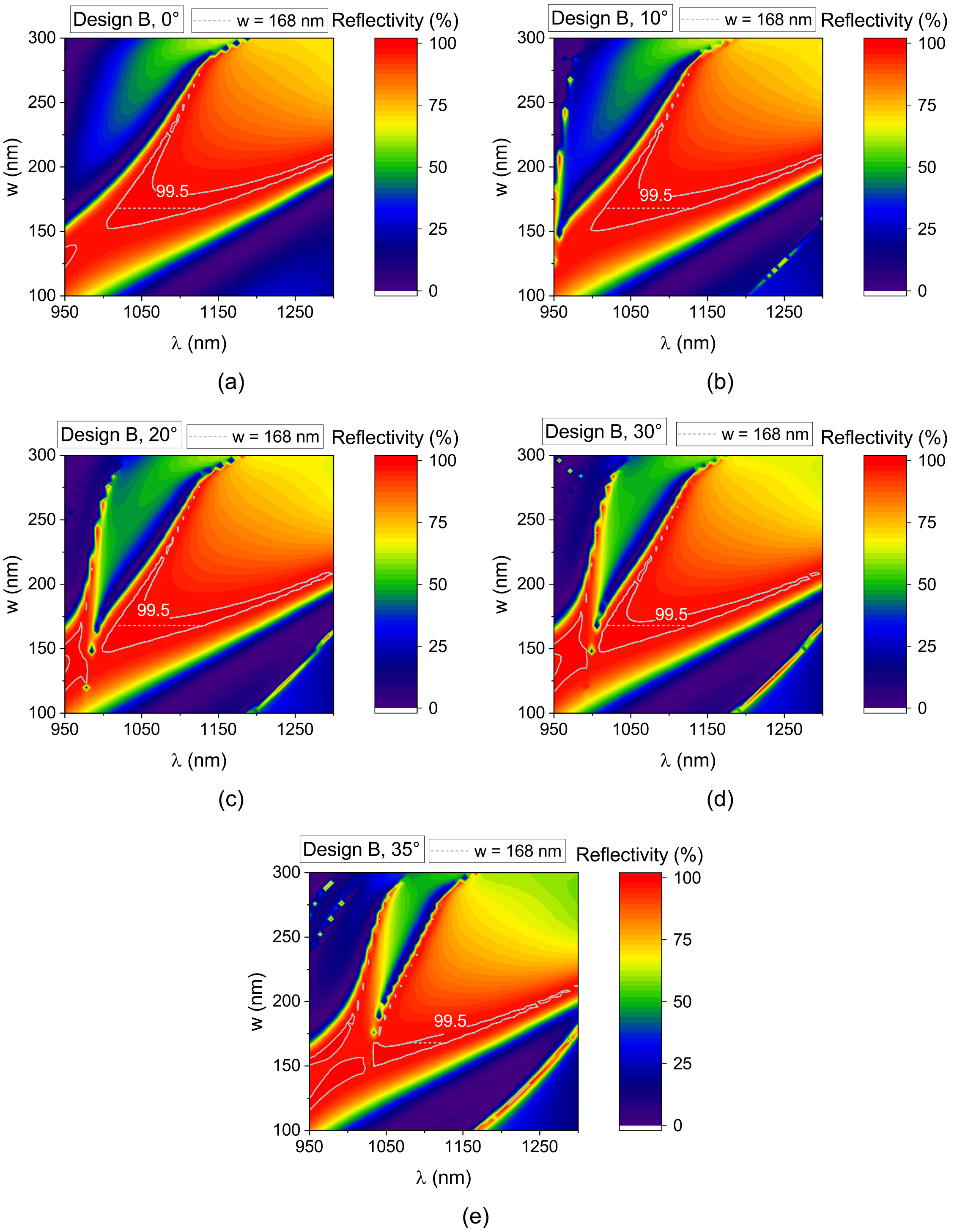

Figure 2.10: Reflectivity matrices for different widths as a function of wavelength for incidence angles of 0, 10, 20, 30, and 35 degrees, for (a), (b), (c), (d), and (e), respectively. The contour lines highlight reflectivity of 99.5%, and the dashed line indicate design B $w_x = 168$ nm.

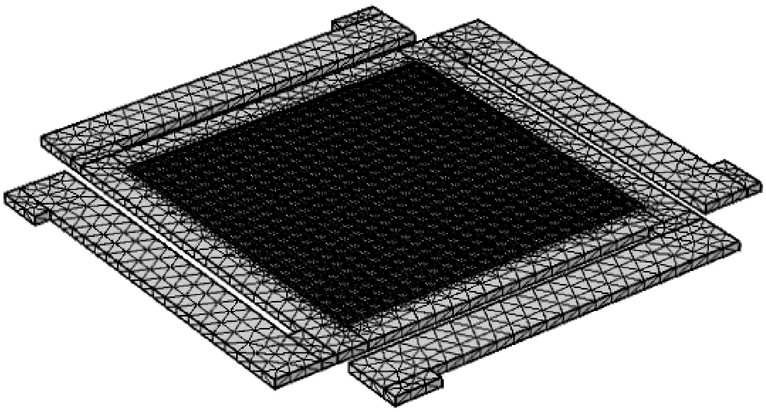

Figure 2.11: Mesh of a PhC MEMS using tetrahedral meshing.

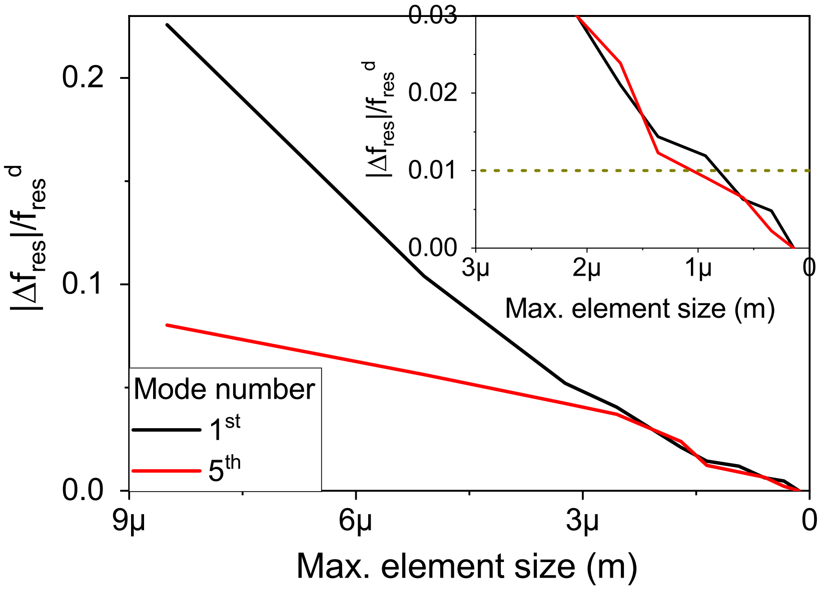

Figure 2.12: Absolute difference $|\Delta f_{\text{res}}|$ between the resonant frequency of the densest mesh $f_{\text{res}}^{\text{d}}$ and the max. mesh element size relative to the resonant frequency of the densest mesh (Δf_{res}) as a function of max. mesh element size.

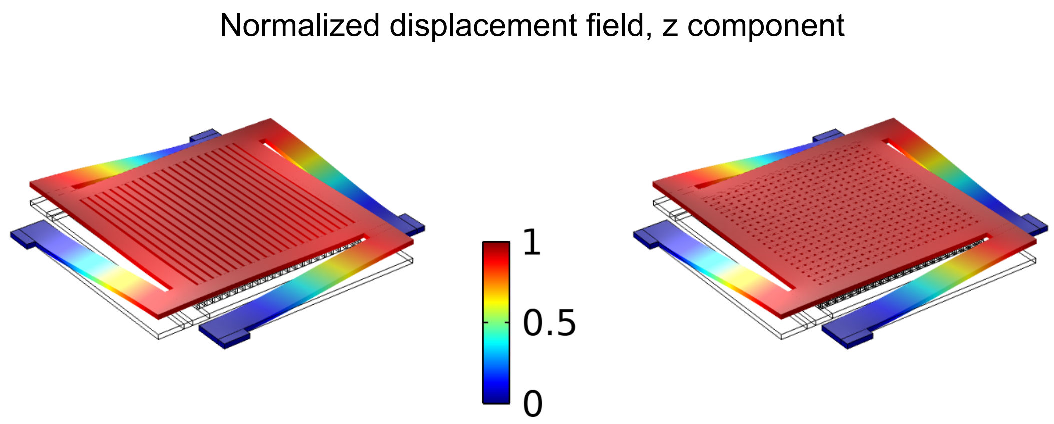

(a) $f_{\text{res}} = 859$ kHz (b) $f_{\text{res}} = 829$ kHz

Figure 2.13: Spatial (x,y,z) mode shape of the fundamental mechanical mode of a 1D (a) and 2D (b) PhC MEMS. The color legend shows the normalized z component of the displacement field.

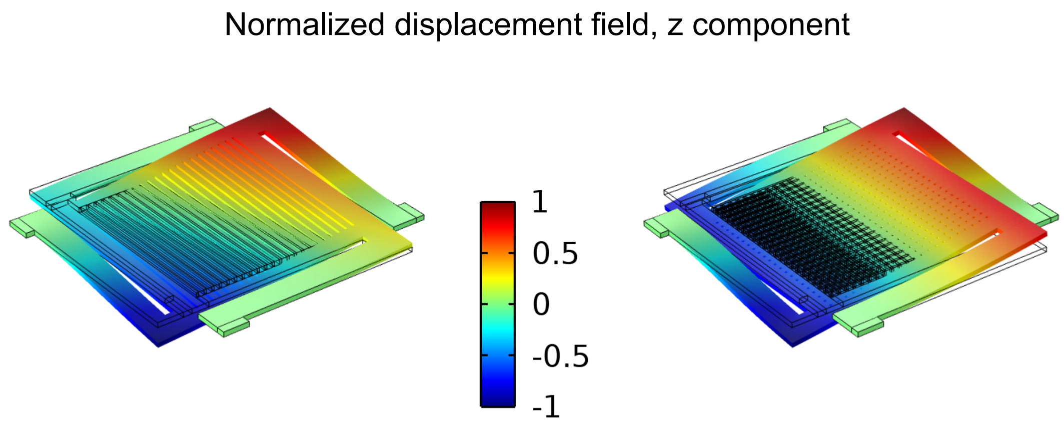

(a) $f_{\text{res}} = 1.2$ MHz (b) $f_{\text{res}} = 1.3$ MHz

Figure 2.14: Spatial (x,y,z) mode shape of the second mechanical mode of a 1D (a) and 2D (b) PhC MEMS. The color legend shows the normalized z component of the displacement field.

symmetric higher order modes where the arms and membrane bend, are to be avoided in MEMS-based VCSELs as they limit the imaging range due to thermal vibrations[61]. Fig. 2.15 shows the first symmetrical higher order, or plate bending, mode. The 2D grating has a higher mechanical stiffness than the 1D elongated bars, which results in a higher first symmetrical higher order mode resonance frequency and less bending of the membrane, with the bending being more uniform.
As seen in Fig. 2.16, the mode spacing is much closer together for a 1D HCG than a 2D PhC. The fifth eigenmode's resonance frequency is 3.4 MHz for a 1D and 5.6 MHz for a 2D PhC. Despite having more symmetric modes due to the uniformity of a 2D PhC MEMS, the first plate bending mode (mode 5) has a significantly increased eigenfrequency.

Figure 2.17 illustrates the optical spectra of a PhC MEMS VCSEL[51][40] with the 2D PhC shown in Figure 2.2, at various applied MEMS voltages. The total wavelength tuning bandwidth is limited since the pattern transfer was outside the ideal case of Fig. 2.5 with a radius of curvature around 19 nm instead of 0 nm. Hence at 30 V, the Fabry-Perot cavity

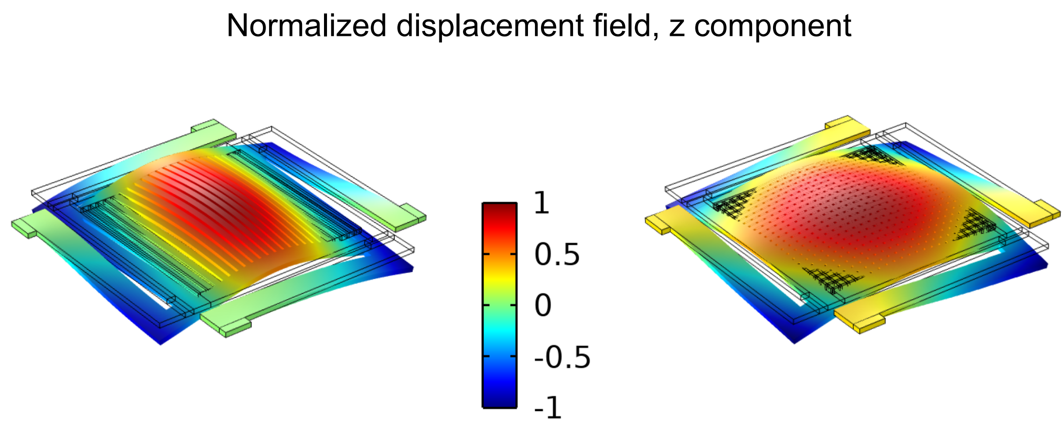

(a) $f_{\text{res}} = 3.4$ MHz (b) $f_{\text{res}} = 5.6$ MHz

Figure 2.15: Spatial (x,y,z) mode shape of the fifth mechanical (second symmetric) mode of a 1D (a) and 2D (b) PhC MEMS. The color legend shows the normalized z component of the displacement field. The 2D PhC mirror has a higher membrane stiffness ($f_{\text{res}} = 5.6$ MHz) due to its mesh, while the long beams of the 1D result in a lower membrane stiffness ($f_{\text{res}} = 3.4$ MHz).

length is outside the lasing region, and the peak is close to the amplified spontaneous emission. Optimizing for the 54 nm RoC the 99.4% reflection bandwidth of 116 nm as shown in Fig. 2.5 (b) is expected to be achievable.
The static linewidths can be seen in Fig. 2.17, which remain constant for different DC biases. However, if the first higher order symmetric mode is excited, this would potentially increase the dynamic linewidth since this wavelength noise would occur intrasweep, i.e., faster than the wavelength sweep rate. Expressed differently, the excitation of the symmetric higher order mode would result in an uncontrolled wavelength sweep, where the wavelength does not monotonically decrease (increase) for a down (up) MEMS sweep but rather oscillates around a decreasing (increasing) wavelength value.

2.4 Reduced MEMS noise

The MEMS mirror may not move smoothly due to various causes, including thermal motion, Brownian motion, electromechanical transients, and mechanical mode-mixing. If the MEMS and the laser diode share an electrode, fluctuations in the laser driving signal can also result in tuning jitter. The criticality of the tuning jitter depends on the amplitude and time scale of the jitter relative to the sweep rate of the MEMS tunable VCSEL, with intrasweep jitter being more harmful for OCT compared to inter-sweep jitter[62].

The mechanical modes of the MEMS will have thermal linewidth associated with them due to the finite temperature of the MEMS, as determined by the equipartition theorem, given by[63]

$$\Delta\nu_{\text{RMS}} = \frac{2\text{FSR}}{\lambda}\sqrt{\frac{k_B T}{K}} \tag{2.5}$$

where FSR is the free spectral range of the optical cavity (30 THz), λ is the wavelength (1060 nm), k_B is the Boltzmann constant, T is the temperature, and K is the spring constant of the mechanical mode. At room temperature, the thermal linewidth of the fundamental mechanical mode ($K = 8.45$ N/m) is 1.24 GHz. The linewidth can be reduced by increasing the stiffness of the MEMS, but the maximum stiffness is limited by the first

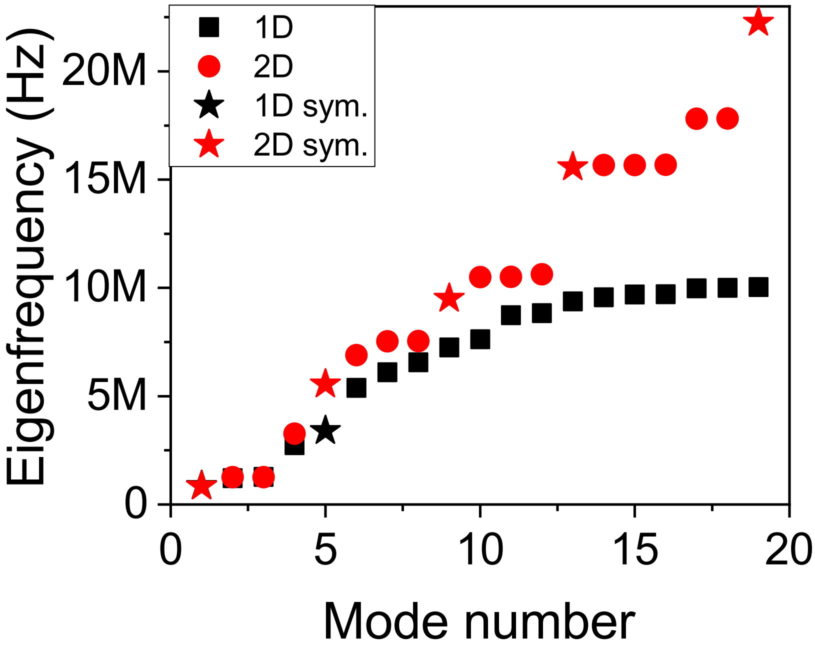

Figure 2.16: Resonance frequency against the mode number for 1D and 2D PhC MEMS. The stars indicate symmetrical modes.

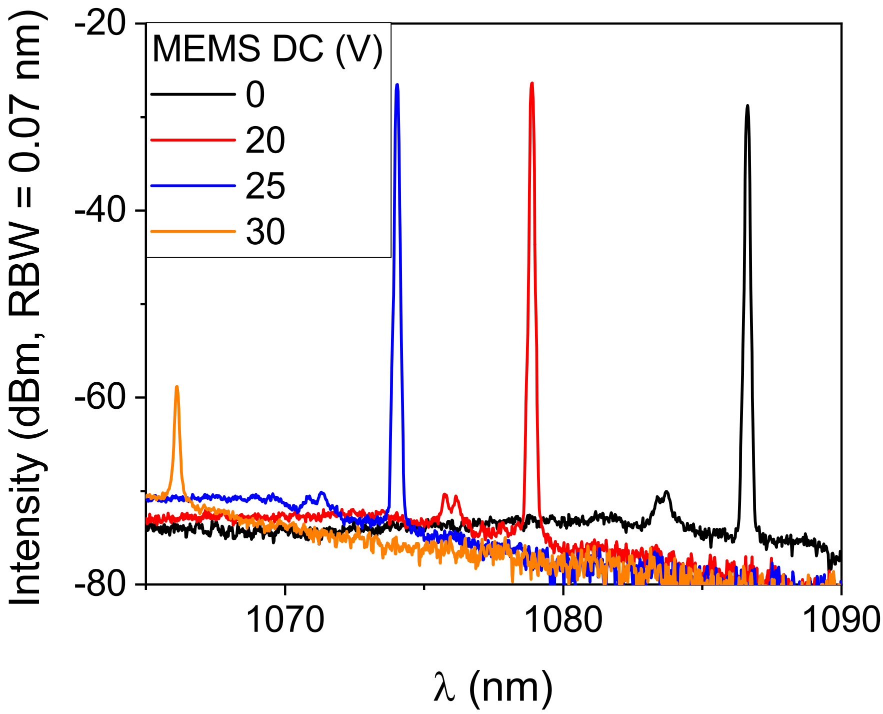

Figure 2.17: Four PhC MEMS VCSEL spectra with the DC voltage of 0, 20, 25, and 30 V.

plate bending mode, which is stiffer for a 2D PhC.

Brownian motion can be caused by impinging air molecules on the membrane and can be enhanced at the mechanical resonance of the MEMS. By packaging the MEMS VCSEL in a vacuum, the Brownian noise can be reduced, and the quality factor of the resonant mechanical modes can be increased, reducing the required alternating actuation voltage and narrowing the noise spectrally. However, transients may become an issue due to the increased quality factor of the resonances.

The intra-sweep intensity noise, also referred to as sliding relative intensity noise, can negatively affect the dynamic range of the OCT system[62]. Charge carrier dynamics are in the nanosecond regime, while MEMS capacitive dynamics are in the milli- to microsecond regime, so it can be assumed that only symmetrical modes can be excited by electrostatics. Forced oscillations using a high bandwidth arbitrary waveform can excite multiple symmetric resonances simultaneously, including higher-order symmetrical modes, which can cause intra-sweep wavelength noise due to mechanical mode mixing. However, due to the innate robustness of a 2D PhC, the higher-order mechanical modes are pushed up in frequency, reducing the spectral overlap between the forced oscillation and the higher mechanical modes.

The use of a robust 2D PhC for MEMS VCSELs offers improved design and optimization opportunities. The design of the 2D PhC unit cell can be adjusted to suit the requirements of any fabrication process as long as the rounded corners remain consistent in size. By analyzing the results of a fabrication test run, the in-plane parameters can be optimized to achieve a wide bandwidth with high reflection. Additionally, the increased mechanical stability of a 2D PhC MEMS has the potential to reduce intra-sweep wavelength noise, which is critical in improving the dynamic range for applications such as SS-OCT and LiDAR.

3 Bidirectional electrostatic actuator

This chapter is based on the draft manuscript to Optica; the draft can be seen in the Appendix A.2.
This chapter outlines the effect of using bidirectional MEMS configurations. The main results are the tunability of the MEMS instability voltage by the applied outer voltage, realizing the actuation of ultra-stiff MEMS with modest MEMS voltage. In addition, the increased effect of electrostatic spring softening in the bidirectional configuration can be taken into the design phase in order to design for a targeted actuation frequency.

3.1 Introduction and motivation

Due to their lightweight, high contrast grating (HCG) microelectromechanical systems (MEMS), vertical cavity surface emitting laser (VCSEL) have enabled ultra-fast swept source (SS) optical coherence tomography (OCT)[28][50].
Due to the parallel plate capacitor configuration, see Fig. 2.1, the movement of the MEMS is nonlinear in relation to the applied voltage, which necessitates an optical k-clock in order to linearize the wavelength sweep.
The broader the tunability of the swept source, the greater the axial resolution of the OCT image; in addition, faster image acquisition minimizes motion blur. In order to get a fast and broadbanded MEMS VCSEL , one has to actuate the MEMS close to the fundamental resonance frequency, shown in Eq. (1.7).
The Doppler-assisted tuning is only limited by the tuning speed of the movable MEMS mirror[45], i.e., in order to increase the sweep rate, one can design a stiff MEMS (large k) resulting in a high resonant frequency (ω_0), given by Eq. (1.7).
However, the stiffer the MEMS, the higher the instability voltage becomes[64]:

$$V_{\text{PI}} = \sqrt{\frac{8kg_0^3}{27\epsilon A}} \tag{3.1}$$

where, g_0 is the initial air gap, ϵ is the permittivity of the air gap, and A is the area of the MEMS electrodes. In order to actuate the MEMS to the maximum excursion ($g_0/3$), for moderate quality factors, the alternating voltage has to be in the vicinity of the pull-in voltage given by Eq. (3.1).
If one designs a MEMS with a fundamental resonance frequency in the MHz regime, the pull-in voltage easily reaches hundreds of volts. This poses an actuation problem since the maximum available actuation voltage from an arbitrary waveform generator (AWG) is 10 V peak to peak. There exist high voltage amplifiers. However, they are limited in the bandwidth of the driving signal, as well as having a limiting slew rate - Slew rate limitation can result in distortion of the post-amplified waveform, resulting in unpredictable MEMS movement.
As is evident from Eq. (3.1), given a desired stiffness k, there are two ways to lower the pull-in voltage, decreasing the air gap size or increasing the area. Decreasing the air gap size leads to a decrease in the maximum displacement, which may reduce the tuning bandwidth well below the gain bandwidth of the multi-quantum well VCSEL , leading to a less-than-optimal tuning range. Increasing the area of the MEMS increases the mass, which in turn decreases the resonance frequency, as is evident by Eq. (1.7). In addition, increasing the MEMS area will lower the resonance frequency of higher-order symmetrical or plate-bending modes. If these modes are excited, it can give rise to unwanted mixing of mechanical modes, leading to an increase in laser dynamic linewidth resulting

in lower OCT imaging depth, see A.1.
In order to address the actuation problem a bidirectional actuator is proposed. The three-plate capacitor is realized using silicon photonics[30]. Fig. 3.1 (a) shows a schematic overview of the structure, Fig. 3.1 (b) shows a microscope image of the device. The de-

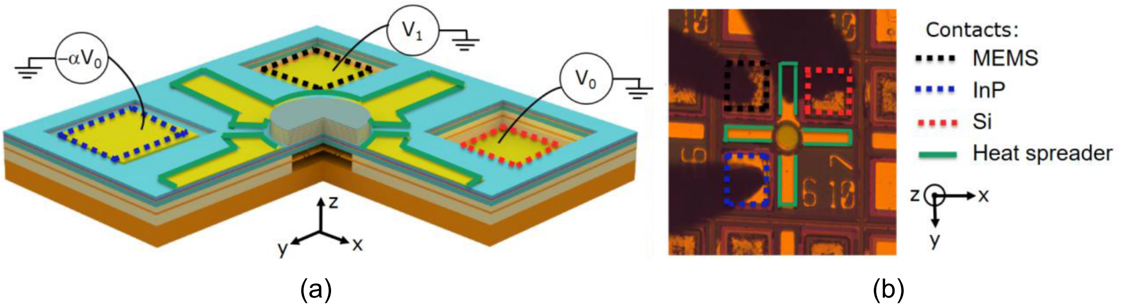

Figure 3.1: Highlighted metal contacts in a device schematic (a) and microscope image (b).

vice consists of an indium phosphide (InP) wafer bonded on a silicon-on-insulator (SOI) substrate. The laser cavity is defined between a top dielectric distributed Bragg reflector (DBR) mirror and a membranized bottom HCG mirror anchored to spring arms. The active material consists of eight quantum wells in indium phosphide above the top air gap. The bottom air gap below the HCG is defined by removing the buried oxide of the SOI, revealing the silicon substrate. The three contacts are highlighted in Fig. 3.1, V_0 $(-\alpha V_0)$ is the voltage on the static outer contacts, and V_1 is the MEMS voltage.

3.2 Derivation of equation of motion

In this section, different bidirectional electrostatic equations of motion are derived.

3.2.1 Bidirectional capacitive actuator

The system under consideration consists of two stationary electrodes (top-electrode located at $z = g_t$ with potential V_t and bottom-electrode located at $z = -g_b$ with potential V_b) and a movable electrode (mass m, spring constant k, and potential V_1) at the resting position $z = 0$, see Fig. 3.2. In the fabricated bidirectional MEMS VCSEL shown in Fig. 3.1, the top electrode is the indium phosphide layer above the top air gap, the bottom electrode is the silicon substrate below the bottom air gap, and finally, the movable center electrode is the silicon device layer of the silicon on insulator wafer, which has been patterned with a 1D HCG mirror and spring arms. All three electrodes have the same area A, and the permittivity of the space between the electrodes is ϵ, resulting in the capacitance of the top and bottom electrodes as[65]

$$C_t = C_t(z) = \epsilon A/\left(g_t - z\right) \text{ and } C_b = C_b(z) = \epsilon A/\left(g_b + z\right), \tag{3.2}$$

respectively.

The complete Hamiltonian of the system, including the capacitors, movable electrode, and electrical power sources, is expressed as[64]:

$$\begin{aligned} H\left(p, z\right) = {} & \frac{p^2}{2m} + \frac{1}{2}kz^2 + \frac{1}{2}C_t(V_t - V_1)^2 + \frac{1}{2}C_b(V_b - V_1)^2 + \\ & + \left[-C_t(V_t - V_1)^2 - C_b(V_b - V_1)^2 + H_{t1} + H_{b1}\right] \end{aligned} \tag{3.3}$$

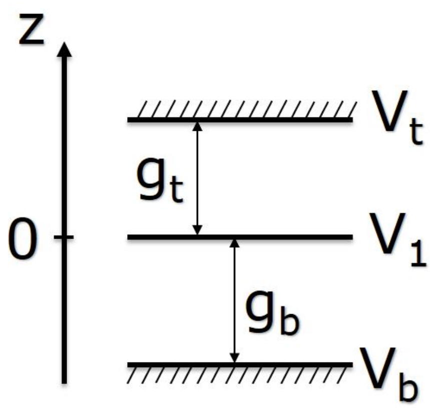

Figure 3.2: Two static outer electrodes, one top, and one bottom, surround a movable electrode in the middle.

where the first term is the kinetic energy (p is the momentum), the second term is the elastic energy stored in the spring, and the next two terms are the energy stored in the capacitors, while the terms in the square bracket are the stored energy in the two electrical power sources that apply the potential differences $V_t - V_1$ and $V_b - V_1$. When the power sources charge up the capacitors, they lose energy as seen in the expression in the square bracket, where H_{t1} and H_{b1} are the initial Hamiltonians of the power sources. When a capacitor C is charged to $Q = CV$ from a constant voltage source, the power source loses energy. The energy loss $\Delta H = -QV = -CV^2$, which is the difference between the energy gained by the capacitor $(CV^2/2)$ and the energy lost by the power source. This energy is typically dissipated as Joule heat in resistive connections or is radiated.

From Hamilton's equations, it follows that $\partial_t z = \dot{z} = \partial_p H(p, z) = p/m$, or $p = m\dot{z}$ as expected, and $\partial_t p = m\ddot{z} = -\partial_z H\,(p, z)$ This evaluates to:

$$m\ddot{z} = -kz + \frac{1}{2}(V_t - V_1)^2 \frac{\partial C_t}{\partial z} + \frac{1}{2}(V_b - V_1)^2 \frac{\partial C_b}{\partial z} \tag{3.4}$$

for a loss-less system.

In Eq. 3.4 the right-hand side represents the restoring force F_{rest}, which is zero at equilibrium position z_{eq}. However, the stability of z_{eq} depends on the sign of $\partial_z F_{\text{rest}}(z) = -k_{\text{eff}}$, where k_{eff} is the effective spring constant at the operating point. A positive k_{eff} indicates a stable system, while k_{eff} = 0 indicates a metastable system and $k_{\text{eff}} < 0$ indicates an unstable system. From Eq. 3.4 we get the stability condition

$$k_{\text{eff}} = k - \frac{1}{2}(V_t - V_1)^2 \frac{\partial^2 C_t}{\partial z^2} - \frac{1}{2}(V_b - V_1)^2 \frac{\partial^2 C_b}{\partial z^2} > 0, \tag{3.5}$$

which must be combined with the static equilibrium condition $F_{\text{rest}}(z_{\text{eq}}) = 0$, i.e.,

$$-kz_{\text{eq}} + \frac{1}{2}(V_t - V_1)^2 \left.\frac{\partial C_t}{\partial z}\right|_{z_{\text{eq}}} + \frac{1}{2}(V_b - V_1)^2 \left.\frac{\partial C_b}{\partial z}\right|_{z_{\text{eq}}} = 0 \tag{3.6}$$

to find the range of stable static operating conditions.

Adding dynamic losses (damping $b\dot{z}$) to Eq. 3.4, carrying out the differentiation and rearranging leads to

$$m\ddot{z} + b\dot{z} + kz = \frac{\epsilon A}{2}\left(\frac{(V_t - V_1)^2}{(g_t - z)^2} - \frac{(V_b - V_1)^2}{(g_b + z)^2}\right), \tag{3.7}$$

where the left-hand side represents the pure mechanical equation of motion and the right-hand side the electrostatic actuation.

3.2.2 Ideal symmetric actuator

Assuming a perfectly symmetric system with $g_t = g_b = g_0$, zero actuation occurs for $V_1 = 0$ V and $V_t = -V_b = -V_0$ (and also for $V_t = V_b$ which is not applicable in this case). Thus, for the perfectly symmetric system, we obtain:

$$m\ddot{z}/g_0 + b\dot{z}/g_0 + kz/g_0 = \frac{\epsilon A V_0^2}{2g_0^3}\left(\frac{(1+V_1/V_0)^2}{(1-z/g_0)^2} - \frac{(1-V_1/V_0)^2}{(1+z/g_0)^2}\right)$$

Assuming that $V_t = -V_b = -V_0$, the position is normalized to the gap g_0 and the actuation voltage V_1 to V_0. The expression can be fully non-dimensionalized as follows:

$$\frac{\ddot{z}/g_0}{\omega_0^2} + 2\zeta\frac{\dot{z}/g_0}{\omega_0} + z/g_0 = \frac{\epsilon A V_0^2}{2kg_0^3}\left(\frac{(1+V_1/V_0)^2}{(1-z/g_0)^2} - \frac{(1-V_1/V_0)^2}{(1+z/g_0)^2}\right) \tag{3.8}$$

where $\omega_0 = \sqrt{k/m}$ is the native resonant frequency of the mechanical system alone and $\zeta = b/\left(2\sqrt{km}\right)$ the damping ratio.

Using the same normalization, the stability criterion becomes

$$1 > \frac{\epsilon A V_0^2}{kg_0^3}\left(\frac{(1+V_1/V_0)^2}{(1-z/g_0)^3} + \frac{(1-V_1/V_0)^2}{(1+z/g_0)^3}\right), \tag{3.9}$$

from which it is apparent that with $V_1 = 0$ V, where $z_{\mathsf{eq}} = 0$ the system is only stable for $V_0^2 < kg_0^3/(2\epsilon A) = V_{\mathsf{0PI_{sym}}}^2$ where $V_{\mathsf{0PI_{sym}}}$ is the pull-in voltage of the symmetric device at zero actuation voltage V_1, henceforth referred to as outer pull-in voltage.
V_{0PI} is plotted in Fig. 3.3, as a function of stiffness ($k = m(2\pi f_0)^2$), where f_0 is the native resonant frequency of the MEMS, and initial air gap (z_0). As is evident, the stiffer the MEMS and the larger the initial air gap, the larger V_{0PI} will be.

The definition of V_{0PI} allows for further simplification of the normalized expression, i.e., the equation of motion

$$\frac{\ddot{z}/g_0}{\omega_0^2} + 2\zeta\frac{\dot{z}/g_0}{\omega_0} + z/g_0 = \frac{V_0^2}{4V_{\mathsf{0PI_{sym}}}^2}\left(\frac{(1+V_1/V_0)^2}{(1-z/g_0)^2} - \frac{(1-V_1/V_0)^2}{(1+z/g_0)^2}\right), \tag{3.10}$$

and the stability criterion

$$1 > \frac{V_0^2}{2V_{\mathsf{0PI_{sym}}}^2}\left(\frac{(1+V_1/V_0)^2}{(1-z/g_0)^3} + \frac{(1-V_1/V_0)^2}{(1+z/g_0)^3}\right). \tag{3.11}$$

Defining $u = z/g_0$, $v = V_1/V_0$ and $\Psi^2 = V_0^2/V_{\mathsf{0PI_{sym}}}^2$ the two equations simplify further to

$$\frac{\ddot{u}}{\omega_0^2} + 2\zeta\frac{\dot{u}}{\omega_0} + u = \frac{1}{4}\Psi^2\left(\frac{(1+v)^2}{(1-u)^2} - \frac{(1-v)^2}{(1+u)^2}\right), \tag{3.12}$$

and

$$1 > \frac{1}{2}\Psi^2\left(\frac{(1+v)^2}{(1-u)^3} + \frac{(1-v)^2}{(1+u)^3}\right), \tag{3.13}$$

respectively.

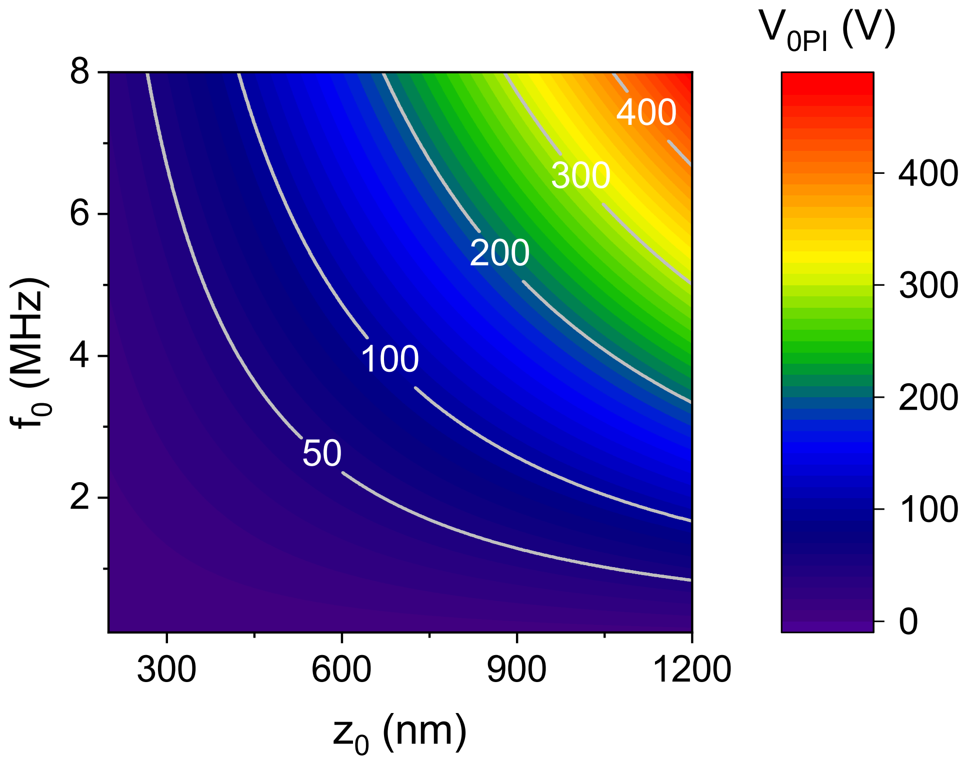

Figure 3.3: Outer pull-in voltage $V_{0\mathrm{PI}}$ as a function of native MEMS resonant frequency f_0 and initial air gap z_0 for a symmetric MEMS.

Under static conditions ($\dot{u} = 0$ and $\ddot{u} = 0$), the coefficient Ψ^2 may be eliminated from Eqs. 3.12 and 3.13 at pull-in ($k_{\mathrm{eff}} = 0$) to yield

$$2u_{\mathrm{pi}}\left(\frac{(1+v_{\mathrm{pi}})^2}{\left(1-u_{\mathrm{pi}}\right)^3}+\frac{(1-v_{\mathrm{pi}})^2}{\left(1+u_{\mathrm{pi}}\right)^3}\right)=\left(\frac{(1+v_{\mathrm{pi}})^2}{\left(1-u_{\mathrm{pi}}\right)^2}-\frac{(1-v_{\mathrm{pi}})^2}{\left(1+u_{\mathrm{pi}}\right)^2}\right),$$

where u_{pi} and v_{pi} are normalized deflection and actuation voltage at pull-in, respectively. Rearranging leads to

$$(1+v_{\mathrm{pi}})^2\left(\frac{2u_{\mathrm{pi}}}{\left(1-u_{\mathrm{pi}}\right)^3}-\frac{1}{\left(1-u_{\mathrm{pi}}\right)^2}\right)=-(1-v_{\mathrm{pi}})^2\left(\frac{2u_{\mathrm{pi}}}{\left(1+u_{\mathrm{pi}}\right)^3}+\frac{1}{\left(1+u_{\mathrm{pi}}\right)^2}\right),$$

and thus

$$\frac{(1-v_{\mathrm{pi}})^2}{(1+v_{\mathrm{pi}})^2}=\frac{-\frac{2u_{\mathrm{pi}}}{\left(1-u_{\mathrm{pi}}\right)^3}+\frac{1}{\left(1-u_{\mathrm{pi}}\right)^2}}{\frac{2u_{\mathrm{pi}}}{\left(1+u_{\mathrm{pi}}\right)^3}+\frac{1}{\left(1+u_{\mathrm{pi}}\right)^2}}=\frac{\left(1+u_{\mathrm{pi}}\right)^3}{\left(1-u_{\mathrm{pi}}\right)^3}\frac{1-3u_{\mathrm{pi}}}{1+3u_{\mathrm{pi}}}.$$

As the left-hand side must be positive, we have $\left|u_{\mathrm{pi}}\right| \leq 1/3$, and that $u_{\mathrm{pi}} = \pm 1/3 \Rightarrow v_{\mathrm{pi}} = \pm 1$, while $u_{\mathrm{pi}} = 0 \Rightarrow v_{\mathrm{pi}} = 0$ (if V_0 is non-zero). It follows that

$$\frac{1-v_{\mathrm{pi}}}{1+v_{\mathrm{pi}}}=\pm\frac{\sqrt{\left(1+u_{\mathrm{pi}}\right)^3\left(1-3u_{\mathrm{pi}}\right)}}{\sqrt{\left(1-u_{\mathrm{pi}}\right)^3\left(1+3u_{\mathrm{pi}}\right)}},$$

where the positive sign is valid for $\left|v_{\mathrm{pi}}\right| \leq 1$.

Solving for the normalized actuation voltage leads to

$$v_{\mathrm{pi}} = \frac{\sqrt{\left(1-u_{\mathrm{pi}}\right)^3\left(1+3u_{\mathrm{pi}}\right)} \mp \sqrt{\left(1+u_{\mathrm{pi}}\right)^3\left(1-3u_{\mathrm{pi}}\right)}}{\sqrt{\left(1-u_{\mathrm{pi}}\right)^3\left(1+3u_{\mathrm{pi}}\right)} \pm \sqrt{\left(1+u_{\mathrm{pi}}\right)^3\left(1-3u_{\mathrm{pi}}\right)}}, \tag{3.14}$$

where the upper sign is valid for $\left|v_{\mathrm{pi}}\right| \leq 1$, and the lower sign is valid for $\left|v_{\mathrm{pi}}\right| \geq 1$.

Solving the static equilibrium condition (Eq. 3.12 with $\dot{u} = 0$ and $\ddot{u} = 0$) for Ψ^2 at pull in yields

$$\Psi^2 = \frac{4u_{\mathrm{pi}}}{\frac{(1+v_{\mathrm{pi}})^2}{\left(1-u_{\mathrm{pi}}\right)^2} - \frac{(1-v_{\mathrm{pi}})^2}{\left(1+u_{\mathrm{pi}}\right)^2}} = \left(\frac{\sqrt{\left(1-u_{\mathrm{pi}}\right)^3\left(1+3u_{\mathrm{pi}}\right)} \pm \sqrt{\left(1+u_{\mathrm{pi}}\right)^3\left(1-3u_{\mathrm{pi}}\right)}}{2}\right)^2 \tag{3.15}$$

and thus

$$\Psi = \left|\frac{V_0}{V_{0\mathrm{PI_{sym}}}}\right| = \left|\frac{\sqrt{\left(1-u_{\mathrm{pi}}\right)^3\left(1+3u_{\mathrm{pi}}\right)} \pm \sqrt{\left(1+u_{\mathrm{pi}}\right)^3\left(1-3u_{\mathrm{pi}}\right)}}{2}\right|,$$

in both cases the upper sign is valid for $\left|v_{\mathrm{pi}}\right| \leq 1$. We see that at $u_{\mathrm{pi}} = \pm 1/3$ we have $\Psi = \sqrt{4/27}$.

Combining Eqs. 3.14 and 3.15 a simple calculation shows that the simple relation $v_{\mathrm{pi}}\Psi^2 = 4u_{\mathrm{pi}}^3$ is valid at pull-in.

3.2.3 Real asymmetric, but almost symmetric, actuator

When accounting for asymmetry in a real device, it is difficult to avoid $g_t \neq g_b$. To address this, $g_b = z_0$ and $g_t = \alpha z_0$ are defined, where α is the asymmetry factor. In addition, the position is normalized to $u = z/z_0$ and set $V_b = V_0$. The actuation voltage V_1 is normalized to V_0 as $v = V_1/V_0$, while V_t remains unassigned. Substituting these assumptions into the general equation of motion, Eq. 3.7, we obtain:

$$m\ddot{u} + b\dot{u} + ku = \frac{\epsilon A V_0^2}{2z_0^3}\left(\frac{(V_t/V_0 - v)^2}{(\alpha - u)^2} - \frac{(1-v)^2}{(1+u)^2}\right)$$

and then it becomes apparent that by applying the bias voltage $V_t = -\alpha V_0$ zero actuation at $V_1 = 0$ V results, and with this assignment we get a normalized equation of motion that is quite similar to that for the symmetric actuator

$$\frac{\ddot{u}}{\omega_0^2} + 2\zeta\frac{\dot{u}}{\omega_0} + u = \frac{\epsilon A V_0^2}{2kz_0^3}\left(\frac{(\alpha+v)^2}{(\alpha-u)^2} - \frac{(1-v)^2}{(1+u)^2}\right)$$

and with the corresponding stability criterion

$$\frac{\epsilon A V_0^2}{kz_0^3}\left(\frac{(\alpha+v)^2}{(\alpha-u)^3} + \frac{(1-v)^2}{(1+u)^3}\right) < 1,$$

from which we see that the pull-in voltage at zero actuation voltage ($v = 0$) is $V_{0\mathrm{PI}}^2 = kz_0^3/(\epsilon A\,(1+1/\alpha))$ which leads to the final non-dimensionalized equation of motion

$$\frac{\ddot{u}}{\omega_0^2} + 2\zeta\frac{\dot{u}}{\omega_0} + u = \frac{V_0^2}{2\,(1+1/\alpha)\,V_{0\mathrm{PI}}^2}\left(\frac{(\alpha+v)^2}{(\alpha-u)^2} - \frac{(1-v)^2}{(1+u)^2}\right) = \tag{3.16}$$

$$= \frac{1}{2\,(1+1/\alpha)}\Psi_\alpha^2\left(\frac{(\alpha+v)^2}{(\alpha-u)^2} - \frac{(1-v)^2}{(1+u)^2}\right), \tag{3.17}$$

with the stability criterion

$$1 > \frac{V_0^2}{(1+1/\alpha)\, V_{\mathrm{0PI}}^2} \left(\frac{(\alpha+v)^2}{(\alpha-u)^3} + \frac{(1-v)^2}{(1+u)^3} \right) = \tag{3.18}$$
$$= \frac{1}{(1+1/\alpha)} \Psi_\alpha^2 \left(\frac{(\alpha+v)^2}{(\alpha-u)^3} + \frac{(1-v)^2}{(1+u)^3} \right).$$

where $\Psi_\alpha^2 \equiv V_0^2 / V_{\mathrm{0PI}}^2$.

Eliminating Ψ_α^2 in static conditions by use of Eqs. 3.16 and 3.18 we get

$$2u_{\mathrm{pi}} \left(\frac{(\alpha+v_{\mathrm{pi}})^2}{(\alpha-u_{\mathrm{pi}})^3} + \frac{(1-v_{\mathrm{pi}})^2}{(1+u_{\mathrm{pi}})^3} \right) = \left(\frac{(\alpha+v_{\mathrm{pi}})^2}{(\alpha-u_{\mathrm{pi}})^2} - \frac{(1-v_{\mathrm{pi}})^2}{(1+u_{\mathrm{pi}})^2} \right)$$

which can be rearranged to

$$(\alpha+v_{\mathrm{pi}})^2 \left(\frac{2u_{\mathrm{pi}}}{(\alpha-u_{\mathrm{pi}})^3} - \frac{1}{(\alpha-u_{\mathrm{pi}})^2} \right) = -(1-v_{\mathrm{pi}})^2 \left(\frac{2u_{\mathrm{pi}}}{(1+u_{\mathrm{pi}})^3} + \frac{1}{(1+u_{\mathrm{pi}})^2} \right)$$

and thus

$$\frac{(1-v_{\mathrm{pi}})^2}{(\alpha+v_{\mathrm{pi}})^2} = \frac{(1+u_{\mathrm{pi}})^3}{(\alpha-u_{\mathrm{pi}})^3} \frac{\alpha-3u_{\mathrm{pi}}}{1+3u_{\mathrm{pi}}}.$$

The left-hand side must be positive, and thus, the normalized pull-in deflection is restricted to the range $-1/3 \le u_{\mathrm{pi}} \le \alpha/3$, and $u_{\mathrm{pi}} = \alpha/3 \Rightarrow v_{\mathrm{pi}} = 1$, $u_{\mathrm{pi}} = -1/3 \Rightarrow v_{\mathrm{pi}} = -\alpha$, and $u_{\mathrm{pi}} = 0 \Rightarrow v_{\mathrm{pi}} = 0$ (as long as V_0 is finite). It follows that

$$\frac{1-v_{\mathrm{pi}}}{\alpha+v_{\mathrm{pi}}} = \pm \frac{\sqrt{(1+u_{\mathrm{pi}})^3 (\alpha-3u_{\mathrm{pi}})}}{\sqrt{(\alpha-u_{\mathrm{pi}})^3 (1+3u_{\mathrm{pi}})}}$$

where the positive sign is valid for the range $-\alpha \le v_{\mathrm{pi}} \le 1$, while the negative sign is valid for v_{pi} outside this range. Solving for v_{pi} leads to

$$v_{\mathrm{pi}} = \frac{\sqrt{(\alpha-u_{\mathrm{pi}})^3 (1+3u_{\mathrm{pi}})} \mp \alpha \sqrt{(1+u_{\mathrm{pi}})^3 (\alpha-3u_{\mathrm{pi}})}}{\sqrt{(\alpha-u_{\mathrm{pi}})^3 (1+3u_{\mathrm{pi}})} \pm \sqrt{(1+u_{\mathrm{pi}})^3 (\alpha-3u_{\mathrm{pi}})}}, \tag{3.19}$$

where the upper sign is valid in the range $-\alpha \le v_{\mathrm{pi}} \le 1$.

Solving the static equation of motion for Ψ_α^2 leads to

$$\Psi_\alpha^2 = \frac{2(1+1/\alpha)\, u_{\mathrm{pi}}}{\frac{(\alpha+v_{\mathrm{pi}})^2}{(\alpha-u_{\mathrm{pi}})^2} - \frac{(1-v_{\mathrm{pi}})^2}{(1+u_{\mathrm{pi}})^2}} = \frac{\left(\sqrt{(\alpha-u_{\mathrm{pi}})^3 (1+3u_{\mathrm{pi}})} \pm \sqrt{(1+u_{\mathrm{pi}})^3 (\alpha-3u_{\mathrm{pi}})} \right)^2}{\alpha (\alpha+1)^2},$$

and thus

$$\Psi_\alpha = \left| \frac{V_0}{V_{\mathrm{0PI}}} \right| = \frac{\left| \sqrt{(\alpha-u_{\mathrm{pi}})^3 (1+3u_{\mathrm{pi}})} \pm \sqrt{(1+u_{\mathrm{pi}})^3 (\alpha-3u_{\mathrm{pi}})} \right|}{(\alpha+1)\sqrt{\alpha}} \tag{3.20}$$

where we see that at $u_{\mathrm{pi}} = -1/3$ ($v_{\mathrm{pi}} = -\alpha$) we have $\Psi_\alpha = \sqrt{8/27} / \left(\sqrt{\alpha}\sqrt{1+\alpha}\right)$ while at $u_{\mathrm{pi}} = \alpha/3$ ($v_{\mathrm{pi}} = 1$) we have $\Psi_\alpha = \alpha\sqrt{8/27}/\sqrt{1+\alpha}$.

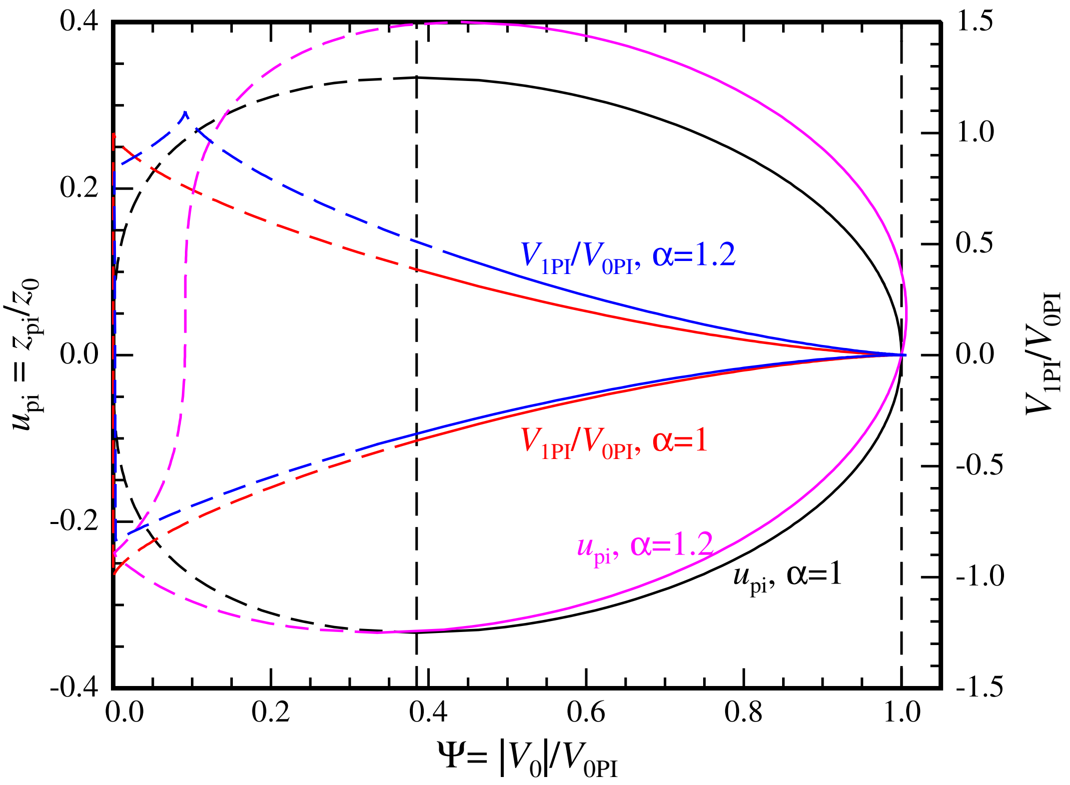

Figure 3.4: Normalized pull-in displacement u_{pi} and normalized pull-in voltage $V_{1\text{PI}}/V_{0\text{PI}}$ as a function of normalized bias voltage $\Psi = V_0/V_{0\text{PI}}$ for two values of the asymmetry factor $\alpha = 1$ and $\alpha = 1.2$. The vertical dashed lines indicate $\Psi = \sqrt{4/27}$ and $\Psi = 1$.

Figure 3.4 shows calculated normalized pull-in displacement u_{pi} and voltage $V_{1\text{PI}}/V_{0\text{PI}}$ as function of normalized bias voltage $V_0/V_{0\text{PI}}$.

If the outer voltage approaches $V_{0\text{PI}}$ the pull-in voltage approaches 0 V, since the electric field between the plates will be so high that only a minute addition to the electric field will lead to an instability point resulting in the MEMS being snapped in.

3.2.4 Numerical solution to static motion

Eq. (3.12) can also be solved numerically using MATLAB's fsolve. A comparison between the analytical solution to the symmetric bidirectional actuator to the numerically generated solution can be seen in Fig. 3.5. As expected, the results are in agreement. Note that unlike Fig. 3.4, the pull-in voltage is normalized to the outer voltage in Fig. 3.5, instead of the outer pull-in voltage.

As indicated by Fig. 3.3, a MEMS with a resonant frequency of 3 MHz and symmetric initial air gaps of 1 µm results in $V_{0\text{PI}} = 137$ V. Assuming the aforementioned geometry, with a MEMS mass of 241.9 fg, numerically solving Eq. (3.12) for the MEMS position (z) as a function of the applied DC bias on the MEMS (V_1), for specific outer voltages (V_0) results in the DC tuning curves in Fig. 3.6. As indicated, the MEMS movement is amplified; for larger outer voltage, the MEMS movement becomes greater and more linear for smaller center voltage. However, the maximum MEMS excursion is decreased for higher outer voltage, i.e., the pull-in occurs earlier, although the starting maximum excursion is twice the distance compared to the unidirectional configuration in static operation.

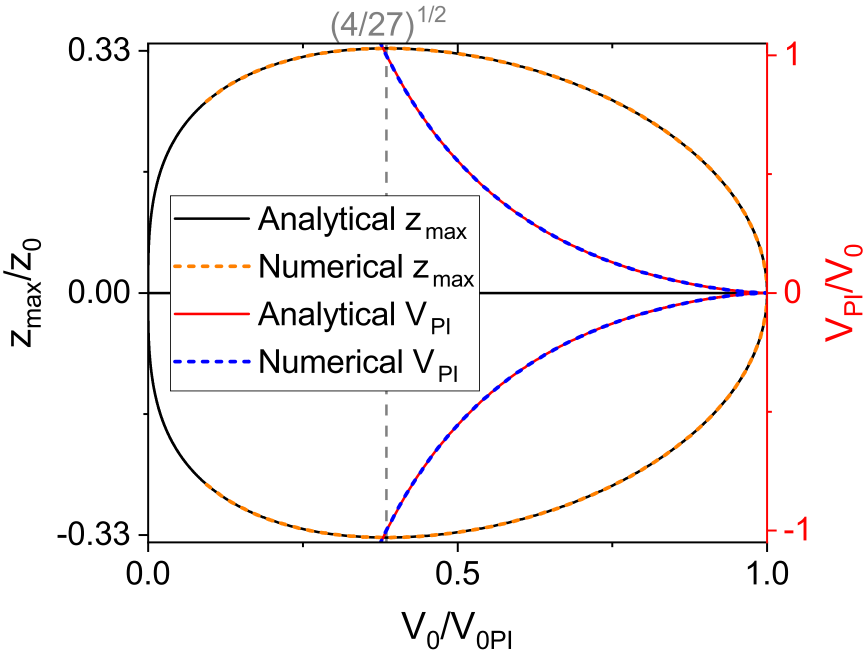

Figure 3.5: Analytical solution Eq. (3.14) and Eq. (3.15) compared to MATLAB's fsolve solution of MEMS displacement (left) and pull-in voltage (right) as a function of outer voltage.

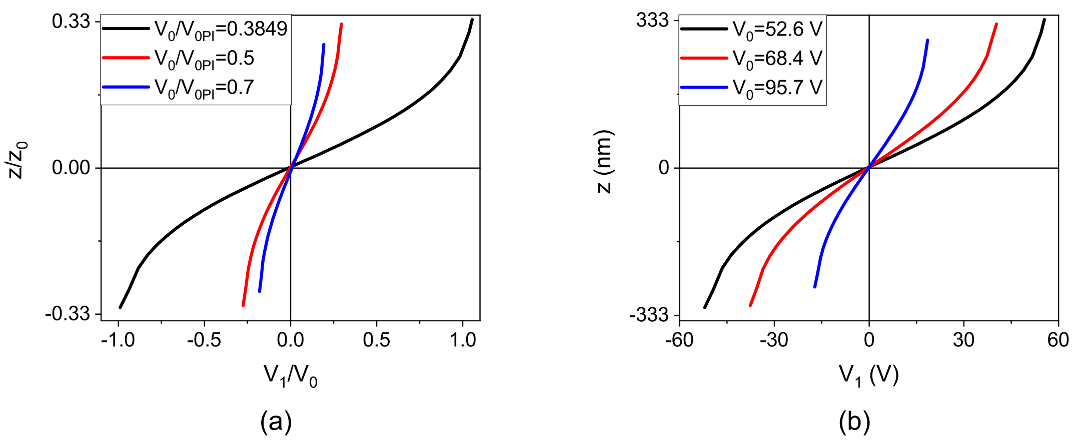

Figure 3.6: Normalized (a) and non-normalized (b) DC tuning curves of a MEMS with a native resonant frequency of 3 MHz, a mass of 241.9 fg, and symmetric initial air gaps of 1 μm. Black, red, and blue curves show 52.6 V, 68.4 V, and 95.7 V outer voltage, respectively.

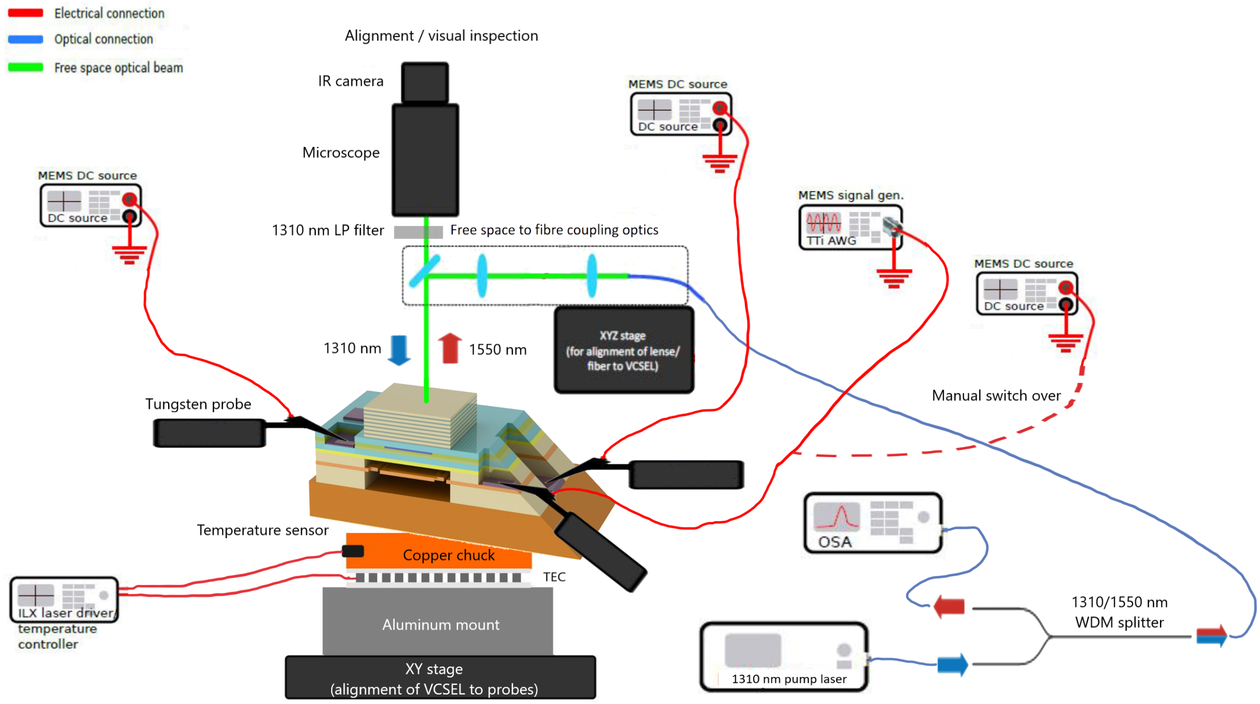

Figure 3.7: Experimental probe setup showing spectral characterization of an optically pumped bidirectional MEMS VCSEL .

3.3 Static experimental results

In this section, the experimental results are compared to the model of the asymmetric bidirectional electrostatic actuator model.

3.3.1 Experimental setup

An illustration of the experimental setup can be seen in Fig. 3.7. The semiconductor laser chip sits on top of a copper chuck, which can be temperature controlled by the connected thermoelectric cooler (TEC). The TEC is on top of an aluminum mount that sits on an XY stage below a microscope. The setup is referred to as a probe station due to its ability to send electrical signals via probes.

The MEMS VCSEL probe station is equipped with three tungsten probes which can be controlled with micrometer screws in the x, y, and z directions. BNC cables connect the probes to two MEMS DC sources in order to apply DC voltages to the silicon substrate below the bottom air gap and the indium phosphide layer above the top air gap. The DC sources used were the two SMU channels from a Keithley 4200-SCS Semiconductor Characterization System[66], which delivered up to ± 210 V. An arbitrary waveform generator (AWG), from TTi[67], is connected to the third probe, which is in contact with the silicon-on-insulator device layer. For the static bidirectional characterization, a third DC source replaces the AWG.

A wavelength-stabilized 1310 nm pump laser, from Innolume[68], is fiber coupled to a 1310/1550 nm wavelength division multiplex (WDM) splitter, from Haphit[69], which guides the pump light in the 1310 nm port through the common port and into the microscope. The free space optics consists of a collimating and focusing lens. A dichroic mirror[70] reflects the incident 1310 nm light into the microscope's optical path. The 1310 nm light then goes through the dielectric top DBR mirror and gets (partly) absorbed in the multiple quantum wells of the VCSEL . The generated 1550 nm laser light is emitted from the top of the wafer

through the top dielectric DBR mirror, reflected by the dichroic mirror, and collimated and focused into the same optical fiber. In order to filter away the reflected pump light, the generated 1550 nm light goes through the common port of the WDM splitter and goes through the 1550 nm port into the optical spectrum analyzer (OSA)[71].
Due to the 1310 nm long pass (LP) filter, only the 1550 nm emission light is seen in the infrared (IR) camera[72] on top of the microscope; two IR camera snapshots are shown in Fig. 3.8

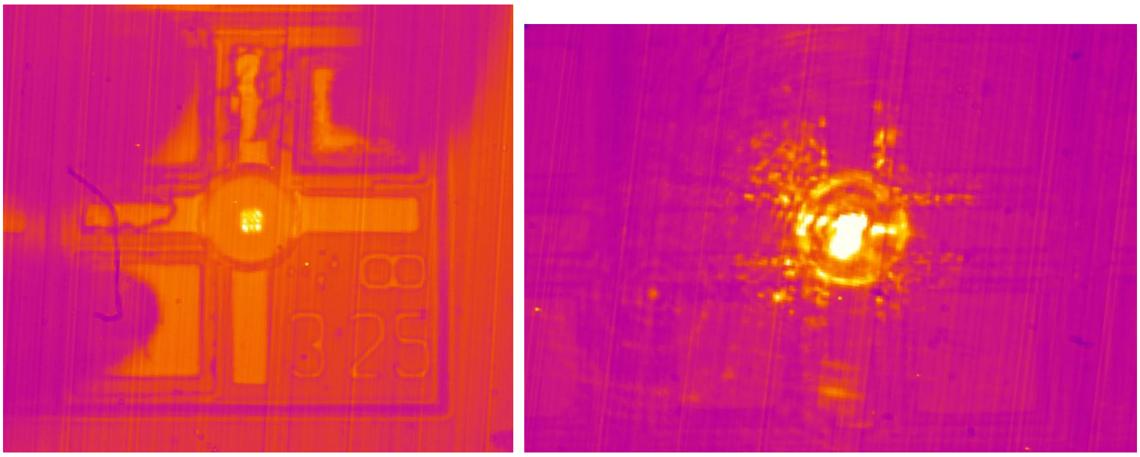

(a) (b)

Figure 3.8: IR camera snapshots showing (a) amplified spontaneous emission with probes touching all three contacts and (b) lasing without probes on contacts.

3.3.2 Experimental results

Fig. 3.9 compares experimental data to the bidirectional model. Fig. 3.9 (a) is similar to

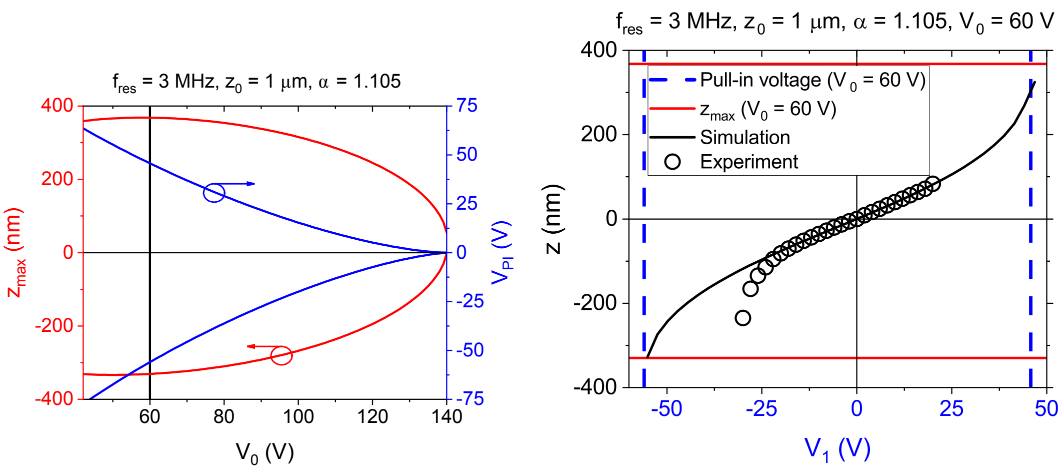

(a) (b)

Figure 3.9: (a) Maximum displacement z_{max} (left), and MEMS pull-in voltage V_{PI}, as a function of outer voltage V_0, for a MEMS with a fundamental resonance frequency of 3 MHz, an initial air gap of 1 μm, and an α coefficient of 1.105. (b) MEMS position z as a function of MEMS voltage V_1.

Fig. 3.5 and Fig. 3.4, the difference being that the axis are not normalized, in addition to the α coefficient being 1.105, resulting in the top air gap being slightly larger than the bottom air gap.

The vertical line highlights an outer voltage of 60 V, resulting in 60 V on the Silicon contact and -66.3 V on the Indium Phosphide contact. Inserting the highlighted case into Eq. (3.12) and numerically solving for the MEMS position z for different MEMS DC biases V_1 results in the solid simulation curve on Fig 3.9 (b). The horizontal lines on Fig. 3.9 (b) show the maximum MEMS excursion z_{max}, at the pull-in voltage (dotted vertical lines), for $V_0 = 60$ V and $\alpha = 1.105$. Experimental results show cavity resonances as circles (assuming a constant tuning efficiency $\frac{\Delta\lambda}{\Delta z}$ of 0.19) overlaying the simulation results, showing very good agreement, except when the MEMS is at maximum excursion towards the silicon substrate. One thing to note is the linear relationship between the MEMS movement and the applied voltage in the center, uniquely attributed to bidirectional actuation. In contrast, in the unidirectional actuator, i.e., the parallel plate capacitor, the force is proportional to the voltage squared. Hence the MEMS movement is proportional to the voltage squared. The linear relationship is advantageous in both OCT and light amplification and ranging (LiDAR), since FFT can be performed without the need for re-sampling.

3.4 Bidirectional dynamic equations

In this section, the dynamic behavior of a bidirectional actuator is examined.
Firstly, the fundamental term resulting from a Taylor expansion assuming low MEMS excursion is investigated. Thereafter higher order terms are included, and finally, the full differential equation is numerically solved, comparing the bidirectional actuator with the unidirectional actuator.

3.4.1 Fundamental term

Assuming an alternating drive signal on the movable electrode, i.e., $V_1(t) = V_a \cos(\omega t)$ where V_a is the amplitude and ω is the actuation frequency, inserted in Eq. (3.17) solved for MEMS position z results in (only including the fundamental sinusoidal term)

$$z(t) = \frac{V_0 V_a}{V_{0PI}^2} \frac{\omega_0^2 z_0 \cos(\omega t - \phi)}{\sqrt{\left(\omega^2 - \omega_0^2\left(1 - \frac{V_0^2}{V_{0PI}^2}\right)\right)^2 + \left(\frac{\omega_0 \omega}{Q}\right)^2}}, \quad \phi = \arctan\left(\frac{\omega_0 \omega}{Q\left(\omega_0^2\left(1 - \frac{V_0^2}{V_{0PI}^2}\right) - \omega^2\right)}\right) \tag{3.21}$$

where Q is the mechanical quality factor, ω_0 is the native mechanical resonant frequency. Eq. (3.21) is a result of a Taylor expansion around $z = 0$.
Eq. (3.21) resembles the result for the standard unidirectional electrostatic actuator[51] (also only including the fundamental term)

$$z(t) = \frac{4}{27} \frac{2 V_0 V_a}{V_{PI}^2} \frac{\omega_0^2 z_0 \cos(\omega t - \phi)}{\sqrt{\left(\omega^2 - \omega_0^2\right)^2 + \left(\frac{\omega_0 \omega}{Q}\right)^2}} + z_{\text{OFST}} \tag{3.22}$$

with $V_{\text{PI}} = 8 z_0^2 k / (27 C_0)$, where C_0 is the equilibrium actuator capacitance, and z_{OFST} is an off-set displacement. One difference between the two equations is that the electrostatic spring softening $\sqrt{1 - V_0^2/V_{0PI}^2}$ is seen in the fundamental term for the bidirectional actuator, compared to the first higher-order term for the unidirectional actuator[51].
In both cases, the MEMS displacement amplitude can be increased by increasing the static electric field V_0; however, in the unidirectional case, increasing the DC field increases the offset from the resting mirror position, which will limit the tuning range. For the bidirectional configuration, this offset is not seen, as opposite polarized DC fields of

equal magnitude ($\alpha = 1$) will result in electrostatic forces of opposite directions but equal in magnitude, resulting in zero net force on the movable electrode. Therefore, the only cost associated with increasing the DC fields is the reduction of the resonant frequency (electrostatic spring softening).

3.4.2 Higher order terms

The fundamental and the first two higher-order displacement terms are as follows

$$L_1 = \frac{V_0 V_a}{V_{\text{0PI}}^2} \frac{z_0}{\frac{\omega^2}{\omega_0^2} - \left(1 - \frac{V_0^2}{V_{\text{0PI}}^2}\right) + i\left(\frac{\omega}{Q\omega_0}\right)} = \frac{V_0 V_a}{V_{\text{0PI}}^2} \frac{\omega_0 z_0 \left(\omega^2 - \omega_0^2\left(1 - \frac{V_0^2}{V_{\text{0PI}}^2}\right) - i\left(\frac{\omega_0\omega}{Q}\right)\right)}{\left(\omega^2 - \omega_0^2\left(1 - \frac{V_0^2}{V_{\text{0PI}}^2}\right)\right)^2 + \left(\frac{\omega_0\omega}{Q}\right)} \tag{3.23}$$

$$L_2 = -\frac{V_0^2}{V_{\text{0PI}}^2} z_0 \frac{\frac{\frac{1}{\alpha^2}-1}{2\left(1+\frac{1}{\alpha}\right)}\left(\frac{V_a^2}{V_0^2} - \frac{L_1^2}{z_0^2}\right)}{\frac{(2\omega)^2}{\omega_0^2} - \left(1 - \frac{V_0^2}{V_{\text{0PI}}^2}\right) + i\left(\frac{2\omega}{Q\omega_0}\right)} \tag{3.24}$$

$$= -\frac{V_0^2}{V_{\text{0PI}}^2} \frac{\left(\frac{\omega_0}{2}\right)^2 z_0 \frac{\frac{1}{\alpha^2}-1}{2\left(1+\frac{1}{\alpha}\right)}\left(\frac{V_a^2}{V_0^2} - \frac{L_1^2}{z_0^2}\right)\left(\omega^2 - \left(\frac{\omega_0}{2}\right)^2\left(1 - \frac{V_0^2}{V_{\text{0PI}}^2}\right) - i\left(\frac{\omega_0\omega}{2Q}\right)\right)}{\left(\omega^2 - \left(\frac{\omega_0}{2}\right)^2\left(1 - \frac{V_0^2}{V_{\text{0PI}}^2}\right)\right)^2 + \left(\frac{\omega_0\omega}{2Q}\right)^2} \tag{3.25}$$

which equals 0 for $\alpha = 1$.

$$L_3 = -\frac{V_0^2}{V_{\text{0PI}}^2} z_0 \frac{\left(\frac{\left(1-\frac{1}{\alpha^2}\right)L_1 L_2}{\left(1+\frac{1}{\alpha}\right)z_0^2} - \frac{V_a L_1^2}{V_0 \alpha z_0^2} + \frac{V_a^2 L_1}{V_0^2 \alpha z_0}\right)}{\frac{(3\omega)^2}{\omega_0^2} - \left(1 - \frac{V_0^2}{V_{\text{0PI}}^2}\right) + i\left(\frac{3\omega}{Q\omega_0}\right)} \tag{3.26}$$

$$= -\frac{V_0^2}{V_{\text{0PI}}^2} \frac{\left(\frac{\omega_0}{3}\right)^2 z_0 \left(\frac{\left(1-\frac{1}{\alpha^2}\right)L_1 L_2}{\left(1+\frac{1}{\alpha}\right)z_0^2} - \frac{V_a L_1^2}{V_0 \alpha z_0^2} + \frac{V_a^2 L_1}{V_0^2 \alpha z_0}\right)\left(\omega^2 - \left(\frac{\omega_0}{3}\right)^2\left(1 - \frac{V_0^2}{(1+\alpha)V_{\text{0PI}}^2}\right) - i\left(\frac{\omega_0\omega}{3Q}\right)\right)}{\left(\omega^2 - \left(\frac{\omega_0}{3}\right)^2\left(1 - \frac{V_0^2}{V_{\text{0PI}}^2}\right)\right)^2 + \left(\frac{\omega_0\omega}{3Q}\right)^2} \tag{3.27}$$

The MEMS displacement, including the first three terms, is then found, by

$$z(t) = \Re(L_1(\omega)\exp(-i\omega t) + L_2(\omega)\exp(-i2\omega t) + L_3(\omega)\exp(-i3\omega t)) \tag{3.28}$$

The transfer curves, for the first three terms, can be seen in Fig. 3.10, for a symmetric ($\alpha = 1$) Silicon MEMS with a quality factor of 4, ambient condition (atmospheric pressure) for similar MEMS[51], and a resonant frequency of 3 MHz, and area of ≈260 μm^2, a thickness of 400 nm, an initial air gap of 1 μm, an outer voltage of $0.5V_{\text{0PI}}$, and an actuation voltage of $0.04V_{\text{0PI}}$, with $V_{\text{0PI}} = 137$ V. As is evident in Fig. 3.10 the fundamental term (L_1) has the greatest magnitude, i.e. $z(t) \approx \Re(L_1(\omega)\exp(-i\omega t))$.
Figure 3.11 shows the MEMS position and voltage waveform as a function of time, including the first three terms, i.e., Eq. (3.28) for $\omega_{\text{act}} = \omega/\omega_0 = 0.8471$ (where $|L_1|$ peaks in Fig. 3.10) and $V(t) = \Re(V_a \exp(-i\omega_{\text{act}}t))$. The solid curves show a peak-to-peak voltage (V_{pp}) of 10 V, the maximum output of an arbitrary waveform generator (AWG). The dashed curves show a peak-to-peak voltage of 42 V, which is the transformed voltage using a T9-1-X65 from minicurcuits[73], with an input of $V_{\text{pp}} = 10$ V. The maximum MEMS excursion increases from ±85 nm to ±360 nm using the transformed signal, which translates to a (blue- and red-shift) wavelength sweep from 32 nm to 136 nm assuming a constant tuning

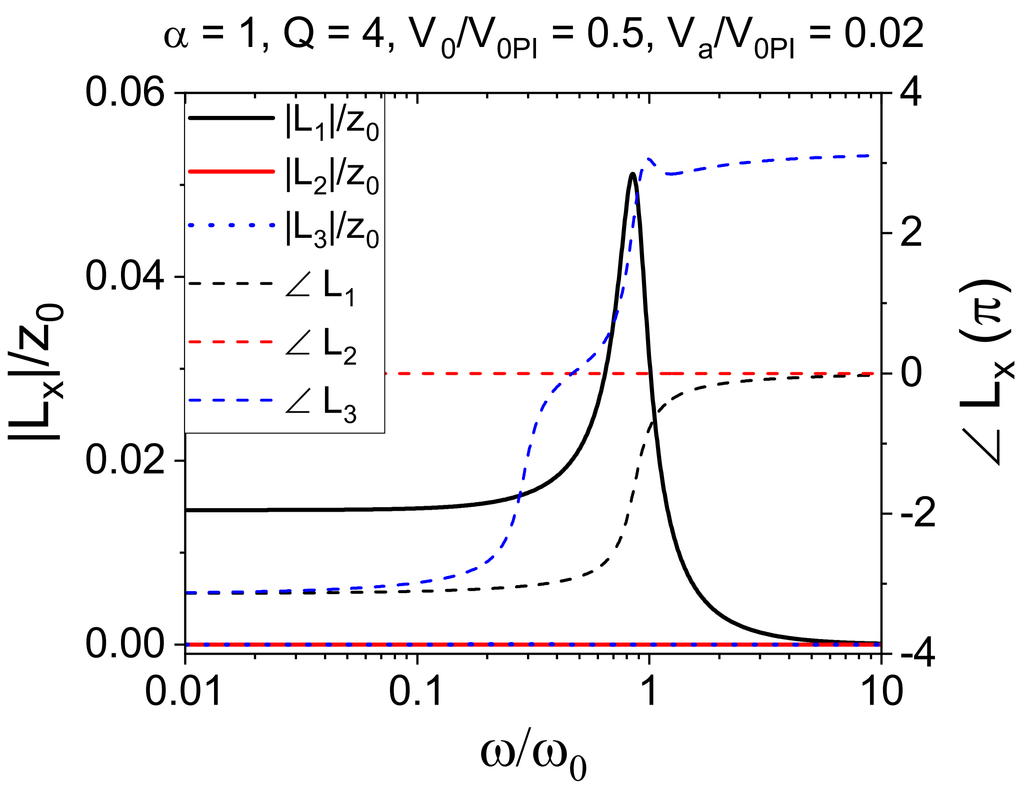

Figure 3.10: Transfer curves, magnitude, and phase, for the first three terms.

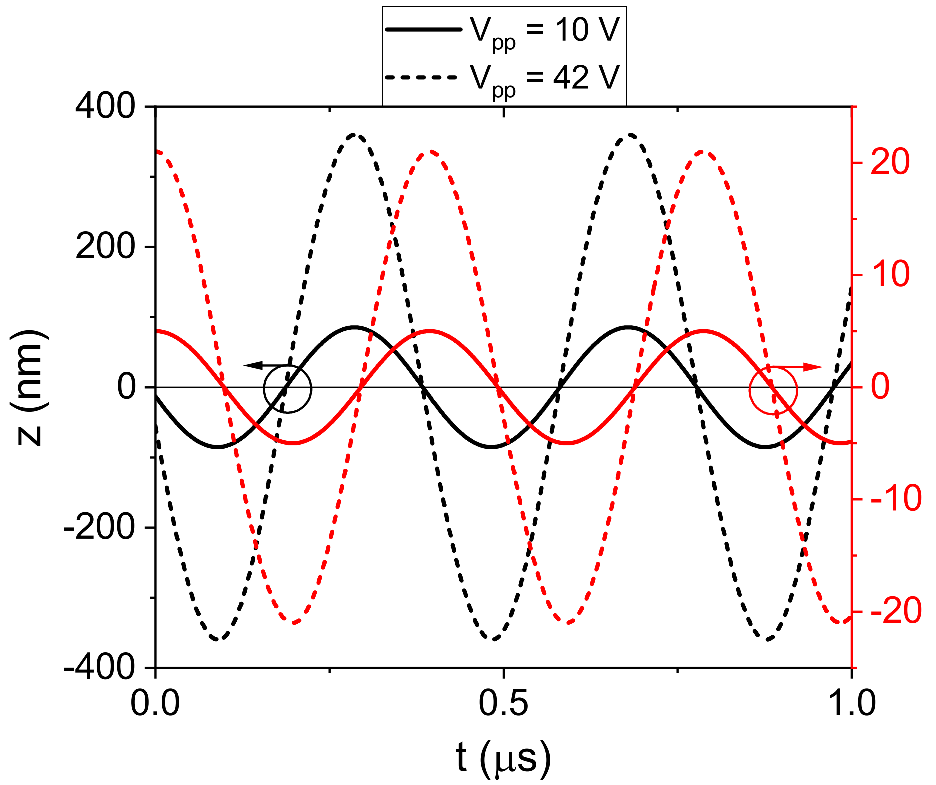

Figure 3.11: MEMS position (left) and voltage (right) as a function of time, for voltage peak to peak amplitude of 10 V (solid) and 42 V (dashed).

efficiency of $\frac{\Delta\lambda}{\Delta z}$ of 0.19. The wavelength sweep can be further increased by increasing the outer voltages; however, this will cause the frequency at which $|L_1|$ peaks to decrease, thereby lowering ω_{act}.
Fig. 3.12 (a) shows the wavelength sweep as a function of outer voltage and drive volt-

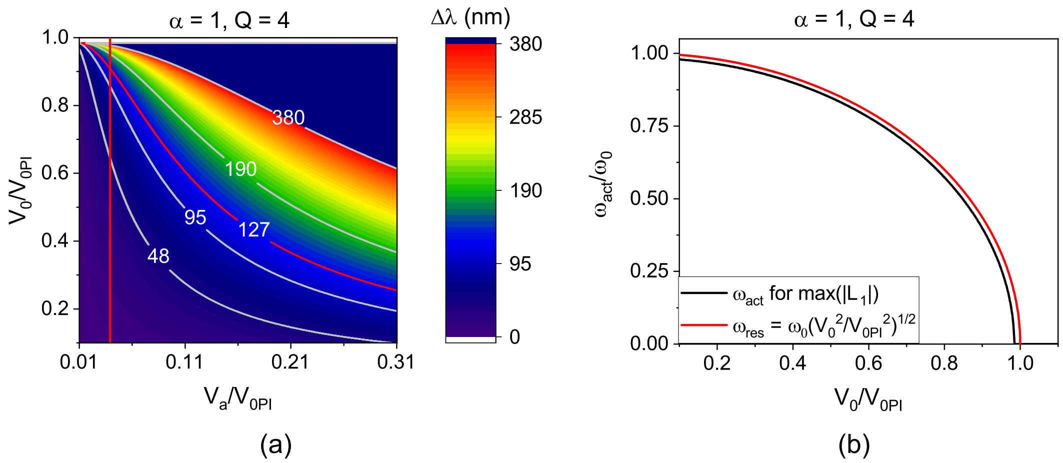

Figure 3.12: (a) Tuning bandwidth as a function of outer voltage normalized to outer pull-in voltage and sinusoidal amplitude normalized to outer pull-in voltage. (b) Actuation frequency normalized to the native resonant frequency as a function of outer voltage normalized to the outer pull-in voltage. The red contour line corresponds to the traditional static pull-in position.

age amplitude and Fig. 3.12 (b) shows the actuation frequency as a function of outer voltage, for a MEMS with Q=4. For higher Q values the difference between ω_{act} for max. $|L_1|$ and spring softening in the fundamental term, $\omega_{\text{res}} = \omega_0(V_0^2/V_{\text{0PI}}^2)^{(1/2)}$ decreases.
The wavelength sweep assumes $z_0 = 1000$ nm, a tuning efficiency of 0.19, and the MEMS movement is less than the gain bandwidth, mirror reflectivity bandwidths (R>99.4%), and the free spectral range of the optical cavity. The vertical line indicates $V_a = 5$ V, and the red contour line indicates static pull in position. As indicated, the tuning bandwidth can be increased by increasing the static outer voltages. However, it decreases the actuation frequency due to electrostatic spring softening.

3.4.3 Quality factor

Decreasing the pressure around the MEMS drastically increases the quality factor because the MEMS movement will be less hindered due to decreased amount of air molecules. Fig. 3.13 shows the effect on the MEMS dynamic movement for different quality factors. The graphs are normalized, meaning they are general regardless of the designed MEMS stiffness.
It is clear that doing low vacuum bonding greatly decreases the required static outer voltage needed for limited available sinusoidal amplitude in order to utilize close to 100% of the gaps. Lowering the required outer voltage means that the actuation frequency ω_{act} can be close to the designed resonant frequency, see Fig. 3.12 (b), allowing very fast tunability.
However, it should be noted, that the Taylor expansion is evaluated at $z = 0$, meaning for very large MEMS excursion, the approximation is expected to fail.

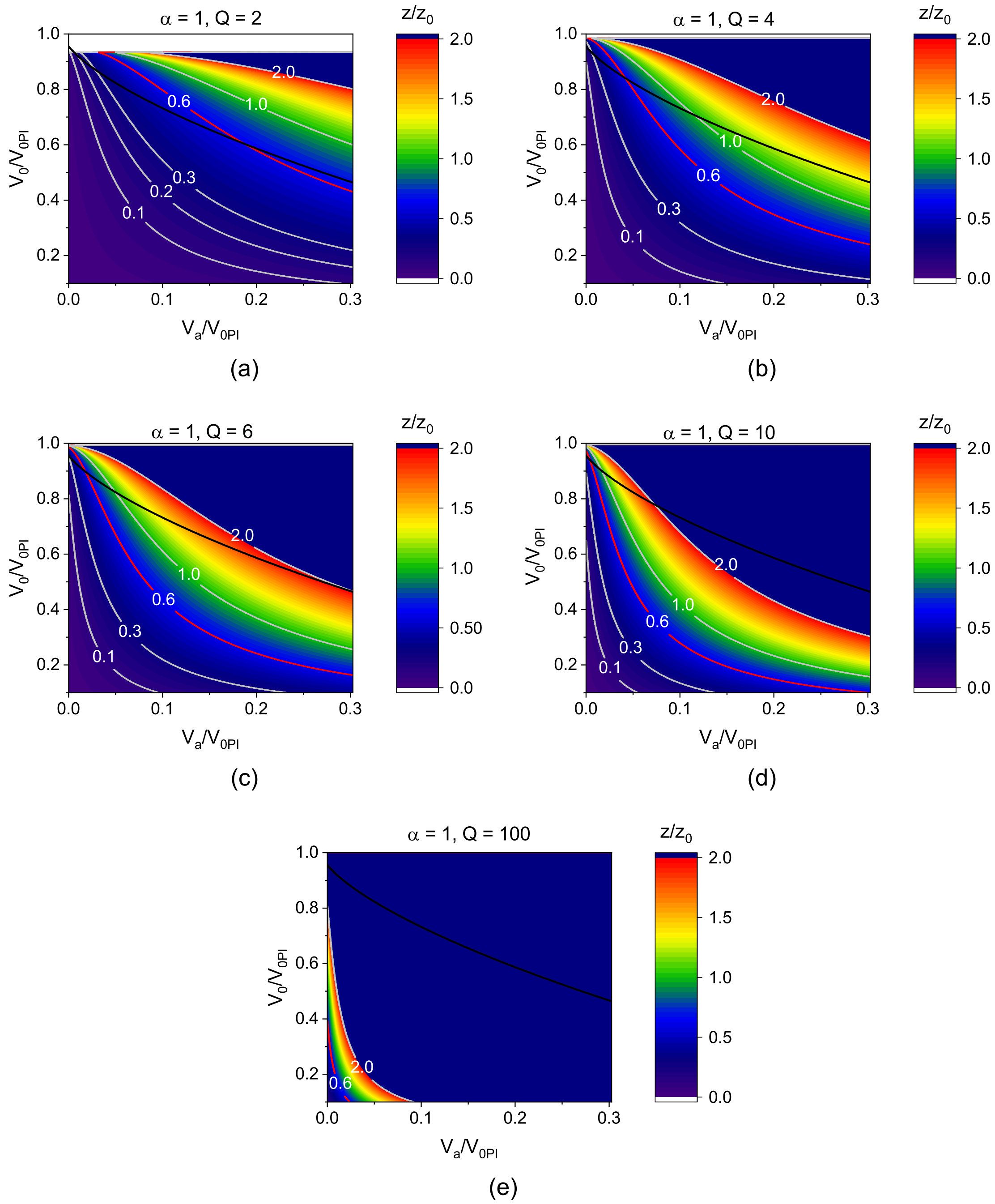

Figure 3.13: Normalized MEMS displacement z/z_0 as a function of outer voltage normalized to the outer pull in voltage $V_0/V_{0\mathrm{PI}}$ and sinusoidal amplitude normalized to the outer pull in voltage $V_a/V_{0\mathrm{PI}}$. The black line shows V_{PI} for the applied outer voltage. The red contour line shows the traditional pull-in position.

3.5 Investigation of the dynamic response of unidirectional and bidirectional actuator

In this section, the full differential equation is solved, i.e., no approximation regarding the MEMS position is assumed.
The dynamic response of the unidirectional actuator is compared to the bidirectional actuator. In both cases, the same MEMS is modeled; see Table 3.1. The unidirectional

Table 3.1: MEMS simulation parameters.

Description	Parameter	Value
Area	A	2.5981E-10 m
Thickness	t_g	4E-7 m
Density	ρ	2328 kg/m^3
Mass	m	2.4194E-13 kg
Permittivity	ϵ	8.85E-12 F/m
Resonant frequency	f_0	3E6 Hz
Quality factor	Q	4
Resistance	R	100 Ω
Air gap	z_0	1E-6 m
Spring constant	k	85.96 N/m
Damping coefficient	b	1.14E-6 Ns/m
Pull in voltage	V_{PI}	105.2 V
Outer pull in voltage	$V_{0\text{PI}}$	136.7 V

MEMS can be employed in a MEMS VCSEL, as seen in [51], where the MEMS is exposed at the top of the wafer. The unidirectional model has the movable MEMS mirror situated at z_0, and the substrate at $z = 0$. The bidirectional MEMS is employed as [74], where the MEMS is sealed by a bonding process of an InP wafer and a SOI wafer. The bidirectional model has the movable MEMS mirror situated at $z = 0$, and the fixed top and bottom contacts at $\pm z_0$. In order for a fair comparison, it is assumed that both MEMS are silicon. In addition, the MEMS movement span is considered, which is the peak-to-peak distance of the sinusoidal movement normalized to the initial air gap size z_0.

3.5.1 Maximum response

For maximum response, a sinusoidal drive signal is used. As previously mentioned, the electrostatic spring softening appears on the fundamental term (assuming a sinusoidal driving signal) for the bidirectional electrostatic actuator. However, for the unidirectional actuator, it appears on the first higher-order term, as a correction to the spring constant, given by[75]

$$K_{elec} = -\frac{\epsilon A V_0^2}{z^3} \tag{3.29}$$

which results in the correction to the resonant frequency given by

$$f = \frac{1}{2\pi}\sqrt{\frac{K_0 + K_{elec}}{m}} \tag{3.30}$$

where $K_0 = m(2\pi f_0)^2$ is the unaffected spring constant.
The first-order effect of electrostatic spring softening for the bidirectional and unidirectional actuator can be seen in Fig. 3.14. As indicated, the effect on the adjusted resonant frequency for the bidirectional actuator is significantly higher, for intermediate V_0 values, compared to the onesided actuator. This is because the MEMS is affected by two DC

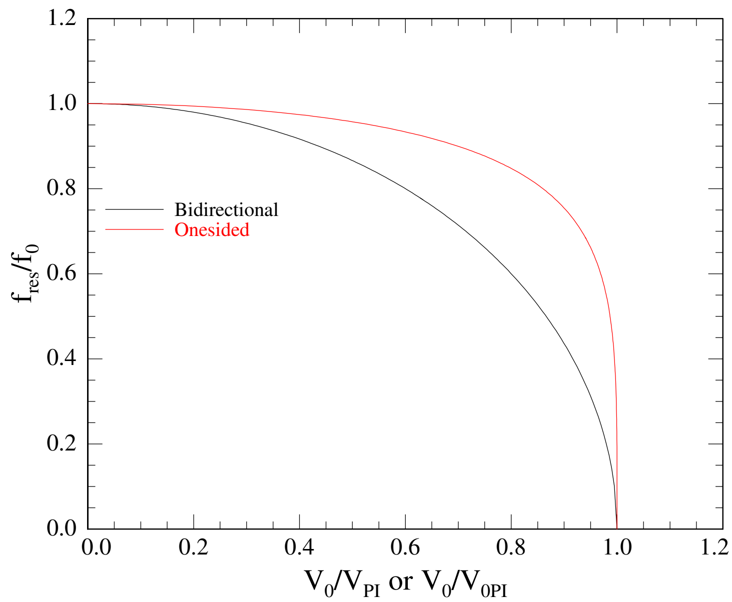

Figure 3.14: First order effect of electrostatic spring softening.

fields in the bidirectional configuration, i.e., from the top and bottom capacitors, while the unidirectional actuator is only effect by one DC field.
The correction of the resonant frequency for the unidirectional actuator shows asymptotic behavior for high static fields since the MEMS is displaced by the applied DC, see Eq. (3.29), in contrast to the bidirectional actuator, therefore the MEMS is doubly affected by the applied DC field. In order to take into account ESS for the unidirectional case three for-loops were used, the first loop specifies the DC voltage V_0, the next loop was used to calculate the DC offset with no AC voltage, subsequently, the resonant frequency given by Eq. (3.30) is calculated, and the last loop was used to calculate the maximum displacement given the previously set DC voltage and a set AC voltage, at the adjusted resonance frequency.
Assuming the actuation frequency follows the trend shown in Fig. 3.14, the normalized displacement for the unidirectional actuator is shown in Fig. 3.15. All calculations were performed using MATLAB's ODE15s. As indicated by Fig. 3.15, for high mechanical quality factors, the transients give rise to pull-in, which is manifested as the repeated pattern in Fig. 3.15 (e) with Q = 100. The time trace for the largest response can be seen in Fig. 3.16.
Fig. 3.16 (a) shows the first 100 f_0 periods, and the transient response can clearly be seen. At around 60 periods, the MEMS overshoots its settled displacement magnitude, nearly reaching the substrate at $z/z_0 = 0$. Fig. 3.16 (b) shows normalized displacement (left) and voltage waveform (right) for the final two f_0 periods. The displacement amplitude is $\approx 1.86z_0$, and the waveform is: $V(t) = V_0 - V_a \cos(2\pi f_a t)$, where $V_0 \approx 15.3$ V and $V_a \approx 18.7$ V. The peak-to-peak displacement amplitude corresponds to $1.86z_0/1z_0 = 186$% gap usage.

The same calculation is performed for the bidirectional MEMS.
Again, assuming the actuation frequency follows the trend shown in Fig. 3.14, the normalized displacement for the bidirectional actuator is shown in Fig. 3.17. The time trace for the largest response can be seen in Fig. 3.18.

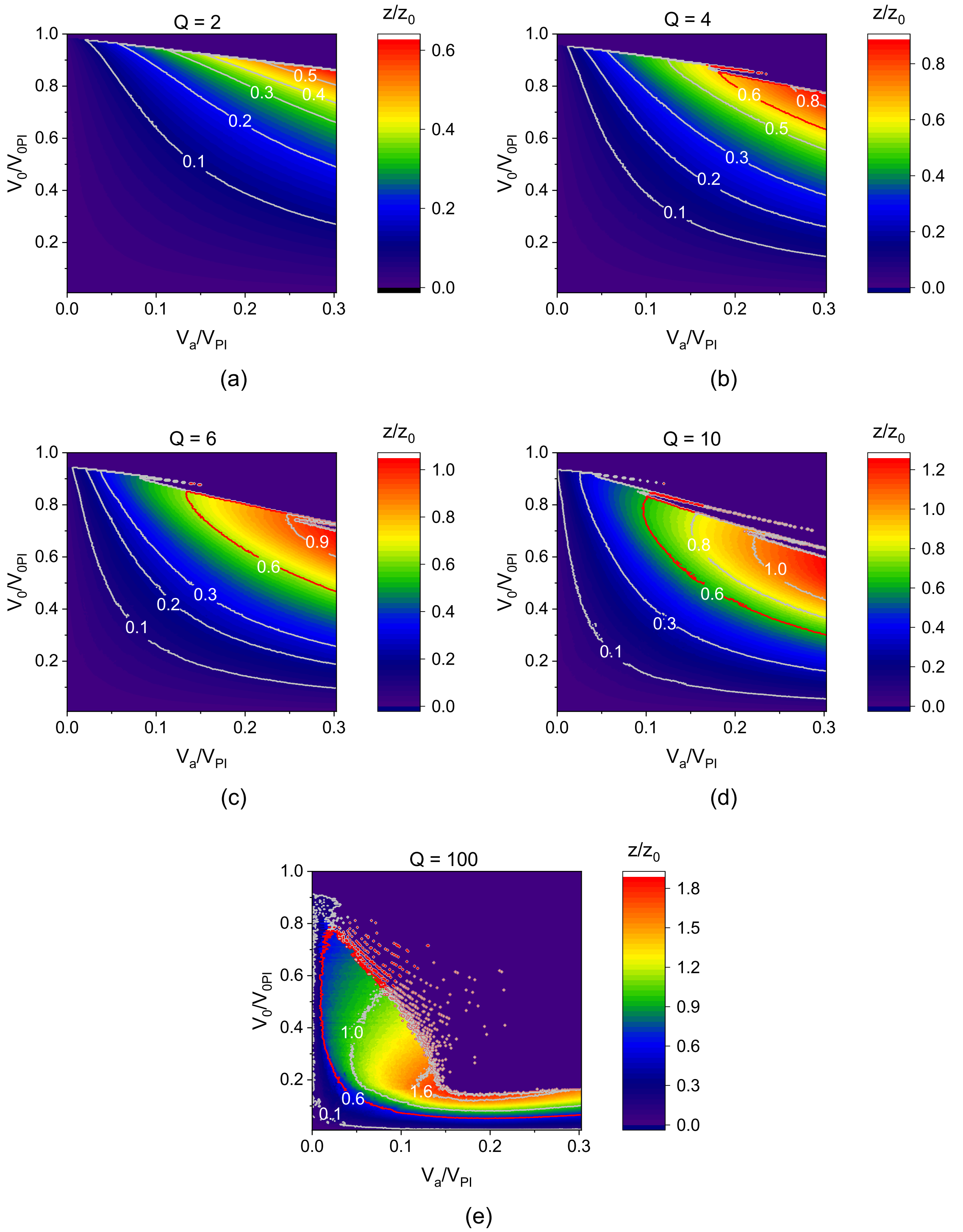

Figure 3.15: Normalized MEMS displacement z/z_0 as a function of outer voltage normalized to the pull-in voltage V_0/V_{PI} and sinusoidal amplitude normalized to the pull-in voltage V_a/V_{PI}, for a unidirectional configuration. The red contour line ($z = 0.6z_0$) highlights the traditional pull-in position.

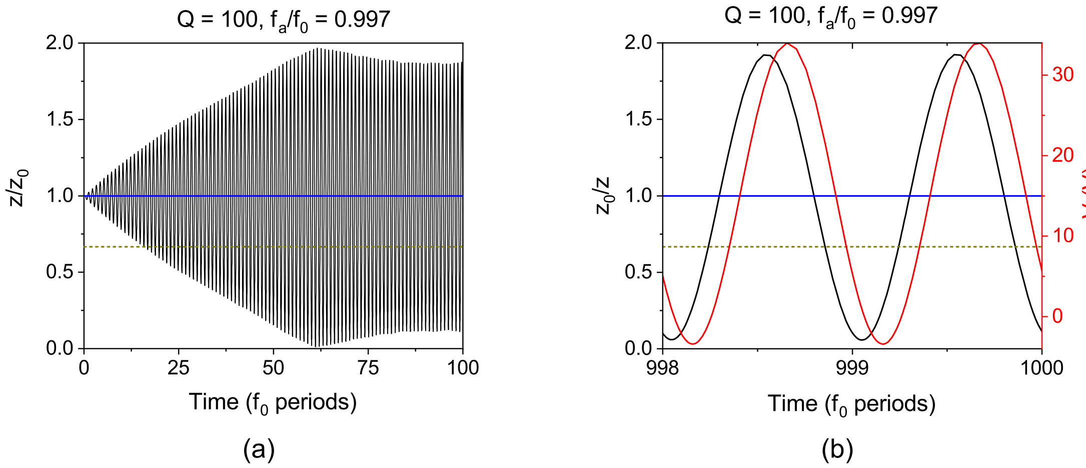

Figure 3.16: Normalized displacement as a function of time, in units of resonance periods. The dashed line highlights the pull-in position $z = 2z_0/3$.

Fig. 3.18 (a) shows the first 100 f_0 periods, and the transient response can clearly be seen. At around 40 periods, the MEMS overshoots its settled displacement magnitude, nearly reaching the bottom and top contacts at $z/z_0 = \pm 1$. Fig. 3.16 (b) shows normalized displacement (left) and voltage waveform (right) for the final two f_0 periods. The displacement amplitude is $\approx 1.85z_0$, and the waveform is: $V(t) = V_a \cos(2\pi f_a t)$, where $V_0 \approx 13.5$ V and $V_a \approx 13.0$ V. The peak-to-peak displacement amplitude corresponds to $1.85z_0/2z_0 = 92.5$% gap usage.

Comparing Fig. 3.15 and Fig. 3.17 for the same Q, the bidirectional maximum amplitude displacement is reached for lower Q values. The absolute maximum being $2z_0$. As expected, the MEMS is more responsive to the driving signal for the bidirectional actuator compared to the unidirectional actuator. It should be noted that the outer pull in voltage $V_{0\text{PI}}$ is around ≈ 30% higher than the traditional pull in voltage V_{PI}, see Table 3.1, which means the max. alternating signal amplitude is ≈ 30% larger in Fig. 3.17 compared to Fig. 3.15.
Comparing Fig. 3.16 (b) and 3.18 (b), the needed alternating voltage is substantial higher for the unidirectional actuator, in addition, the actuation frequency is almost identical.
Comparing the Taylor approximated displacement (Fig. 3.13) and the solution to the differential equation (Fig. 3.17) for the bidirectional actuator, it becomes clear that transients are not included in the approximation. In addition, the approximation overestimates the MEMS excursion at high gap usage. However for low alternating voltage amplitude V_a the agreement is decent. The reason is that the MEMS displacement is not considerable, i.e., it falls within the validity of the approximation.

3.6 Combining static and dynamic actuation

In order to linearize a MEMS sweep, it is customary to use a driving signal below the native resonant mechanical frequency. This forced oscillation lies somewhere between DC and the native resonant frequency. Therefore, it is of interest to combine dynamic and static results.
Applying an outer voltage V_0 to fixed electrodes for the bidirectional actuator has implications for static and dynamic MEMS actuation. The pull-in instability voltage can be tuned for static actuation by the applied outer voltage, as shown in Fig. 3.4. In addition, the static maximum MEMS excursion is affected by the applied outer voltage, reaching its

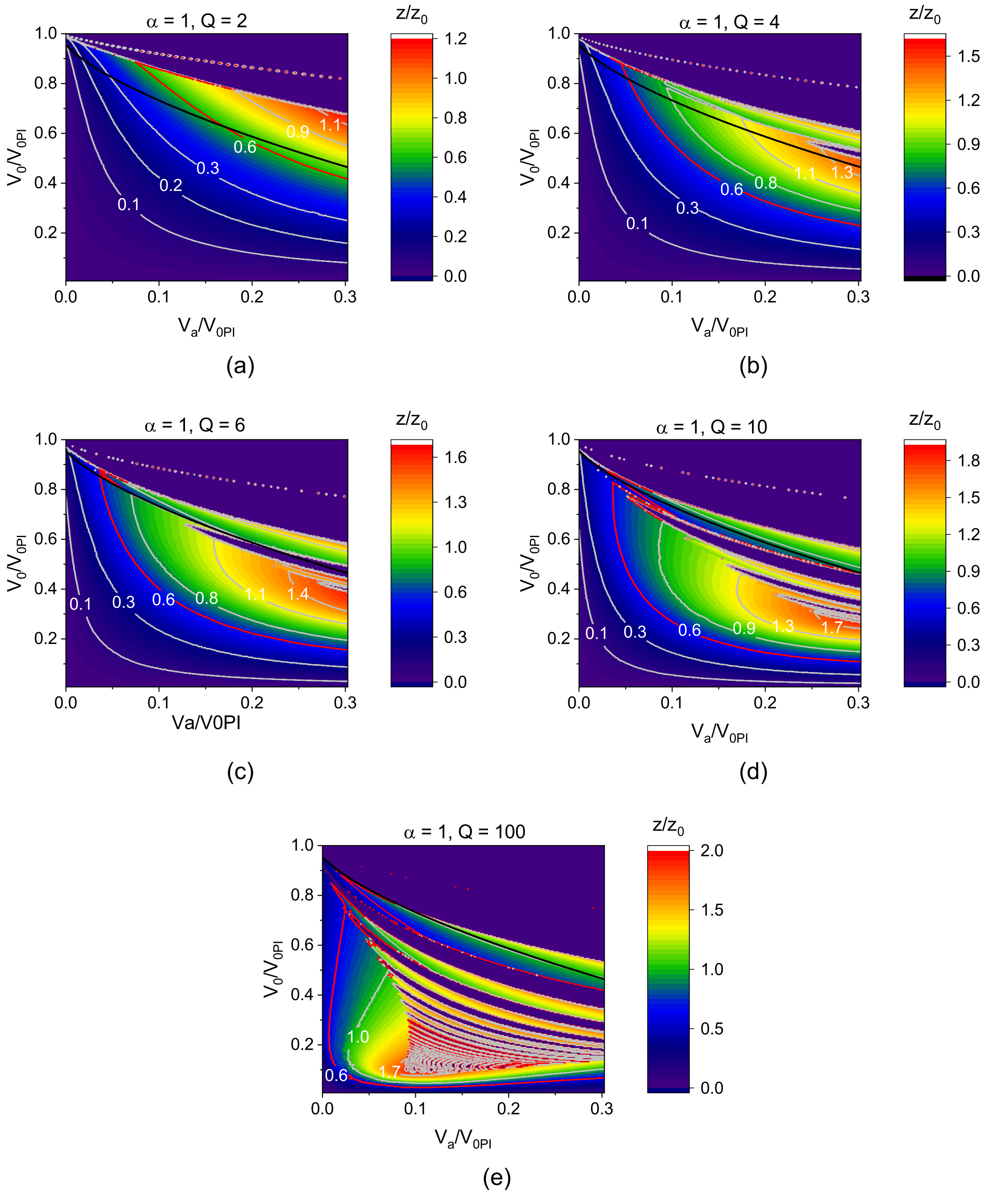

Figure 3.17: Normalized MEMS displacement z/z_0 as a function of outer voltage normalized to the outer pull-in voltage $V_0/V_{0\text{PI}}$ and sinusoidal amplitude normalized to the outer pull-in voltage $V_a/V_{0\text{PI}}$, for the bidirectional configuration. The black line shows V_{PI} for the applied outer voltage. The red contour line shows the traditional pull-in position.

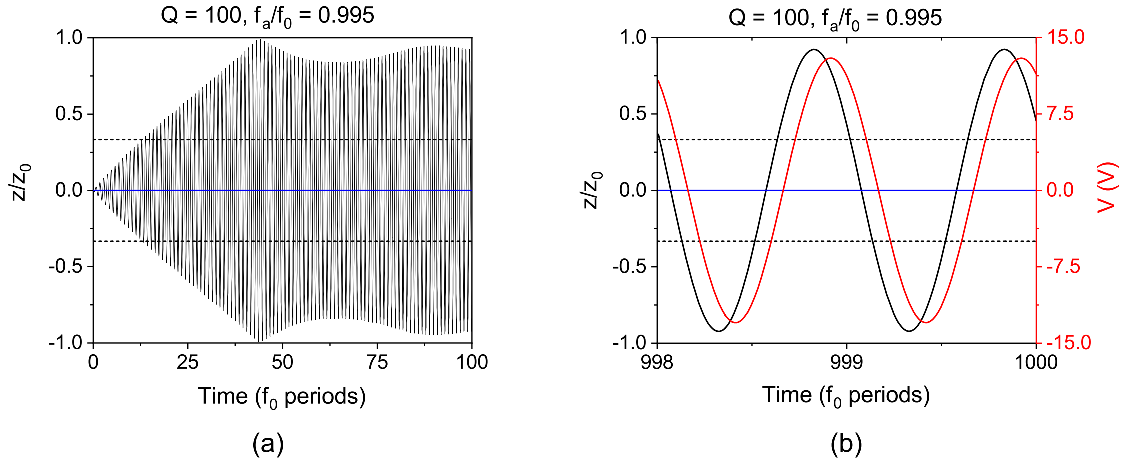

Figure 3.18: Normalized displacement as a function of time, in units of resonance periods. The dashed line highlights the traditional pull-in positions at $z = \pm z_0/3$. Since V_0 is only 13.5 V, this is a good approximation.

maximum, i.e., $z = \pm z_0/3$, when $V_0 = \sqrt{4/27}V_{\mathrm{0PI}}$. For dynamic actuation, the electrostatic spring softening changes the resonant frequency, shown in Fig. 3.14, as:

$$f_{\mathrm{res}} = f_0 \times \sqrt{1 - \frac{V_0^2}{V_{0PI}^2}} \tag{3.31}$$

where f_{res} is the effective resonant frequency for the native mechanical resonant frequency f_0 with spring softening.

Assuming a maximum voltage constraint on the MEMS, i.e., the x-axis in Fig. 3.4, there exists a minimum outer voltage, right y-axis in Fig. 3.4, in order to make the pull-in on the MEMS equal to the maximum voltage constraint. Assuming the aforementioned, the static and dynamic effects of the outer voltage are depicted in Fig. 3.19. The figure shows the minimum outer voltage (Min.V_0) normalized to the outer pull-in voltage, normalized maximum displacement, and normalized adjusted resonant frequency as a function of a maximum voltage constraint on the MEMS (Max.V_1) normalized to the outer pull-in voltage. As can be seen, the smaller the maximum voltage constraint, the higher the outer voltage needs to be, which reduces the maximum static MEMS displacement, and in addition, reduces the dynamic resonant frequency.

In real applications, one is limited by the output of the electronic waveform generator, i.e., the realistic operating condition for stiff MEMS lies on the left side of the vertical line at Max. $V_1/V_{\mathrm{0PI}} = \sqrt{4/27}$.

Fig. 3.20 (a) and (b) show the native resonant frequency, f_0, as a function of maximum MEMS voltage max V_1, the red line indicates a 5 V maximum voltage constraint.

The contour plot on Fig. 3.20 (a) shows minimum outer voltage, Min. V_0 required to tune the MEMS pull-in voltage to be equal to max V_1. As expected, the stiffer the MEMS (higher f_0), the higher the outer voltage is needed for the same maximum voltage constraint. The higher the maximum voltage constraint on the MEMS, the less outer voltage is needed; the triangle in the bottom right corner shows no values by virtue of the available MEMS voltage being sufficient to achieve maximum actuation. The edge of the triangle indicates Min $V_0 \approx 0$ V, e.g., Max $V_1 = 5$ V, and $f_0 \approx 150$ kHz, Min $V_0 \approx 0.7$ V, i.e., close to 0 V. MEMS with a fundamental resonance higher than 150 kHz benefit from the bidirectional configuration (assuming max. $V_1 = 5$ V).

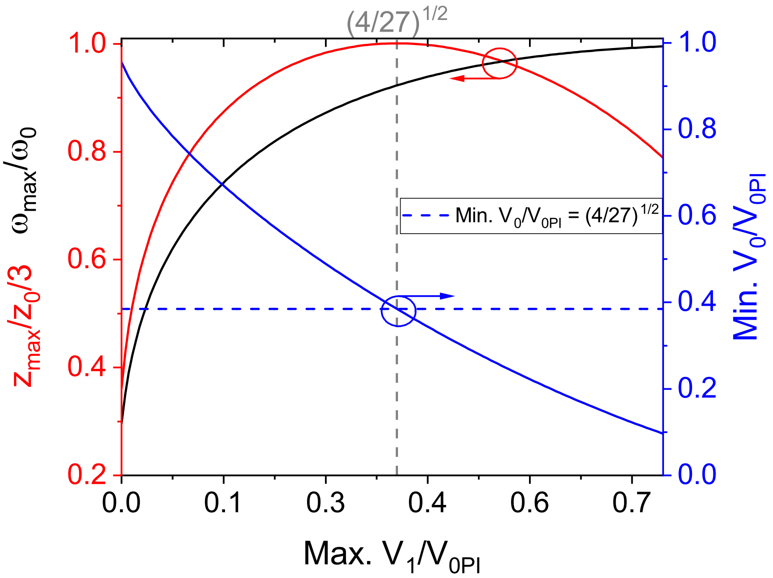

Figure 3.19: Normalized maximum displacement and normalized resonant frequency (left) and normalized minimum outer voltage (right) as a function of maximum MEMS voltage Max.V_1 normalized to the outer pull-in voltage. The dashed vertical (horizontal) line shows when the MEMS voltage is equal to the outer voltage, which results in maximum MEMS displacement $z_{\text{max}}/z_0/3 = 1$.

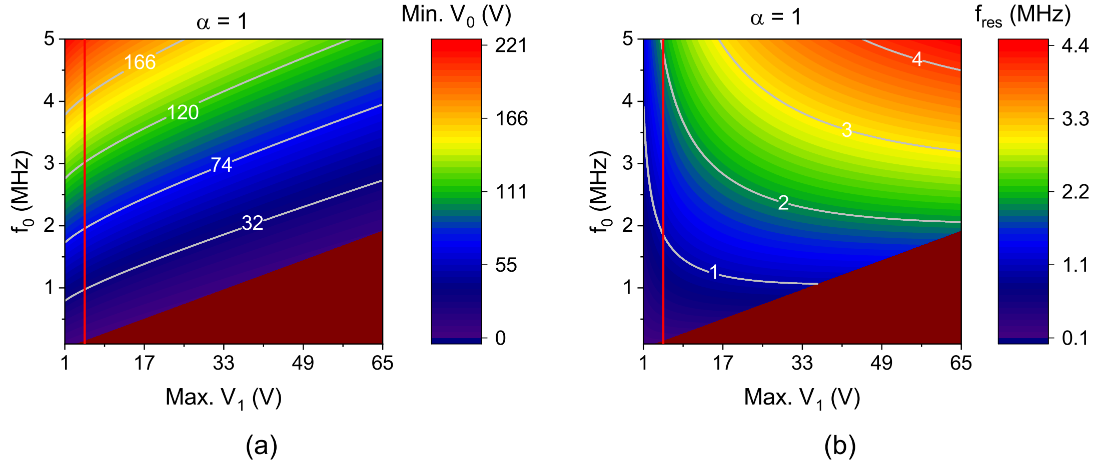

Figure 3.20: (a) Native resonant frequency, f_0, as a function of maximum MEMS voltage max V_1, contour plot showing minimum outer voltage, Min. V_0 required to tune the MEMS pull-in voltage to be equal to max V_1. (b) Native resonant frequency, f_0, as a function of maximum MEMS voltage max V_1, contour plot showing the effective resonant frequency, f_{res}, assuming Min. V_0 is applied to the outer contacts. The vertical line highlighting Max. $V_1 = 5$ V.

The contour on Fig. 3.20 (b) shows f_{res}, assuming Min. V_0 is applied to the outer contacts. The triangle in the bottom right shows no values, for the same reason as before, while at the edge of the triangle $f_{\text{res}} = f_0$, since the minimum outer voltage is 0 V, see Eq. (3.31). As indicated by Fig. 3.20 (b), the higher f_0 is, the higher f_{res} becomes (assuming constant Max. V_1), meaning that even though designing a stiffer MEMS, leads to a higher required outer voltage, which reduces the resonance frequency, one can design for a desired actuation frequency taking into account electrostatic spring softening.
As indicated by Fig. 3.20, a small increase in drive voltage will result in substantially better performance, i.e., less required outer voltage leading to a higher adjusted resonance frequency. Instead of using a high-voltage amplifier, one can use a low-power transformer, e.g., T9-1-X65 from minicurcuits[73], which has a relatively high gain and a bandwidth from 0.5 to 20 MHz. T9-1-X65 is a 1:25 high-frequency transformer, which means a 10 V peak-to-peak (Max. $V_1 = 5$ V) input signal turns into a 42 V peak-to-peak (Max. $V_1 = 21$ V) output signal at 20 MHz.
Fig. 3.21 (a) shows a bidirectional device pumped with 1310 nm CW diode, with an

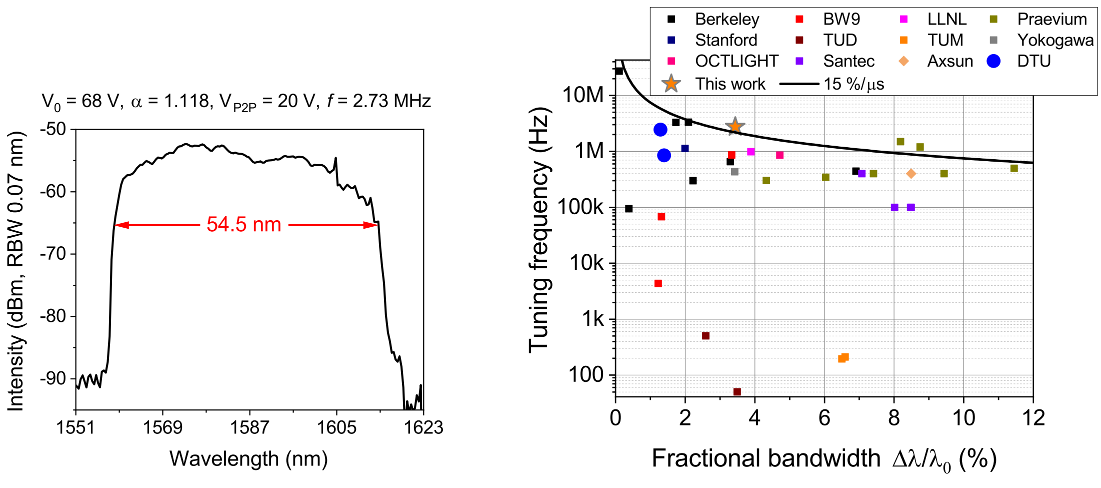

Figure 3.21: (a) Spectrum of bidirectional AC actuation at 2.73 MHz showing bandwidth of 54.5 nm. (b) Tuning frequency as a function of fractional bandwidth, Fig. 3.21 (a) is depicted as "This work".

outer voltage of 68 V, $\alpha = 1.118$, a peak-to-peak AC voltage of 20 V (high impedance), an actuation frequency of 2.73 MHz, resulting in a lasing bandwidth of 54.5 nm. The experimental setup can be seen on Fig. 3.7.
The black curve, in Fig. 3.21 (b), indicates a sweep rate of 15% fractional bandwidth pr. microsecond. The two results from Praevium[37] above the black curve use a high-voltage amplifier (Model 2100HF, Trek, Inc.) in order to amplify the waveform. In addition, the bidirectional MEMS design has not been pushed to its limits, i.e., the tuning frequency and fractional bandwidth can be increased.
Traditionally, because of the maximum constraint on voltage, one could either have ultra stiff/fast MEMS with limited bandwidth or slow/sloppy MEMS with large bandwidth. But by utilizing the bidirectional design, this trade-off is avoided, so it is possible to actuate very stiff MEMS without compromising the tuning bandwidth and needing a high-voltage amplifier. This can open up new application areas for swept source VCSEL for applications requiring fast actuation and large bandwidth.

4 Experimental complications and outlook

This chapter highlights the experimental issues and suggests room for improvement for the next fabrication iteration.
Efforts were made to make the sub-optimal lasers functional, owing to the extensive turnaround time of approximately one year for a fabrication run. This initiative yielded crucial insights into laser characterization and packaging, which will prove advantageous for upcoming testers and final packaging processes.

4.1 Fabrication

Electron beam lithography and subsequent etching define the MEMS spring arms and the HCG. Several variations of MEMS were employed with different stiffness. Two types of MEMS were fabricated, a square and a hexagonal design, see Fig. 4.1. The side lengths were purposely varied on the wafer. In order to estimate the outer pull-in voltage, a resonant frequency calculation was performed in COMSOL, as done in Chapter 2, to extract the fundamental resonant frequency. This was done by importing the mask file into COMSOL, where extrusion is performed to go from 2D to 3D. An example of the smallest 10 μm and largest 25 μm hexagonal MEMS can be seen in Fig. 4.2. The extrusion thickness of the Silicon MEMS in all simulations was 400 nm. The side length of the square design was varied from 20 μm to 35 μm in steps of 5 μm, and the side length of the hexagon was varied from 10 μm to 25 μm. The results for the MEMS variation for the square design can be seen in Table 4.1. The result for the MEMS variation for the hexagon design is summarized in Table 4.2.

Table 4.1: MEMS variation for the square design.

Side length	f_0	$V_{0\mathrm{PI}}$
(μm)	(MHz)	(V)
20	1.0	45.6
25	0.61	27.8
30	0.40	18.4
35	0.28	12.9

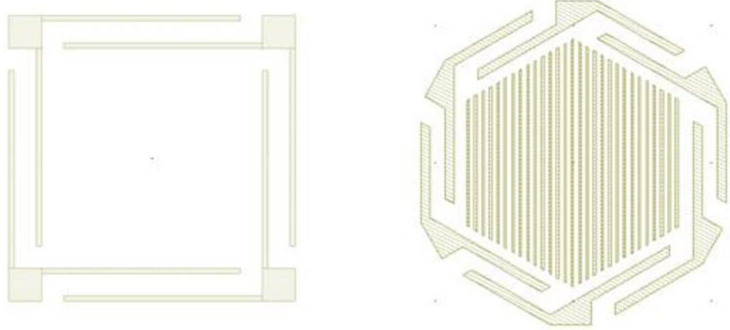

Figure 4.1: Square and hexagonal MEMS designs.

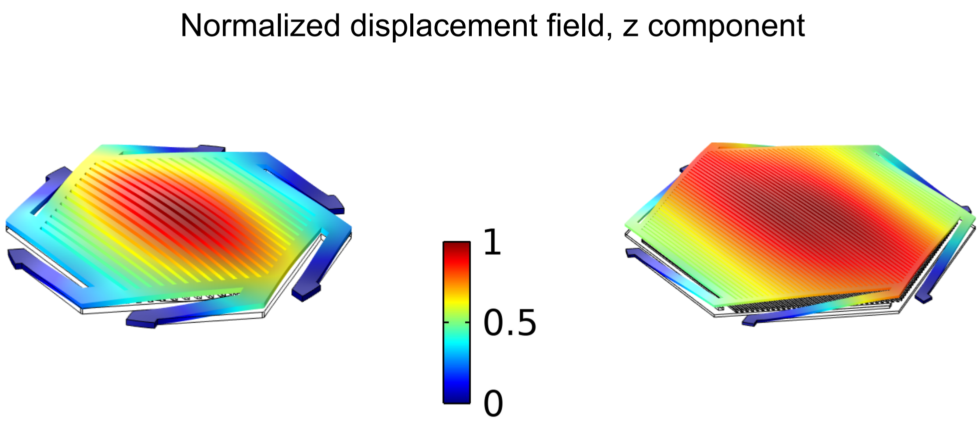

(a) $f_0 = 3.88$ MHz (b) $f_0 = 386$ kHz

Figure 4.2: Spatial (x,y,z) mode shape of the fundamental mechanical mode of a 10 μm (a) and a 25 μm (b) hexagonal MEMS. The color legend shows the normalized z component of the displacement field.

As shown in Fig. 3.1 (b), three numbers are shown in order to identify the MEMS varia-

Table 4.2: MEMS variation for the hexagon design.

Side length	f_0	$V_{0\text{PI}}$
(μm)	(MHz)	(V)
10	3.9	176.8
20	0.66	30.3
25	0.39	17.6

tion. The first number indicates the section. The mask is divided into 9 different sections, all consisting of an 8×8 laser grid, sorted in a 3-by-3 array. The 9 sections, having a 24×24 laser grid, are then repeated in a 3-by-3 array; this pattern is repeated until the wafer is filled.

Sections 7, 8, and 9 are all square MEMS with a sidelength of 20 μm. Sections 1, 2, 4, and 5, have the square MEMS with the variation shown in Table 4.1, where two rows are fabricated for each sidelength. Finally, sections 3 and 6 have hexagonal MEMS with the sidelengths shown in Table 4.2, as follows: three rows with side length of 10 μm, three rows with a sidelength of 20 μm, and finally two rows with a side length of 25 μm. The second number in Fig. 3.1 (b) indicates the sidelength of the MEMS, meaning the bidirectional MEMS VCSEL depicted belongs to section 6, i.e., it has a hexagonal MEMS, with a 10 μm sidelength.

When creating the bottom air gap, in order to prevent the sticking of the very light MEMS, a critical point drying (CPD) release is performed. In CPD the sacrificial layer goes from solid to gas, thereby skipping the liquid phase, which can potentially destroy the tunability of the MEMS.

During fabrication, the CPD process was unsuccessful, resulting in only the stiffest MEMS surviving the process, i.e., the hexagonal MEMS with 10 μm sidelength. In the next fabrication iteration, it might be beneficial to increase the number of stiff MEMS in order to be more resilient against unsuccessful CPD. An alternative solution is to use the hydrogen fluoride (HF) vapor etcher[76]. The HF vapor etcher is used for etching the sacrificial oxide in SOI thereby releasing silicon MEMS structures. An anhydrous hydrogen fluoride

(HF) gas is used as an etchant, and ethanol vapor serves as a catalyst in the process. This allows for dry etching of silicon dioxide and eliminates issues associated with wet etching, such as small structures collapsing due to the surface tension of water during under etching.
The 90 degree counterclockwise rotated number depicted in Fig. 3.1 (b) indicates which column in the 8×8 grid the laser belongs to, i.e. column 7 for the depicted laser. The duty cycle (DC) of the 1D HCG is varied in each column, as indicated in Table 4.3.
The period remained constant at 650 nm and the designed thickness was 400 nm. The

Table 4.3: HCG duty cycle variation.

Column number	DC	width
		nm
1	0.61	396.5
2	0.62	403.0
3	0.63	409.5
4	0.64	416.0
5	0.65	422.5
6	0.66	429.0
7	0.67	435.5
8	0.68	442.0

calculated reflectivity spectra can be seen in Fig. 4.3, as well as the calculated dielectric DBR reflectivity spectrum (provided by Proff. Kresten Yvind).
As indicated, the lower wavelengths for the lower DC columns have a chance of bottom

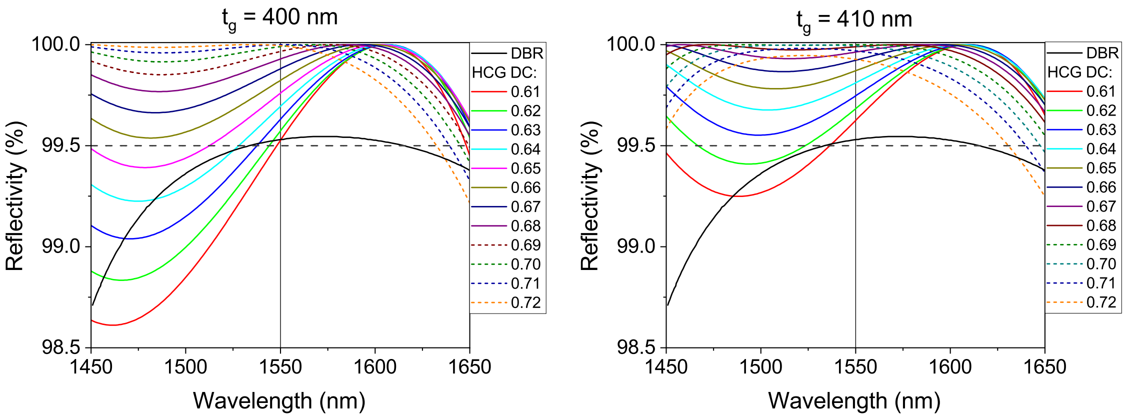

(a) (b)

Figure 4.3: Reflectivity spectra of DBR and HCGs with different DCs with a HCG thickness of 400 nm (a) and 410 nm (b).

emitting instead of top-emitting due to the reflectivity of the HCG being lower than the top DBR reflectivity. In the next iteration, an upshift in the DC values can be beneficial in order to ensure top emission, i.e., the reflectivity of the HCG stays above the DBR reflectivity. This is indicated by the dashed curves in Fig. 4.3, where the reflectivity spectra DC 0.69, 0.70, 0.71, and 0.72 are shown.
According to specifications, the purchased wafer from IQE silicon had a device layer thickness of 400 ± 5 nm[29]. As indicated by Fig. 4.3 the thickness substantially affects the reflectivity spectra. In the present case, a thinner device layer corresponds to more rows

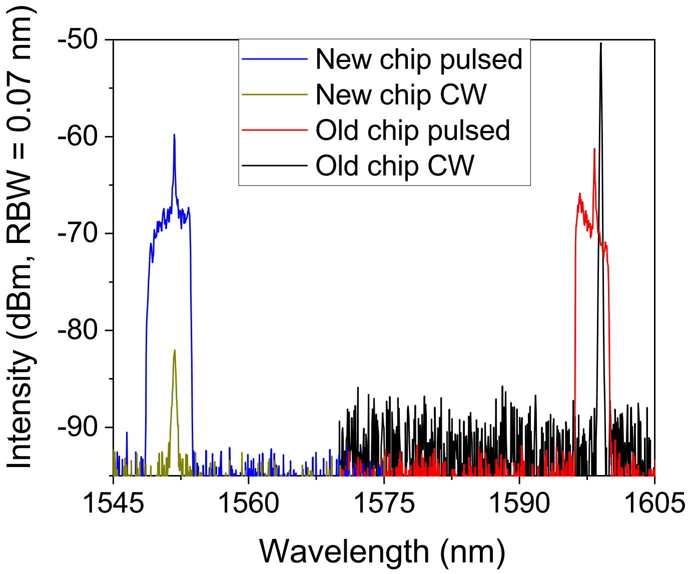

Figure 4.4: Spectra showing the new and the old chip pumped with a 980 nm pulsed pump and a CW 1310 nm pump.

below the high reflectivity criterion (R=99.5%), indicated by the dashed horizontal line. For the next iteration, thickness measurement before patterning would optimize the design process in order to fabricate more top-emitting devices. The above calculations assumed perfect pattern transfer from the mask to the device. It is crucial to measure the patterned HCG using scanning electron microscopy (SEM) to ensure that the pattern transfer is acceptable, and if not, adjust e-beam mask parameters accordingly.
Assuming good control of the HCG parameters, it would be worth adding an additional dielectric DBR pair on top of the current 7 in order to increase DBR reflectivity bandwidth, with $R > 99.5$%, to potentially increase the lasing bandwidth, assuming that the mirror reflectivities are the limiting factor.

4.2 Pulse pumping

Initial characterization of fabricated devices was performed with a pulse pump[77]. The setup was similar to the one shown in Fig. 3.7, but instead of a 1310 nm pump, and 976 nm pulse pump was used, in addition, the 1310/1550 nm WDM splitter was replaced by a 976/1550 nm WDM splitter.
Lasing was observed at room temperature for the pulse pump, however not when pumping CW with the 1310 nm pump. As the pulse duty cycle was at 1%, and the pulse width was 500 ns, no heating is assumed to be generated while pulse pumping. An older chip, with different gain media[29], showed room temperature lasing; the chips are compared in Fig. 4.4. As indicated by Fig. 4.4 for the old chip the CW output has higher intensity compared to the pulsed output, which is expected, since the duty cycle for CW output is 100%. In contrast, for the new chip, the CW spectrum has lower intensity compared to when the laser is pumped by the pulse pump. This indicates that lasing does not occur when the new chip is pumped with the 1310 nm CW pump, due to insufficient gain due to thermal losses.

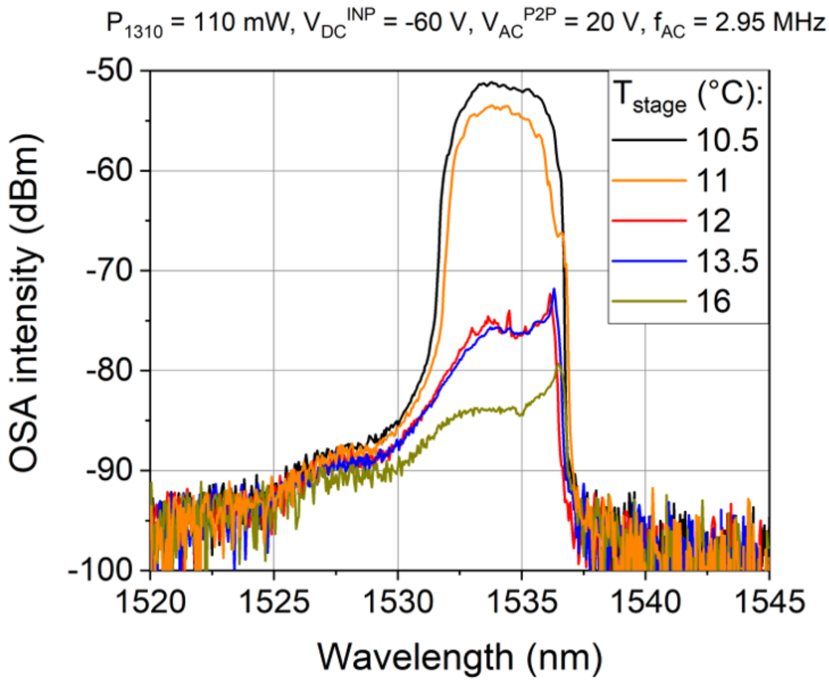

Figure 4.5: Spectra taken at different stage temperatures. Lasing occurs at around $11°$C. RBW = 0.07 nm.

4.3 Lasing slightly below room temperature

The copper chuck the chip is mounted on can be temperature controlled, see Fig. 3.7. Fig 4.5 shows spectra taken at different stage temperatures. Cooling the stage resulted in CW lasing using 1310 nm pump light. The laser is biased with -60 V on the InP (top) contact and sinusoidal drive with a peak-to-peak voltage of 20 V (high impedance) on the MEMS (middle) contact. A drastic increase in intensity is seen when the stage is around $11°$C, indicating lasing in contrast to amplified spontaneous emission (ASE). This shows that the temperature dependant loss is too high in the cavity in order to support lasing at room temperature. Adding some heat-guiding layers might improve the thermal properties of the MEMS VCSEL.

4.4 Condensation

The laboratory where the characterization was performed is temperature-controlled but not humidity controlled. Since the dew point of water changes as a function of humidity, the temperature at which condensation occurs varies. Since the MEMS VCSEL relies on electrostatic tuning, it is important that no current flows, i.e., there is no electrical short. Water condensation can provide a short between the contacts; see Fig. 4.6.

In order to minimize water condensation on top of the chip, a dry air chamber was designed (see Appendix A.7); see Fig. 4.7 Martin Nielsen fabricated the dry air chamber from the mechanical workshop at DTU.

The dry air in the form of N_2 is continuously pumped to lower the humidity so that water condensation does not form on the chip surface when lowering the temperature.

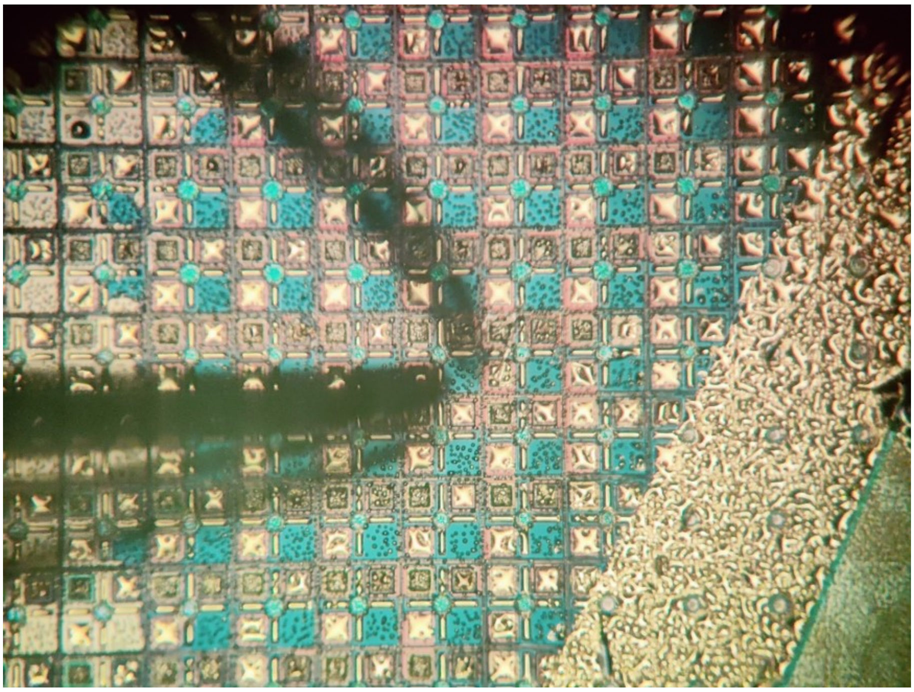

Figure 4.6: When cooling below the dew point temperature, condensation occurs on the chip surface.

4.5 Bidireciontal driver

To realize increased drive amplitude, a bidirectional driver was made by two electrical engineering students, Theodor Nørby-Lassen, and Leo Uhre Jakobsen; see Appendix A.4 for a schematic of the device. The two students were supervized by Proff. Kresten Yvind, and co-supervized by the PhD student and Kjeld Dalgaard. A picture of the final device can be seen in Fig. 4.8. The driver interfaces with a zero insertion force (ZIF) socket, shown in green to the bottom right in Fig. 4.8 (c). The driver consists of two DC-to-DC converters for the two stationary contacts. The potentiometer with "Amplitude" written above controls the amplitude, which can go as high as 200 V, and the balance turning knob, refers to the α coefficient in Chapter 3. The AWG interfaces with a BNC connection with a 50 Ω termination, reducing unwanted reflections in the drive signal. The drive signal is then transformed via a T9-1X65 from minicurcuits[73], turning a 10 V peak-to-peak signal into 42 V peak-to-peak at frequencies up to 20 MHz.

In order to interface with the ZIF socket, the chips have to be diced out and mounted on a mounting board. Since the processed InP wafer is a fraction of the thickness of the SOI wafer (650 ± 50 μm handle wafer thickness)[29], the crack caused by the diamond scribe, shown in Fig. 4.9 will follow the crystal planes of the silicon handle wafer. After the scribe, the chip was placed face down in a curved chip holder, where force was applied to the backside for the crack to propagate along the handle wafer crystal plane. Owing to the thickness of the SOI wafer, quite a lot of force is needed, compared to e.g. GaAs chips.

To wire bond to the electrical contact, a ball wire bonder[78] was used; an angled top view is seen in Fig. 4.10.

The laser chip sits on top of a thermoelectric cooler[80] (CP0734-238, see also Appendix A.5, for specifications) on top of a 14-pin chip mounting board. At the bottom of Fig. 4.10, a blue 10 kΩ thermistor is seen[81]. The chip and the TEC are glued by a two-part silver epoxy[82] (see also Appendix A.6 for specifications).

A top view through a microscope can be seen in Fig. 4.11. When bonding, it was important

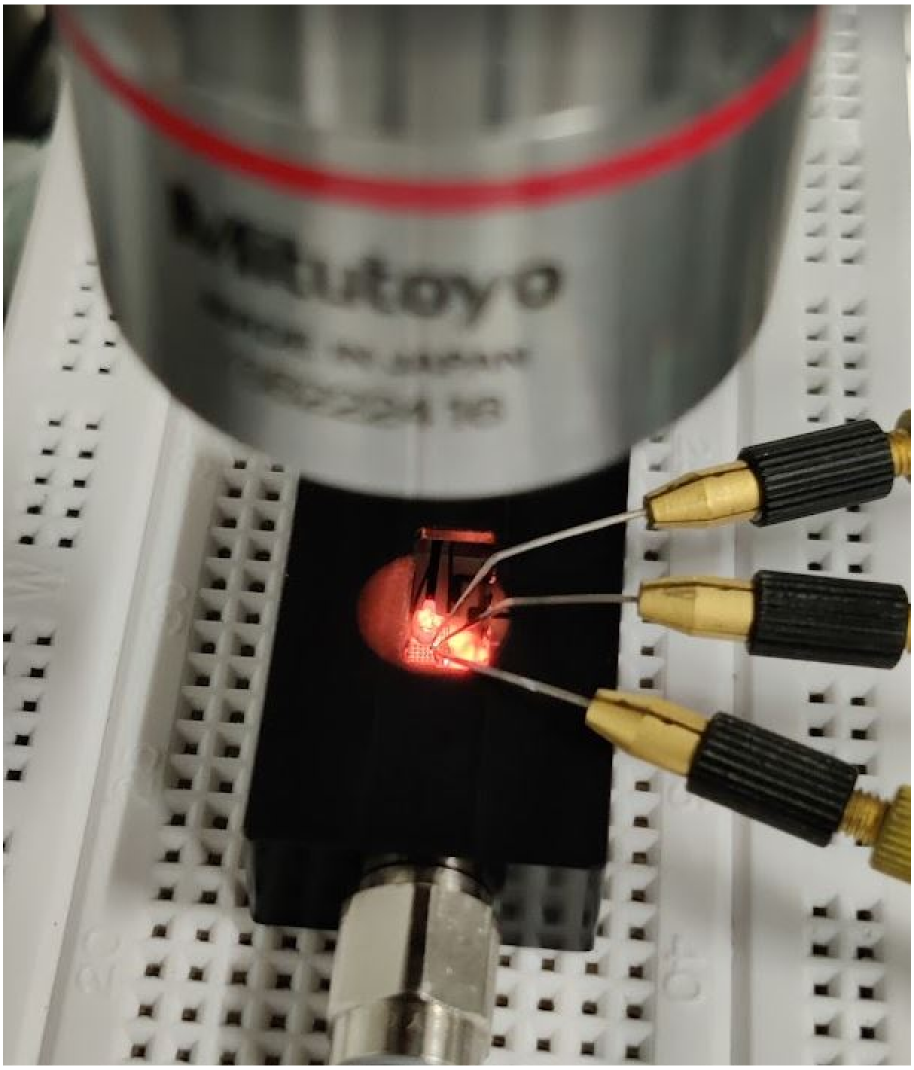

Figure 4.7: Dry air chamber below a microscope objective. Three tungsten probes are seen to the right, in contact with the laser chip.

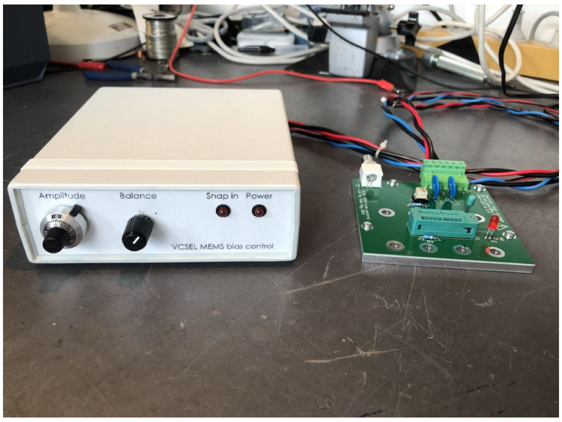

(a)

(b)

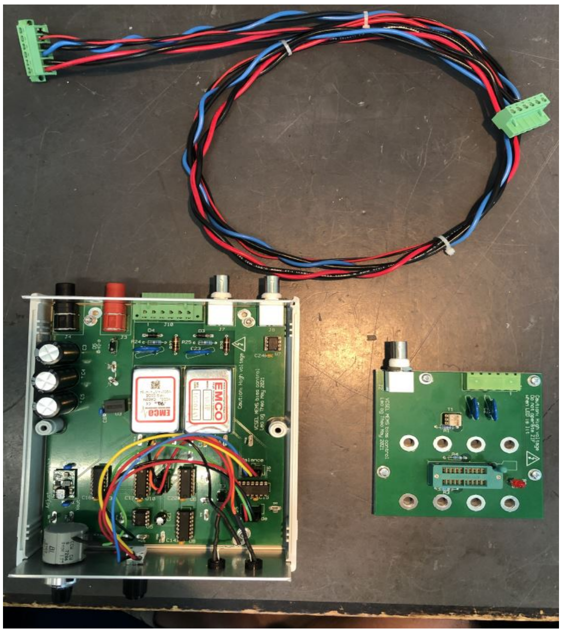

(c)

Figure 4.8: Bidirectional driver designed by Theodor Nørby-Lassen, and Leo Uhre Jakobsen.

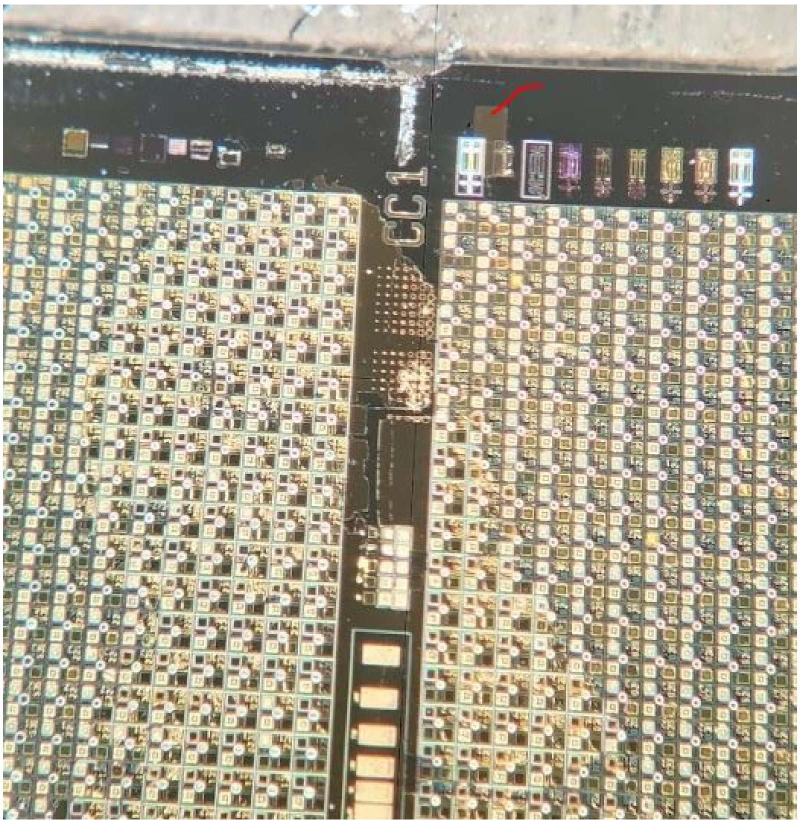

Figure 4.9: Miscroscope image of the laser chip showing a scribe at the top caused by a diamond scriber.

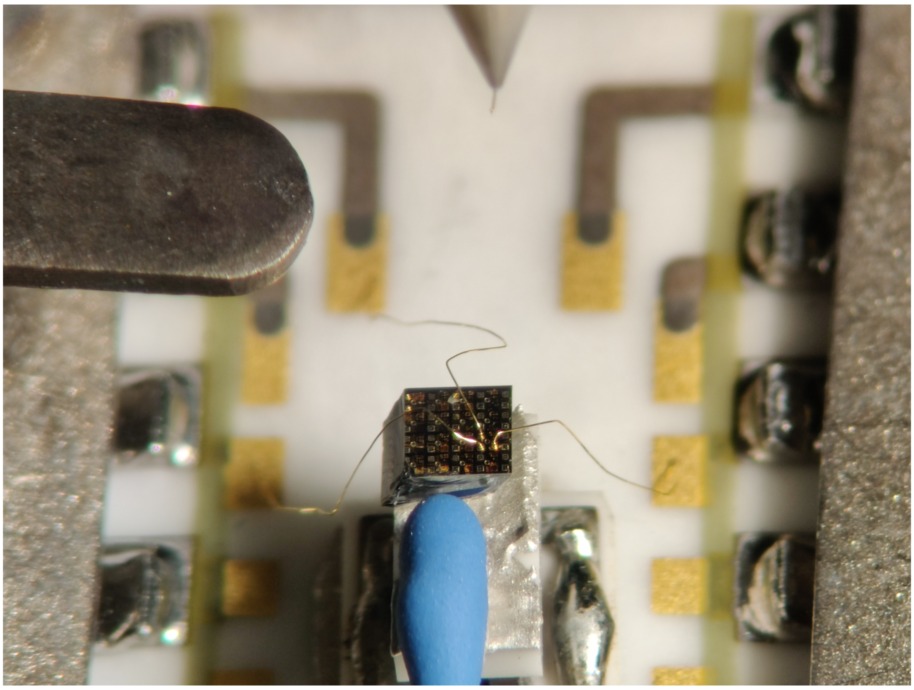

Figure 4.10: Wirebonding with ball wire bonder[78]. The laser chip is glued[79] on top of a TEC[80], next to a thermistor[81].

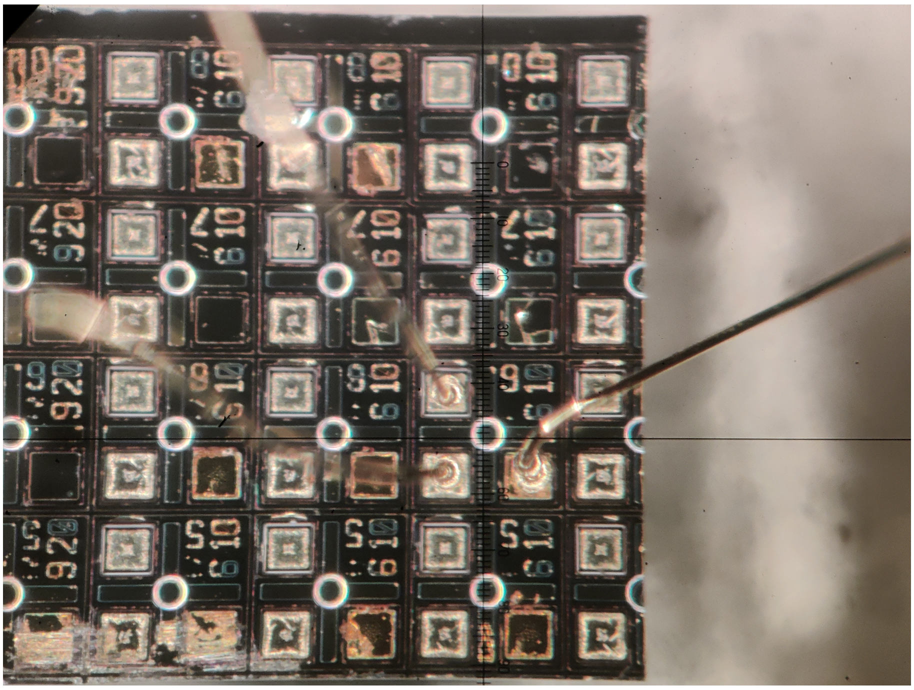

Figure 4.11: Microscope top view of the wire-bonded laser.

to hit just at the center of the contact; if not completely centered, the gold ball would reach the sides of the contact, thereby shorting the different layers, resulting in no electrostatic actuation being possible. Shorting between different layers was also observed for some unwire-bonded lasers, which can be caused by sidewall coverage during the metalization of the contacts. In the next iteration, the lasers would benefit from an insulating layer, e.g. SiO_2 covering the sidewalls, see Fig. 1.8, which would minimize shorting from the sidewalls of the contact openings.

The metalization of the three contacts consists of two steps. In the initial step, Ni (30 nm), Ge (50 nm), Au (250 nm), is deposited on the n-InP layer only. Subsequently, Ti (25 nm), Pt (75 nm), and Au (300 nm) is deposited on all contacts, i.e. on top of the Ni-Ge-Au of the n-InP contact, as well as the n-Si device layer, and the p-Si substrate. After deposition, rapid thermal annealing is performed for 15 seconds at 430 degrees in order to alloy the n-InP contact.

Fig. 4.12 shows an overview of a single device, highlighting the contacts. Energy-dispersive X-ray (EDX) spectroscopy was performed on the MEMS (device layer) contact and the silicon (substrate) contact. The results are in Fig. 4.13. Even though the same metalization was performed on both contacts, the spectra are quite different. As expected, the silicon contact shows mostly gold since the depth of origin of most of the x-rays in bulk gold (M_α with the energy of 2.1230 keV) is around 42 nm for a 12 kV SEM[83]. However, the MEMS contact shows platinum and silicon, which means that gold has diffused into the silicon device layer. The difference in spectra is believed to be related to the difference in the thickness of the underlying layers, which is 400 nm for the device layer and 650 μm for the substrate. Due to the much thinner device layer, it has reached a higher temperature than the substrate during annealing, which has resulted in a silicon-gold eutectic being formed. The eutectic was impossible to (gold) wire bond to.

In future iterations, a lower RTA target temperature can be utilized to avoid the eutectic forming, e.g., below the gold-silicon eutectic temperature of $363°$C[84]. An alternative could also be to first alloy, by RPA, the two metalization steps on the n-InP contact only,

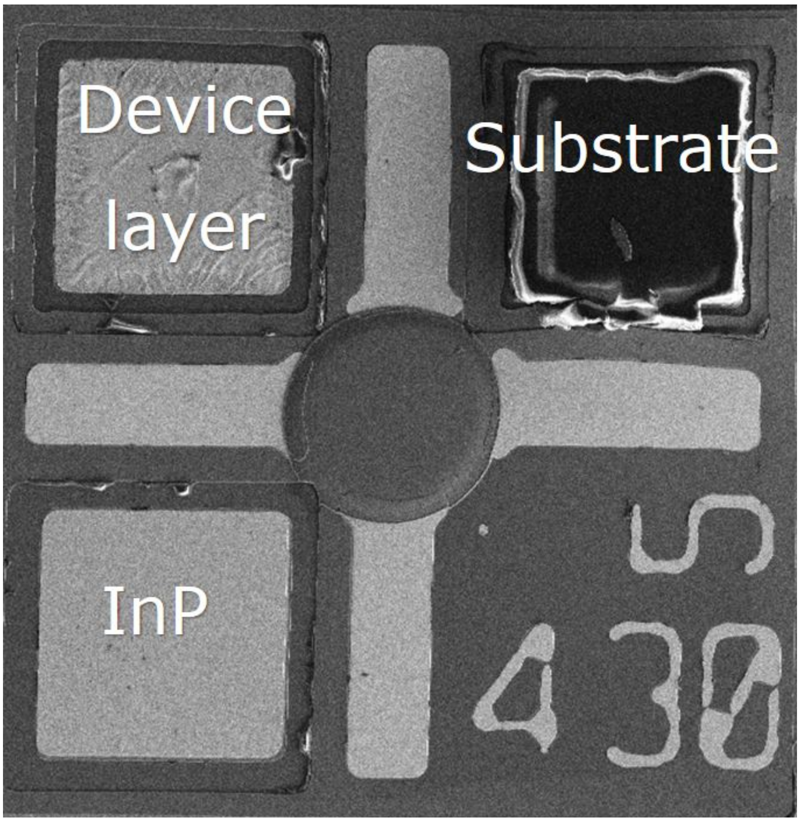

Figure 4.12: SEM top view of device

whereafter the metalization on the MEMS and silicon contacts can be performed. The drawback of this approach is the added fabrication steps.
Two pump wavelengths were possible, either 976 nm or 1310 nm, as designed by the reflectivity dips in the DBR top mirror. Senior Research Engineer Henrik Frederiksen deposited the DBR at the Chalmers University of Technology. In Fig. 4.14, the designed DBR spectrum is compared to a measured spectrum. Postdoc Hitesh Kumar Sahoo measured the spectrum with photo-luminescence; see Appendix A.8. A good agreement is seen between the designed and fabricated DBR spectrum, allowing top pumping through the DBR mirror with either a 976 nm or a 1310 nm pump laser.
When pumping CW with a 976 nm pump, more absorption is seen in the quantum wells and the silicon device layer and handle wafer. This resulted in the TEC working harder to keep the same temperature. Therefore, the 1310 nm pump was preferred due to less thermally induced losses.
In order to further reduce the absorption of the 1310 nm pump, a metalization of the backside of the wafer was performed to reflect pump light, minimizing 1310 nm absorption in the TEC itself. In future fabrication iterations, for optically pumped devices, it will be beneficial to add a metalization step for the backside of the handle wafer, in order to minimize absorption in the TEC when packaging.
When pumping with nitrogen to reduce the chance of water condensation, the TEC had to work harder to cool since the nitrogen temperature was not controlled, meaning that the TEC and laser chip were heated due to convection if the targeted temperature was below room temperature. For final packaging, the laser can be packaged in a dry air environment, e.g., a transistor-outline-can (TO-can), removing the need for continuous nitrogen pumping.

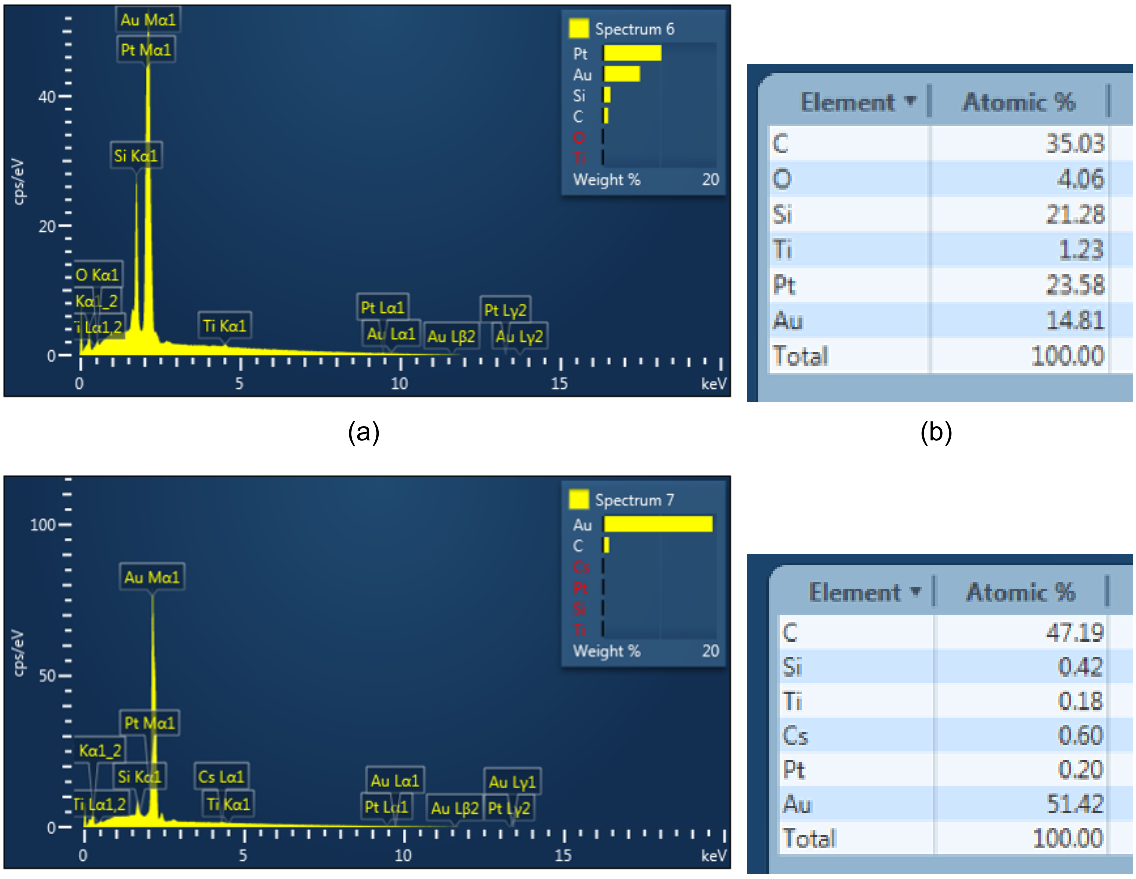

Element	Atomic %
C	35.03
O	4.06
Si	21.28
Ti	1.23
Pt	23.58
Au	14.81
Total	100.00

Element	Atomic %
C	47.19
Si	0.42
Ti	0.18
Cs	0.60
Pt	0.20
Au	51.42
Total	100.00

Figure 4.13: EDX analysis of the MEMS contact (a) and (b), and the silicon contact (c) and (d).

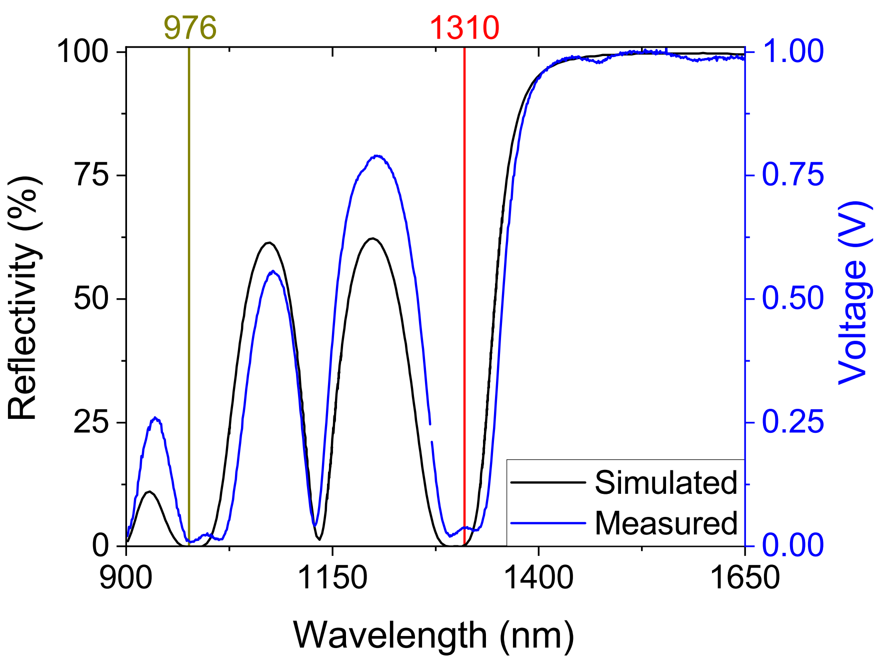

Figure 4.14: Measured and simulated DBR spectrum.

A linear temperature controller, see Appendix A.9, was used to control the TEC. Due to the high thermal conductivity of the small TEC the temperature adjustments were faster than the control loop in the proportional-integral-derivative (PID) controller, resulting in overshoots (below and above) of the measured temperature compared to the set temperature value. To solve this, two resistors were added, one in series and one in parallel; see Fig. 4.15. The resistors used were a 2 Ω 3 W[85] (see Appendix A.10 for specifications)

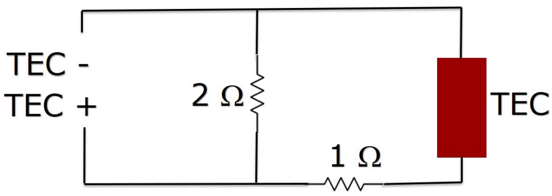

(a)

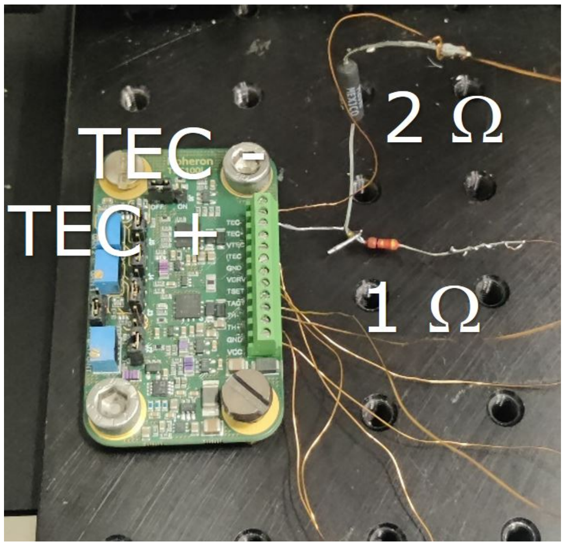

(b)

Figure 4.15: (a) TEC circuit (b) picture of the TEC controller with the resistors added.

and a 1 Ω 1 W[86] (see Appendix A.11).

This ad hoc approach served two purposes. Firstly, it slowed down the dynamics of the TEC to match the driver's PID control loop, and secondly, it restricted the maximum output of the TEC driver to be within the limits of the TEC element. In future iterations for final packaging, an application-specific integrated circuit (ASIC) can be designed in order to have a temperature controller with a PID loop more suited for the small form factor of the laser-TEC-thermistor system.

4.6 Dielectric breakdown

After wire bonding, electric discharge was observed when applying a large outer voltage, e.g., 100 V, as shown in Fig. 4.16. The dielectric strength of air is around 3 kV/mm[87], and with the example given in Fig. 4.16, the electric field is around 0.8 kV/mm. However, whether electric discharge occurs depends on the shape, conducting material, air humidity, and pressure. The same voltage difference provided by the tungsten probes did not generate electric discharge. In future iterations, increasing the distance between the contacts will be beneficial to avoid electric discharge occurring. Expanding the size of an individual device will decrease the overall number of devices on a wafer. Nevertheless, this is the preferable approach to avoid being restricted in the DC voltage on the static outer contacts for wire-bonded packaged devices.

An ad hoc approach was implemented in order to decrease the likelihood of discharge by using silicon oil on the wire-bonded contacts; see Fig. 4.17. Assuming discharge occurs at the surface, not between the gold wires above the chip.

The benefit of using silicon oil can be threefold. Firstly, it is non-electrically conducting and has a decent thermal conductivity, which means it can be used between and on the

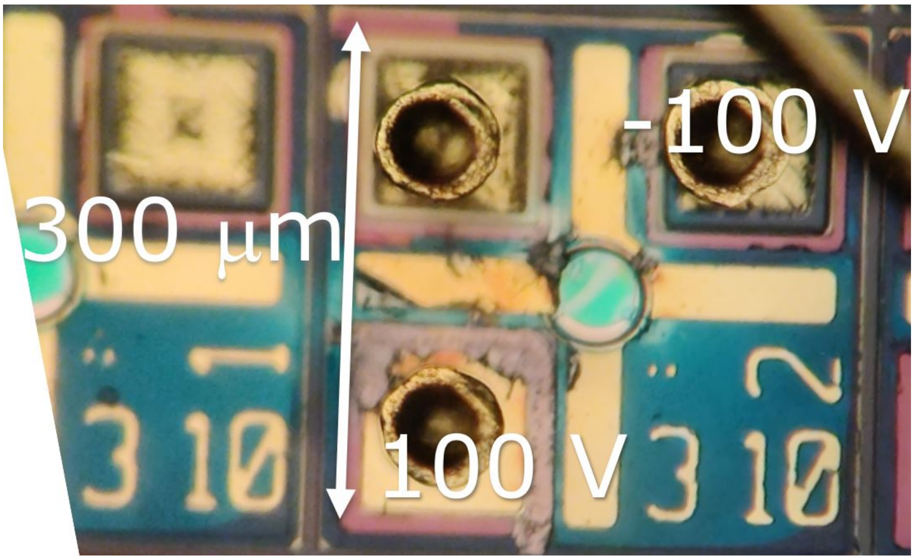

Figure 4.16: Device destroyed by electric discharge.

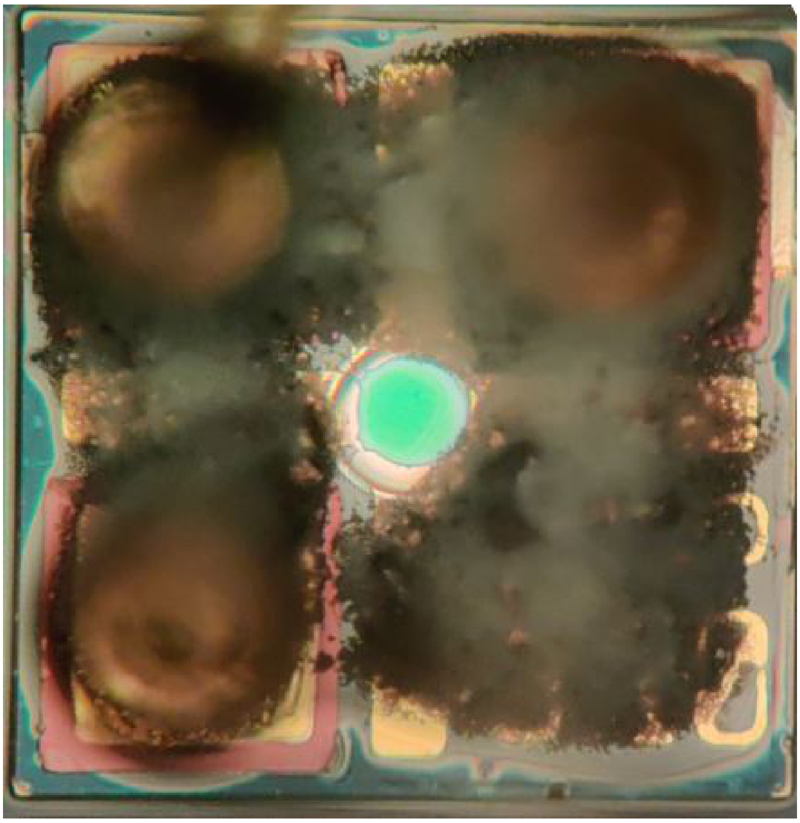
Figure 4.17: Silicone oil painted on top of a MEMS VCSEL.

contacts without causing a short. Applying silicon oil on the device might decrease the device's thermal resistance, resulting in less thermally induced losses. Secondly, silicon oil has a higher dielectric strength (18 kV/mm[88]) than air, reducing the risk of surface-generated electric discharge. Thirdly, the oil is extremely wetting, filling the gap between the gold ball and the vertical sidewalls in the contacts and even filling up the contact depressions. Since the oil is very hydrophobic, it can minimize water condensation, reducing the chance of electric shorts. Because of the aforementioned benefits, it would be beneficial to use silicon oil in future packaging. One could even do flip-chip packaging in silicon oil, assuming bottom emission through the Si substrate, to reduce the device's thermal resistance further.

5 Tailorable pulse source

This chapter outlines a new possible application enabled by the bidirectional-driven 2D PhC MEMS VCSEL.

5.1 Introduction and motivation

Sending the electrically controlled frequency-modulated optical output of the MEMS VCSEL to a semiconductor optical amplifier allows for independent frequency and amplitude modulation. Combining the two components results in an optical arbitrary waveform generator (OAWG). The freedom to independently control the chirp and amplitude of a pulse enables one to perfectly match an optical input pulse to a highly dispersive medium, e.g., a dispersion compensating fibre (DCF), resulting in an unchirped output pulse, resulting in minimal temporal pulse width and maximum peak power. This feature enables high peak power optical pulse generation in a much cheaper configuration than conventional ultrafast pulse generation.

In the above-described setup, creating an OAWG with a bandwidth of 20 THz, 20000 times faster than an electrical AWG, while still having the same footprint is possible.

5.2 Coherence

This section investigates the wavelength change in single roundtrip in the MEMS VCSEL cavity. Thereafter the Doppler shift of a uniformly moving mirror is shown. Finally, the two results are compared.

The total optical cavity length of a MEMS VCSEL is given by:

$$L_{\text{tot}} = L_g + L_{\text{AR}} + L_0 + \Delta L(t) \tag{5.1}$$

where L_g is the optical length of the gain medium, $L_{\text{AR}} = \lambda_0/4$, is the optical length of the perfect antireflection (AR) coating, L_0 is the initial air gap size, and $\Delta L(t)$ is the time-dependent gap change. The penetration depth of the two mirrors can be included in the gain length and the initial gap size.

The instantaneous wavelength is given by:

$$\lambda_m = \frac{2L_{\text{tot}}}{m} \tag{5.2}$$

where m is the longitudinal mode number.

The MEMS mirror is moving at a speed of v, i.e.:

$$\Delta L = vt \tag{5.3}$$

where t is time.

The roundtrip time inside the cavity is:

$$t_r = \frac{2L_{\text{tot}}}{c} \tag{5.4}$$

where c is the speed of light.

Since the only thing that changes with respect to time is the last term in Eq. (5.1), inserting Eq. (5.1) into Eq. (5.2) results in the wavelength change given by:

$$\Delta\lambda = \frac{2\Delta L(t)}{m} \tag{5.5}$$

Inserting Eq. (5.3) leads to

$$\Delta\lambda = \frac{2vt}{m} \tag{5.6}$$

Letting the time be equal to the roundtrip time $t = t_r$ results in:

$$\Delta\lambda = \frac{2vt_r}{m} = \frac{2v\frac{2L_{\text{tot}}}{c}}{m} = \frac{4vL_{\text{tot}}}{mc} \tag{5.7}$$

Which is the wavelength change in a single round trip.
The wavelength change in a round trip relative to the instantaneous wavelength results in:

$$\frac{\Delta\lambda}{\lambda_0} = \frac{\Delta\lambda}{\lambda_m} = \frac{4vL_{\text{tot}}}{mc} \Big/ \frac{2L_{\text{tot}}}{m} = 2\frac{v}{c} \tag{5.8}$$

The frequency of a plane wave reflected of a moving mirror is given by[89]:

$$f = f_0 \frac{1 - 2\frac{v}{c}\cos(\alpha) + \frac{v^2}{c^2}}{1 - \frac{v^2}{c^2}} \tag{5.9}$$

where f_0 is the frequency of the incident wave, α is the incidence angle, v is the velocity of the mirror, and c is the speed of light.
Assuming normal incidence ($\alpha = 0$) Eq. (5.9) simplifies to:

$$f = f_0 \frac{1 - 2\frac{v}{c} + \frac{v^2}{c^2}}{1 - \frac{v^2}{c^2}} \tag{5.10}$$

The mirror speed is not close to relativistic speeds, i.e., $v << c$, canceling out the squared terms resulting in:

$$f = f_0 \frac{1 - 2\frac{v}{c}}{1} = f_0\left(1 - 2\frac{v}{c}\right) = f_0 - 2f_0\frac{v}{c} \tag{5.11}$$

Rearranging leads to:

$$f - f_0 = -2f_0\frac{v}{c} \tag{5.12}$$

Resulting in:

$$\Delta f = -2f_0\frac{v}{c} \tag{5.13}$$

A final rearrangement results in:

$$\frac{\Delta f}{f_0} = -\frac{\Delta\lambda}{\lambda_0} = -2\frac{v}{c} \tag{5.14}$$

Comparing Eq. (5.8) and Eq. (5.14), a resemblance is clearly seen.

To generate an initial signal, it is crucial that there exists a well-defined phase relation between the electric field at different times, which is known as temporal coherence. The result of the two derivations above is that the wavelength change pr. roundtrip is equal to the Doppler shift pr. roundtrip. This results in the lasing line being coherently shifted across the full spectrum for the ideal laser. In contrast, classical grating-based tunable lasers build up lasing from spontaneous emission, and the different wavelengths do not have mutual coherence when the tuning speed is fast. Hence, the MEMS tunable VCSEL is fundamentally distinct from other widely tunable lasers, and this is the foundation for the pulse-generating capabilities of the MEMS VCSEL combined with a SOA.
The concept of compressing the output of a fast, widely tunable laser has been investigated[46]. However, their implementation used a Fourier-domain mode-locked laser (FDML), which is a fiber-ring laser matched to a scanning filter. Although the laser emission does not have to build up from spontaneous emission in each sweep, the starting seed is still random spontaneous emission, resulting in a lack of coherence across the spectrum and pulse durations of 60-70 ps.

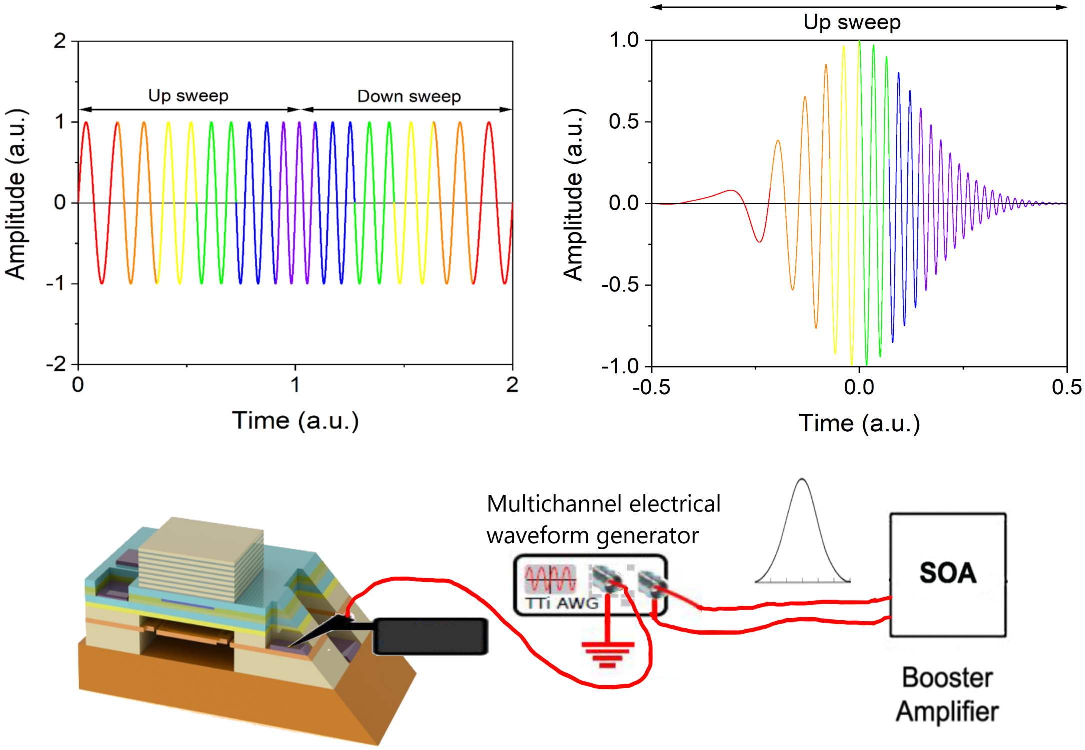

Figure 5.1: CW output of the MEMS VCSEL (left) and output of the SOA (right) showing a chirped Gaussian pulse.

5.3 Experimental setup

The experimental setup could be as the one shown in Fig. 3.7, but instead of the output going to the OSA, it should instead be fiber coupled to an SOA. An illustration of the output of the MEMS VCSEL, as well as the SOA, can be seen in Fig. 5.1. The MEMS VCSEL is run continuous wave (CW) while the MEMS oscillates. In the figure on the left in Fig. 5.1, we see a full oscillation, i.e., an up and a down sweep. In the upsweep, the cavity length decreases, resulting in going from (red) long to short wavelengths (blue), while the opposite is true for a down sweep. As indicated, the MEMS and the SOA are coupled to a multichannel electrical waveform generator allowing the signals to be synced. The figure on the right in Fig. 5.1 shows the output after the SOA, where the SOA has been modulated by a Gaussian pulse, which results in a chirped Gaussian pulse in the optical domain. The chirp, i.e., the change in carrier frequency within the Gaussian envelope, is controlled by the AWG, as it controls the MEMS movement. In addition, the envelope is also controlled by the AWG via the SOA.
The output of the SOA is then sent to a DCF in order to align all the wavelengths of the original signal in time, i.e., unchirping the pulse.
The output of the DCF can then be measured by a photodetector and a fast oscilloscope for pulses in the picosecond range. However, for pulses in the femtosecond range, an autocorrelation is needed, ideally in the form of frequency-resolved optical gating (FROG).

5.4 Numerical calculations

In order to match an input pulse to the DCF, calculations are performed backward. Starting from a desired output pulse in the time domain (Fig. 5.2 (a)), which has a corresponding spectrum (Fig. 5.2 (b)). As indicated, the pulse has no chirp; the wavelength does not change as a function of time. The temporal full-width half-max (FWHM) is set to 100 fs, and the corresponding spectrum has an FWHM of 39 nm. The dispersion of the DCF can be seen in Fig. 5.2 (c). The resulting spectrum after 12 km fiber propagation can be seen in Fig. 5.2 (d), as indicated the pulse now has considerable dispersion. The temporal pulse resulting from the inverse Fourier transform can be seen in Fig. 5.2 (e). This is the targeted input pulse for the goal output.

The same procedure can be performed for a target pulse of 200 fs; the backward calculation can be seen in Fig. 5.3. Comparing Fig. 5.2 and Fig. 5.3, the dispersion slope of the target pulse is the same, the only difference being the duration of the pulse. The reason for this is that the dispersion of the fiber is imprinted on the pulse because it starts with no dispersion before entering the fiber.

To translate the bandwidth in Fig 5.2 (e) to MEMS VCSEL movement, a fit is made, which is then divided by the assumed tuning efficiency of 0.19; the resulting MEMS movement is shown in Fig. 5.4. As indicated by Fig. 5.4 the MEMS movement is quite linear but not perfectly so. In order to achieve linear MEMS movement, one has to excite it with an arbitrary waveform, which usually contains an abrupt temporal section containing high-frequency components. However, an alternative route is to use a sinusoidal drive voltage resulting in a high mechanical response. The MEMS moves sinusoidally when excited by a sinusoidal drive signal, moving fastest as it crosses the resting position $z = 0$. When the slope is steepest, the MEMS moves approximately linearly. There are two main factors in determining the velocity of the MEMS, i.e., the displacement amplitude, as well as actuation frequency. Looking at Fig. 5.4, it is clear that quite a lot of displacement is needed, assuming ambient condition (Q=4), the largest displacement span is around 1500 nm ($z_0 = 1000$ nm) in Fig. 3.17 (b). Which is achieved for an outer voltage of $V_0 = 0.49V_{0\text{PI}}$ and drive amplitude of $V_a = 0.31V_{0\text{PI}}$. Assuming this displacement, a sinusoidal fit is made in order to capture the MEMS movement shown in Fig. 5.4, which resulted in a frequency of 692 kHz.

Since the graphs in Fig. 3.17 are normalized, and the actuation frequency is a function of the outer voltage, as shown in Fig. 3.14, the first order correction to the electrostatic spring softening. It follows that in order for the actuation frequency to be equal to the sinusoidal fit ($f = 692$ kHz), one only needs to solve:

$$f_0 = \frac{f_{\text{res}}}{\sqrt{1 - \frac{V_0^2}{V_{0\text{PI}}^2}}} = \frac{f_{\text{res}}}{\sqrt{1 - \frac{(0.49\cancel{V_{0\text{PI}}})^2}{\cancel{V_{0\text{PI}}^2}}}} \tag{5.15}$$

where f_{res}, the adjusted resonance with spring softening, is equal to the desired actuation frequency. This results in a native resonant frequency of 793 kHz. The differential equation for the symmetric electrostatic actuator is solved with MATLAB's ODE solver with the specified native MEMS resonant frequency. The result for the last two resonant periods is depicted in Fig. 5.5. As indicated by Fig. 5.5 the two MEMS movements agree quite well. For the native resonant frequency used, the outer voltage pull-in equals $V_{0\text{PI}} = 36$ V, meaning that the outer voltage is $V_0 = 18$ V and the sinusoidal drive amplitude equals $V_a = 11.5$ V, which is easily achieved with a transformer. Since the native resonant mechanical frequency can be designed, one can design MEMS that are suited for specified output temporal pulse widths.

Note that lasing does not have to occur across the entire MEMS movement, indeed if that was the case, the FBW would be in the excess of 17% (assuming $\lambda_0 = 1550$ nm), which is much higher than any reported values in literature. Assuming the lasing bandwidth exceeds the bandwidth of the targeted input pulse, i.e., lasing will build up before the highlighted MEMS movement in red in Fig. 5.5.

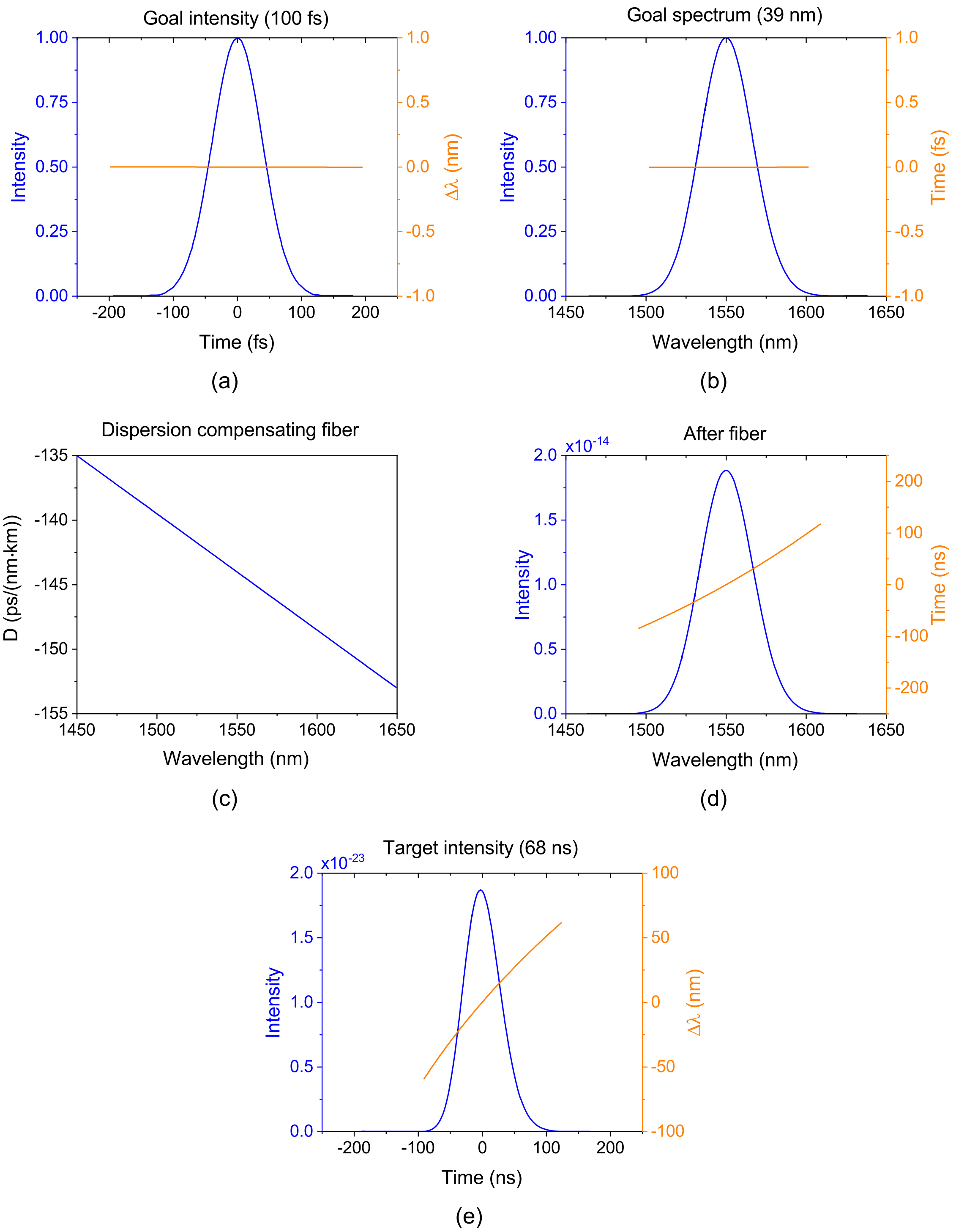

Figure 5.2: (a) Ideal compressed output pulse. (b) The spectrum of the ideal output pulse. (c) Dispersion of dispersion compensating fiber. (d) The spectrum after the output pulse has traveled 12 km in the DCF. (e) Target amplitude and frequency chirp.

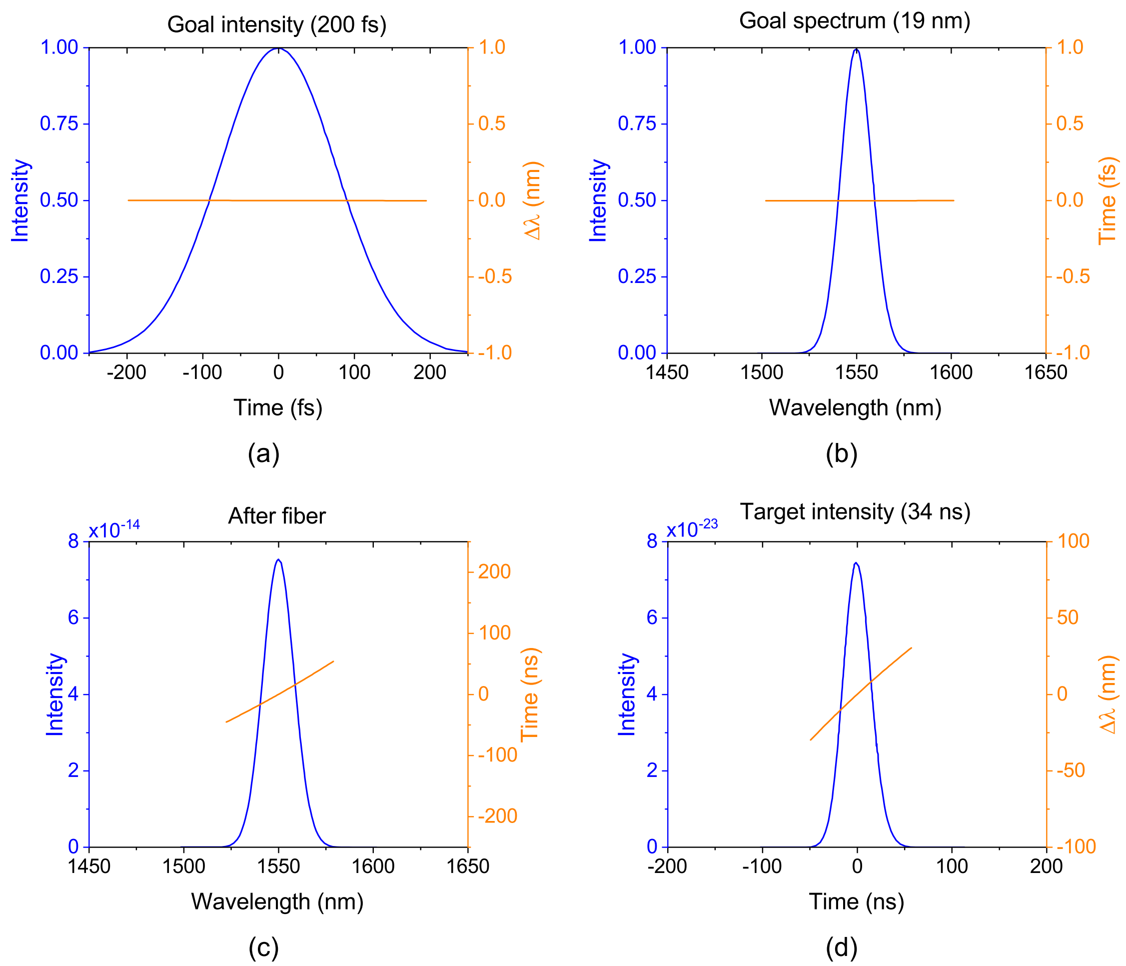

Figure 5.3: (a) Ideal compressed output pulse. (b) The spectrum of the ideal output pulse. (c) The spectrum after the output pulse has traveled 12 km in the DCF. (d) Target amplitude and frequency chirp.

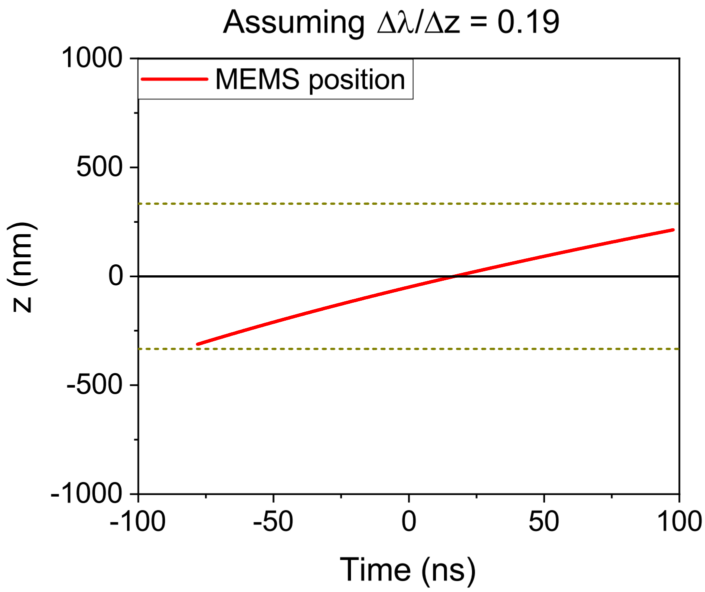

Figure 5.4: MEMS movement matching the bandwidth of the targeted input pulse shown in Fig. 5.2 (e), assuming a tuning efficiency of 0.19. The dashed lines indicate the traditional pull-in at ± 333 nm.

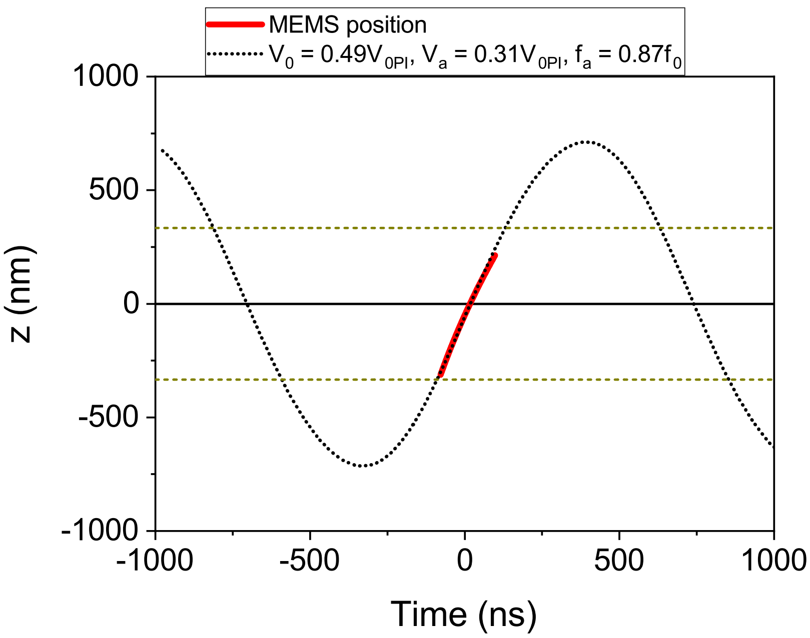

Figure 5.5: MEMS movement (solid red) matching the bandwidth of the targeted input pulse shown in Fig. 5.2 (e), assuming a tuning efficiency of 0.19. Sinusoidal driven MEMS movement (dotted black) for a MEMS with $f_0 = 793$ kHz, $Q = 4$. The dashed lines indicate the traditional pull-in at ± 333 nm.

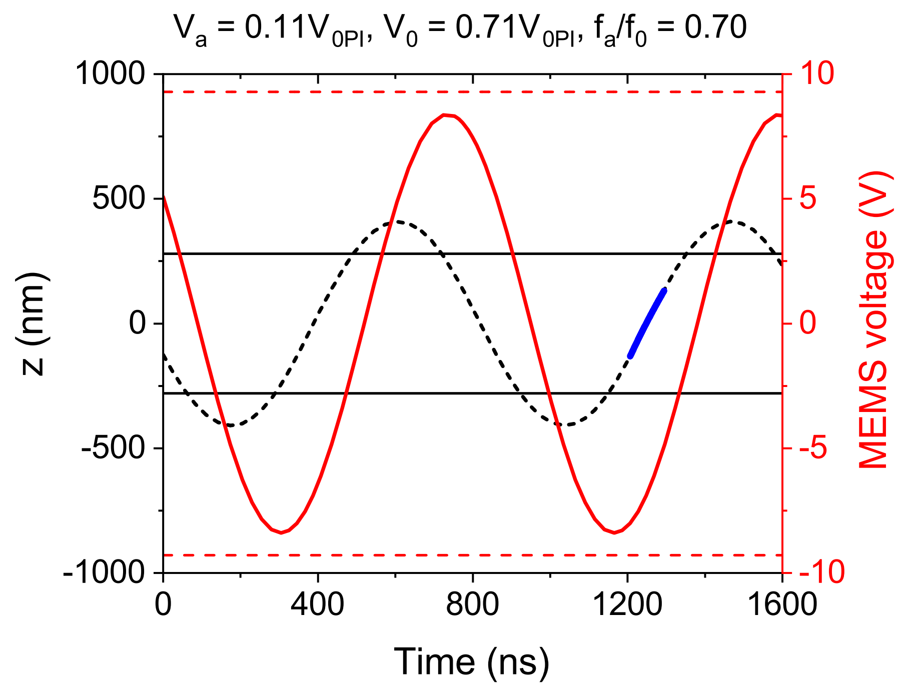

Figure 5.6: Left axis shows MEMS movement (solid blue) matching the bandwidth of the targeted input pulse shown in Fig. 5.3 (e), assuming a tuning efficiency of 0.19. Sinusoidal driven MEMS movement (dashed black) for a MEMS with $f_0 = 1.65$ MHz, $Q = 4$. The black vertical lines indicate the adjusted pull-in at ± 279 nm. The right axis shows voltage waveform (solid red), and vertical lines (dashed red) indicate MEMS pull-in voltage.

More realistic bandwidth levels, where the laser does not go in and out of lasing between up and down sweeps is around 10% FBW (11.45%), which has been realized centered around 1310 nm[31]. Assuming $\lambda_0 = 1550$ nm, a tuning efficiency of 0.19, this corresponds to a peak sinusoidal amplitude of 408 nm, or a displacement span of 816 nm, i.e., a normalized displacement of 0.816, assuming $z_0 = 1000$ nm. Again assuming $Q = 4$, the resulting outer voltage and drive voltage become, $V_0 = 0.71V_{\text{0PI}}$ and $V_a = 0.11V_{\text{0PI}}$ respectively. Following the same procedure as before, with the sinusoidal fit and solving Eq. (5.15), results in the displacement and voltage waveform seen in Fig. 5.6. As shown in Fig. 5.6, the sinusoidal movement again captures the chirp of the input pulse given in Fig. 5.3; however, the displacement amplitude is considerably lower compared to Fig. 5.5. For lasing to occur across the entire MEMS movement, the FBW is 10%, with the same assumptions as before. The outer voltage pull-in for the MEMS in Fig. 5.6 is 75.3 V, which results in $V_0 = 53.5$ V and $V_a = 8.4$ V, and an actuation frequency of $f_a = 1.16$ MHz. Assuming 10% FBW results in coherence between subsequent pulses, as the laser is coherently swept across the bandwidth without laser light being built up from spontaneous emission.

Fig. 5.7 shows the backward calculated, targeted input pulse, for the same goal pulse of 100 fs, for different DCF fiber lengths. The longer the fibre, the larger the chirp. The longer the pulse is dispersed, translates to a lower requirement for the MEMS speed (slope of the MEMS movement), as shown in Fig. 5.7 (b). An increase in the goal output temporal width for a specific fiber length translates to a decrease in the required MEMS movement while the slope remains intact. The drive pulse of the SOA determines the ”duration of the slope”. This means the same MEMS can be utilized to create both pulses of e.g., 100 fs and 200 fs. Using sinusoidal drive, it is advantageous that the MEMS moves fast,

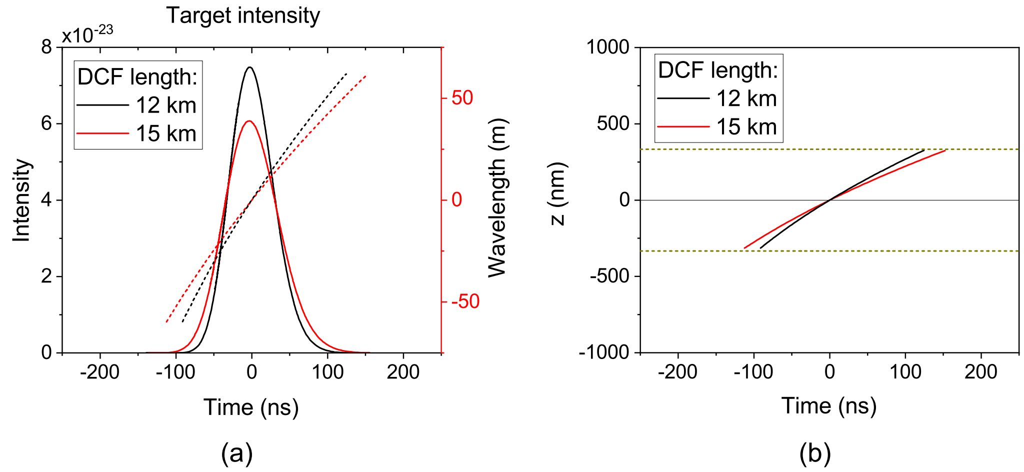

Figure 5.7: (a) Targeted input pulse for the same output pulse with a temporal width of 100 fs, for different fiber lengths. (b) Corresponding required MEMS movement.

resulting in ideally less fiber length, which results in sinusoidal actuation being good for relatively low fiber lengths and relatively high temporal widths of the goal output pulse.
Since the amplitude and frequency modulation is decoupled, one can imagine the SOA outputting a sinc^2, sech, or square waveform instead of a Gaussian, meaning the pulses can be tailored, limited by the large signal bandwidth of the SOA or the SOA driver, whichever is lowest.
Assuming the target input pulse seen in Fig. 5.2 (e), the calculation can be performed forwards; the result can be seen in Fig. 5.8. The bandwidth of the input pulse is slightly increased in the tails of the Gaussian; however, the envelope is identical to Fig. 5.2 (e). The output pulse, shown in Fig. 5.8 (d), has a FWHM of 91 fs, close to the goal intensity shown in Fig. 5.2 (a). The time-bandwidth product (TBP) equals 0.44, indicating a transform-limited Gaussian pulse. As a result of the temporal compression, the peak intensity has increased by more than 7×10^5 (neglecting fiber loss of ≈ 5 dB). This numerically shows the pulse-generating capabilities of the MEMS VCSEL coupled to the SOA, realizing ultrashort pulses with high peak power.
The simulations presented here do not include non-linear effects, however, using a variable optical attenuator (VOA) between the SOA and the DCF the nonlinear effects can be minimized. In order to realize the tailorable pulse source, feedback control, and machine learning are most likely needed. The input pulse chirp can be characterized by a Mach–Zehnder interferometer (MZI) setup, and a photo-detector with an oscilloscope can determine the pulse envelope. The output pulse can be characterized using FROG to give both amplitude and spectrum. Knowing the input and output pulses of the fiber, for several different parameters, one can get a good estimate of the transfer function of the fiber. One can then implement an inverse machine learning method, in order to estimate what the input pulse chirp and envelope need to be, in order to realize a targeted output pulse.
If realized, the presented pulse source will greatly reduce the cost of ultrashort pulse generators due to the mass production capabilities of the semiconductor chip platform, both in terms of the MEMS VCSEL and the SOA. This would take ultrafast science out of the university laboratories into applications previously not thought of since the price alone of the state-of-the-art ultrafast pulse source had made it irrelevant.

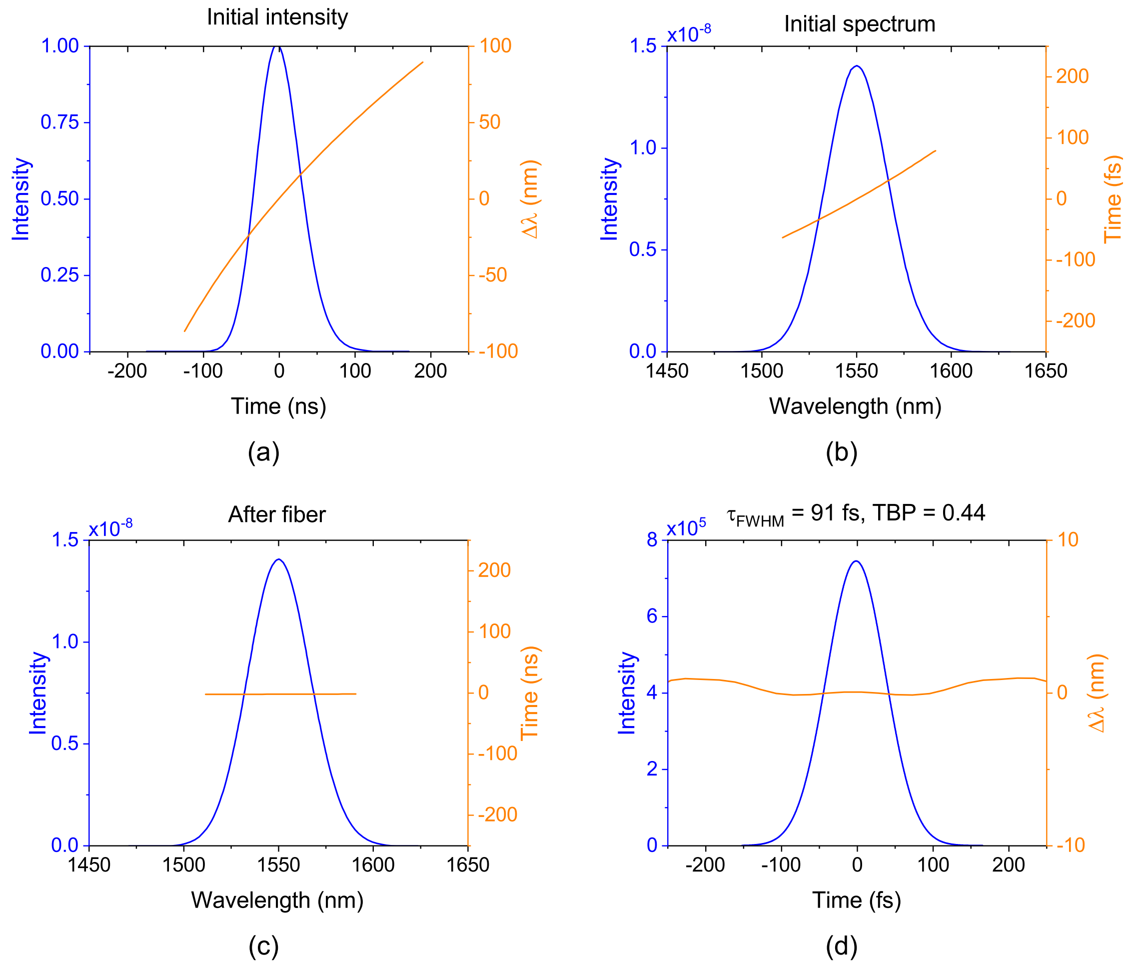

Figure 5.8: (a) Input pulse. (b) The spectrum of the input pulse. (c) The spectrum after the pulse has traveled 12 km in the DCF. (d) Output pulse.

6 Conclusion

Due to the robustness of the PhC MEMS VCSEL higher order modes are pushed up in frequency, decreasing the likelihood of spectral overlap between the unwanted mechanical modes and that of a broadbanded driving signal. As a result, the PhC MEMS VCSEL holds immense potential to reduce the dynamic linewidth in SS-OCT and LiDAR applications, thereby increasing the state-of-the-art imaging depth. Increased imaging depth could increase the application areas for SS-OCT beyond (mostly) ophthalmology, e.g., SS-OCT could be used more broadly in an intraoperative setting (iOCT). Increasing LiDAR range for autonomous vehicles would give the system more time to react in case of an emergency or obstruction ahead.

The bidirectional MEMS VCSEL shows many promising features, including linear wavelength tuning and control of the MEMS environment. In addition, the increased electrostatic spring softening in the bidirectional actuator makes the MEMS more susceptible to applied drive voltage, enabling the actuation of very stiff MEMS possible without needing high slew rate high voltage amplifiers and without needing high vacuum to realize large MEMS displacement, and as a consequence large tuning bandwidths at MHz speeds.
Due to the modular approach, the benefits of an SOI-defined MEMS are not limited to the InP system for wavelengths around 1550 nm but can be applied to the GaAs platform for wavelengths around 980 nm and 1060 nm. This increases the potential applications where a bidirectional MEMS VCSEL can be employed.

Design improvement for the next fabrication iteration includes using an HF vapor etcher for a more reliant release of the MEMS structure, measurement of device layer thickness before HCG or PhC patterning, and ensuring good pattern transfer. To prevent shorts from occurring, an insulating layer should cover the contact depression sidewalls before metalization. To ensure bondable contacts, the annealing temperature should not approach the silicon-gold eutectic temperature during metalization.
To avoid electric discharge when packaging bidirectional MEMS VCSELs, it is important to consider the distance between adjacent contacts since the DC voltages applied are quite substantial. This can be aided by silicon oil due to its high dielectric strength. In addition, the oil reduces the chance of water condensation and decreases thermal resistance.

A new application area for MEMS VCSELs, namely ultrashort pulse generation, is presented.
The increased electrostatic spring softening in the bidirectional configuration results in an analytical expression for the adjusted resonant frequency; this can be utilized in order to design MEMS for targeted velocities matching the dispersion slope of the dispersion compensating element. This enables bidirectional MEMS VCSELs to be used to make AOWGs.

There are still technological challenges that remain to be addressed before AOWG can be materialized. Some of the challenges include achieving high bandwidth ($\approx 10\%\Delta\lambda/\lambda_0$) ideally electrically pumped $\lambda_0 = 1550$ nm EC MEMS VCSELs. This dissertation can provide inspiration and design consideration in order to realize a broadbanded bidirectional MEMS VCSEL.
Experimental investigation of the coherence properties of SCD MEMS VCSEL compared to EC MEMS VCSEL will give insights into the Doppler assisted tuning mechanism. The pulse generation and subsequent compression will reveal difference in coherence in the

two-mirror and three mirror laser.

Comparing bidirectional MEMS VCSEL which are vacuum bonded and ambient pressure bonded in the pulse compression experiment, will give insights into the effect of Brownian motion on the coherence properties of the laser. In addition, experimentally comparing the dynamic linewidths of HCG and PhC excited by a broadband arbitrary waveform will highlight the difference between the more robust PhC mirror compared to the traditional HCG.

List of publications

Published

- Arnhold Simonsen, Søren Engelberth Hansen, Masoud Payandeh, Andrey Marchevsky, Gyeong Cheol Park, Hitesh Kumar Sahoo, Elizaveta Semenova, Ole Hansen, and Kresten Yvind. “Bidirectional electrostatic MEMS tunable VCSELs”. In: *2021 27th International Semiconductor Laser Conference (ISLC)*. 2021, pp. 1–2. DOI: 10.1109/ISLC51662.2021.9615710

Under preperation

- Kresten Yvind, Thor Ansbæk, Arnhold Simonsen, Gyeong Cheol Park, US patent application: DTU Ref. 96441: ”Robust mirror for scanning MOEMS”. priority date: 28.02.2022
- Arnhold Simonsen, Gyeong Cheol Park, Thor Ersted Ansbæk, Ole Hansen, and Kresten Yvind. ”Design of robust photonic crystal mirror for MEMS VCSELs”. Submitted to Optics Express
- Arnhold Simonsen, Masoud Payandeh, Søren Engelbert Hansen, Andrey Marchevsky, Gyeong Cheol Park, Hitesh Kumar Sahoo, Elizaveta Semenova, Ole Hansen, and Kresten Yvind. ”Bidirectional electrostatic MEMS tunable VCSELs”. In internal review process. Plan to submit to Optica.

Bibliography

[1] Albert Einstein. "Strahlungs-Emission und Absorption nach der Quantentheorie". In: *Deutsche Physikalische Gesellschaft* 18 (Jan. 1916), pp. 318–323.

[2] T. Maiman. "Stimulated optical radiation in ruby". eng. In: *Nature* 187.4736 (1960), pp. 493–494. ISSN: 14764687, 00280836. DOI: 10.1038/187493a0.

[3] A. Schawlow and C. Townes. "Infrared and optical masers". eng. In: *Physical Review* 112.6 (1958), pp. 1940–1949. ISSN: 0031899x, 15366065. DOI: 10.1103/PhysRev.112.1940.

[4] J. Geusic, H. Marcos, and L. Vinuitert. "Laser oscillation in Nd-doped yttrium aluminum yttrium gallium + gadolinium garnets". eng. In: *Applied Physics Letters* 4.10 (1964), 182–. ISSN: 10773118, 00036951.

[5] A. Javan, D. Herriott, and W. Bennet. "Population inversion and continous optical maser oscillation in a gas discharge containing a He-Ne mixture". eng. In: *Physical Review Letters* 6.1 (1961), pp. 106–+. ISSN: 10797114, 00319007. DOI: 10.1103/PhysRevLett.6.106.

[6] C. Patel. "Interpretation of CO_2 optical maser experiments". eng. In: *Physical Review Letters* 12.21 (1964), 588–. ISSN: 10797114, 00319007. DOI: 10.1103/PhysRevLett.12.588.

[7] R. Hall et al. "Coherent light emission from GaAs junctions". eng. In: *Physical Review Letters* 9.9 (1962), 366–. ISSN: 00319007, 10797114. DOI: 10.1103/PhysRevLett.9.366.

[8] P. P. Sorokin and J. R. Lankard. "Stimulated Emission Observed from an Organic Dye, Chloro-aluminum Phthalocyanine". In: *IBM Journal of Research and Development* 10.2 (1966), pp. 162–163. DOI: 10.1147/rd.102.0162.

[9] Amnon Yariv. *Quantum electronics*. eng. Wiley, 1975, XVII, 570 S (unknown). ISBN: 0471971766, 9780471971764.

[10] Kenichi Iga. "Forty years of vertical-cavity surface-emitting laser: Invention and innovation". eng. In: *Japanese Journal of Applied Physics* 57.8 (2018), 08PA01. ISSN: 13474065, 00214922. DOI: 10.7567/JJAP.57.08PA01.

[11] Bahaa E A Saleh and Malvin Carl Teich. "Fundamentals of photonics". eng. In: (2007).

[12] Finisar. *VCSEL optical modes*. https://www.finisar.com/sites/default/files/downloads/application_note_vcsel_optical_modes.pdf.

[13] D. Huffaker, J. Shin, and D. Deppe. "Low-threshold half-wave vertical-cavity lasers". eng. In: *Electronics Letters* 30.23 (1994), pp. 1946–1947. ISSN: 1350911x, 00135194. DOI: 10.1049/el:19941348.

[14] K. Lear et al. "Selectively oxidized vertical-cavity surface-emitting lasers with 50-percent power conversion efficiency". eng. In: *Electronics Letters* 31.3 (1995), pp. 208–209. ISSN: 1350911x, 00135194. DOI: 10.1049/el:19950125.

[15] Connie J. Chang-Hasnain. "VCSEL Array for 3D Sensing". eng. In: *Moc 2019 - 24th Microoptics Conference* (2019), pp. 18–19. DOI: 10.23919/MOC46630.2019.8982831.

[16] Kostadinka Bizheva et al. "Sub-micrometer axial resolution OCT for in-vivo imaging of the cellular structure of healthy and keratoconic human corneas". eng. In: *Biomedical Optics Express* 8.2 (2017), 279932. ISSN: 21567085. DOI: 10.1364/BOE.8.000800.

[17] Dilraj S. Grewal and Angelo P. Tanna. "Diagnosis of glaucoma and detection of glaucoma progression using spectral domain optical coherence tomography". eng. In: *Current Opinion in Ophthalmology* 24.2 (2013), pp. 150–161. ISSN: 15317021, 10408738. DOI: 10.1097/ICU.0b013e32835d9e27.

[18] Pearse A. Keane et al. "Evaluation of Age-related Macular Degeneration With Optical Coherence Tomography". eng. In: *Survey of Ophthalmology* 57.5 (2012), pp. 389–414. ISSN: 18793304, 00396257. DOI: 10.1016/j.survophthal.2012.01.006.

[19] Gianni Virgili et al. "Optical coherence tomography (OCT) for detection of macular oedema in patients with diabetic retinopathy". eng. In: *Cochrane Database of Systematic Reviews (online)* 7 (2011), p. CD008081. ISSN: 1469493x, 13616137. DOI: 10.1002/14651858.CD008081.pub2.

[20] Benjamin J. Vakoc et al. "Cancer imaging by optical coherence tomography: Preclinical progress and clinical potential". eng. In: *Nature Reviews Cancer* 12.5 (2012), pp. 363–368. ISSN: 14741768, 1474175x. DOI: 10.1038/nrc3235.

[21] Ireneusz Grulkowski et al. "Retinal, anterior segment and full eye imaging using ultrahigh speed swept source OCT with vertical-cavity surface emitting lasers". In: *Biomed. Opt. Express* 3.11 (Nov. 2012), pp. 2733–2751. DOI: 10.1364/BOE.3.002733. URL: https://opg.optica.org/boe/abstract.cfm?URI=boe-3-11-2733.

[22] Dan P. Popescu et al. "Optical coherence tomography: Fundamental principles, instrumental designs and biomedical applications". eng. In: *Biophysical Reviews* 3.3 (2011), pp. 155–169. ISSN: 18672469, 18672450. DOI: 10.1007/s12551-011-0054-7.

[23] Masanori Nakahama et al. "Giant wavelength-temperature dependence and electrothermal tuning of MEMS VCSEL". eng. In: *Ieee Photonic Society 24th Annual Meeting, Pho 2011* (2011), p. 6110856. DOI: 10.1109/PHO.2011.6110856.

[24] L. S. Watkins et al. "High power VCSEL devices for atomic clock applications". eng. In: *Proceedings of Spie - the International Society for Optical Engineering* 9616 (2015). Ed. by Edward W. Taylor, 96160J. ISSN: 1996756x, 0277786x. DOI: 10.1117/12.2187112.

[25] C. Paranthoen et al. "33 nm wavelength tuning of a 1550 nm VCSEL in CW operation based on the liquid crystal micro-cells technology". eng. In: *Conference Digest - Ieee International Semiconductor Laser Conference* (2021), 2 pp. ISSN: 19476981, 08999406. DOI: 10.1109/ISLC51662.2021.9615666.

[26] Luca Carletti. "High index contrast gratings, Gratings baseret på høj indeks kontrast". und. 2011.

[27] John D Joannopoulos et al. "Photonic crystals: molding the flow of light". eng. In: (2008).

[28] Michael C.Y. Huang, Y. Zhou, and Connie J. Chang-Hasnain. "A surface-emitting laser incorporating a high-index-contrast subwavelength grating". eng. In: *Nature Photonics* 1.2 (2007), pp. 119–122. ISSN: 17494893, 17494885. DOI: 10.1038/nphoton.2006.80.

[29] Hitesh Kumar Sahoo. "Wavelength tunable MEMS VCSELs". eng. 2017.

[30] Hitesh Kumar Sahoo et al. "Tunable MEMS VCSEL on Silicon Substrate". In: *IEEE Journal of Selected Topics in Quantum Electronics* 25.6 (2019), pp. 1–7. DOI: 10.1109/JSTQE.2019.2927575.

[31] V. Jayaraman et al. "High-sweep-rate 1310nm MEMS-VCSEL with 150nm continuous tuning range". eng. In: *Electronics Letters* 48.14 (2012), pp. 867–869. ISSN: 1350911x, 00135194. DOI: 10.1049/el.2012.1552.

[32] Massachusetts Institute of Technology. Department of Electrical Engineering et al. "Wideband Electrically Pumped 1050-nm MEMS-Tunable VCSEL for Ophthalmic Imaging". eng. In: (2015).

[33] Kevin T. Cook, Pengfei Qiao, and Connie J. Chang-Hasnain. "1060 nm HCG MEMS-VCSEL with 73 nm tuning range". eng. In: *Optics Infobase Conference Papers* 2017 (2017). DOI: 10.1364/FIO.2017.FTu4E.1.

[34] Connie J. Chang-Hasnain. "High-contrast grating VCSELs". eng. In: *Springer Series in Optical Sciences* 166 (2013), pp. 291–317. ISSN: 15561534, 03424111. DOI: 10.1007/978-3-642-24986-0_9.

[35] C. Gierl et al. "Surface micromachined tunable 1.55 µm-VCSEL with 102nm continuous single-mode tuning". eng. In: *Optics Express* 19.18 (2011), pp. 17336–17343. ISSN: 10944087. DOI: 10.1364/OE.19.017336.

[36] Pengfei Qiao et al. "Wavelength-Swept VCSELs". In: *IEEE Journal of Selected Topics in Quantum Electronics* 23.6 (2017), pp. 1–16. DOI: 10.1109/JSTQE.2017.2707181.

[37] Jason Zhang et al. "Multi-MHz MEMS-VCSEL swept-source optical coherence tomography for endoscopic structural and angiographic imaging with miniaturized brushless motor probes". In: *Biomed. Opt. Express* 12.4 (Apr. 2021), pp. 2384–2403. DOI: 10.1364/BOE.420394. URL: https://opg.optica.org/boe/abstract.cfm?URI=boe-12-4-2384.

[38] SANTEC. *SANTEC*. https://www.santec.com/en/products/oct/lasers-for-swept-source-oct/.

[39] AXSUN. *AXSUN*. https://downloads.axsun.com/public/datasheets/Axsun_OCT_vcsel_datasheet.pdf.

[40] Arnhold Simonsen. "Advanced mirrors for MEMS VCSELs, Avancerede spejle til MEMS VCSELs". eng. 2019.

[41] Hitesh Kumar Sahoo et al. "Tunable MEMS VCSEL on Silicon substrate [arXiv]". eng. In: *Arxiv* (2019), 7 pp.

[42] Ömer Oralkan et al. "Capacitive micromachined ultrasonic transducers: Next-generation arrays for acoustic imaging?" eng. In: *Ieee Transactions on Ultrasonics, Ferroelectrics, and Frequency Control* 49.11 (2002), pp. 1596–1610. ISSN: 15258955, 08853010. DOI: 10.1109/TUFFC.2002.1049742.

[43] Steven T. Cundiff and Andrew M. Weiner. "Optical arbitrary waveform generation". eng. In: *Nature Photonics* 4.11 (2010), pp. 760–766. ISSN: 17494893, 17494885. DOI: 10.1038/nphoton.2010.196.

[44] Andrew M. Weiner. *Ultrafast Optics*. eng. Wiley Blackwell, 2009, pp. 1–580. ISBN: 0470473452, 0470473460, 0471415391, 1118211472, 1282188321, 9780470473450, 9780470473467, 9780471415398, 9781118211472, 9781282188327. DOI: 10.1002/9780470473467.

[45] Christian Jirauschek and Robert Huber. "Wavelength shifting of intra-cavity photons: Adiabatic wavelength tuning in rapidly wavelength-swept lasers". In: *Biomed. Opt. Express* 6.7 (July 2015), pp. 2448–2465. DOI: 10.1364/BOE.6.002448. URL: https://opg.optica.org/boe/abstract.cfm?URI=boe-6-7-2448.

[46] Christoph M. Eigenwillig et al. "Picosecond pulses from wavelength-swept continuous-wave Fourier domain mode-locked lasers". eng. In: *Nature Communications* 4.1 (2013), p. 1848. ISSN: 20411723. DOI: 10.1038/ncomms2870.

[47] Osman O. Ahsen et al. "Swept source optical coherence microscopy using a 1310 nm VCSEL light source". eng. In: *Optics Express* 21.15 (2013), pp. 18021–18033. ISSN: 10944087. DOI: 10.1364/OE.21.018021.

[48] Kevin Cook et al. "Resonant-antiresonant coupled cavity VCSELs". In: *Optics Express* 27 (Feb. 2019), p. 1798. DOI: 10.1364/OE.27.001798.

[49] OCTLIGHT. *OCTLIGHT*. https://octlight.com/.

[50] Arnhold Simonsen et al. “Bidirectional electrostatic MEMS tunable VCSELs”. In: *2021 27th International Semiconductor Laser Conference (ISLC)*. 2021, pp. 1–2. DOI: 10.1109/ISLC51662.2021.9615710.
[51] Thor Ansbæk et al. “Resonant MEMS tunable VCSEL”. eng. In: *I E E E Journal on Selected Topics in Quantum Electronics* 19.4 (2013), p. 1702306. ISSN: 15584542, 1077260x. DOI: 10.1109/JSTQE.2013.2257164.
[52] Connie J. Chang-Hasnain and Weijian Yang. “High-contrast gratings for integrated optoelectronics”. In: *Adv. Opt. Photon.* 4.3 (Sept. 2012), pp. 379–440. DOI: 10.1364/AOP.4.000379. URL: https://opg.optica.org/aop/abstract.cfm?URI=aop-4-3-379.
[53] MG MOHARAM et al. “Formulation for stable and efficient implementation of the rigorous coupled-wave analysis of binary gratings”. eng. In: *Journal of the Optical Society of America A-optics Image Science and Vision* 12.5 (1995), pp. 1068–1076. ISSN: 23751169, 07403232.
[54] Bart Dhoedt. *Rigorous optical diffraction software, RODIS*. 1995. URL: http://photonics.intec.ugent.be/publications/phd.asp?ID=85.
[55] Connie J. Chang-Hasnain et al. “High-contrast grating VCSELs”. eng. In: *Ieee Journal on Selected Topics in Quantum Electronics* 15.3 (2009), p. 4909070. ISSN: 15584542, 1077260x. DOI: 10.1109/JSTQE.2009.2015195.
[56] Martin A. Afromowitz. “Refractive index of $Ga_{1-x}Al_xAs$”. In: *Solid State Communications* 15.1 (1974), pp. 59–63. ISSN: 0038-1098. DOI: https://doi.org/10.1016/0038-1098(74)90014-3. URL: https://www.sciencedirect.com/science/article/pii/0038109874900143.
[57] Alberto Tibaldi, Pierluigi Debernardi, and Renato Orta. “High-Contrast Gratings Performance Issues in Tunable VCSELs”. eng. In: *Ieee Journal of Quantum Electronics* 51.12 (2015), pp. 1–1. ISSN: 15581713, 00189197. DOI: 10.1109/JQE.2015.2502903.
[58] Kun Li et al. “Widely tunable 1060-nm VCSEL with high-contrast grating mirror”. eng. In: *Optics Express* 25.10 (2017), pp. 11844–11854. ISSN: 10944087. DOI: 10.1364/OE.25.011844.
[59] Hrennikoff. “Solution of problems of elasticity by the framework method”. und. In: *Journal of Applied Mechanics* 8.4 (1941), A169–A175. ISSN: 15289036, 00218936. DOI: 10.1115/1.4009129.
[60] Sweden COMSOL AB Stockholm. *COMSOL Multiphysics® v. 6.1*. 2022. URL: https://www.comsol.com/.
[61] Bart Johnson et al. “Linewidth considerations for MEMS tunable VCSEL LiDAR”. eng. In: *Optics Express* 30.10 (2022), pp. 17230–17242. ISSN: 10944087. DOI: 10.1364/OE.456719.
[62] Benjamin R. Biedermann et al. “Dispersion, coherence and noise of Fourier domain mode locked lasers”. eng. In: *Optics Express* 17.12 (2009), pp. 9947–9961. ISSN: 10944087. DOI: 10.1364/OE.17.009947.
[63] Demis D. John et al. “Wideband Electrically Pumped 1050-nm MEMS-Tunable VCSEL for Ophthalmic Imaging”. eng. In: *Journal of Lightwave Technology* 33.16 (2015), pp. 3461–3468. ISSN: 15582213, 07338724. DOI: 10.1109/JLT.2015.2397860.
[64] Stephen D. Senturia. *Microsystem design*. eng. Kluwer Acad. Publ., 2001, XXVI, 689 S. (unknown). ISBN: 0306476010, 0792372468, 1280200898, 9780306476013, 9780792372462, 9781280200892.
[65] Simon. Ramo, John R. Whinnery, and Theodore. Van Duzer. *Fields and Waves in Communication Electronics*. eng. Wiley, 1965, 754 s.
[66] Keithley. *4200-SCS Semiconductor Characterization System*. https://download.tek.com/document/4200SCS_Brochure.pdf.

[67] TTi. *AIM-TGF4000*. https://resources.aimtti.com/datasheets/AIM-TGF4000_series_data_sheet-Iss1.pdf.

[68] Innolume. *FBG-13XX-PM-350*. https://www.innolume.com/wp-content/uploads/2021/05/FBG-13XX-PM-350_400.pdf.

[69] Haphit. *980/1310/1550/1590nm High Power PM WDM Filter*. https://www.haphit.com/pdf/FPWM_980_1550nm_High_Power_PM_WDM_Filter.pdf.

[70] Thorlabs. *DMSP950T - Ø1/2" Shortpass Dichroic Mirror, 950 nm Cutoff*. https://www.thorlabs.com/thorproduct.cfm?partnumber=DMSP950T.

[71] Anritsu. *Optical spectrum analyzer MS9740B*. https://www.anritsu.com/en-us/test-measurement/products/ms9740b.

[72] Xenics. *XEVA 320 SERIES*. https://www.xenics.com/files/technical_resources/Xeva%20320%20Series/XDS015-Xeva-320-Series.pdf.

[73] minicircuits. *minicircuits*. https://www.minicircuits.com/pdfs/T9-1-X65.pdf.

[74] Hitesh Kumar Sahoo et al. "Wavelength tunable MEMS VCSELs for OCT imaging". eng. In: *Proceedings of Spie* 10552 (2018). Ed. by Kent D., 105520I (6 pp.) ISSN: 1996756x, 0277786x. DOI: 10.1117/12.2289545.

[75] Thor Ansbæk. "Vertical-cavity surface-emitting lasers for medical diagnosis". English. PhD thesis. 2012. ISBN: 87-92062-83-0.

[76] SPTS. *uEtch*. https://www.spts.com/product/uetch-hf-release-etch.

[77] Thorlabs. *BL976-PAG900*. https://www.thorlabs.com/drawings/e6ae26c1e8adc86e-9D8A4325-E086-6890-D2D6B8934096AD09/BL976-PAG900-SpecSheet.pdf.

[78] Kulicked Soffa. *Manual ball bonder*. http://www.pdpequipment.co.uk/pdp_files/k&s%20manual%20wire%20bonders_files/KS4524.pdf.

[79] EPOTEK. *H20E*. https://www.epotek.com/docs/en/Datasheet/H20E.pdf.

[80] CUIdevices. *CP076581-238P*. https://www.cuidevices.com/product/resource/cp07-m.pdf.

[81] muRata. *NXFT15XH103FEAB030*. https://www.murata.com/en-global/products/productdetail?partno=NXFT15XH103FEAB030.

[82] EPO-TEK. *H20E*. https://www.epotek.com/docs/en/Datasheet/H20E.pdf.

[83] Nanolab labadvisor. *Specific Process Knowledge/Characterization/EDX*. https://labadviser.nanolab.dtu.dk/.

[84] Shaurya Prakash and Junghoon Yeom. *Nanofluidics and Microfluidics: Systems and Applications*. eng. Elsevier Inc., 2014, pp. 1–294. ISBN: 1437744699, 1437744702, 9781437744699, 9781437744705. DOI: 10.1016/C2010-0-66159-1.

[85] Vishay. *Wirewound Resistors, Industrial, Precision Power, Silicone Coated, Axial Lead*. https://eu.mouser.com/datasheet/2/427/rsns-1762136.pdf.

[86] Vishay. *Power Metal Film Leaded Resistors*. https://eu.mouser.com/datasheet/2/427/pr010203-1762580.pdf.

[87] J. L. R. Hayden. "The dielectric strength of the vacuum: Electrostatic ionization gradient of metal electrodes". In: *Journal of the American Institute of Electrical Engineers* 41.11 (1922), pp. 852–853. DOI: 10.1109/JoAIEE.1922.6591649.

[88] electrolube. *Silicone Heat Transfer Compound Plus*. https://www.macdermidalpha.com/sites/default/files/2022-07/HTSP-Thermal-Management-EN-11Jan22-TB.pdf.

[89] Aleksandar Gjurchinovski. "The Doppler effect from a uniformly moving mirror". eng. In: *European Journal of Physics* 26.4 (2005), pp. 643–646. ISSN: 01430807, 13616404. DOI: 10.1088/0143-0807/26/4/009.

A Appendix

A.1 Appendix 1

Design of robust photonic crystal mirror for MEMS VCSELs

Arnhold Simonsen[1,*], Gyeong Cheol Park[2], Thor Ersted Ansbæk[3], Ole Hansen[1], and Kresten Yvind[1,3]

[1] *Technical University of Denmark, Anker Engelunds Vej 1, 2800 Kgs. Lyngby, Denmark*
[2] *Electronics and Telecommunications Research Institute, 218 Gajeong-ro, Yuseong-gu, Daejeon South Korea*
[3] *OCTLIGHT, Diplomvej 381, 2800 Kgs. Lyngby, Denmark*
[*] *arnsim@dtu.dk*

Abstract: Wavelength tunable lasers with narrow dynamic linewidths are essential in many applications, such as optical coherence tomography and LiDAR. In this letter, we present a 2D mirror design that provides large optical bandwidth and high reflection while being stiffer than 1D mirrors.
Specifically, we investigate the effect of rounded corners of rectangles as they are transferred from the CAD to the wafer by lithography and etching.

1. Introduction

Thin mirrors, such as 1D photonic crystal (PhC) or high contrast grating (HCG) mirrors with their high reflectance and wide bandwidth, have enabled a new class of microelectromechanical system (MEMS) vertical cavity surface emitting lasers (VCSELs) with faster wavelength sweep than previously possible [1, 2]. The HCG functions as one of the mirrors in a MEMS-VCSEL. The MEMS HCG has several mechanical modes of operation; the fundamental mode (piston mode), where the spring arms are bending out of plane and the mirror remains flat, is most commonly the desired operating mode. Higher order modes include anti-symmetric modes, where the HCG membrane is twisted, and symmetric higher order modes, where the arms and the membrane are bending. Higher order modes are to be avoided in MEMS-VCSELs as thermal vibration limits the imaging range [3].
Due to the much smaller mass and spring constant of the MEMS mirror, one of the current challenges in swept source optical coherence tomography (SS-OCT) is wavelength noise. Applying a waveform with a fundamental frequency below the first mechanical resonance of the MEMS, targeting piston actuation, may contain high frequency components. The high frequency components may overlap with the eigenfrequencies of higher order symmetrical modes of the MEMS, thereby unintentionally exciting them. This forced oscillation can therefore result in unwanted mode mixing between mechanical modes, where more than one mode is excited simultaneously, resulting in intra-sweep spectral oscillations of the MEMS VCSEL. For 1D HCG MEMS, the mixing of symmetrical mechanical modes can increase the wavelength noise during a sweep.
Here we represent a possible solution to reduce the wavelength noise. Instead of using a 1D HCG, we propose a more mechanically robust 2D PhC, which increases the resonance frequency of higher order mechanical modes.
In contrast to 1D HCG, which consists of elongated bars with one direction of periodicity, 2D PhC consists of a mesh-like pattern consisting of bars in two orthogonal directions. The cross-striped pattern makes the grating more robust and prevents the bars from sticking to each other during fabrication [4].
Fig. 1 (a) shows a scanning electron micrograph (SEM) of a fabricated 2D PhC. The mirror is

membranized and anchored to four spring arms, allowing out-of-plane actuation. Below the PhC mirror, there is an air-gap and the active laser material [5]. Fig. 1 (b) shows a SEM image, top

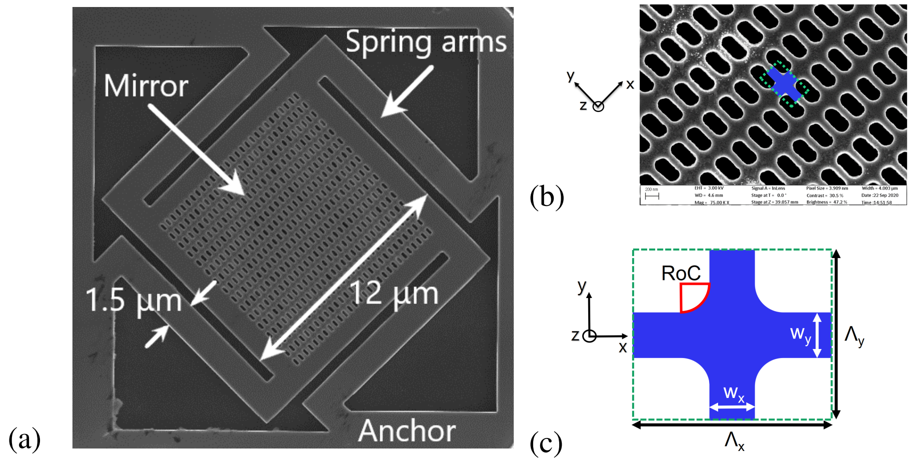

Fig. 1. 2D PhC MEMS mirror. (a) Top view SEM image of the GaAs MEMS VCSEL showing the PhC mirror, with a thickness of 280 nm, supported by four springs above an air-gap and the active laser material. (b) Zoom in SEM image of the 2D grating of the MEMS mirror. The unit cell is highlighted in blue. (c) In-plane model of the unit cell showing all in-plane parameters.

view, of the mesh-like pattern of the 2D PhC mirror. A unit cell is highlighted with green dotted lines. Fig. 1 (c) shows a 2D model of the unit cell, which can be thought of as an intersection of a bar with period Λ_x and a crossbar with period Λ_y, in the x and y direction respectively. The bar width is w_x, and the crossbar width is w_y. The thickness of the membrane is t_g. Regardless of the chosen type of lithography and etching, when transferring the computer aided graphics (CAD) design, with rectangular air holes, into the grating mirror, the corners of the crosses will become rounded, with a radius of curvature (RoC), the rounded corners are therefore included in the model. A 90 degree rotational symmetric unit cell leads to a polarization independent mirror [4, 6]. However, a 180 degree symmetric unit cell resulting in high reflectivity for a specific polarization (e.g. TM) and low reflectivity in the orthogonal direction results in stable polarized laser output. When a polarization sensitive semiconductor optical amplifier (SOA) is used after the MEMS-VCSEL to amplify the output power, the polarized output of the VCSEL can be aligned to the SOA polarization.

The fabrication tolerance of a 2D polarization independent PhC has been investigated [4]. However, the increased mechanical stability and the tolerance to the rounded corners have, to the best of the authors' knowledge, not been investigated before. The rounding of the corners has a substantial influence on the optical properties of the PhC and must be taken into account during the design phase; see section 3.

2. Approach

The finite element method (FEM) (COMSOL) was used to model the mechanical properties of the MEMS structure, with the structural mechanics module using solid mechanics physics. A fixed constraint boundary condition was used at the anchoring positions of the spring arms; see Fig. 2. An eigenfrequency solver was used to determine the resonant frequencies of the system. Rigorous coupled wave analysis (RCWA) [7] (in-house developed) was used to extract the reflectivity contours of the periodic 2D PhC. Two polarization dependent designs are simulated with high reflectivity for the electric field polarized along the x direction. The in-plane design parameters were optimized for a fixed thickness but different radii of curvature; see Table 1.

Table 1. Design parameters for design A and B.

Design	t_g (nm)	Λ_x/Λ_y (nm)/(nm)	w_x/w_y (nm)/(nm)	RoC (nm)	Materials
A	280	334/618	180/259	0	GaAs/air
B	280	311/634	168/241	54	GaAs/air

As is evident by Table 1, design A has an ideal zero RoC, while design B has a more realistic manufacturable RoC of 54 nm. Both designs were modelled as GaAs (with dispersion [8]) suspended in air.
The in-plane parameters were optimized for a large reflectivity bandwidth (with $R > 99.4\%$ as required for VCSEL lasing). Starting from a larger RoC results in a smaller high index footprint and in-plane parameters (w_x, w_y, Λ_x), as indicated by parameters for design A and B, see Table 1. Excluding the rounded corners, the high index footprint is 0.151 μm^2 and 0.141 μm^2 for designs A and B, respectively. Including the rounded corners increases the high index footprint of design B to 0.143 μm^2.
The relative permittivity of the 2D periodic structure can be expressed in a Fourier series given by:

$$\epsilon_r(x, y) = \sum_{m=-\infty}^{\infty} \sum_{n=-\infty}^{\infty} a_{m,n} \mathrm{e}^{\mathrm{j}2\pi\left(\mathrm{mx}/\Lambda_\mathrm{x}+\mathrm{ny}/\Lambda_\mathrm{y}\right)} \tag{1}$$

where $j^2 = -1$ is the imaginary unit, and $a_{m,n}$ is the m, n^{th} Fourier component of the relative permittivity given by:

$$a_{m,n} = \frac{1}{\Lambda_x \Lambda_y} \int_{-\Lambda_y/2}^{\Lambda_y/2} \int_{-\Lambda_x/2}^{\Lambda_x/2} \epsilon_r(x, y) \mathrm{e}^{-\mathrm{j}2\pi\left(\mathrm{mx}/\Lambda_\mathrm{x}+\mathrm{ny}/\Lambda_\mathrm{y}\right)} \mathrm{dxdy} \tag{2}$$

Similar equations are given for the relative permeability, which in the present case equals 1.
To resolve the rounded corners using RCWA, it is essential to calculate the Fourier expansion coefficients with high precision. This is done by discretizing the real-space grid in the x-y plane, see Fig. 1 (c), to a very high degree, e.g., 1024 × 1024 grid points, as done in this paper. Subsequently, the Fourier harmonic components of the permittivity and permeability are calculated using a discrete Fourier transform function (MATLAB's fftn), and the result is then rearranged using MATLAB's fftshift. In addition to using a fine discretized space, it is imperative to use a large number of harmonic components to ensure converged reflection values. Finally, the Fourier harmonic components are arranged in convolution matrices for relative permittivity and relative permeability.

3. Results

Fig. 2 shows the first symmetrical higher order mechanical mode for a 1D and 2D mirror with the outline shown in Fig. 1. The increased mechanical stiffness of the 2D grating increases the first symmetrical higher order mode resonance frequency as well as decreases the bending of the membrane in addition to making the bending more uniform.
The mode spacing is considerably denser for a 1D HCG compared to a 2D PhC, as is evident in Fig. 3. The resonance frequency of the fifth eigenmode is 3.4 MHz and 5.6 MHz for a 1D and 2D PhC, respectively. Due to the uniformity of a 2D PhC MEMS, there are more symmetric modes.

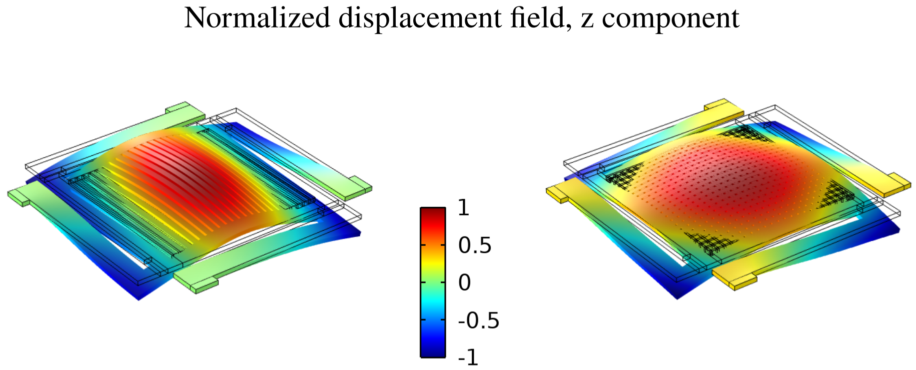

(a) f_{res} = 3.4 MHz

(b) f_{res} = 5.6 MHz

Fig. 2. Spatial (x,y,z) mode shape of the fifth mechanical (second symmetric) mode of a 1D (a) and 2D (b) PhC MEMS. The color legend shows the normalized z component of the displacement field. The 2D PhC mirror has a higher membrane stiffness (f_{res} = 5.6 MHz) due to its mesh, while the long beams of the 1D has a lower membrane stiffness (f_{res} = 3.4 MHz).

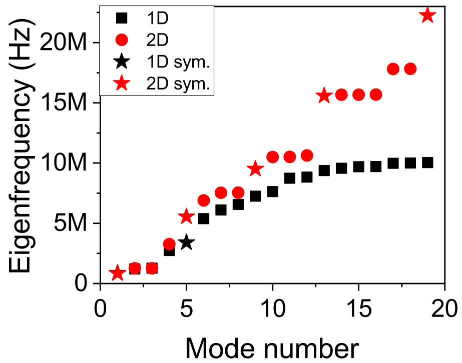

Fig. 3. Resonance frequency as a function of mode number for 1D and 2D PhC MEMS. The stars highlight symmetrical modes.

However, the eigenfrequency of the first plate bending mode (mode 5) is significantly increased. Fig. 4 shows the reflectivity matrix for different RoC as a function of wavelength.

The rectangle in Fig. 4 highlights the 10% fractional bandwidth (FBW) ($\Delta\lambda/\lambda_c$) around the center wavelength λ_c (vertical line), where the reflectivity is larger than 99.4%. The 10% FBW criterion for design A, Fig. 4 (a), is met with a RoC between 0 and 19 nm, while for design B, Fig. 4 (b), the criterion is met between 49 and 76 nm. The added high index footprint due to the rounded corners (compared to a design with perfectly rectangular air holes) has a profound impact on the reflectivity spectrum. Generally, by increasing the RoC, the high reflectivity bandwidth initially increases on the long wavelength side, and by further increase the dip in the center drops below the high reflectivity criterion (R=99.4%). However, if the high index footprint, resulting from in-plane parameters ($w_x, w_y, \Lambda_x, \Lambda_y$), excluding RoC, is small (design B), it will need the added footprint provided by the RoC to meet the broadbanded reflectivity criterion. This indicates the existence of a high index footprint window ensuring broadbanded reflection. Since the rounded corners add an additional high index footprint, they must be included in the design

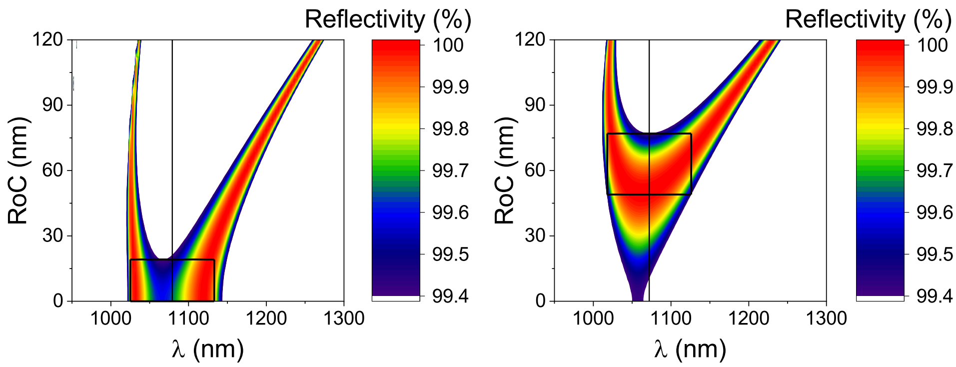

(a) (b)

Fig. 4. Reflectivity contour for different RoC as a function of wavelength, for a near to ideal zero radius of curvature, design A (a) and, a more realistic manufacturable radius of curvature, design B (b). The rectangle highlights the 10% FBW ($\Delta\lambda/\lambda_c$) around the center wavelength λ_c (vertical line), where the reflectivity is higher than 99.4%.

in order to fabricate working 2D PhC mirrors for VCSELs.

Fig. 5 shows the optical spectra, at different applied MEMS voltage, of a PhC MEMS VCSEL [9] with the 2D PhC as seen in Fig. 1. The total wavelength tuning bandwidth is limited since the pattern transfer was outside the ideal case of Fig. 4 (a) with a radius of curvature around 19 nm instead of 0 nm. Hence at 30 V, the Fabry-Perot cavity length is outside the lasing region, and the peak is close to the amplified spontaneous emission. Optimizing for the 54 nm RoC the 99.5% reflection bandwidth of 116 nm as shown in Fig. 4 (b) is expected to be achievable. The static linewidths can be seen in Fig. 5, which remain constant for different DC biases. However, if the first higher order symmetric mode is excited, this would potentially increase the dynamic linewidth since this wavelength noise would occur intrasweep, i.e., faster than the wavelength sweep rate. Expressed differently, the excitation of the symmetric higher order mode would result in an uncontrolled wavelength sweep, where the wavelength does not monotonically decrease (increase) for a down (up) MEMS sweep but rather oscillates around a decreasing (increasing) wavelength value.

4. Discussion

MEMS is susceptible to various types of tuning jitter, i.e., the MEMS mirror does not move smoothly due to mechanisms such as (but not limited to): thermal motion, Brownian motion, electromechanical transients, and mechanical mode-mixing. If the MEMS and the laser diode share an electrode, current fluctuations in the laser driving signal can cause tuning jitter for the MEMS as well. Whether the tuning jitter mechanism is of critical importance depends on the amplitude and time scale of the jitter relative to the sweep-rate of the MEMS tunable VCSEL. Generally, intra-sweep jitter is more detrimental for OCT compared to inter-sweep jitter [10]. As a consequence of the finite temperature of the MEMS, as formulated in the equipartition theorem, the mechanical modes of the MEMS will have thermal linewidth associated with them [11]:

$$\Delta\nu_{RMS} = \frac{2\text{FSR}}{\lambda}\sqrt{\frac{k_B T}{K}} \tag{3}$$

FSR is the free spectral range of the optical cavity (30 THz), λ is the wavelength (1060 nm), k_B is the Boltzmann constant, T is the temperature, and K is the spring constant of the mechanical mode. At room temperature, the thermal linewidth of the fundamental mechanical mode ($K =$

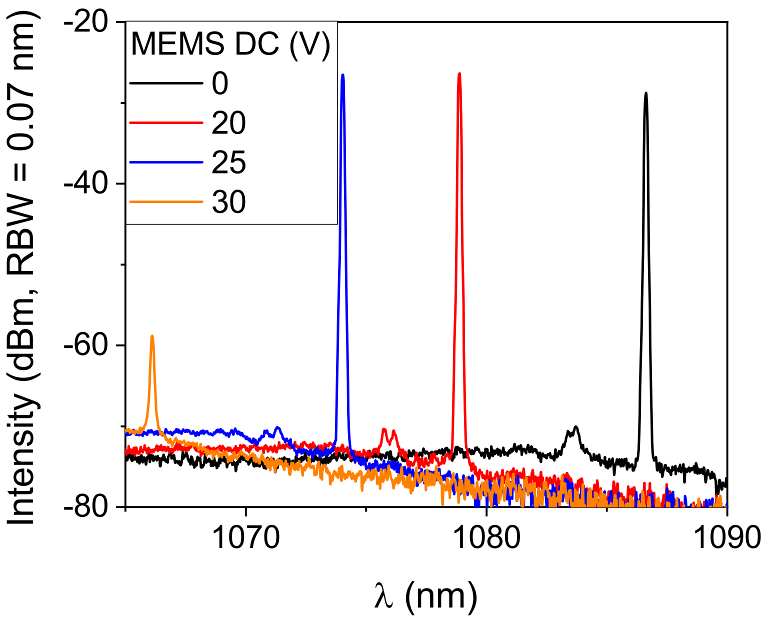

Fig. 5. Four PhC MEMS VCSEL spectra with the DC voltage of 0, 20, 25, and 30 V.

8.45 N/m) is 1.24 GHz. The linewidth can be decreased by increasing the stiffness (K) of the MEMS, e.g., by making the spring arms shorter. However, the maximum stiffness of the piston mode is limited by the first plate bending mode, which is stiffer for a 2D PhC.

When the MEMS is operated at atmospheric pressure, the Brownian motion is mostly caused by the impinging air molecules on the membrane. The amplitude of the Brownian motion may be enhanced at the (symmetric and anti-symmetric) mechanical resonance of the MEMS. By packaging the MEMS VCSEL in vacuum, one can dramatically reduce the Brownian noise and, in addition, increase the quality factor of the resonant mechanical modes. This will reduce the required alternating actuation voltage, as well as narrowing the noise spectrally. However, because of the increased quality factor of the resonances, transients may become an issue.

An anti-symmetric mode will not change the cavity length, so it will not contribute to the wavelength noise of the MEMS VCSEL - They can, however, contribute to intensity noise. The intra-sweep intensity noise, also referred to as sliding relative intensity noise (RIN), will negatively affect the dynamic range of the OCT system - this will add background noise to the images, generated by fringe signal modulation [10].

Charge carrier dynamics are in the nanosecond regime, while MEMS capacitive dynamics are in the milli- to microsecond regime. Consequently, when a bias is applied between a parallel plate capacitor, it can be assumed that the charge carriers are spread out uniformly across the plates. For this reason, one can assume that only symmetrical modes can be excited by electrostatics. A forced oscillation, using a high bandwidth arbitrary waveform, can excite multiple symmetric resonances simultaneously. Higher order symmetrical modes include bending of the membrane, contrary to the first resonance, where the membrane remains flat. These higher order modes, if excited, occur intra-sweep, which induces wavelength noise during a sweep. Due to the innate robustness of a 2D PhC, the higher order mechanical modes get pushed up in frequency. Therefore, one can reduce the spectral overlap between the forced oscillation and that of the higher mechanical modes. Thus one can avoid having intra-sweep wavelength noise caused by mechanical mode mixing.

5. Conclusion

We have outlined the improvement and design considerations of using a robust 2D PhC for MEMS VCSELs. The 2D PhC unit cell can be optimized for any fabrication process, given the rounded corners are consistent in size. After establishing the RoC resulting from a fabrication test run, one can optimize the in-plane parameters in order to achieve a large bandwidth with very high reflection.
The added mechanical stability of a 2D PhC MEMS has the potential to minimize intra-sweep wavelength noise, which is important to enhance the dynamic range in applications such as SS-OCT and LiDAR.

Funding. The authors would like to acknowledge the support of the Independent Research Fund Denmark (DFF STEPS 8022-00110A) and Horizon 2020 (H2020-EU.1.3.1 NETLAS 860807 Marie Skłodowska-Curie Actions, ITN network).

Disclosures. The authors declare no conflicts of interest.

Data availability. Data underlying the results are not publicly available but may be obtained by request from the corresponding author.

References

1. M. C. Huang, Y. Zhou, and C. J. Chang-Hasnain, "A surface-emitting laser incorporating a high-index-contrast subwavelength grating," Nat. Photonics **1**, 119–122 (2007).
2. A. Simonsen, S. E. Hansen, M. Payandeh, A. Marchevsky, G. C. Park, H. Kumar Sahoo, E. Semenova, O. Hansen, and K. Yvind, "Bidirectional electrostatic MEMS tunable VCSELs," in *2021 27th International Semiconductor Laser Conference (ISLC),* (2021), pp. 1–2.
3. B. Johnson, J. Jabbour, M. Malonson, E. Mallon, S. Woo, T. Ford, N. Kemp, and P. Whitney, "Linewidth considerations for MEMS tunable VCSEL LiDAR," Opt. Express **30**, 17230–17242 (2022).
4. K. Ikeda, K. Takeuchi, K. Takayose, I.-S. Chung, J. Mørk, and H. Kawaguchi, "Polarization-independent high-index contrast grating and its fabrication tolerances," Appl. Opt. **52**, 1049–1053 (2013).
5. T. Ansbæk, I.-S. Chung, E. S. Semenova, O. Hansen, and K. Yvind, "Resonant MEMS Tunable VCSEL," IEEE J. Sel. Top. Quantum Electron. **19**, 1702306–1702306 (2013).
6. K. Ikeda, K. Takayose, T. Katayama, and H. Kawaguchi, "Design and Fabrication of a Polarization-Independent HCG," 2013 Conf. on Lasers Electro-optics Pac. Rim (cleo-pr) p. 2 pp. (2013).
7. M. G. Moharam and T. K. Gaylord, "Rigorous coupled-wave analysis of planar-grating diffraction," J. Opt. Soc. Am. **71**, 811–818 (1981).
8. M. A. Afromowitz, "Refractive index of $Ga_{1-x}Al_xAs$," Solid State Commun. **15**, 59–63 (1974).
9. T. Ansbæk, I.-S. Chung, E. Semenova, and K. Yvind, "1060-nm tunable monolithic high index contrast subwavelength grating vcsel," I E E E Photonics Technol. Lett. **25**, 365–367 (2013).
10. B. R. Biedermann, W. Wieser, C. M. Eigenwillig, T. Klein, and R. Huber, "Dispersion, coherence and noise of Fourier domain mode locked lasers," Opt. Express **17**, 9947–9961 (2009).
11. D. D. John, C. B. Burgner, B. Potsaid, M. E. Robertson, B. K. Lee, W. J. Choi, A. E. Cable, J. G. Fujimoto, and V. Jayaraman, "Wideband Electrically Pumped 1050-nm MEMS-Tunable VCSEL for Ophthalmic Imaging," J. Light. Technol. **33**, 3461–3468 (2015).

A.2 Appendix 2

Bidirectional electrostatic MEMS tunable VCSELs

Arnhold Simonsen[1,*], Masoud Payandeh[1], Søren Engelbert Hansen[1], Andrey Marchevsky[1], Gyeong Cheol Park[2], Hitesh Kumar Sahoo[1], Elizaveta Semenova[1], Ole Hansen[1], and Kresten Yvind[1]

[1] *Technical University of Denmark, Anker Engelunds Vej 1, 2800 Kgs. Lyngby, Denmark*
[2] *Electronics and Telecommunications Research Institute, 218 Gajeong-ro, Yuseong-gu, Daejeon South Korea*
[*] *Corresponding author: arnsim@dtu.dk*

Compiled April 4, 2023

Abstract.

http://dx.doi.org/10.1364/ao.XX.XXXXXX

Due to their lightweight, high contrast grating (HCG) microelectromechanical (MEMS), vertical cavity surface emitting lasers (VCSELs) have enabled ultra-fast swept-source optical coherence tomography (SS-OCT)[1][2].

The MEMS consists of a mirror supported by spring arms above an air gap and active laser material[3]. Due to the parallel plate capacitor configuration, the movement of the MEMS is nonlinear in relation to the applied voltage, which necessitates an optical k-clock in order to linearize the wavelength sweep.

The broader the tunability of the swept source, the greater the axial resolution of the OCT image; in addition, faster image acquisition minimizes motion blur. In order to get a fast and broadbanded MEMS VCSEL, one has to actuate the MEMS close to the fundamental resonance frequency, given by:

$$\omega_0 = \sqrt{\frac{k}{m}} \tag{1}$$

where ω_0 is the angular fundamental resonant frequency, k and m are the spring constant and mass of the MEMS, respectively.

The Doppler-assisted tuning is only limited by the tuning speed of the movable MEMS mirror[4], i.e., in order to increase the sweep rate, one can design a stiff MEMS (large k) resulting in a high resonant frequency (ω_0), given by Eq. (1).

However, the stiffer the MEMS, the higher the instability voltage becomes:

$$V_{\mathrm{PI}} = \sqrt{\frac{8kg_0^3}{27\epsilon A}} \tag{2}$$

where, g_0 is the initial air gap, ϵ is the permittivity of the air gap, and A is the area of the MEMS electrodes. In order to actuate the MEMS to the maximum excursion ($g_0/3$), the alternating voltage has to be close to the pull-in voltage given by Eq. (2).

If one designs a MEMS with a fundamental resonance frequency in the MHz regime, the pull-in voltage easily reaches hundreds of volts. This poses an actuation problem since the maximum available actuation voltage from an arbitrary waveform generator (AWG) is 10 V peak to peak. There exist high voltage amplifiers. However, they are limited in the bandwidth of the driving signal, as well as having a limiting slew rate - Slew rate limitation can result in distortion of the post-amplified waveform, resulting in unpredictable MEMS movement.

As is evident from Eq. (2), given a desired stiffness k, there are two ways to lower the pull-in voltage, decreasing the air gap size or increasing the area. Decreasing the air gap size leads to a decrease in the maximum displacement, which may reduce the tuning bandwidth well below the gain-bandwidth of the multi-quantum well VCSEL, leading to a less-than-optimal tuning range. Increasing the area of the MEMS increases the mass, which in turn decreases the resonance frequency, as is evident by Eq. (1). In addition, increasing the MEMS area will lower the resonance frequency of higher-order symmetrical or plate-bending modes. If these modes are excited, it can give rise to unwanted mixing of mechanical modes, leading to an increase in laser dynamic linewidth resulting in lower OCT imaging depth[Cite 2D HCG paper].

To address the actuation problem, we propose a three-plate capacitor configuration, contrary to the conventional two-parallel plate capacitor. The three-plate capacitor is realized using silicon photonics[5]. Fig. 1 (a) shows a schematic overview of the structure, Fig. 1 (b) shows a microscope image of the device, and Fig. 1 (c) shows an illustration of the mathematical model. The device consists of InP wafer bonded on a silicon on insulator (SOI) substrate. The three contacts are highlighted in Fig. 1, V_0 ($-\alpha V_0$) is the voltage on the static outer contacts, and V_1 is the MEMS voltage.

The governing equation of motion for the model is (see supplementary material):

$$m\ddot{z} + b\dot{z} + kz = \frac{\epsilon A}{2}\left(\frac{(\alpha V_0 + V_1)^2}{(\alpha z_0 - z)^2} - \frac{(V_0 - V_1)^2}{(z_0 + z)^2}\right) \tag{3}$$

Where m is the mass, b is the damping coefficient, k is the spring constant, ϵ is the permittivity between the electrodes, A is the area, α is the asymmetry factor, V_0 is the static electrode voltage, V_1 is the MEMS voltage, and z is the MEMS position, and z_0 and αz_0 are the initial air gaps. The equation can be solved for the position and instability voltage V_{PI} on V_1; see supplementary material. Unlike the unidirectional case, the bidirectional configuration has two pull-in voltages – one on the MEMS and an outer pull-in voltage when the MEMS is grounded, given by:

$$V_{0\mathrm{PI}} = \sqrt{\frac{kz_0^3}{(1 + 1/\alpha)\epsilon_0 A}} \tag{4}$$

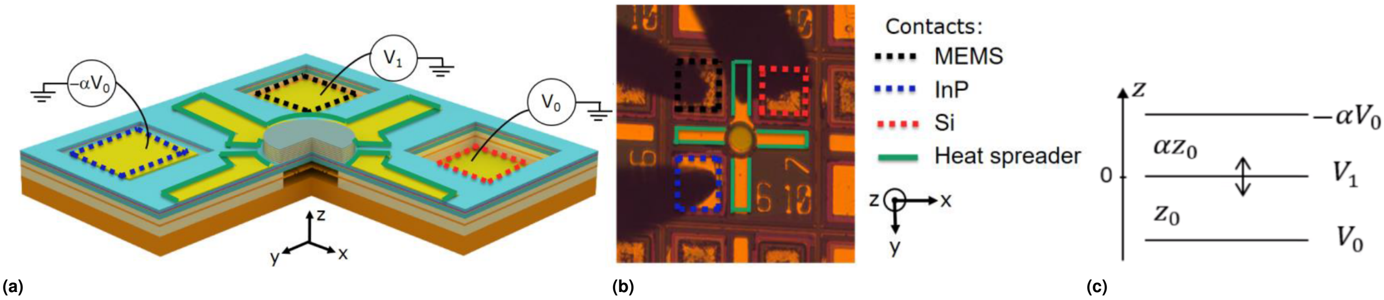

Fig. 1. Highlighted metal contacts in a device schematic (a) and microscope image (b). Illustration of the bidirectional model (c).

$V_{0\mathrm{PI}}$ is plotted in Fig. 2 ($\alpha = 1$), as a function of stiffness ($k = m(2\pi f_0)^2$, where f_0 is the native resonant frequency of the MEMS), and initial air gap (z_0). As is evident, the stiffer the MEMS and the larger the initial air gap, the larger V_{0PI} will be.

A MEMS with a resonance frequency of 3 MHz and symmetric initial air gaps of 1 µm results in $V_{0\mathrm{PI}} = 137$ V. Assuming the aforementioned geometry, with a MEMS mass of 241.9 fg, solving Eq. (3) for the MEMS position (z) as a function of the applied DC bias on the MEMS (V_1), for specific outer voltages (V_0) results in the DC tuning curves in Fig. 3. As indicated, the MEMS movement is amplified; for larger outer voltage, the MEMS movement becomes greater and more linear for smaller center voltage. However, the maximum MEMS excursion is decreased for higher outer voltage, i.e. the pull-in occurs earlier, although the starting maximum excursion is twice the distance compared to the unidirectional configuration.

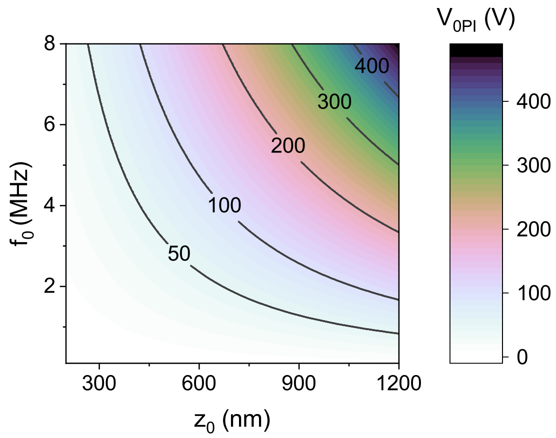

Fig. 2. Outer pull-in voltage $V_{0\mathrm{PI}}$ as a function of native MEMS resonant frequency f_0 and initial air gap z_0 for a symmetric MEMS ($\alpha = 1$).

Another way of illustrating the effect of the DC field on the MEMS is shown in Fig. 4. By controlling the outer DC field, the pull-in on the MEMS can be controlled, as can be seen in Fig. 4 (a) (right axis). As the outer voltage ($V_0/V_{0\mathrm{PI}}$) is increased the pull-in voltage (V_{PI}/V_0) on the MEMS decreases. This is a general result irrespective of the designed stiffness of the MEMS. If the outer voltage approaches $V_{0\mathrm{PI}}$ the pull-in voltage approaches 0 V, since the electric field between the plates will be so high that only a minute addition to the electric field will lead to an instability point resulting in the MEMS being snapped in. Fig. 4 (a) (left axis) shows the maximum displacement $z_{\max}/z_0$ (at the pull-in voltage), and in the aforementioned case, the displacement will also go to 0, since no actuation occurs. However, when the outer voltage is equal to $0.3849V_{0\mathrm{PI}}$, the pull-in on the MEMS approaches the same value, which is half the classical pull-in voltage. This will result in the maximum possible MEMS excursion: $z_{\max} = \pm z_0/3$. However, operating close to the pull-in voltage for stiff MEMS will require substantial voltage (in this case, 52.6 V), which is more than available from an AWG. By increasing the outer voltage, the pull-in voltage can reach the vicinity of the maximum output of the AWG, thereby realizing actuation. As can be seen in Fig. 4 (a) left, the cost of increasing the outer voltage is a decrease in maximum MEMS excursion. However, the starting condition is twice that of the traditional unidirectional actuation distance, i.e., one-third of the initial air gap.

Assuming a maximum voltage constraint on the MEMS, given by the maximum output of the AWG, there exists a minimum outer voltage in order to make the pull-in on the MEMS equal to the maximum voltage constraint. A minimum outer voltage (Min.V_0) and normalized maximum displacement are plotted as a function of a maximum voltage constraint on the MEMS (Max.V_1) in Fig. 4 (b). As can be seen, the smaller the maximum voltage constraint, the higher the outer voltage needs to be, which reduces the maximum MEMS displacement.

Fig. 5 compares experimental data to the bidirectional model. Fig. 5 (a) is similar to Fig 4 (a), the difference being that $\alpha = 1.105$ and not 1, i.e., the top air gap is slightly larger, in addition to not having normalized axes. The vertical line highlights an outer voltage of 60 V, resulting in 60 V on the Silicon contact and -66.3 V on the Indium Phosphide contact. Inserting the highlighted case into Eq. (3) and solving for the MEMS position z for different MEMS DC biases V_1 results in the solid simulation curve on Fig 5 (b). The horizontal lines on Fig. 5 (b) show the maximum MEMS excursion z_{max}, at the pull-in voltage (dotted vertical lines), for $V_0 = 60$ V and $\alpha = 1.105$. Experimental results show cavity resonances as circles (assuming a constant tuning efficiency $\frac{\Delta\lambda}{\Delta z}$ of 0.19) overlaying the simulation results, showing very good agreement, except when the MEMS is at maximum excursion towards the substrate. One thing to note is the linear relationship between the MEMS movement and the applied voltage in the center, uniquely attributed to bidirectional actuation. In contrast, in the unidirectional actuator, i.e., the parallel plate capacitor, the force is proportional to the voltage squared. Hence the MEMS movement is proportional to the voltage squared. The linear relationship is advantageous in both OCT and light

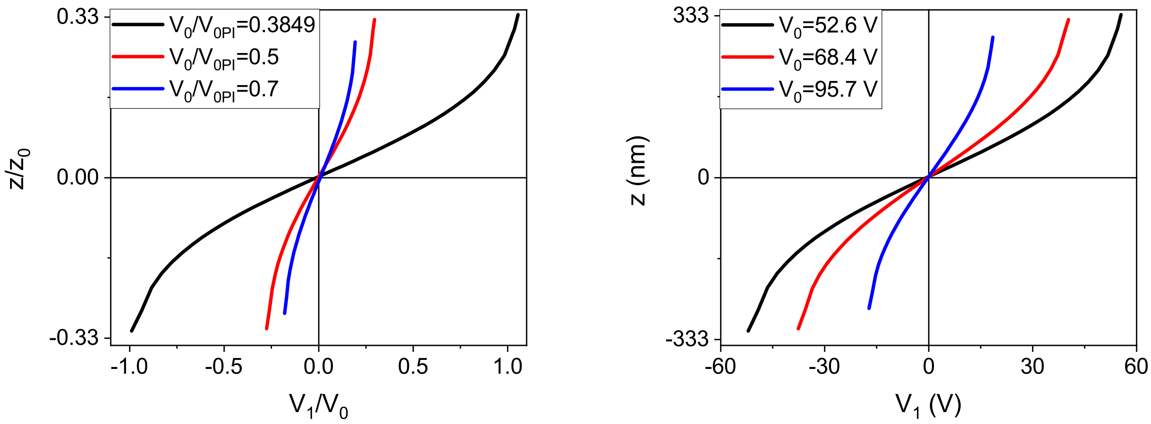

(a) (b)

Fig. 3. Normalized (a) and non-normalized (b) DC tuning curves of a MEMS with a native resonant frequency of 3 MHz, a mass of 241.9 fg, and symmetric initial air gaps of 1 μm. Black, red, and blue curves show 52.6 V, 68.4 V, and 95.7 V outer voltage, respectively.

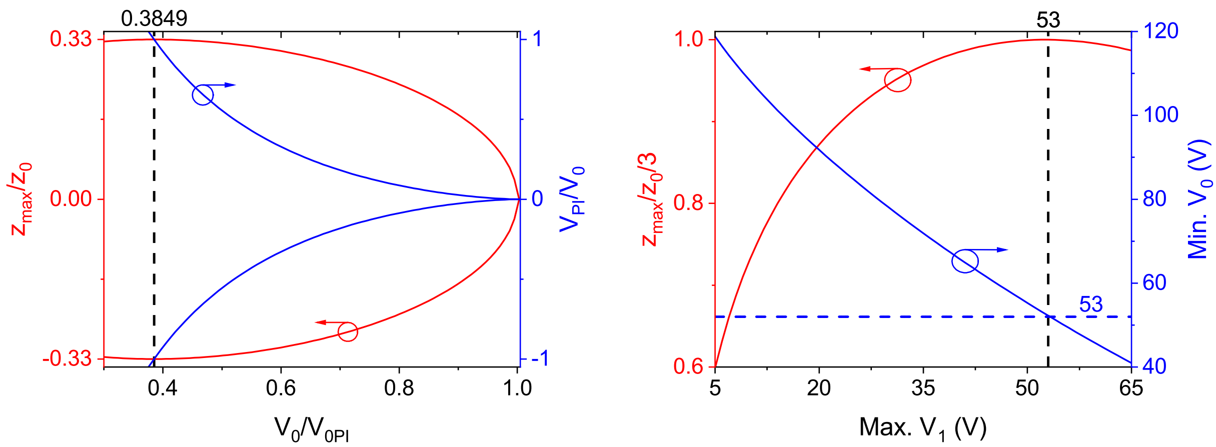

(a) (b)

Fig. 4. (a) Maximum displacement $z_{\max}$ normalized to initial air-gap z_0 (left), and MEMS pull-in voltage V_{PI} normalized to outer voltage V_0 (right), as a function of outer voltage V_0 normalized to the outer voltage pull-in $V_{0\mathrm{PI}}$. (b) Normalized maximum displacement (left) and minimum outer voltage (right) as a function of maximum MEMS voltage Max.V_1. The dashed vertical (horizontal) line shows when the MEMS voltage is equal to the outer voltage (53 V), which results in maximum MEMS displacement $z_{\max}/z_0/3 = 1$.

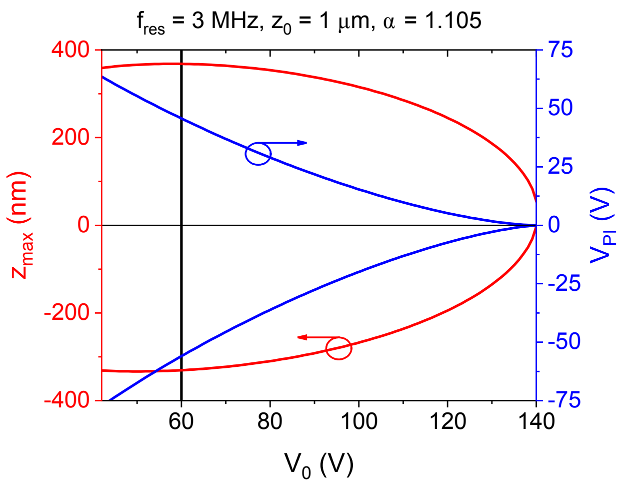

(a)

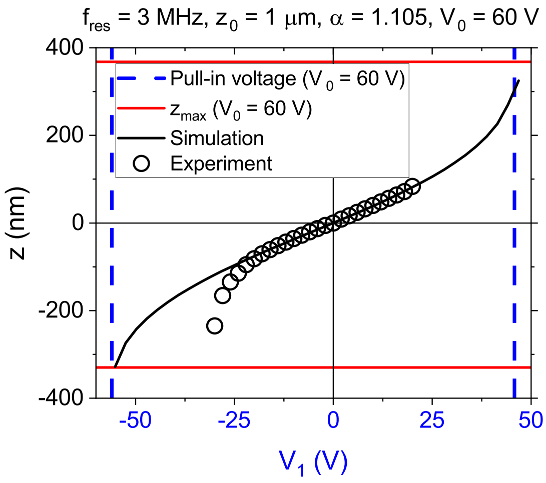

(b)

Fig. 5. (a) Maximum displacement z_{max} (left), and MEMS pull-in voltage V_{PI}, as a function of outer voltage V_0, for a MEMS with a fundamental resonance frequency of 3 MHz, an initial air gap of 1 μm, and an α coefficient of 1.105. (b) MEMS position z as a function of MEMS voltage V_1.

amplification and ranging (LiDAR).

Biasing the MEMS with an alternating voltage ($V_1 = V_a \cos(\omega t)$), inserted in Eq. (3) and solving for the MEMS position z (only including the fundamental harmonic term) results in:

$$z = \frac{V_0 V_a}{V_{OPI}^2} \frac{\omega_0^2 z_0 \cos(\omega t - \phi)}{\sqrt{\left(\omega^2 - \omega_0^2\left(1 - \frac{V_0^2}{V_{0PI}^2}\right)\right)^2 + \left(\frac{\omega_0 \omega}{Q}\right)^2}} \quad \textbf{(5)}$$

where V_a is the amplitude of the AC signal, ω_0 is the resonance frequency, ω is the actuation frequency, t is time, ϕ is a phase, and Q is the mechanical quality factor of the resonance. As can be seen on Eq. (5), the MEMS moves sinusoidally with a phase lack compared to the driving signal (V_1). Interestingly V_0 appears in front of the displacement amplitude of the MEMS, which means the MEMS alternating displacement amplitude can be amplified by increasing the static outer voltage. This is interesting because, traditionally, in the unidirectional case, one is limited by the maximum amplitude output of the AWG (V_a). Since the voltage limitation on the AWG is ±5 V, the AWG will not move the MEMS any substantial distance. One could amplify the alternating signal with a high-voltage amplifier. However, they are often accompanied by slew rate limitation, i.e., they have a hard time following a fast-moving AC signal without distorting it. In addition, high-voltage amplifiers require a lot of power to run. These limitations are circumvented by using the bidirectional configuration, where the displacement amplitude can be amplified by increasing the static field between the plates. However, as can be seen in the denominator in Eq. (5), there is a cost associated with increasing the outer voltage, and that is that the resonance frequency decreases. This is referred to as electrostatic spring softening. The adjusted resonance frequency taking into account electrostatic spring softening, is:

$$f_{\text{res}} = f_0 \times \sqrt{1 - \frac{V_0^2}{V_{0PI}^2}} \quad \textbf{(6)}$$

where f_{res} is the effective resonant frequency for the native mechanical resonant frequency f_0 with spring softening. Fig. 6 (a) and (b) show the native resonant frequency, f_0, as a function of maximum MEMS voltage max V_1, the red line indicates a 5 V maximum voltage constraint.

The contour plot on Fig. 6 (a) shows minimum outer voltage, Min. V_0 required to tune the MEMS pull-in voltage to be equal to max V_1. As expected, the stiffer the MEMS (higher f_0), the higher the outer voltage is needed for the same maximum voltage constraint. The higher the maximum voltage constraint on the MEMS, the less outer voltage is needed; the triangle in the bottom right corner shows no values by virtue of the available MEMS voltage being sufficient to achieve maximum actuation. The edge of the triangle indicates Min $V_0 \approx 0$ V, e.g., Max $V_1 = 5$ V, and $f_0 \approx 150$ kHz, Min $V_0 \approx 0.7$ V, i.e., close to 0 V. MEMS with a fundamental resonance higher than 150 kHz benefit from the bidirectional configuration (assuming max. $V_1 = 5$ V).

The contour on Fig. 6 (b) shows f_{res}, assuming Min. V_0 is applied to the outer contacts. The triangle in the bottom right shows no values, for the same reason as before, while at the edge of the triangle $f_{\text{res}} = f_0$, since the minimum outer voltage is 0 V, see Eq. (6). As indicated by Fig. 6 (b), the higher f_0 is, the higher f_{res} becomes (assuming constant Max. V_1), meaning that even though designing at stiffer MEMS, leads to a higher required outer voltage, which reduces the resonance frequency, one can design for a desired actuation frequency taking into account electrostatic spring softening.

As indicated by Fig. 6, a small increase in drive voltage will result in substantially better performance, i.e., less required outer voltage leading to a higher adjusted resonance frequency. Instead of using a high-voltage amplifier, one can use a low-power transformer, e.g., T9-1-X65 from minicurcuits[6], which has a relatively high gain and a bandwidth from 0.5 to 20 MHz. T9-1-X65 is a 1:25 high-frequency transformer, which means a 10 V peak-to-peak (Max. $V_1 = 5$ V) input signal turns into a 42 V peak-to-peak (Max. $V_1 = 21$ V) output signal at 20 MHz.

Fig. 7 (b) is a result of merging two graphs from [7], with some additions[8–11], showing figures of merit electrically and optically pumped MEMS VCSELs. Fig. 7 (a) shows a bidirectional

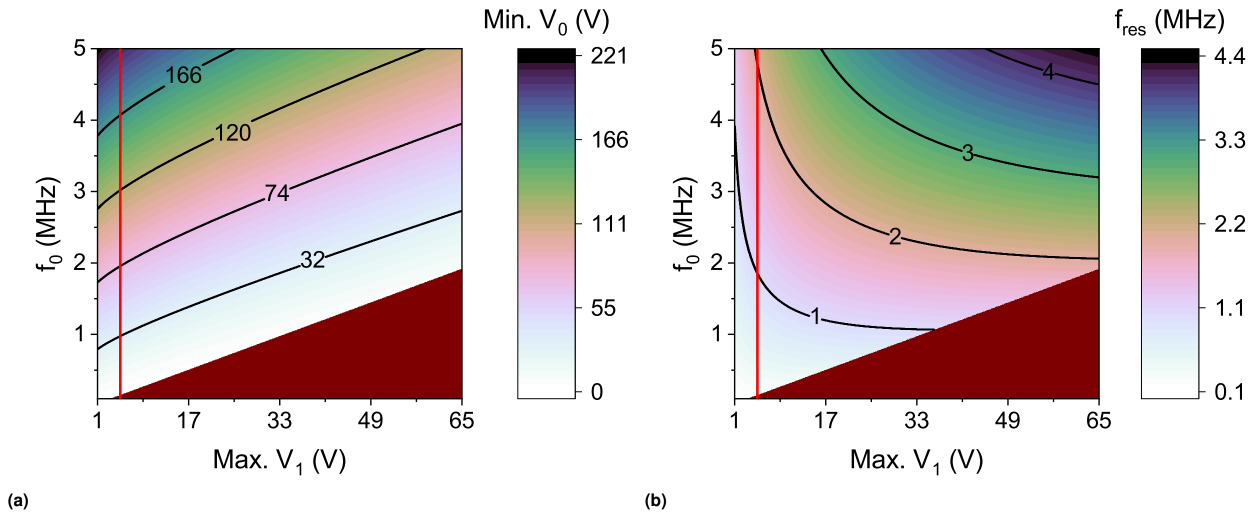

Fig. 6. (a) Native resonant frequency, f_0, as a function of maximum MEMS voltage max V_1, contour plot showing minimum outer voltage, Min. V_0 required to tune the MEMS pull-in voltage to be equal to max V_1. (b) Native resonant frequency, f_0, as a function of maximum MEMS voltage max V_1, contour plot showing the effective resonant frequency, f_{res}, assuming Min. V_0 is applied to the outer contacts. The vertical line highlighting Max. $V_1 = 5$ V.

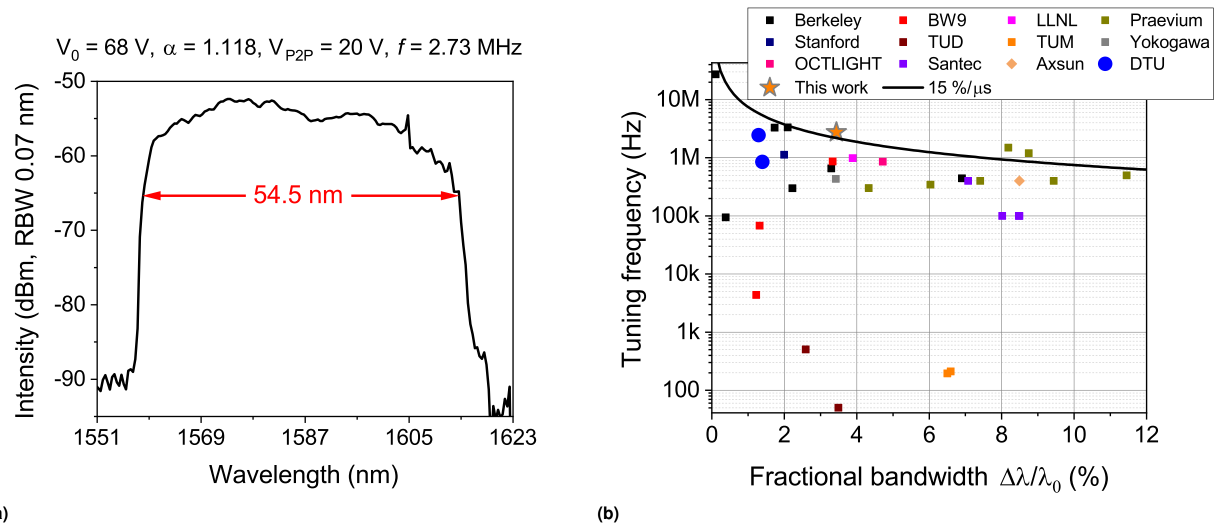

Fig. 7. (a) Spectrum of bidirectional AC actuation at 2.73 MHz showing bandwidth of 54.5 nm. (b) Tuning frequency as a function of fractional bandwidth, Fig. 7 (a) is depicted as "This work".

device pumped with 1310 nm CW diode, with an outer voltage of 68 V, $\alpha = 1.118$, peak-to-peak AC voltage of 20 V (high impedance), an actuation frequency of 2.73 MHz, resulting in a lasing bandwidth of 54.5 nm. Fig. 7 (b) shows the figures of merit of a swept source VCSEL, namely tuning frequency and fractional bandwidth; the device in Fig. 7 (a) is depicted as "This work" in Fig. 7 (b). The black curve indicates a sweep rate of 15% fractional bandwidth pr. microsecond. The two results from Praevium[8] above the black curve use a high-voltage amplifier (Model 2100HF, Trek, Inc.) in order to amplify the waveform. In addition, the bidirectional MEMS design has not been pushed to its limits, i.e., the tuning frequency and fractional bandwidth can both be increased.

Traditionally, because of the maximum constraint on voltage, one could either have ultra stiff/fast MEMS with limited bandwidth or slow/sloppy MEMS with large bandwidth. But by utilizing the bidirectional design, this trade-off is avoided, so it is possible to actuate very stiff MEMS without compromising the tuning bandwidth and without needing a high-voltage amplifier. This can open up new application areas for swept source VCSEL for applications requiring fast actuation and large bandwidth.

Funding. The authors would like to acknowledge the support of the Independent Research Fund Denmark (DFF STEPS 8022-00110A) and Horizon 2020 (H2020-EU.1.3.1 NETLAS 860807 Marie Skłodowska-Curie Actions, ITN network).

REFERENCES

1. M. C. Huang, Y. Zhou, and C. J. Chang-Hasnain, Nat. Photonics **1**, 119 (2007).
2. A. Simonsen, S. E. Hansen, M. Payandeh, A. Marchevsky, G. C. Park, H. Kumar Sahoo, E. Semenova, O. Hansen, and K. Yvind, “Bidirectional electrostatic MEMS tunable VCSELs,” in *2021 27th International Semiconductor Laser Conference (ISLC),* (2021), pp. 1–2.
3. T. Ansbæk, I.-S. Chung, E. S. Semenova, O. Hansen, and K. Yvind, IEEE J. Sel. Top. Quantum Electron. **19**, 1702306 (2013).
4. C. Jirauschek and R. Huber, Biomed. Opt. Express **6**, 2448 (2015).
5. H. K. Sahoo, T. Ansbæk, L. Ottaviano, E. Semenova, F. Zubov, O. Hansen, and K. Yvind, IEEE J. Sel. Top. Quantum Electron. **25**, 1 (2019).
6. minicircuits, “minicircuits,” https://www.minicircuits.com/pdfs/T9-1-X65.pdf.
7. P. Qiao, K. T. Cook, K. Li, and C. J. Chang-Hasnain, IEEE J. Sel. Top. Quantum Electron. **23**, 1 (2017).
8. J. Zhang, T. Nguyen, B. Potsaid, V. Jayaraman, C. Burgner, S. Chen, J. Li, K. Liang, A. Cable, G. Traverso, H. Mashimo, and J. G. Fujimoto, Biomed. Opt. Express **12**, 2384 (2021).
9. V. Jayaraman, G. D. Cole, M. Robertson, A. Uddin, and A. Cable, Electron. Lett. **48**, 867 (2012).
10. SANTEC, “SANTEC,” https://www.santec.com/en/products/oct/lasers-for-swept-source-oct/.
11. AXSUN, “AXSUN,” https://downloads.axsun.com/public/datasheets/Axsun_OCT_vcsel_datasheet.pdf.

A.3 Appendix 3

Bidirectional electrostatic MEMS tunable VCSELs: supplemental document

Abstract.

1. DERIVATION OF BIDIRECTIONAL SYSTEM EQUATIONS

A. Bidirectional capacitive actuator

We consider a system comprising two fixed electrodes (top-electrode at $z = g_t$ and potential V_t and bottom-electrode at $z = -g_b$ and potential V_b) with a movable electrode (mass m, spring constant k and potential V_1) at rest position $z = 0$ in-between, see Fig. S1. The electrodes all have

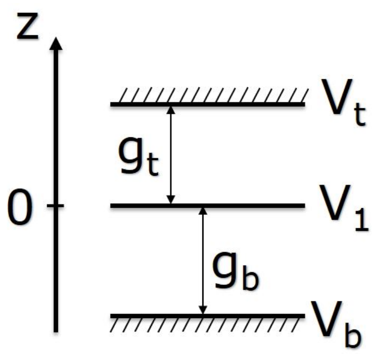

Fig. S1. Two static outer electrodes, one top and one bottom, surround a movable electrode in the middle.

the same area A, and the permittivity of the gap between electrodes is ϵ; thus, the capacitance of the top and bottom capacitors is[1]

$$C_t = C_t(z) = \epsilon A / (g_t - z) \text{ and } C_b = C_b(z) = \epsilon A / (g_b + z), \tag{S1}$$

respectively.

The total Hamiltonian of the system of capacitors, movable electrode and electrical power sources is[2]

$$\begin{aligned} H(p,z) = \frac{p^2}{2m} + \frac{1}{2}kz^2 + \frac{1}{2}C_t(V_t - V_1)^2 + \frac{1}{2}C_b(V_b - V_1)^2 + \\ + \left[-C_t(V_t - V_1)^2 - C_b(V_b - V_1)^2 + H_{t1} + H_{b1}\right] \end{aligned} \tag{S2}$$

where the first term is the kinetic energy (p is the momentum), the second term is the elastic energy stored in the spring, and the next two terms are the energy stored in the capacitors, while the terms in the square bracket are the stored energy in the two electrical power sources that apply the potential differences $V_t - V_1$ and $V_b - V_1$. When the power sources charge up the capacitors, they lose energy as seen in the expression in the square bracket, where H_{t1} and H_{b1} are the initial Hamiltonians of the power sources. In general, when a capacitor C is charged to $Q = CV$ from a constant voltage source, the charge Q flows out of the power source, which therefore looses the energy $\Delta H = -QV = -CV^2$ even though the capacitor only gains $CV^2/2$; the energy difference is lost either as Joule heat in resistive connections or is radiated.

From Hamilton's equations we then have $\partial_t z = \dot{z} = \partial_p H(p,z) = p/m$, or $p = m\dot{z}$ as expected, and $\partial_t p = m\ddot{z} = -\partial_z H(p,z)$ which evaluates to

$$m\ddot{z} = -kz + \frac{1}{2}(V_t - V_1)^2 \frac{\partial C_t}{\partial z} + \frac{1}{2}(V_b - V_1)^2 \frac{\partial C_b}{\partial z} \tag{S3}$$

for a loss-less system.

In Eq. S3 the right-hand side is the restoring force F_{rest}, and for equilibrium the restoring force evaluates to zero, $F_{\text{rest}} = 0$. However, the equilibrium position z_{eq} calculated from the condition $F_{\text{rest}}(z_{\text{eq}}) = 0$ may be stable, metastable, or unstable depending on the sign of $\partial_z F_{\text{rest}}(z) = -k_{\text{eff}}$ where k_{eff} is the effective spring constant in the operating point, i.e., stability requires $k_{\text{eff}} > 0$, while the system is metastable at $k_{\text{eff}} = 0$ and unstable at $k_{\text{eff}} < 0$. From Eq. S3 we get the stability condition

$$k_{\text{eff}} = k - \frac{1}{2}(V_t - V_1)^2 \frac{\partial^2 C_t}{\partial z^2} - \frac{1}{2}(V_b - V_1)^2 \frac{\partial^2 C_b}{\partial z^2} > 0, \tag{S4}$$

which must be combined with the static equilibrium condition $F_{\text{rest}}(z_{\text{eq}}) = 0$, i.e.,

$$-kz_{\text{eq}} + \frac{1}{2}(V_t - V_1)^2 \left.\frac{\partial C_t}{\partial z}\right|_{z_{\text{eq}}} + \frac{1}{2}(V_b - V_1)^2 \left.\frac{\partial C_b}{\partial z}\right|_{z_{\text{eq}}} = 0 \tag{S5}$$

to find the range of stable static operating conditions.

Adding dynamic losses (damping $b\dot{z}$) to Eq. S3, carrying out the differentiation and rearranging leads to

$$m\ddot{z} + b\dot{z} + kz = \frac{\epsilon A}{2}\left(\frac{(V_t - V_1)^2}{(g_t - z)^2} - \frac{(V_b - V_1)^2}{(g_b + z)^2}\right), \tag{S6}$$

where the left-hand side represents the pure mechanical equation of motion and the right-hand side the electrostatic actuation.

B. Ideal symmetric actuator

The ideal system is symmetric and has $g_t = g_b = g_0$, and then for $V_1 = 0$ V zero actuation results for $V_t = -V_b = -V_0$ (and also for $V_t = V_b$ which is of no use here). For the perfect symmetric system, we then have

$$m\ddot{z}/g_0 + b\dot{z}/g_0 + kz/g_0 = \frac{\epsilon A V_0^2}{2g_0^3}\left(\frac{(1 + V_1/V_0)^2}{(1 - z/g_0)^2} - \frac{(1 - V_1/V_0)^2}{(1 + z/g_0)^2}\right)$$

with the assumption that $V_t = -V_b = -V_0$. Here the position is normalized to the gap g_0 and actuation voltage V_1 to V_0. The expression can be fully non-dimensionalized as follows

$$\frac{\ddot{z}/g_0}{\omega_0^2} + 2\zeta\frac{\dot{z}/g_0}{\omega_0} + z/g_0 = \frac{\epsilon A V_0^2}{2kg_0^3}\left(\frac{(1 + V_1/V_0)^2}{(1 - z/g_0)^2} - \frac{(1 - V_1/V_0)^2}{(1 + z/g_0)^2}\right) \tag{S7}$$

where $\omega_0 = \sqrt{k/m}$ is the native resonant frequency of the mechanical system alone and $\zeta = b/\left(2\sqrt{km}\right)$ the damping ratio.

Using the same normalization, the stability criterion becomes

$$1 > \frac{\epsilon A V_0^2}{kg_0^3}\left(\frac{(1 + V_1/V_0)^2}{(1 - z/g_0)^3} + \frac{(1 - V_1/V_0)^2}{(1 + z/g_0)^3}\right), \tag{S8}$$

from which it is apparent that with $V_1 = 0$ V, where $z_{\text{eq}} = 0$ the system is only stable for $V_0^2 < kg_0^3/(2\epsilon A) = V_{0\text{PI}_{\text{sym}}}^2$ where $V_{0\text{PI}_{\text{sym}}}$ is the pull-in voltage of the symmetric device at zero actuation voltage V_1. This definition allows for further simplification of the normalized expressions, i.e., the equation of motion

$$\frac{\ddot{z}/g_0}{\omega_0^2} + 2\zeta\frac{\dot{z}/g_0}{\omega_0} + z/g_0 = \frac{V_0^2}{4V_{0\text{PI}_{\text{sym}}}^2}\left(\frac{(1 + V_1/V_0)^2}{(1 - z/g_0)^2} - \frac{(1 - V_1/V_0)^2}{(1 + z/g_0)^2}\right), \tag{S9}$$

and the stability criterion

$$1 > \frac{V_0^2}{2V_{0\text{PI}_{\text{sym}}}^2}\left(\frac{(1 + V_1/V_0)^2}{(1 - z/g_0)^3} + \frac{(1 - V_1/V_0)^2}{(1 + z/g_0)^3}\right). \tag{S10}$$

Defining $u = z/g_0$, $v = V_1/V_0$ and $\Psi^2 = V_0^2/V_{0\text{PI}_{\text{sym}}}^2$ the two equations simplify further to

$$\frac{\ddot{u}}{\omega_0^2} + 2\zeta\frac{\dot{u}}{\omega_0} + u = \frac{1}{4}\Psi^2\left(\frac{(1 + v)^2}{(1 - u)^2} - \frac{(1 - v)^2}{(1 + u)^2}\right), \tag{S11}$$

and

$$1 > \frac{1}{2}\Psi^2 \left(\frac{(1+v)^2}{(1-u)^3} + \frac{(1-v)^2}{(1+u)^3} \right), \tag{S12}$$

respectively.

Under static conditions ($\dot{u} = 0$ and $\ddot{u} = 0$), the coefficient Ψ^2 may be eliminated from Eqs. S11 and S12 at pull-in ($k_{\text{eff}} = 0$) to yield

$$2u_{\text{pi}} \left(\frac{(1+v_{\text{pi}})^2}{(1-u_{\text{pi}})^3} + \frac{(1-v_{\text{pi}})^2}{(1+u_{\text{pi}})^3} \right) = \left(\frac{(1+v_{\text{pi}})^2}{(1-u_{\text{pi}})^2} - \frac{(1-v_{\text{pi}})^2}{(1+u_{\text{pi}})^2} \right),$$

where u_{pi} and v_{pi} are normalized deflection and actuation voltage at pull-in, respectively. Rearranging leads to

$$(1+v_{\text{pi}})^2 \left(\frac{2u_{\text{pi}}}{(1-u_{\text{pi}})^3} - \frac{1}{(1-u_{\text{pi}})^2} \right) = -(1-v_{\text{pi}})^2 \left(\frac{2u_{\text{pi}}}{(1+u_{\text{pi}})^3} + \frac{1}{(1+u_{\text{pi}})^2} \right),$$

and thus

$$\frac{(1-v_{\text{pi}})^2}{(1+v_{\text{pi}})^2} = \frac{-\frac{2u_{\text{pi}}}{(1-u_{\text{pi}})^3} + \frac{1}{(1-u_{\text{pi}})^2}}{\frac{2u_{\text{pi}}}{(1+u_{\text{pi}})^3} + \frac{1}{(1+u_{\text{pi}})^2}} = \frac{(1+u_{\text{pi}})^3}{(1-u_{\text{pi}})^3} \frac{1-3u_{\text{pi}}}{1+3u_{\text{pi}}}.$$

As the left-hand side must be positive, we have $|u_{\text{pi}}| \leq 1/3$, and that $u_{\text{pi}} = \pm 1/3 \Rightarrow v_{\text{pi}} = \pm 1$, while $u_{\text{pi}} = 0 \Rightarrow v_{\text{pi}} = 0$ (if V_0 is non-zero). It follows that

$$\frac{1-v_{\text{pi}}}{1+v_{\text{pi}}} = \pm \frac{\sqrt{(1+u_{\text{pi}})^3 (1-3u_{\text{pi}})}}{\sqrt{(1-u_{\text{pi}})^3 (1+3u_{\text{pi}})}},$$

where the positive sign is valid for $|v_{\text{pi}}| \leq 1$.

Solving for the normalized actuation voltage leads to

$$v_{\text{pi}} = \frac{\sqrt{(1-u_{\text{pi}})^3 (1+3u_{\text{pi}})} \mp \sqrt{(1+u_{\text{pi}})^3 (1-3u_{\text{pi}})}}{\sqrt{(1-u_{\text{pi}})^3 (1+3u_{\text{pi}})} \pm \sqrt{(1+u_{\text{pi}})^3 (1-3u_{\text{pi}})}}, \tag{S13}$$

where the upper sign is valid for $|v_{\text{pi}}| \leq 1$, and the lower sign is valid for $|v_{\text{pi}}| \geq 1$.

Solving the static equilibrium condition (Eq. S11 with $\dot{u} = 0$ and $\ddot{u} = 0$) for Ψ^2 at pull in yields

$$\Psi^2 = \frac{4u_{\text{pi}}}{\frac{(1+v_{\text{pi}})^2}{(1-u_{\text{pi}})^2} - \frac{(1-v_{\text{pi}})^2}{(1+u_{\text{pi}})^2}} = \left(\frac{\sqrt{(1-u_{\text{pi}})^3 (1+3u_{\text{pi}})} \pm \sqrt{(1+u_{\text{pi}})^3 (1-3u_{\text{pi}})}}{2} \right)^2 \tag{S14}$$

and thus

$$\Psi = \left| \frac{V_0}{V_{0\text{PI}_{\text{sym}}}} \right| = \left| \frac{\sqrt{(1-u_{\text{pi}})^3 (1+3u_{\text{pi}})} \pm \sqrt{(1+u_{\text{pi}})^3 (1-3u_{\text{pi}})}}{2} \right|,$$

in both cases the upper sign is valid for $|v_{\text{pi}}| \leq 1$. We see that at $u_{\text{pi}} = \pm 1/3$ we have $\Psi = \sqrt{4/27}$.

Combining Eqs. S13 and S14 a simple calculation shows that the simple relation $v_{\text{pi}}\Psi^2 = 4u_{\text{pi}}^3$ is valid at pull-in.

C. Real asymmetric, but almost symmetric, actuator

In a real device, it is almost impossible to avoid that $g_t \neq g_b$ such that the system is asymmetric. To account for the asymmetry, we take $g_b = z_0$ and $g_t = \alpha z_0$, where α is the asymmetry factor; moreover we want to work with normalized positions $u = z/z_0$. Likewise we take $V_b = V_0$ and normalize the actuation voltage V_1 to V_0, i.e., $v = V_1/V_0$ while V_t for now remains unassigned. When these assumptions are used in the general equation of motion Eq. S6 we get

$$m\ddot{u} + b\dot{u} + ku = \frac{\epsilon A V_0^2}{2z_0^3}\left(\frac{(V_t/V_0 - v)^2}{(\alpha - u)^2} - \frac{(1-v)^2}{(1+u)^2}\right)$$

and then it becomes apparent that by applying the bias voltage $V_t = -\alpha V_0$ zero actuation at $V_1 = 0$ V results, and with this assignment we get a normalized equation of motion that is quite similar to that for the symmetric actuator

$$\frac{\ddot{u}}{\omega_0^2} + 2\zeta\frac{\dot{u}}{\omega_0} + u = \frac{\epsilon A V_0^2}{2kz_0^3}\left(\frac{(\alpha+v)^2}{(\alpha-u)^2} - \frac{(1-v)^2}{(1+u)^2}\right)$$

and with the corresponding stability criterion

$$\frac{\epsilon A V_0^2}{kz_0^3}\left(\frac{(\alpha+v)^2}{(\alpha-u)^3} + \frac{(1-v)^2}{(1+u)^3}\right) < 1,$$

from which we see that the pull-in voltage at zero actuation voltage ($v = 0$) is $V_{0\mathrm{PI}}^2 = kz_0^3/(\epsilon A\,(1 + 1/\alpha))$ which leads to the final non-dimensionalized equation of motion

$$\frac{\ddot{u}}{\omega_0^2} + 2\zeta\frac{\dot{u}}{\omega_0} + u = \frac{V_0^2}{2\,(1+1/\alpha)\,V_{0\mathrm{PI}}^2}\left(\frac{(\alpha+v)^2}{(\alpha-u)^2} - \frac{(1-v)^2}{(1+u)^2}\right) = \tag{S15}$$

$$= \frac{1}{2\,(1+1/\alpha)}\Psi_\alpha^2\left(\frac{(\alpha+v)^2}{(\alpha-u)^2} - \frac{(1-v)^2}{(1+u)^2}\right), \tag{S16}$$

with the stability criterion

$$1 > \frac{V_0^2}{(1+1/\alpha)\,V_{0\mathrm{PI}}^2}\left(\frac{(\alpha+v)^2}{(\alpha-u)^3} + \frac{(1-v)^2}{(1+u)^3}\right) = \tag{S17}$$

$$= \frac{1}{(1+1/\alpha)}\Psi_\alpha^2\left(\frac{(\alpha+v)^2}{(\alpha-u)^3} + \frac{(1-v)^2}{(1+u)^3}\right).$$

where $\Psi_\alpha^2 \equiv V_0^2/V_{0\mathrm{PI}}^2$.

Eliminating Ψ_α^2 in static conditions by use of Eqs. S15 and S17 we get

$$2u_{\mathrm{pi}}\left(\frac{(\alpha+v_{\mathrm{pi}})^2}{(\alpha-u_{\mathrm{pi}})^3} + \frac{(1-v_{\mathrm{pi}})^2}{(1+u_{\mathrm{pi}})^3}\right) = \left(\frac{(\alpha+v_{\mathrm{pi}})^2}{(\alpha-u_{\mathrm{pi}})^2} - \frac{(1-v_{\mathrm{pi}})^2}{(1+u_{\mathrm{pi}})^2}\right)$$

which can be rearranged to

$$(\alpha+v_{\mathrm{pi}})^2\left(\frac{2u_{\mathrm{pi}}}{(\alpha-u_{\mathrm{pi}})^3} - \frac{1}{(\alpha-u_{\mathrm{pi}})^2}\right) = -(1-v_{\mathrm{pi}})^2\left(\frac{2u_{\mathrm{pi}}}{(1+u_{\mathrm{pi}})^3} + \frac{1}{(1+u_{\mathrm{pi}})^2}\right)$$

and thus

$$\frac{(1-v_{\mathrm{pi}})^2}{(\alpha+v_{\mathrm{pi}})^2} = \frac{(1+u_{\mathrm{pi}})^3}{(\alpha-u_{\mathrm{pi}})^3}\frac{\alpha-3u_{\mathrm{pi}}}{1+3u_{\mathrm{pi}}}.$$

The left-hand side must be positive, and thus, the normalized pull-in deflection is restricted to the range $-1/3 \le u_{\mathrm{pi}} \le \alpha/3$, and $u_{\mathrm{pi}} = \alpha/3 \Rightarrow v_{\mathrm{pi}} = 1$, $u_{\mathrm{pi}} = -1/3 \Rightarrow v_{\mathrm{pi}} = -\alpha$, and $u_{\mathrm{pi}} = 0 \Rightarrow v_{\mathrm{pi}} = 0$ (as long as V_0 is finite). It follows that

$$\frac{1-v_{\mathrm{pi}}}{\alpha+v_{\mathrm{pi}}} = \pm\frac{\sqrt{(1+u_{\mathrm{pi}})^3\,(\alpha-3u_{\mathrm{pi}})}}{\sqrt{(\alpha-u_{\mathrm{pi}})^3\,(1+3u_{\mathrm{pi}})}}$$

where the positive sign is valid for the range $-\alpha \leq v_{\mathrm{pi}} \leq 1$, while the negative sign is valid for v_{pi} outside this range. Solving for v_{pi} leads to

$$v_{\mathrm{pi}} = \frac{\sqrt{(\alpha - u_{\mathrm{pi}})^3 (1 + 3u_{\mathrm{pi}})} \mp \alpha \sqrt{(1 + u_{\mathrm{pi}})^3 (\alpha - 3u_{\mathrm{pi}})}}{\sqrt{(\alpha - u_{\mathrm{pi}})^3 (1 + 3u_{\mathrm{pi}})} \pm \sqrt{(1 + u_{\mathrm{pi}})^3 (\alpha - 3u_{\mathrm{pi}})}}, \tag{S18}$$

where the upper sign is valid in the range $-\alpha \leq v_{\mathrm{pi}} \leq 1$.

Solving the static equation of motion for Ψ_α^2 leads to

$$\Psi_\alpha^2 = \frac{2(1 + 1/\alpha)\, u_{\mathrm{pi}}}{\frac{(\alpha + v_{\mathrm{pi}})^2}{(\alpha - u_{\mathrm{pi}})^2} - \frac{(1 - v_{\mathrm{pi}})^2}{(1 + u_{\mathrm{pi}})^2}} = \frac{\left(\sqrt{(\alpha - u_{\mathrm{pi}})^3 (1 + 3u_{\mathrm{pi}})} \pm \sqrt{(1 + u_{\mathrm{pi}})^3 (\alpha - 3u_{\mathrm{pi}})}\right)^2}{\alpha (\alpha + 1)^2},$$

and thus

$$\Psi_\alpha = \left| \frac{V_0}{V_{0\mathrm{PI}}} \right| = \frac{\left| \sqrt{(\alpha - u_{\mathrm{pi}})^3 (1 + 3u_{\mathrm{pi}})} \pm \sqrt{(1 + u_{\mathrm{pi}})^3 (\alpha - 3u_{\mathrm{pi}})} \right|}{(\alpha + 1)\sqrt{\alpha}} \tag{S19}$$

where we see that at $u_{\mathrm{pi}} = -1/3$ ($v_{\mathrm{pi}} = -\alpha$) we have $\Psi_\alpha = \sqrt{8/27} / \left(\sqrt{\alpha}\sqrt{1+\alpha}\right)$ while at $u_{\mathrm{pi}} = \alpha/3$ ($v_{\mathrm{pi}} = 1$) we have $\Psi_\alpha = \alpha\sqrt{8/27} / \sqrt{1+\alpha}$.

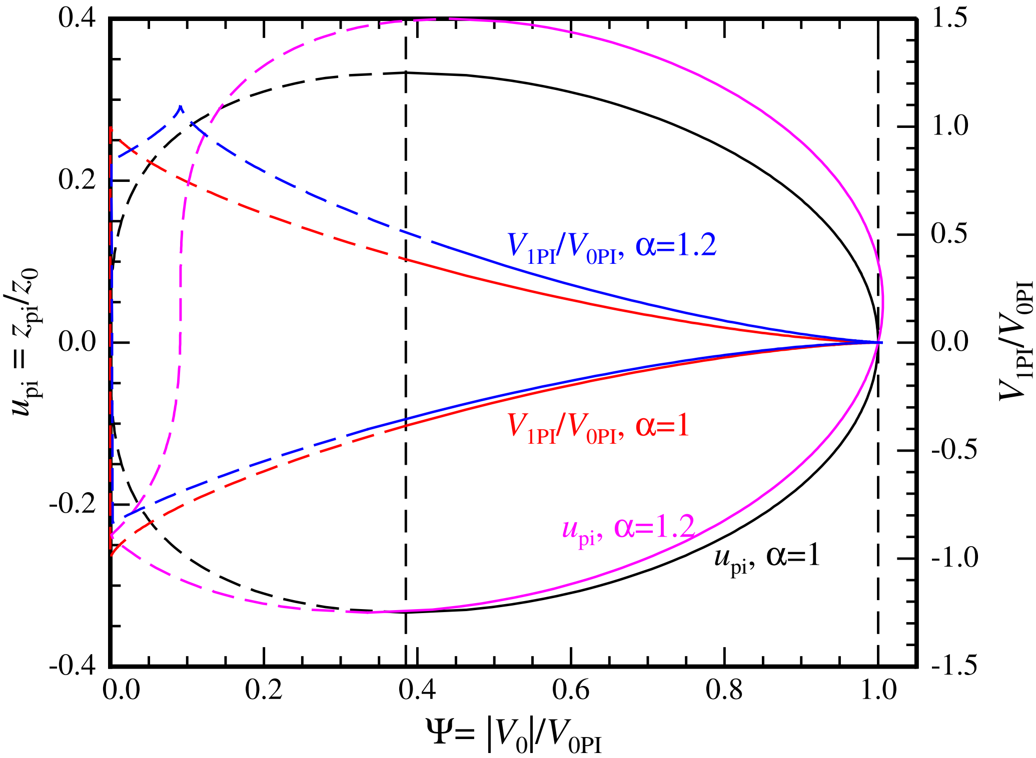

Fig. S2. Normalized pull-in displacement u_{pi} and normalized pull-in voltage $V_{1\mathrm{PI}}/V_{0\mathrm{PI}}$ as a function of normalized bias voltage $\Psi = V_0/V_{0\mathrm{PI}}$ for two values of the asymmetry factor $\alpha = 1$ and $\alpha = 1.2$. The vertical dashed lines indicate $\Psi = \sqrt{4/27}$ and $\Psi = 1$.

Figure S2 shows calculated normalized pull-in displacement u_{pi} and voltage $V_{1\mathrm{PI}}/V_{0\mathrm{PI}}$ as function of normalized bias voltage $V_0/V_{0\mathrm{PI}}$.

2. BIDIRECTIONAL DYNAMIC EQUATIONS

Assuming an alternating drive signal on the movable electrode, i.e., $V_1(t) = V_a \cos(\omega t)$ where V_a is the amplitude and ω is the actuation frequency, inserted in Eq. (S16) solved for MEMS position z results in (only including the fundamental sinusoidal term)

$$z(t) = \frac{V_0 V_a}{V_{0PI}^2} \frac{\omega_0^2 z_0 \cos(\omega t - \phi)}{\sqrt{\left(\omega^2 - \omega_0^2\left(1 - \frac{V_0^2}{V_{0PI}^2}\right)\right)^2 + \left(\frac{\omega_0 \omega}{Q}\right)^2}}, \quad \phi = \arctan\left(\frac{\omega_0 \omega}{Q(\omega_0^2\left(1 - \frac{V_0^2}{V_{0PI}^2}\right) - \omega^2)}\right) \tag{S20}$$

where Q is the mechanical quality factor, ω_0 is the native mechanical resonant frequency. Eq. (S20) resembles the result for the standard unidirectional electrostatic actuator[3] (also only including the fundamental term)

$$z(t) = \frac{4}{27} \frac{2 V_0 V_a}{V_{PI}^2} \frac{\omega_0^2 z_0 \cos(\omega t - \phi)}{\sqrt{(\omega^2 - \omega_0^2)^2 + (\frac{\omega_0 \omega}{Q})^2}} + z_{\mathrm{OFST}} \tag{S21}$$

with $V_{PI} = 8 z_0^2 k / (27 C_0)$, where C_0 is the equilibrium actuator capacitance, and z_{OFST} is an off-set displacement. One difference between the two equations is that the electrostatic spring softening $\sqrt{1 - V_0^2 / V_{0PI}^2}$ is seen in the fundamental term for the bidirectional actuator, compared to the first higher-order term for the unidirectional actuator[3].

In both cases, the MEMS displacement amplitude can be increased by increasing the static electric field V_0; however, in the unidirectional case, increasing the DC field increases the offset from the resting mirror position, which will limit the tuning range. For the bidirectional configuration, this offset is not seen, as opposite polarized DC fields of equal magnitude ($\alpha = 1$) will result in electrostatic forces of opposite directions but equal in magnitude, resulting in zero net force on the movable electrode. Therefore, the only cost associated with increasing the DC fields is the reduction of the resonant frequency (electrostatic spring softening). When designing a stiff MEMS, this reduction can be taken into account in order to realize a targeted sweep rate, as seen in Fig.6 in the parent article.

A. Higher order terms

The fundamental and the first two higher-order displacement terms are as follows

$$L_1 = \frac{V_0 V_a}{V_{0\mathrm{PI}}^2} \frac{z_0}{\frac{\omega^2}{\omega_0^2} - \left(1 - \frac{V_0^2}{V_{0\mathrm{PI}}^2}\right) + i\left(\frac{\omega}{Q\omega_0}\right)} = \frac{V_0 V_a}{V_{0\mathrm{PI}}^2} \frac{\omega_0 z_0 \left(\omega^2 - \omega_0^2\left(1 - \frac{V_0^2}{V_{0\mathrm{PI}}^2}\right) - i\left(\frac{\omega_0 \omega}{Q}\right)\right)}{\left(\omega^2 - \omega_0^2\left(1 - \frac{V_0^2}{V_{0\mathrm{PI}}^2}\right)\right)^2 + \left(\frac{\omega_0 \omega}{Q}\right)} \tag{S22}$$

$$L_2 = -\frac{V_0^2}{V_{0\mathrm{PI}}^2} z_0 \frac{\frac{\frac{1}{\alpha^2} - 1}{2\left(1 + \frac{1}{\alpha}\right)}\left(\frac{V_a^2}{V_0^2} - \frac{L_1^2}{z_0^2}\right)}{\frac{(2\omega)^2}{\omega_0^2} - \left(1 - \frac{V_0^2}{V_{0\mathrm{PI}}^2}\right) + i\left(\frac{2\omega}{Q\omega_0}\right)} \tag{S23}$$

$$= -\frac{V_0^2}{V_{0\mathrm{PI}}^2} \frac{\left(\frac{\omega_0}{2}\right)^2 z_0 \frac{\frac{1}{\alpha^2} - 1}{2\left(1 + \frac{1}{\alpha}\right)}\left(\frac{V_a^2}{V_0^2} - \frac{L_1^2}{z_0^2}\right)\left(\omega^2 - \left(\frac{\omega_0}{2}\right)^2\left(1 - \frac{V_0^2}{V_{0\mathrm{PI}}^2}\right) - i\left(\frac{\omega_0 \omega}{2Q}\right)\right)}{\left(\omega^2 - \left(\frac{\omega_0}{2}\right)^2\left(1 - \frac{V_0^2}{V_{0\mathrm{PI}}^2}\right)\right)^2 + \left(\frac{\omega_0 \omega}{2Q}\right)^2} \tag{S24}$$

which equals 0 for $\alpha = 1$.

$$L_3 = -\frac{V_0^2}{V_{0\mathrm{PI}}^2} z_0 \frac{\left(\frac{\left(1 - \frac{1}{\alpha^2}\right) L_1 L_2}{\left(1 + \frac{1}{\alpha}\right) z_0^2} - \frac{V_a L_1^2}{V_0 \alpha z_0^2} + \frac{V_a^2 L_1}{V_0^2 \alpha z_0}\right)}{\frac{(3\omega)^2}{\omega_0^2} - \left(1 - \frac{V_0^2}{V_{0\mathrm{PI}}^2}\right) + i\left(\frac{3\omega}{Q\omega_0}\right)} \tag{S25}$$

$$= -\frac{V_0^2}{V_{0\mathrm{PI}}^2} \frac{\left(\frac{\omega_0}{3}\right)^2 z_0 \left(\frac{\left(1 - \frac{1}{\alpha^2}\right) L_1 L_2}{\left(1 + \frac{1}{\alpha}\right) z_0^2} - \frac{V_a L_1^2}{V_0 \alpha z_0^2} + \frac{V_a^2 L_1}{V_0^2 \alpha z_0}\right)\left(\omega^2 - \left(\frac{\omega_0}{3}\right)^2\left(1 - \frac{V_0^2}{(1+\alpha) V_{0\mathrm{PI}}^2}\right) - i\left(\frac{\omega_0 \omega}{3Q}\right)\right)}{\left(\omega^2 - \left(\frac{\omega_0}{3}\right)^2\left(1 - \frac{V_0^2}{V_{0\mathrm{PI}}^2}\right)\right)^2 + \left(\frac{\omega_0 \omega}{3Q}\right)^2} \tag{S26}$$

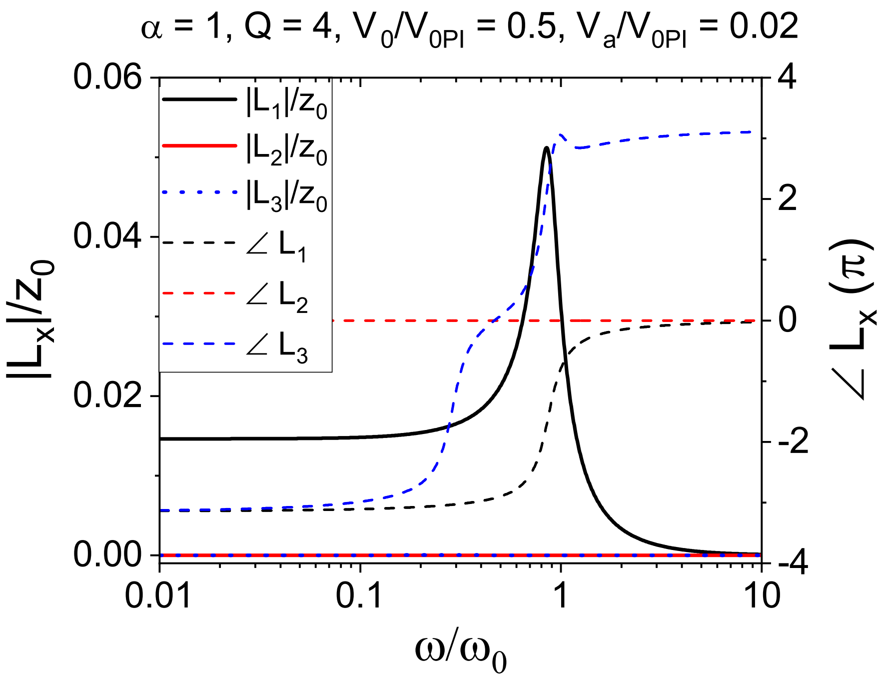

Fig. S3. Transfer curves, magnitude, and phase, for the first three terms.

The MEMS displacement, including the first three terms, is then found, by

$$z(t) = \Re(L_1(\omega)\exp(-i\omega t) + L_2(\omega)\exp(-i2\omega t) + L_3(\omega)\exp(-i3\omega t)) \tag{S27}$$

The transfer curves, for the first three terms, can be seen in Fig. S3, for a symmetric ($\alpha = 1$) Silicon MEMS with a quality factor of 4 and a resonant frequency of 3 MHz, and area of 260 μm^2, a thickness of 400 nm, an initial air gap of 1 μm, an outer voltage of $0.5V_{0\mathrm{PI}}$, and an actuation voltage of $0.04V_{0\mathrm{PI}}$, with $V_{0\mathrm{PI}} = 137$ V. As is evident in Fig. S3 the fundamental term (L_1) has the greatest magnitude, i.e. $z(t) \approx \Re(L_1(\omega)\exp(-i\omega t))$.
Figure S4 shows the MEMS position and voltage waveform as a function of time, including the first three terms, i.e., Eq. (S27) for $\omega_{\mathrm{act}} = \omega/\omega_0 = 0.8471$ (where $|L_1|$ peaks in Fig. S3) and $V(t) = \Re(V_a\exp(-i\omega_{\mathrm{act}}t))$. The solid curves show a peak-to-peak voltage (V_{pp}) of 10 V, the maximum output of an arbitrary waveform generator (AWG). The dashed curves show a peak-to-peak voltage of 42 V, which is the transformed voltage using a T9-1-X65 from minicurcuits[4], with an input of $V_{\mathrm{pp}} = 10$ V. The maximum MEMS excursion increases from ± 85 nm to ± 360 nm using the transformed signal, which translates to a (blue- and red-shift) wavelength sweep from 32 nm to 136 nm assuming a constant tuning efficiency of $\frac{\Delta\lambda}{\Delta z}$ of 0.19. The wavelength sweep can be further increased by increasing the outer voltages; however, this will cause the frequency at which $|L_1|$ peaks to decrease, thereby lowering ω_{act}.

Fig. S5 (a) shows the wavelength sweep as a function of outer voltage and drive voltage amplitude, and Fig. S5 (b) shows the actuation frequency as a function of outer voltage. As indicated, the tuning bandwidth can be increased by increasing the static outer voltages; however, it decreases the actuation frequency due to electrostatic spring softening.

REFERENCES

1. S. Ramo, J. R. Whinnery, and T. Van Duzer, *Fields and Waves in Communication Electronics* (Wiley, 1965).
2. S. D. Senturia, *Microsystem design* (Kluwer Acad. Publ., 2001).
3. T. Ansbæk, I.-S. Chung, E. Semenova, O. Hansen, and K. Yvind, “Resonant mems tunable vcsel,” I E E E J. on Sel. Top. Quantum Electron. **19**, 1702306 (2013).
4. minicircuits, “minicircuits,” https://www.minicircuits.com/pdfs/T9-1-X65.pdf.

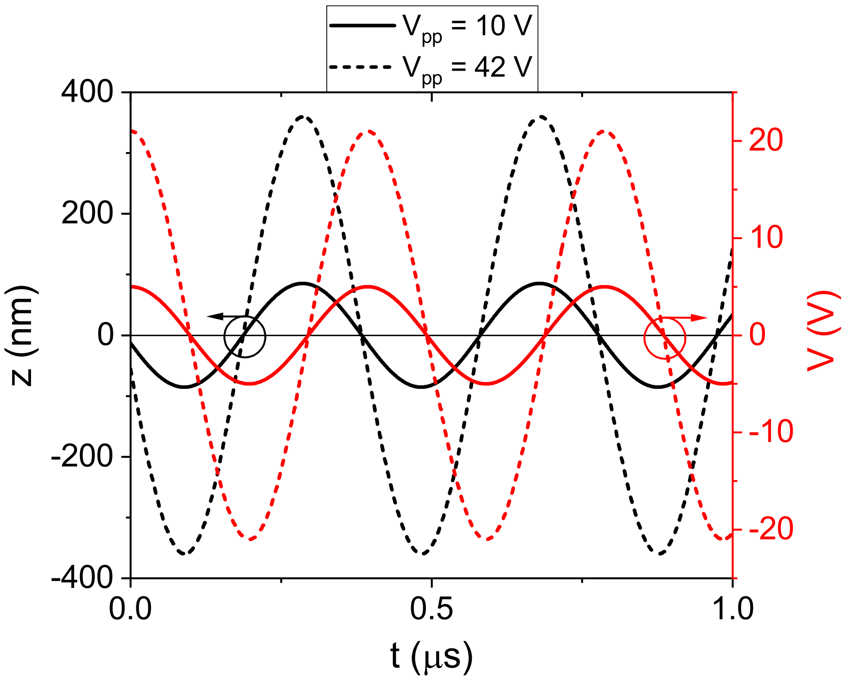

Fig. S4. MEMS position (left) and voltage (right) as a function of time, for voltage peak to peak amplitude of 10 V (solid) and 42 V (dashed).

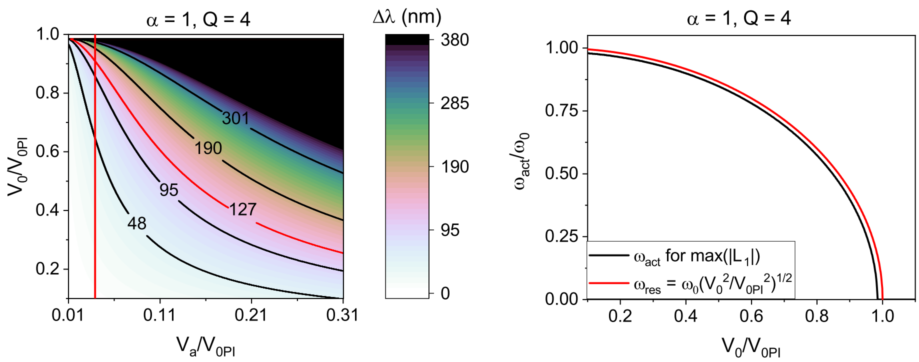

Fig. S5. (a) Tuning bandwidth as a function of outer voltage normalized to outer pull-in voltage and sinusoidal amplitude normalized to outer pull-in voltage. (b) Actuation frequency normalized to the native resonant frequency as a function of outer voltage normalized to the outer pull-in voltage.

A.4 Appendix 4

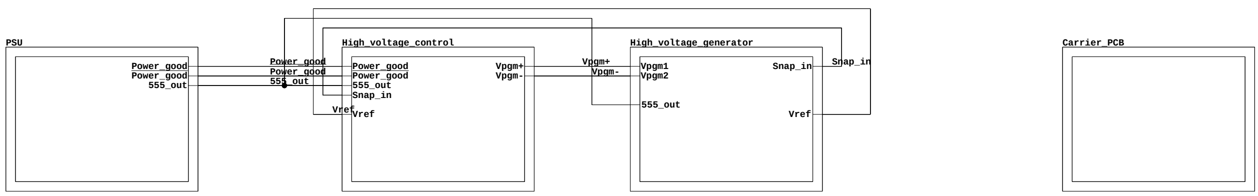

Project

Fagpakkeprojekt

Size	Hierachy name	Rev
A3		A

Drawn by	Sheet	of	Date
Leo og Theo	1	5	03/05/2021:13:37

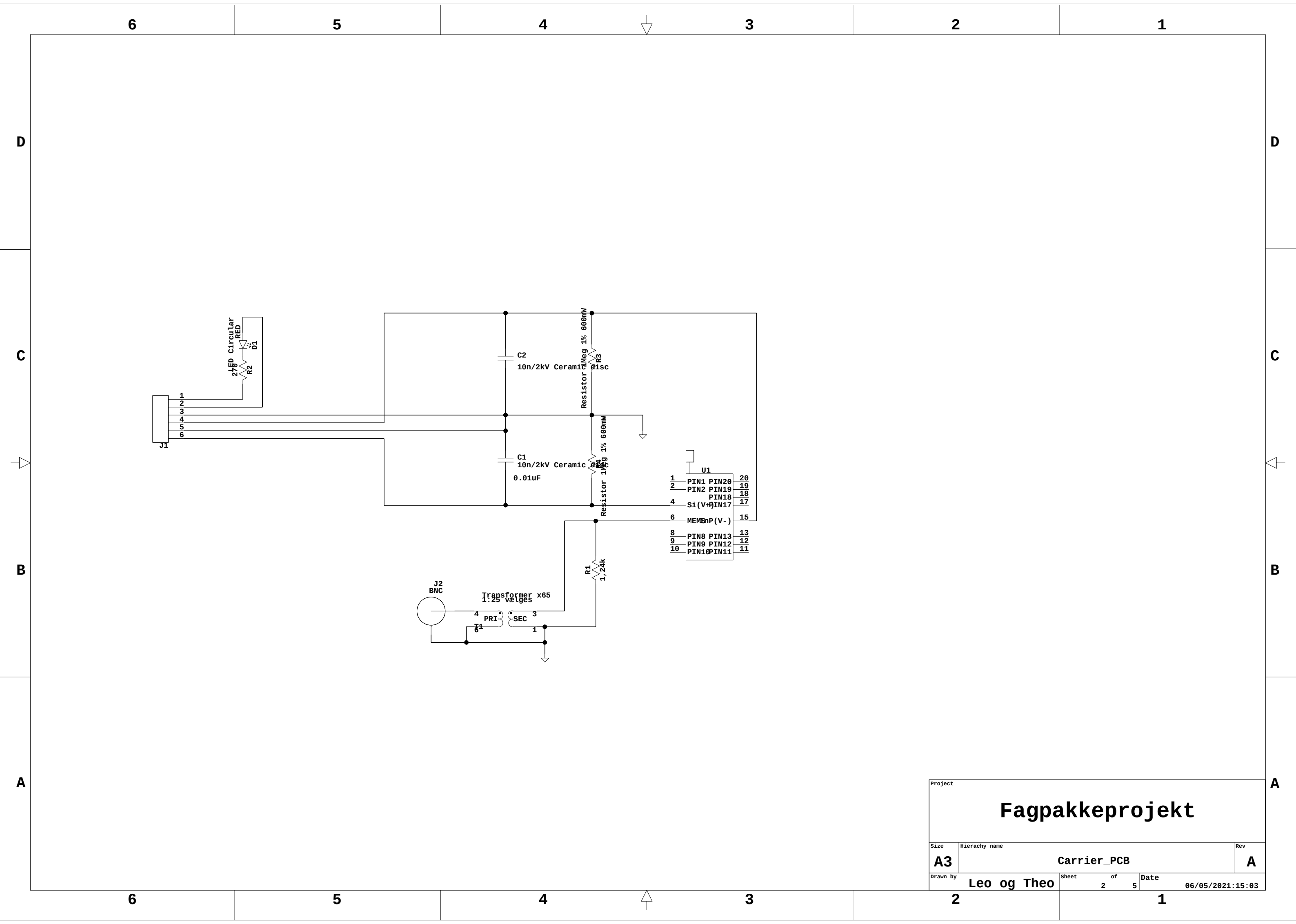
LED Circular
RED
D1
270
R2
J1
1
2
3
4
5
6
C2
10n/2kV Ceramic disc
Resistor 1Meg 1% 600mW
R3
C1
10n/2kV Ceramic disc
0.01uF
Resistor 1Meg 1% 600mW
R4
U1
PIN1
PIN2
Si(V+)
MEMS
PIN8
PIN9
PIN10
PIN20
PIN19
PIN18
PIN17
InP(V-)
PIN13
PIN12
PIN11
R1
1,24k
J2
BNC
Transformer x65
1:25 vælges
PRI
SEC
T1
Project
Fagpakkeprojekt
Size
A3
Hierachy name
Carrier_PCB
Rev
A
Drawn by
Leo og Theo
Sheet
2
of
5
Date
06/05/2021:15:03

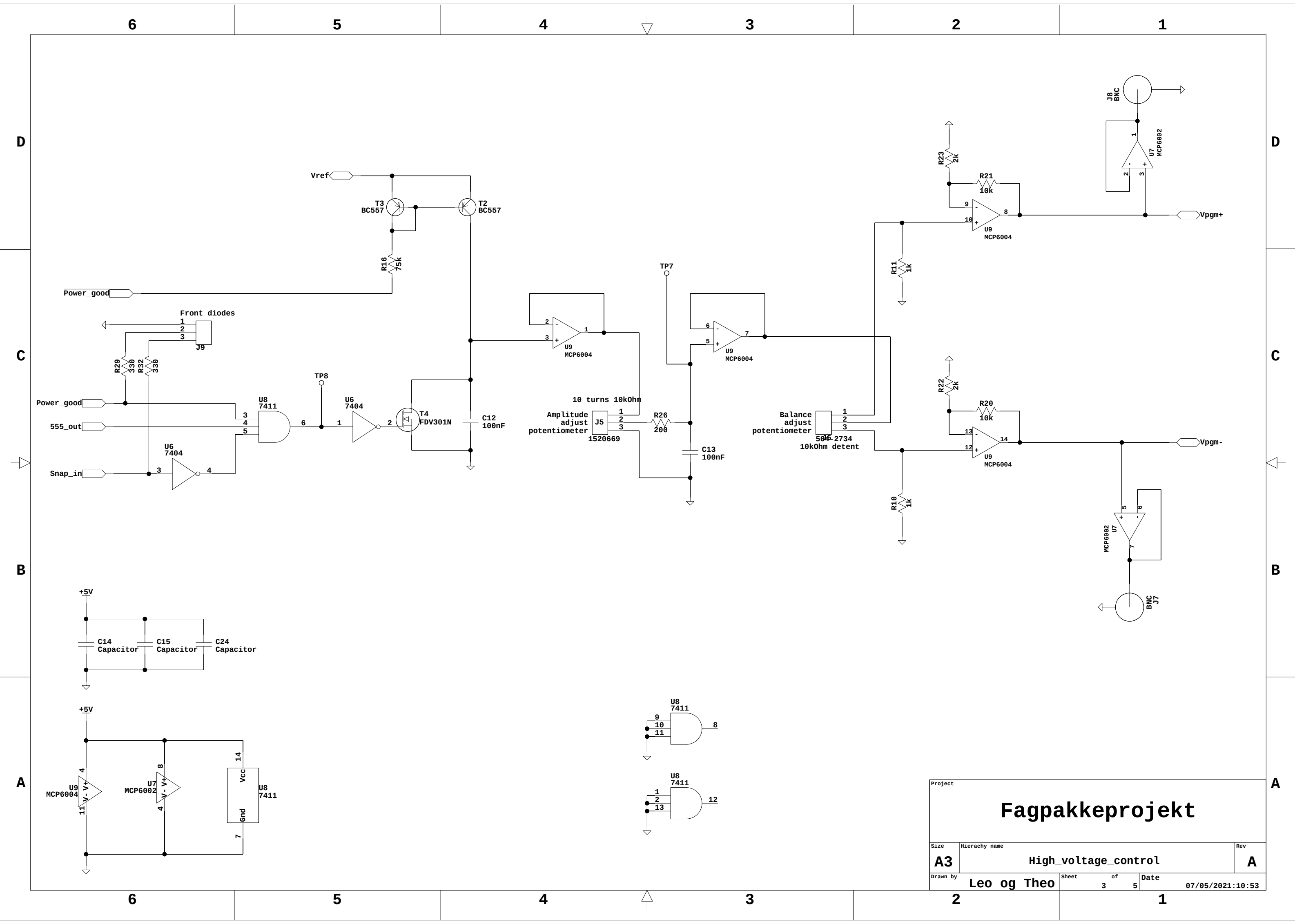

Vref
T3
BC557
T2
BC557
R16
75k
Power_good
Front diodes
1
2
3
J9
R29
330
R32
330
Power_good
555_out
Snap_in
U8
7411
U6
7404
TP8
U6
7404
T4
FDV301N
C12
100nF
U9
MCP6004
TP7
U9
MCP6004
10 turns 10kOhm
Amplitude
adjust
potentiometer
J5
1520669
R26
200
C13
100nF
Balance
adjust
potentiometer
500-2734
10kOhm detent
R23
2k
R21
10k
U9
MCP6004
R11
1k
Vpgm+
J8
BNC
U7
MCP6002
R22
2k
R20
10k
U9
MCP6004
R10
1k
Vpgm-
U7
MCP6002
BNC
J7
+5V
C14
Capacitor
C15
Capacitor
C24
Capacitor
+5V
U9
MCP6004
U7
MCP6002
Vcc
Gnd
U8
7411
U8
7411
U8
7411
Project
Fagpakkeprojekt
Size
A3
Hierachy name
High_voltage_control
Rev
A
Drawn by
Leo og Theo
Sheet
3
of
5
Date
07/05/2021:10:53

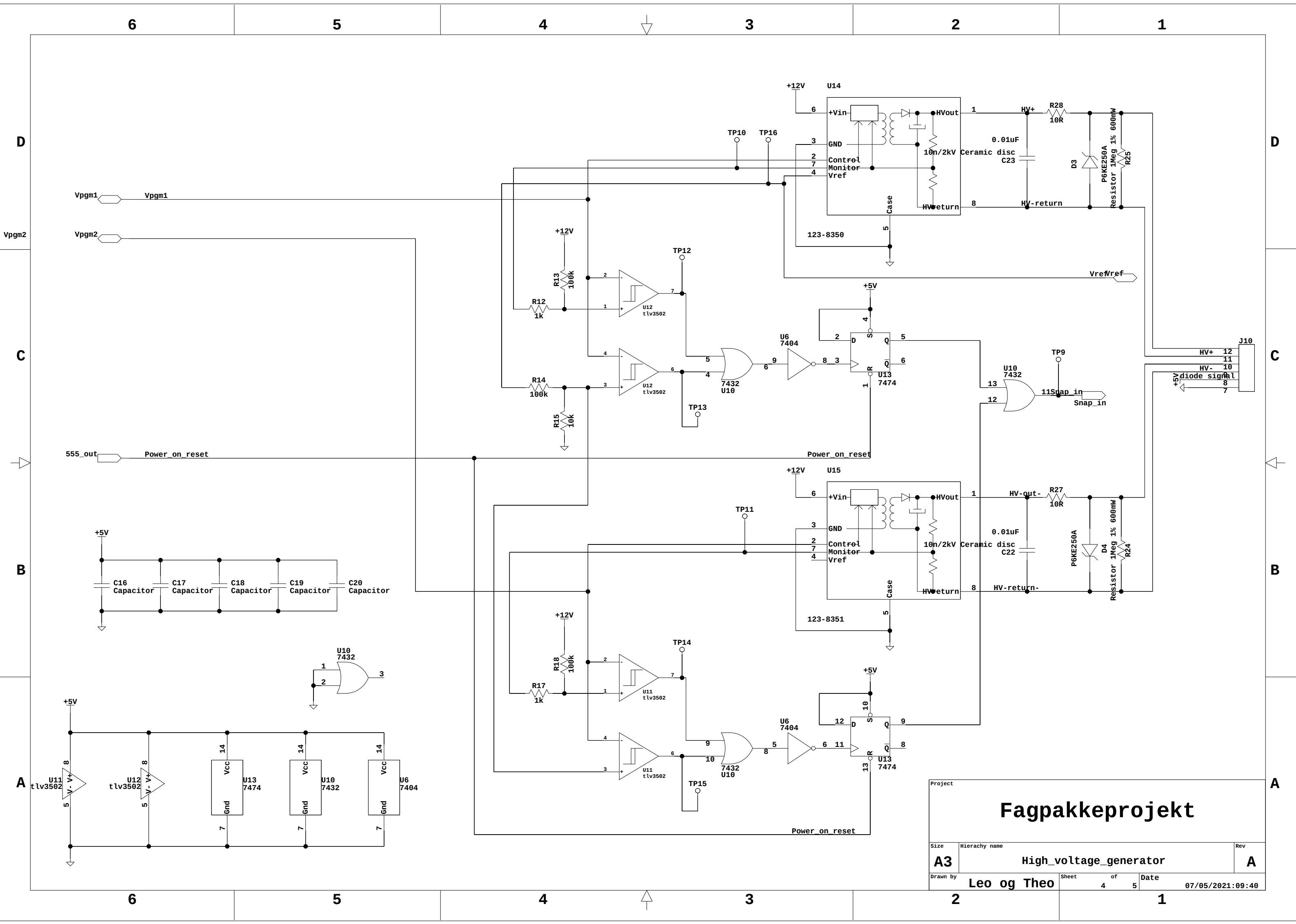

Fagpakkeprojekt
Size A3
Hierachy name High_voltage_generator
Rev A
Drawn by Leo og Theo
Sheet 4 of 5
Date 07/05/2021:09:40
U14
123-8350
U15
123-8351
Vpgm1
Vpgm2
555_out
Power_on_reset
Vref
Snap_in
HV+
HV-return
HV-out-
J10
diode signal
0.01uF
10n/2kV Ceramic disc
C23
C22
R28 10R
R27 10R
D3 P6KE250A
D4 P6KE250A
R25 Resistor 1Meg 1% 600mW
R24 Resistor 1Meg 1% 600mW
U12 tlv3502
U11 tlv3502
U10 7432
U6 7404
U13 7474
R12 1k
R13 100k
R14 100k
R15 10k
R17 1k
R18 100k
C16 Capacitor
C17 Capacitor
C18 Capacitor
C19 Capacitor
C20 Capacitor
TP9
TP10
TP11
TP12
TP13
TP14
TP15
TP16
+12V
+5V

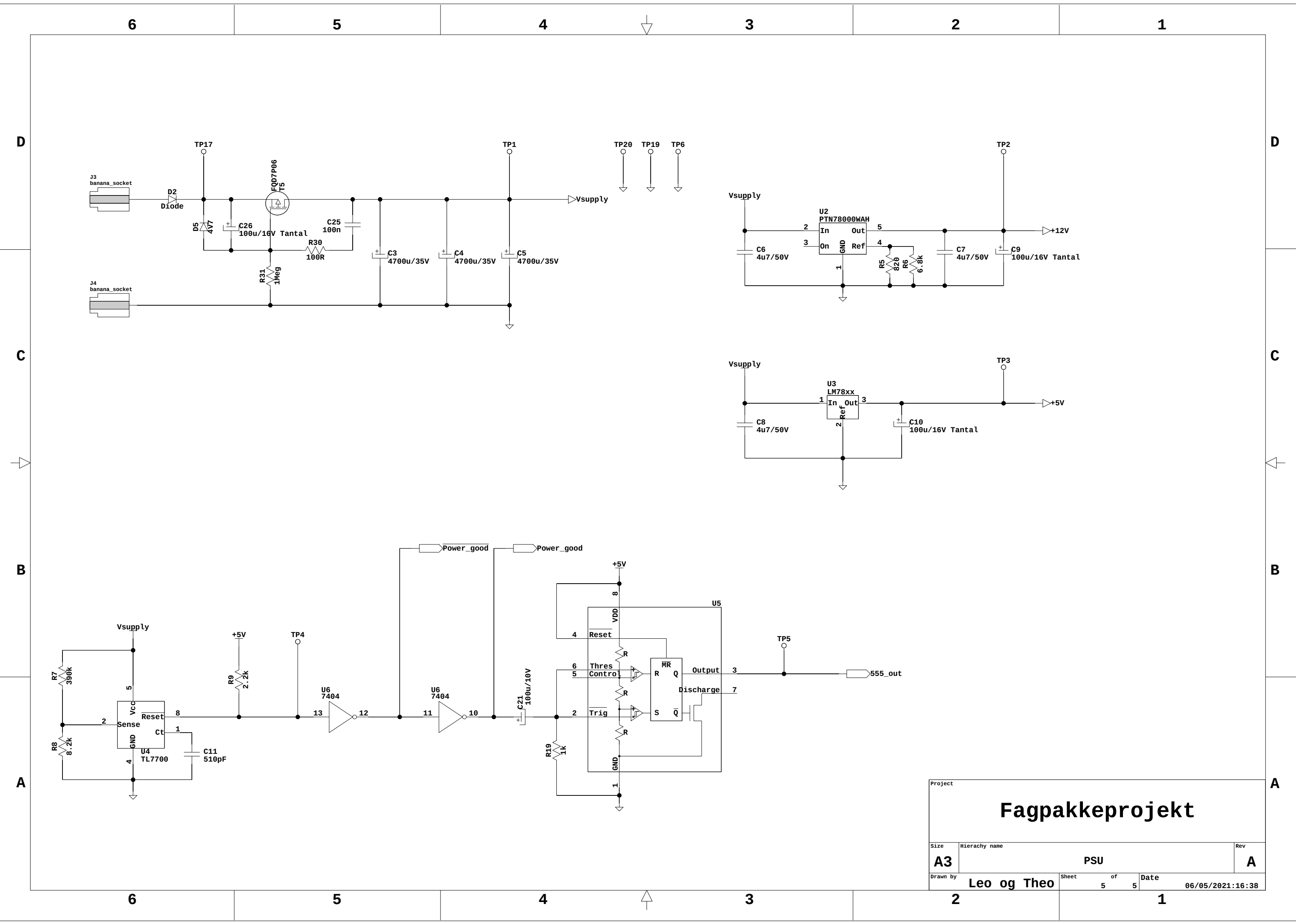

Project

Fagpakkeprojekt

Size	Hierachy name	Rev
A3	PSU	A

Drawn by	Sheet	of	Date
Leo og Theo	5	5	06/05/2021:16:38

A.5 Appendix 5

SERIES: CP07-M | DESCRIPTION: PELTIER MODULE

FEATURES

- micro size (less than 10 x 10 mm)
- wide ΔT max
- Qmax up to 1.9 W
- Au plating available, suitable for soldering
- precise temperature control
- solid state construction

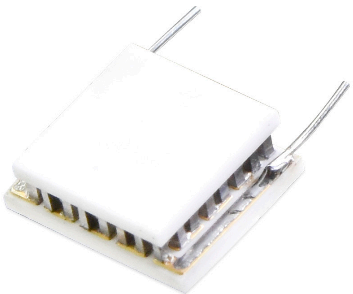

RoHS

MODEL

	input voltage[1] max (Vdc)	input current[2] max (A)	internal resistance[3] typ (Ω±10%)	output Qmax[4] T_h=27°C (W)	output Qmax[4] T_h=50°C (W)	output ΔTmax[5] T_h=27°C (°C)	output ΔTmax[5] T_h=50°C (°C)
CP0734-238	0.5	0.7	0.52	0.2	0.2	70	77
CP0734-277P[6]	0.5	0.7	0.52	0.2	0.2	70	77
CP073450-238	1.0	0.7	1.04	0.4	0.5	70	77
CP074933-238	1.3	0.7	1.43	0.6	0.7	70	77
CP074933-277P[6]	1.3	0.7	1.43	0.6	0.7	70	77
CP074965-239	2.1	0.7	2.35	0.9	1.0	70	77
CP074965-238P[6]	2.1	0.7	2.35	0.9	1.0	70	77
CP076581-238	3.9	0.7	4.17	1.7	1.9	70	77
CP076581-238P[6]	3.9	0.7	4.17	1.7	1.9	70	77

Notes:
1. Maximum voltage at ΔT max and T_h=27°C
2. Maximum current to achieve ΔT max
3. Measured by AC 4-terminal method at 25°C
4. Maximum heat absorbed at cold side occurs at I_{max}, V_{max}, and ΔT=0°C
5. Maximum temperature difference occurs at I_{max}, V_{max}, and Q=0W (ΔT max measured in a vacuum at 1.3 Pa)
6. Gold plating on both sides.

SOLDERABILITY[7]

parameter	conditions/description	min	typ	max	units
soldering to plates	soldering iron temperature			150	°C

Note: 7. Only for gold plated models. The solder that holds the peltier together melts at 235°C. Caution must taken to not leave the soldering iron in contact with the surface too long, or damage to the peltier could occur.

SPECIFICATIONS

parameter	conditions/description	min	typ	max	units
solder melting temperature	connection between thermoelectric pairs	235			°C
assembly compression				0.8	MPa
RoHS	yes				

MECHANICAL DRAWING

units: mm

	MATERIAL	PLATING
ceramic plate	96% AL_2O_3	
wire leads	Ø0.25-0.3 mm annealed copper	tin
sealer	no sealing	
ceramic surface	Au plating on select models	

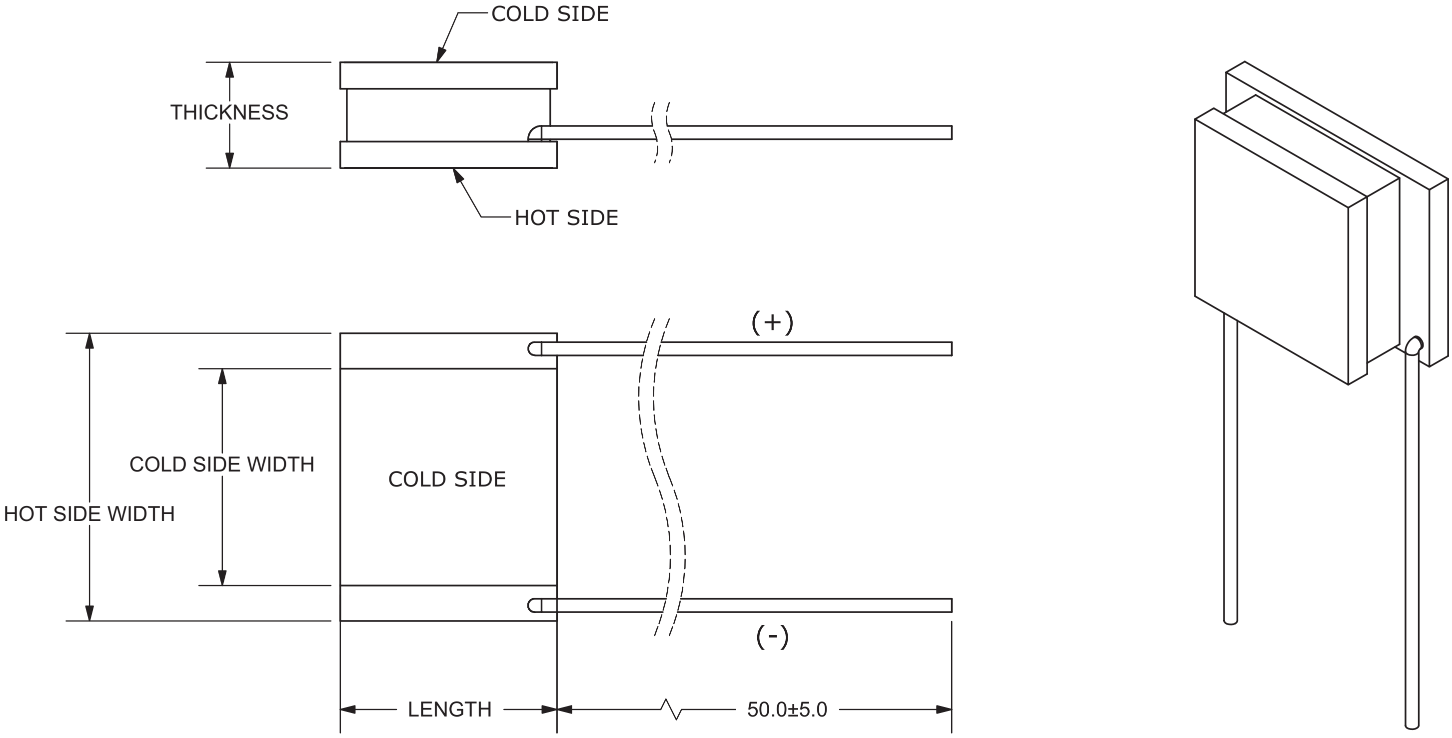

MODEL NO.	LENGTH (mm)	HOT SIDE WIDTH (mm)	COLD SIDE WIDTH (mm)	THICKNESS (mm)	GOLD PLATING HOT/ COLD SIDES
CP0734-238	3.4 ±0.3	3.4 ±0.3	1.8 ±0.3	2.38 ±0.15	NO
CP0734-277P	3.4 ±0.3	3.4 ±0.3	1.8 ±0.3	2.77 ±0.15	YES
CP073450-238	3.4 ±0.3	5.0 ±0.3	3.4 ±0.3	2.38 ±0.15	NO
CP074933-238	4.9 ±0.3	3.3 ±0.3	3.3 ±0.3	2.38 ±0.15	NO
CP074933-277P	4.9 ±0.3	3.3 ±0.3	3.3 ±0.3	2.77 ±0.15	YES
CP074965-239	4.9 ±0.3	6.5 ±0.3	4.9 ±0.3	2.38 ±0.15	NO
CP074965-238P	4.9 ±0.3	6.5 ±0.3	4.9 ±0.3	2.77 ±0.15	YES
CP076581-238	6.5 ±0.3	8.1 ±0.3	6.5 ±0.3	2.38 ±0.15	NO
CP076581-238P	6.5 ±0.3	8.1 ±0.3	6.5±0.3	2.77 ±0.15	YES

CP0734-238 PERFORMANCE (Th=27°C)

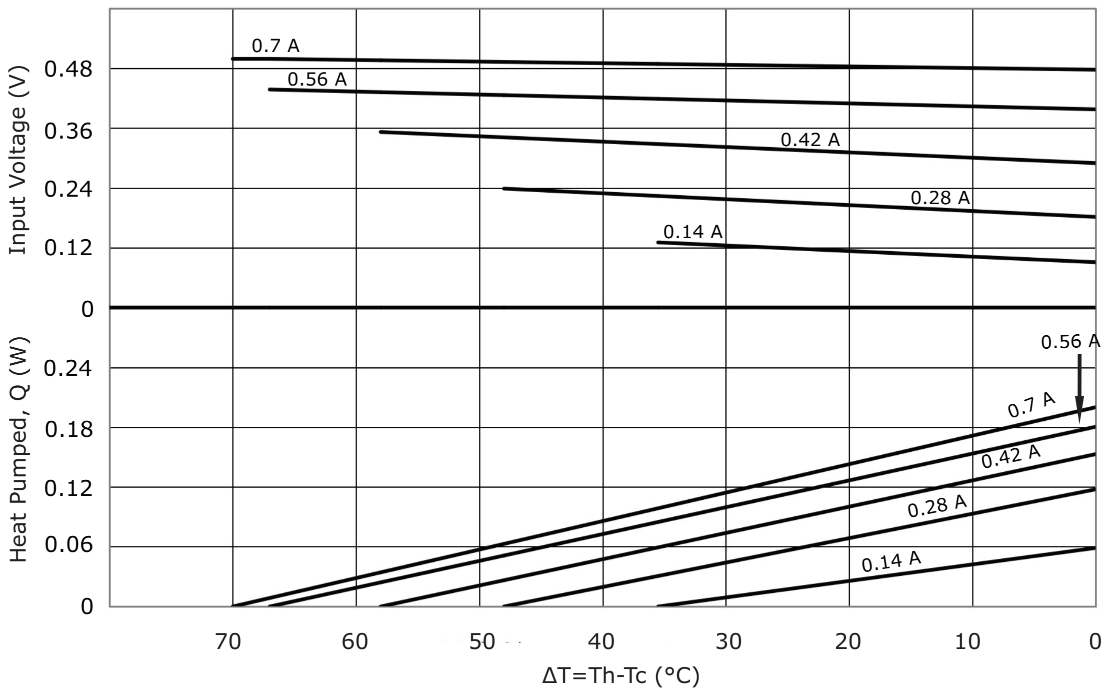

CP0734-238 PERFORMANCE (Th=50°C)

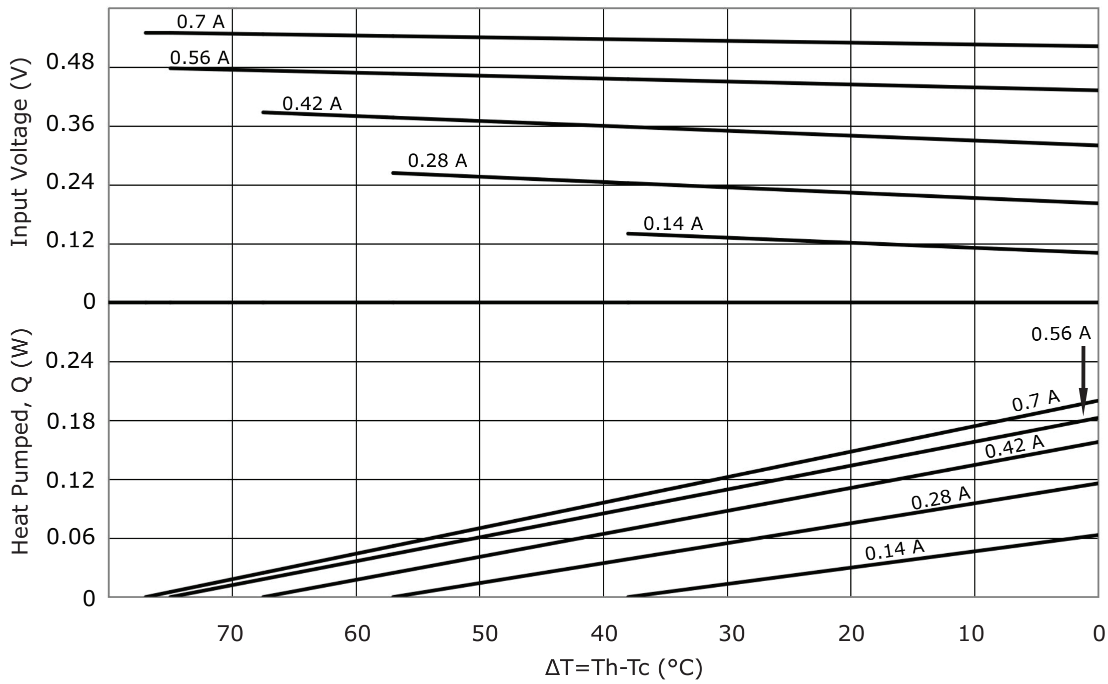

CP0734-277P PERFORMANCE (Th=27°C)

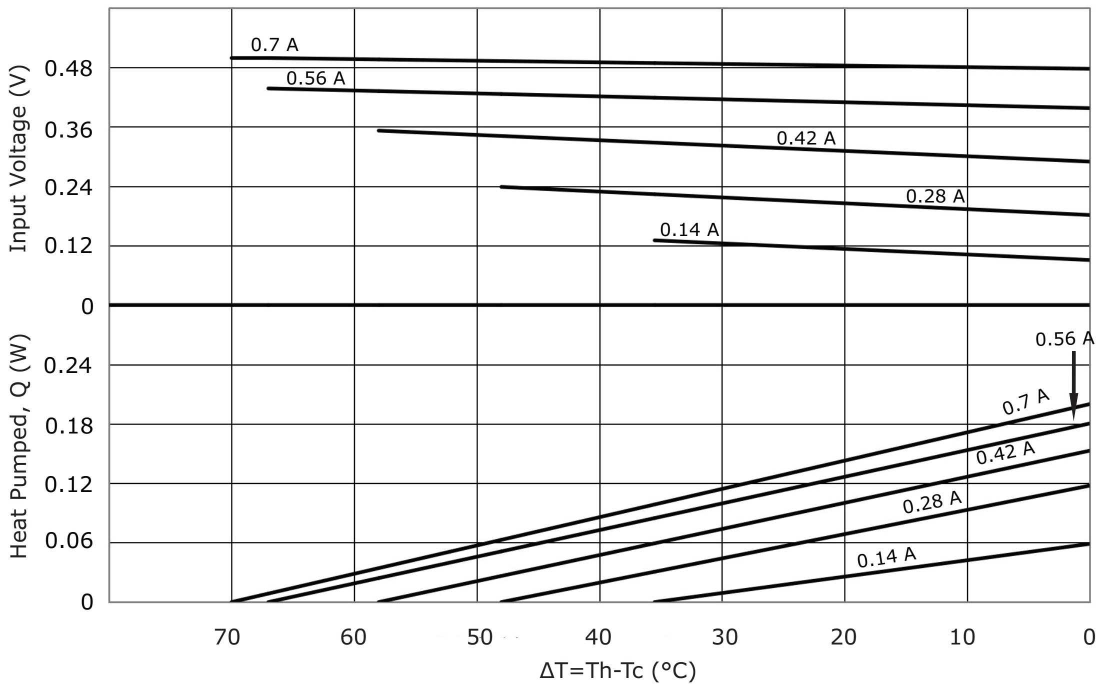

CP0734-277P PERFORMANCE (Th=50°C)

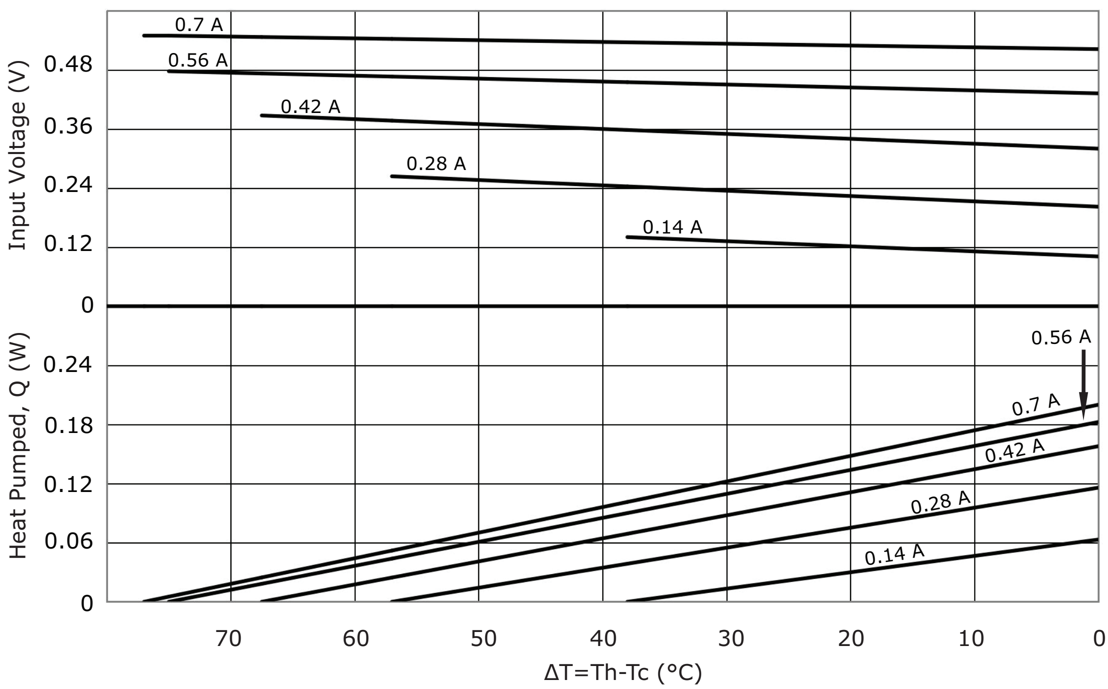

CP073450-238 PERFORMANCE (Th=27°C)

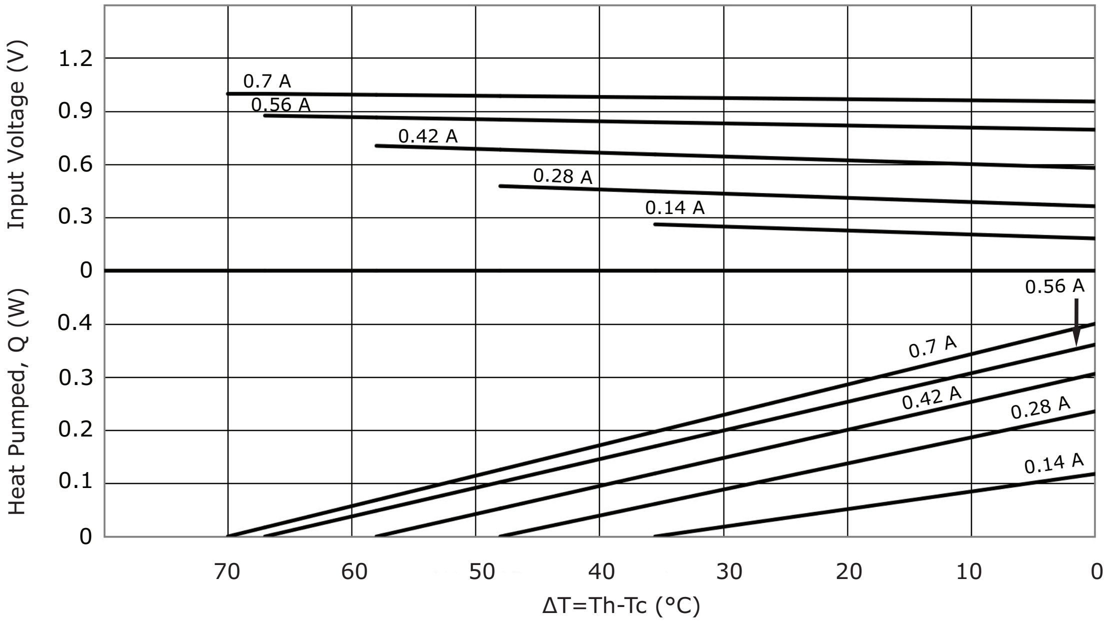

CP073450-238 PERFORMANCE (Th=50°C)

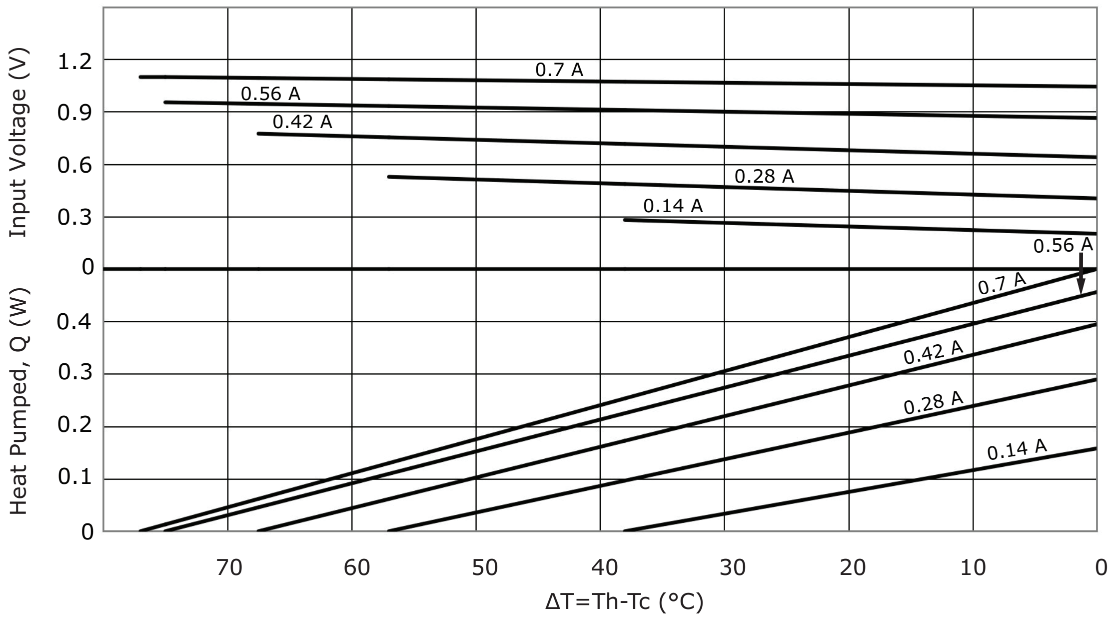

CP074933-238 PERFORMANCE (Th=27°C)

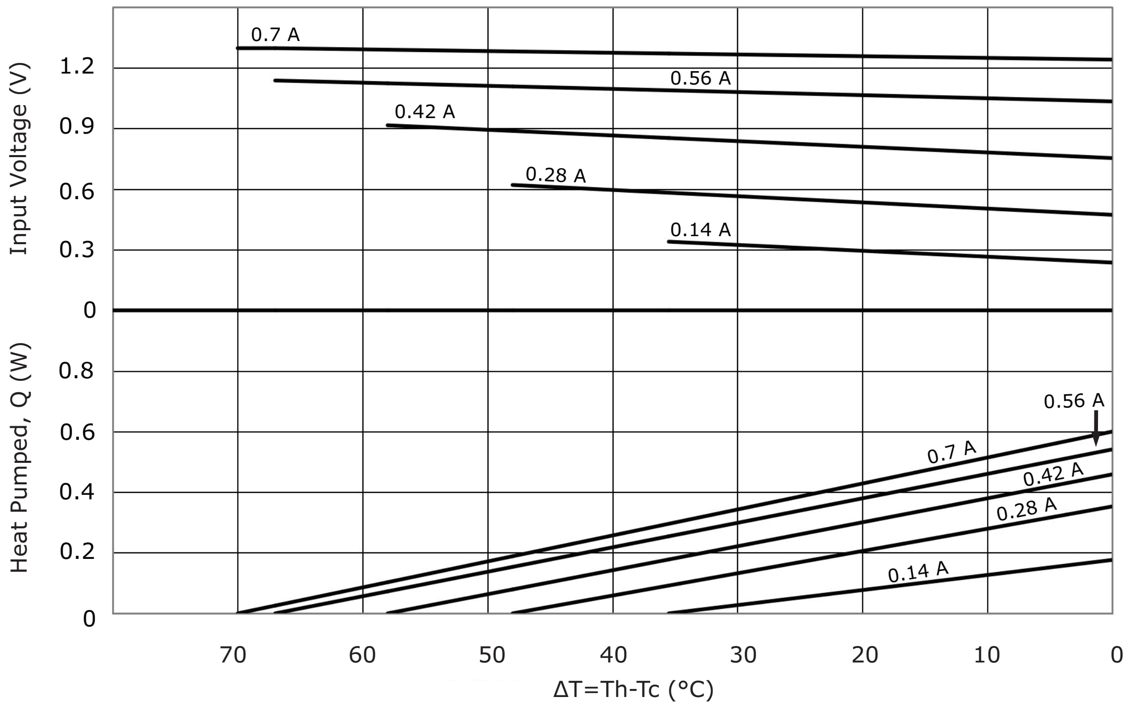

CP074933-238 PERFORMANCE (Th=50°C)

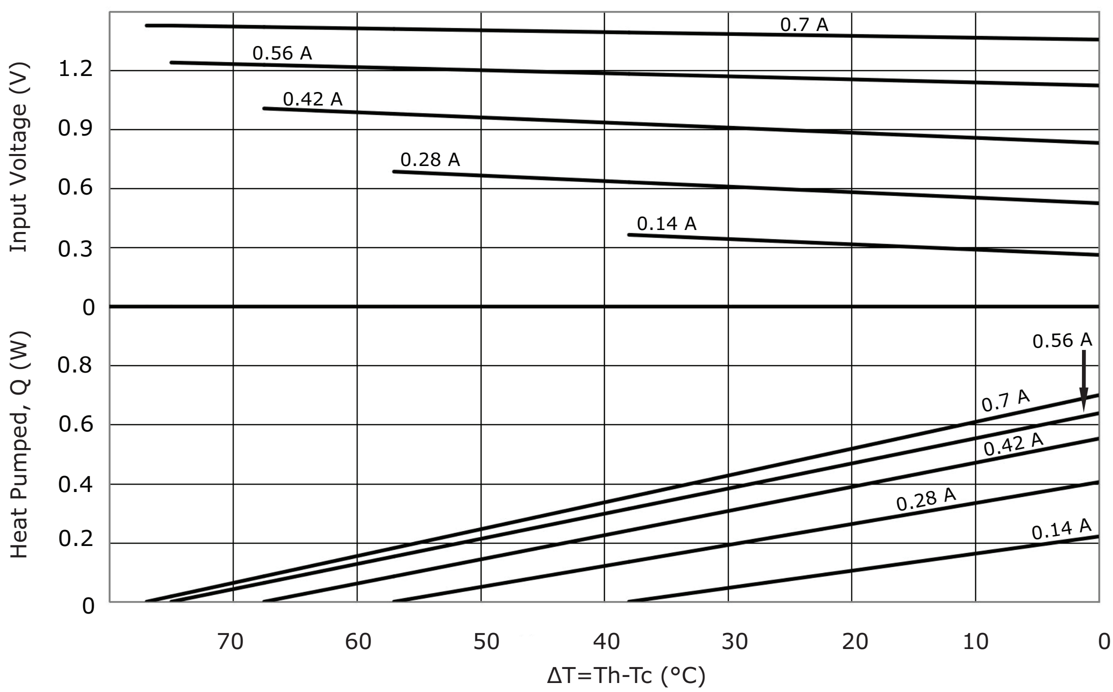

CP074933-277P PERFORMANCE (Th=27°C)

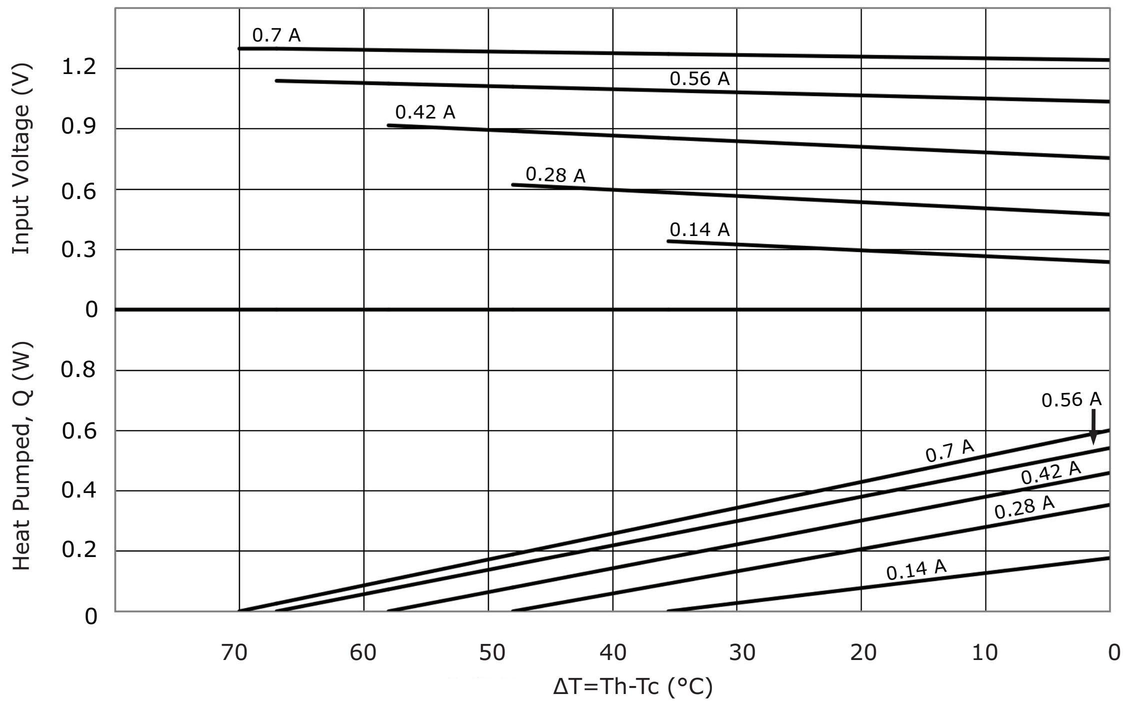

CP074933-277P PERFORMANCE (Th=50°C)

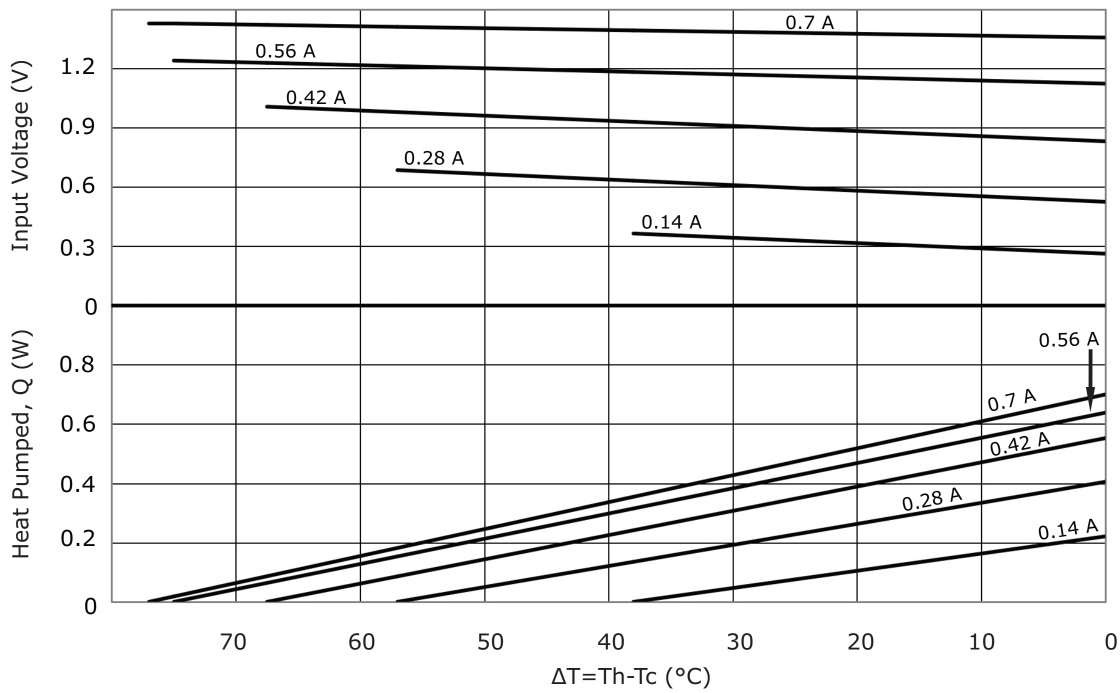

CP074965-239 PERFORMANCE (Th=27°C)

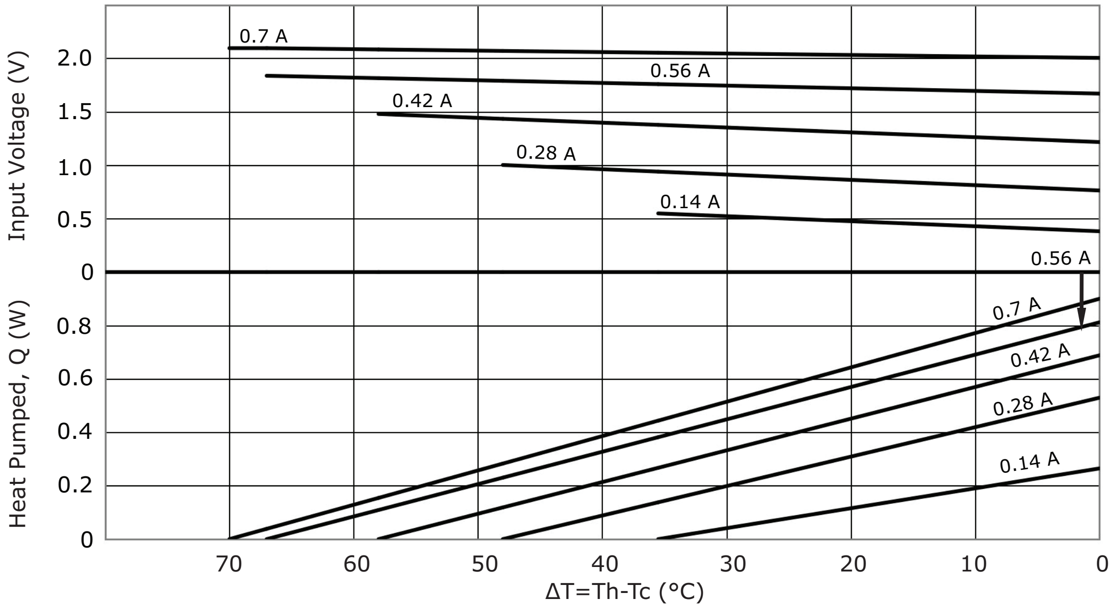

CP074965-239 PERFORMANCE (Th=50°C)

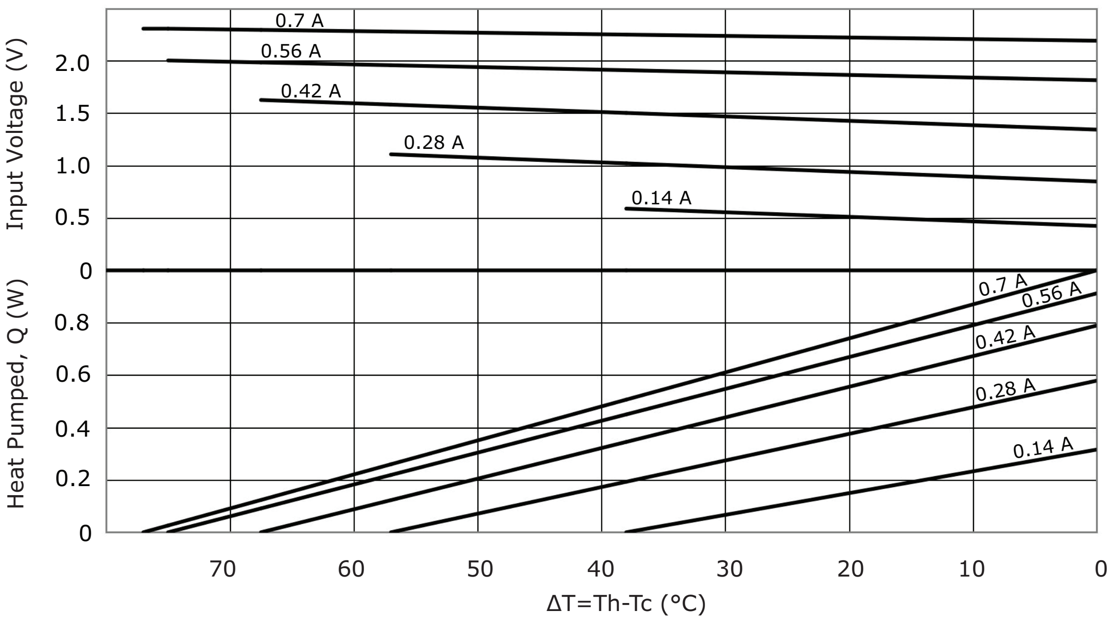

CP074965-238P PERFORMANCE (Th=27°C)

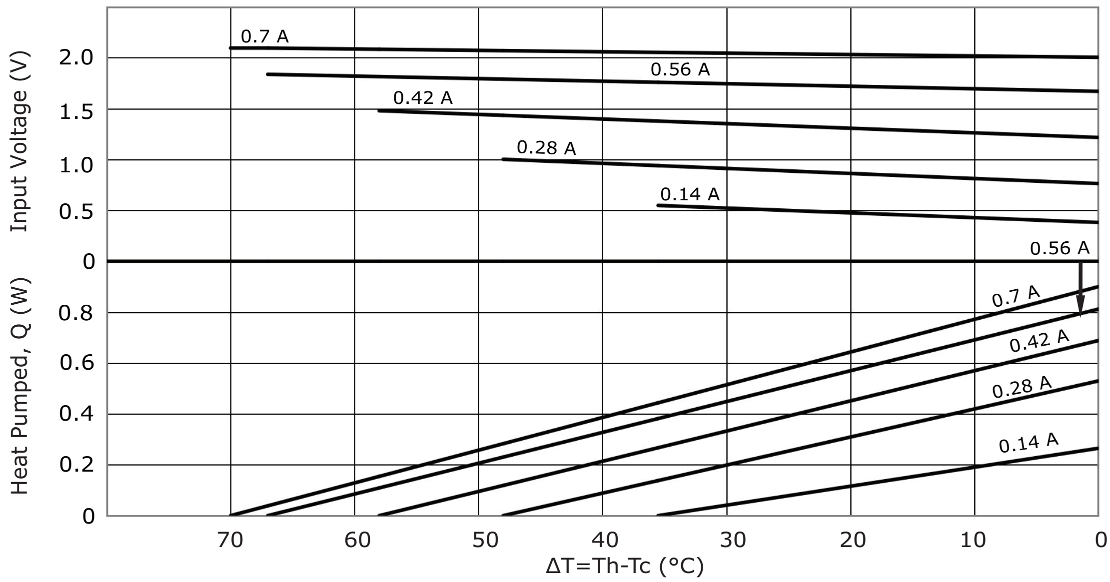

CP074965-238P PERFORMANCE (Th=50°C)

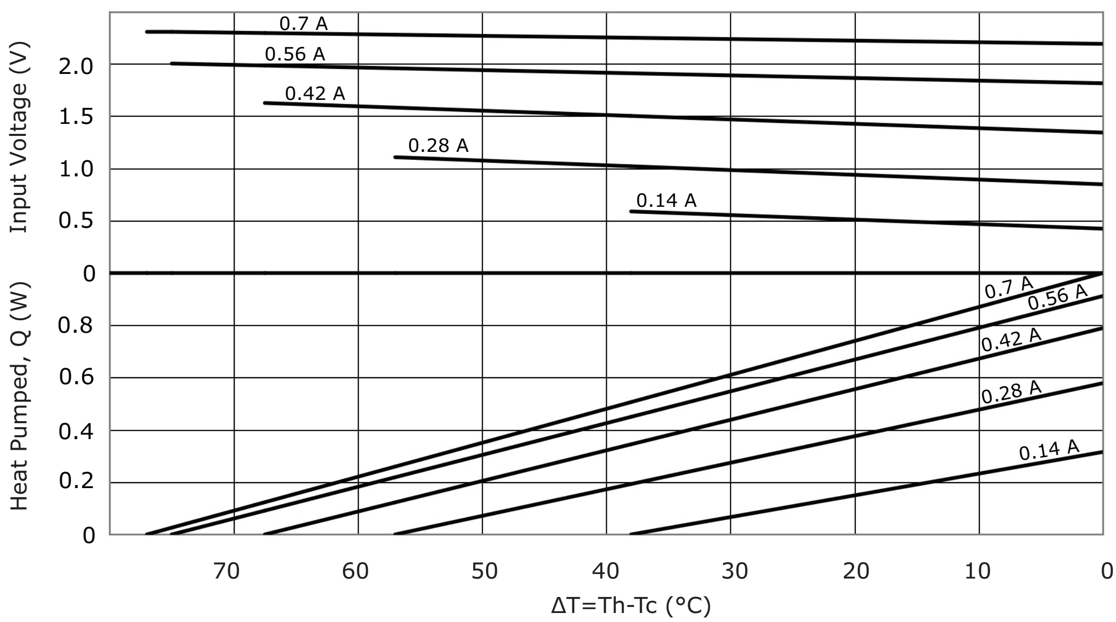

CP076581-238 PERFORMANCE (Th=27°C)

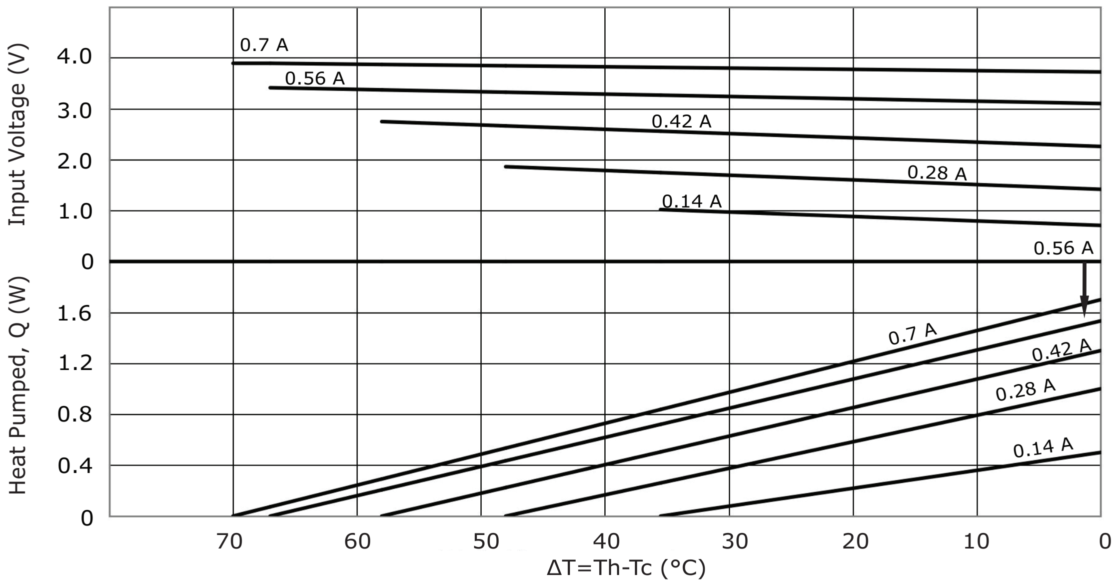

CP076581-238 PERFORMANCE (Th=50°C)

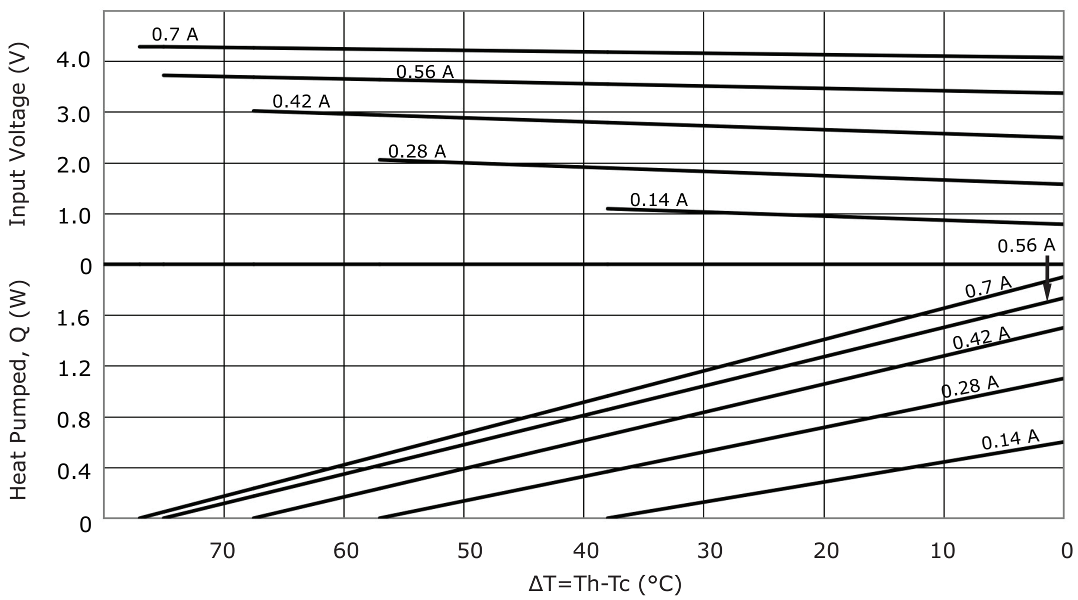

CP076581-238P PERFORMANCE (Th=27°C)

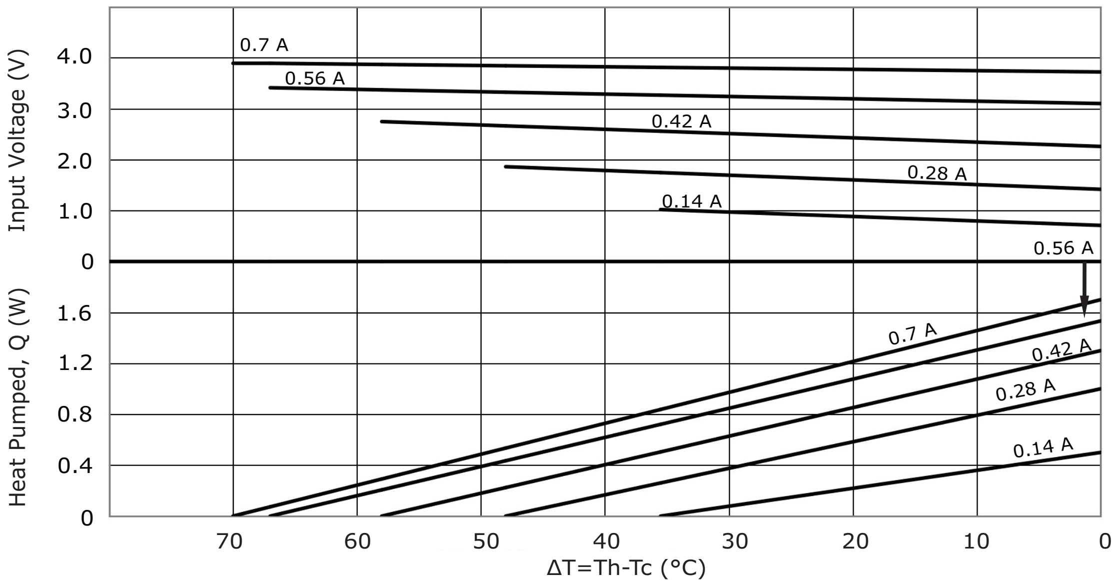

CP076581-238P PERFORMANCE (Th=50°C)

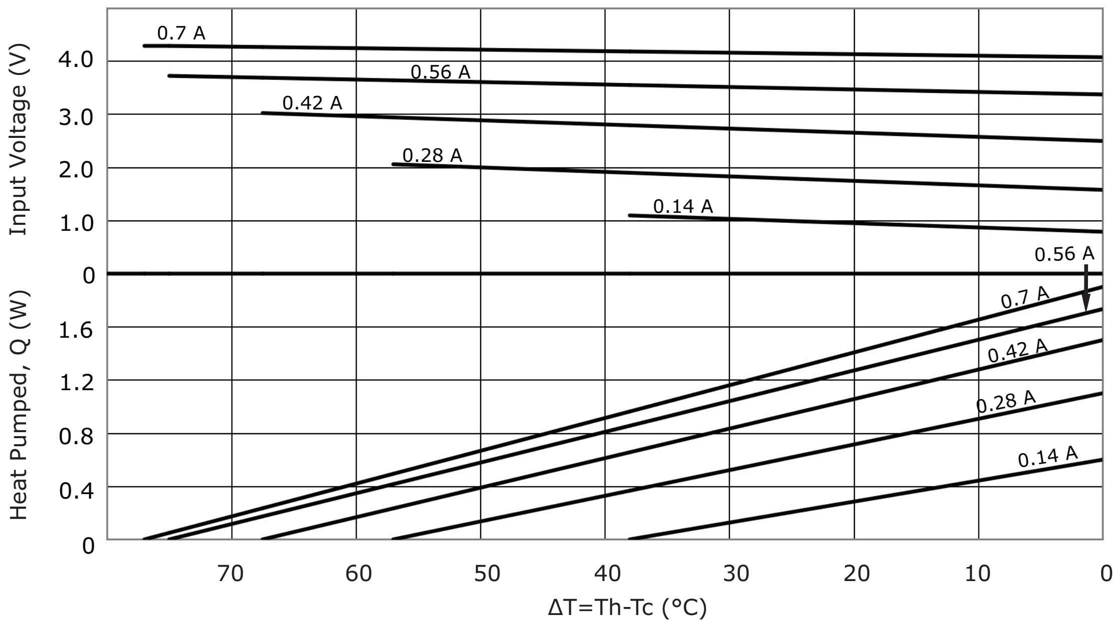

REVISION HISTORY

rev.	description	date
1.0	initial release	07/08/2020
1.01	logo, datasheet style update	08/05/2022

The revision history provided is for informational purposes only and is believed to be accurate.

A.6 Appendix 6

EPO-TEK® H20E

Technical Data Sheet
For Reference Only
Electrically Conductive, Silver Epoxy

Date:	February 2021	
Rev:	XVIII	
No. of Components:	Two	
Mix Ratio by Weight:	1 : 1	
Specific Gravity:	Part A: 2.03 Part B: 3.07 Syringe: 2.67	
Pot Life:	2.5 Days	
Shelf Life- Bulk:	One year at room temperature	
Shelf Life- Syringe:	One year at -40°C	

Recommended Cure: 150°C / 1 Hour

Minimum Alternative Cure(s):
May not achieve performance properties below
150°C / 5 Minutes
120°C / 15 Minutes
80°C / 3 Hours

NOTES:
- Container(s) should be kept closed when not in use.
- Filled systems should be stirred thoroughly before mixing and prior to use.
- Performance properties (rheology, conductivity, others) of the product may vary from those stated on the data sheet when bi-pak/syringe packaging or post-processing of any kind is performed. Epoxy's warranties shall not apply to any products that have been reprocessed or repackaged from Epoxy's delivered status/container into any other containers of any kind, including but not limited to syringes, bi-paks, cartridges, pouches, tubes, capsules, films or other packages.

Product Description: EPO-TEK® H20E is a two component, 100% solids silver-filled epoxy system designed specifically for chip bonding in microelectronic and optoelectronic applications. It is also used extensively for thermal management applications due to its high thermal conductivity. It has proven itself to be extremely reliable over many years of service and is still the conductive adhesive of choice for new applications. Also available in a single component frozen syringe.

Typical Properties: Cure condition: 150°C / 1 Hour Different batches, conditions & applications yield differing results. Data below is not guaranteed. To be used as a guide only, not as a specification. * denotes test on lot acceptance basis

PHYSICAL PROPERTIES:				
* Color (before cure):		Part A: Silver	Part B: Silver	
* Consistency:		Smooth thixotropic paste		
* Viscosity (23°C) @ 100 rpm:		2,200 - 3,200	cPs	
Thixotropic Index:		4.6		
* Glass Transition Temp:		≥ 80	°C (Dynamic Cure: 20-200°C/ISO 25 Min; Ramp -10-200°C @20°C/Min)	
Coefficient of Thermal Expansion (CTE):				
	Below Tg:	31	$x\ 10^{-6}$ in/in°C	
	Above Tg:	158	$x\ 10^{-6}$ in/in°C	
Shore D Hardness:		75		
Lap Shear @ 23°C:		1,475	psi	
Die Shear @ 23°C:		≥ 10	Kg	3,556 psi
Degradation Temp:		425	°C	
Weight Loss:				
	@ 200°C:	0.59	%	
	@ 250°C:	1.09	%	
	@ 300°C:	1.67	%	
Suggested Operating Temperature:		< 300	°C (Intermittent)	
Storage Modulus:		808,700	psi	
Ion Content	Cl^-:	73 ppm	Na^+:	2 ppm
	NH_4^+:	98 ppm	K^+:	3 ppm
* Particle Size:		≤ 45	microns	

ELECTRICAL AND THERMAL PROPERTIES:		
Thermal Conductivity:	2.5	W/mK *based on standard method: Laser Flash*
Thermal Conductivity:	29	W/mK *based on Thermal Resistance Data:* $R = L \times K^{-1} \times A^{-1})$
Thermal Resistance (Junction to Case):		TO-18 package with nickel-gold metallized 20 x 20 mil chips and bonded with H20E (2mils thick) *EPO-TEK® H20E*: 6.7 to 7.0°C/W *Solder:* 4.0 to 5.0°C/W
* Volume Resistivity @ 23°C:	≤ 0.0004	Ohm-cm

Epoxies and Adhesives for Demanding Applications™

EPOXY TECHNOLOGY, INC.
14 FORTUNE DRIVE, BILLERICA, MA 01821 (978) 667-3805, FAX (978) 663-9782
www.epotek.com

A Meridian Adhesives Group Company

EPO-TEK® H20E

Technical Data Sheet
For Reference Only
Electrically Conductive, Silver Epoxy

EPO-TEK® H20E Suggested Applications

- **Semiconductor IC Packaging**
  - Die-attaching chips to leadframes; compatible with Si and MEM's chips, 260ºC lead-free reflow and JEDEC Level I packaging requirements.
  - Capable of being snap cured in-line, as well as traditional box oven techniques.
  - Adhesive for solderless flip chip packaging and ultra fine pitch SMD printing.
- **Hybrid Micro-electronics**
  - A comparable alternative to solder and eutectic die attach, in terms of thermal peformance; very commonly no more than 1-2ºC/watt difference in thermal resistance.
  - Die-attaching of quartz crystal oscillators (QCO) to the Au posts of TO-can style lead-frame.
  - Used with GaAs chips for microwave/radar applications up to 77GHz.
  - SMD attach adhesive which can be cured simultaneously with die-attach processes.
    - Compatible with Au, Ag, Ag-Pd terminations of capacitors and resistor SMDs.
  - NASA approved low outgassing adhesive.
  - Adhesive for EMI and Rf shielding of Rf, microwave and IR devices.
- **Electronic & PCB Circuit Assembly**
  - Used to make electrical contacts in acoustical applications of speakers/microphones.
  - Electrical connection of piezo's to PCB. Pads of PZT are connected to many kinds of circuits using H20E, including ink jet heads, MEMs and ultrasound devices.
  - Automotive applications include pressure sensing and accelerometer circuits.
  - Electrically conductive adhesive (ECA) for connections of circuits to Cu coils in Rf antenna applications such as smart cards and RFID tags.
  - ECA for attaching SMDs to membrane switch flex circuits. Compatible with Ag-PTF and carbon graphite PCB pads. A low temperature "solder free" solution.
  - Solar-Photovoltaic industry
    - ECA for the electrical connection of transparent conductive oxide (TCO) to PCB pads.
    - Replacement of solder joints of Cu/Sn ribbon wire, from cell-to-cell; a common "solar cell stringing" adhesive.
    - Die-attach of III-V semiconductor chips to substrates used in solar concentrator technology, such as CdTe and GaAs.
    - An effective heat-sink on thermal substrates using Cu, BeO, aluminum nitride, etc.
    - Ability to be dispensed in high volumes via dots, arrays, and writing methods.
- **Opto-Electronic Packaging Applications**
  - Adhesive for fiber optic components using DIP, Butterfly or custom hybrid IC packages. As an ECA, it attaches waveguides, die bonds laser diodes and heat sinks the high power laser circuits.
  - Die-attaching IR-detector chips onto PCBs or TO-can style headers.
  - Die-attaching LED chips to substrates using single chip packages, or arrays.
    - Adhesion to Ag, Au and Cu plated leadframes and PCBs.
  - Electrical connection of ITO to PCBs found in LCD industry.
    - A low temp ECA for OLED displays and organically printable electronics.

EPO-TEK® H20E Advantages & Application Notes:

Processing Info: It can be applied by many dispensing, stamping, and screen printing techniques.
- Dispensing: Compatible with pressure/time delivery, auger screws, fluid jetting and G27 needles, in a single-component fashion.
- Screen Printing: Best using >200 metal mesh, with polymer squeegee blade with 80D hardness.
- Stamping: Small dots 6 mil in diameter can be realized.

Misc/Other Notes:
- Many technical papers written over 30-40 year lifetime. Contact techserv@epotek.com
- Over 1 trillion chips attached at a single company: no failures, Six Sigma and Certified Parts Supplier award winner.
- Versatility in curing techniques including box oven, SMT style tunnel oven, heater gun, hot plate, IR, convection, or inductor coil.
- Many custom modified products available, for the following improvements: viscosity and appearance, flexibility and thermal conductivity. Contact techserv@epotek.com for your best recommendation.

EPOXY TECHNOLOGY, INC.
14 FORTUNE DRIVE, BILLERICA, MA 01821 (978) 667-3805, FAX (978) 663-9782
www.epotek.com
A Meridian Adhesives Group Company

A.7 Appendix 7

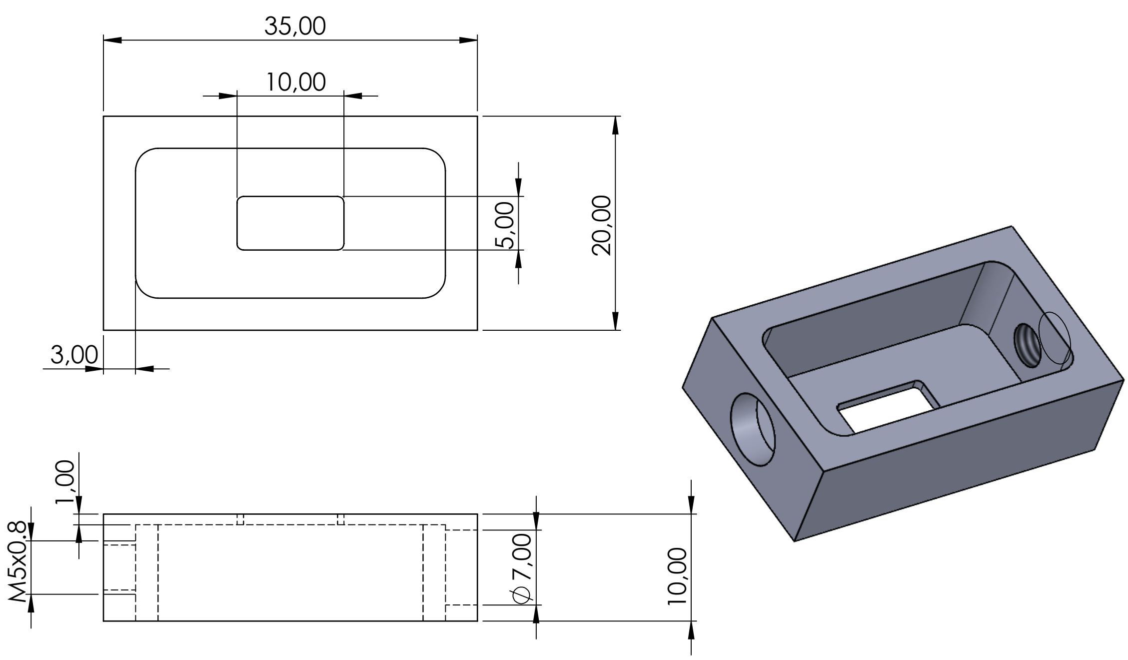

O:\Public\workshop\Martin\Solidworks\2022\Fotonik\Arnhold\

Title:	Chamber v2
Material:	POM
Date:	25. august 2022

Mechanical Workshop

Made By:	**Martin Nielsen**

A.8 Appendix 8

Nanometrics RPM

Date	: December 10, 2020 11:21:27	Operator	: hikus
Wafer ID	: Chalmers_DBR_2020	Batch ID	:
Material	: Au	Thickness	: 500 µm
Filename	: c:\nanometrics\rpm\data\hikus\chalmers_dbr_2020.spl		
Description	: Mirror Chalmers 2020		
Recipe	:		
Calibration	: G150InGaAs_Refl_2020.cal		

Scan parameters		Wavelength settings		Analysis Parameters	
Radius	: 0.0 mm	Center	: N/A	Half Power	: 0.500
Angle	: 0.0 deg	Range	: 900.0 to 1750.0 nm	Side Peak	: 0.900
Scan rate	: 60 pts/s	Resolution	: 1.06 nm/pixel (820)	F-P dip Thresh.	: 0.800
Temperature	: 24.5 C	Slit width	: 0.100 mm	Noise Thresh.	: 0.050
Smoothed	: No	Grating	: 150g/mm-1250		
		Detector	: InGaAs		
		Gain	: x1 (corr.)		
		Filter	: None		

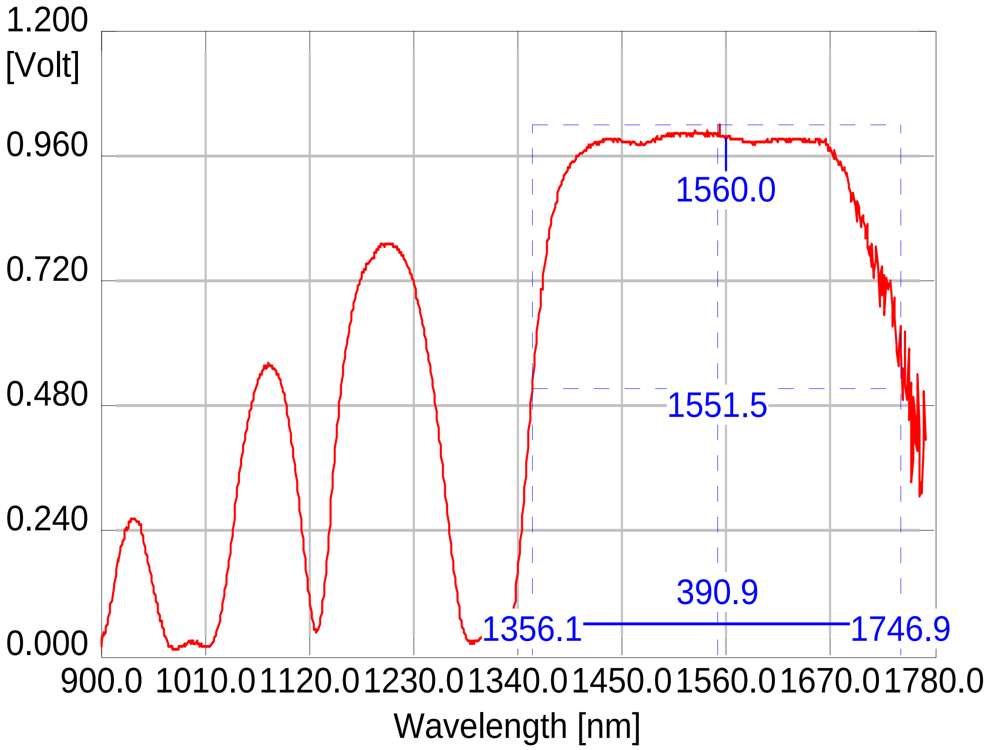

Results

SB min	: 1356.1 nm
SB max	: 1746.9 nm
SB center	: 1551.5 nm
SB width	: 390.9 nm
SB height	: 1.015 Volt
F-P dip	: 1560.0 nm
F-P height	: 97.6 % (1.015 Volt)
F-P width	: 3.3 nm

A.9 Appendix 9

Linear temperature controller

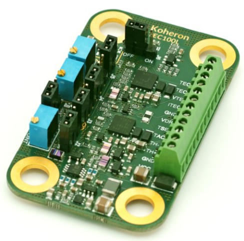

Koheron TEC100L is a compact, high stability temperature controller. It features a high-precision analog front-end, adjustable PID gains and can drive up to 1 A current.

Specifications

	TEC100L-50
Current	-1.15 A to 1.15 A
Adjustment range	5 kΩ to 20 kΩ (40°C to 10°C)
Supply voltage	4.5 V to 5.5 V, nom. 5 V
Supply current	1.3 A
Compliance voltage at 1 A	-4.5 V to 4.5 V
Temperature coefficient	0.002 °C/°C
24h stability	0.005 °C
Quiescent current	3 mA
Operating temperature	0 °C to 50 °C
Outside dimensions	63 mm x 38 mm x 12 mm
Weight	18 g

Stability

The figure below shows the variation of the thermistor resistance stabilized at 26.5 °C during 24 hours at 25 °C ambient temperature. Thermistor resistance drift is less than 1 Ω (temperature drift < 2 mK).

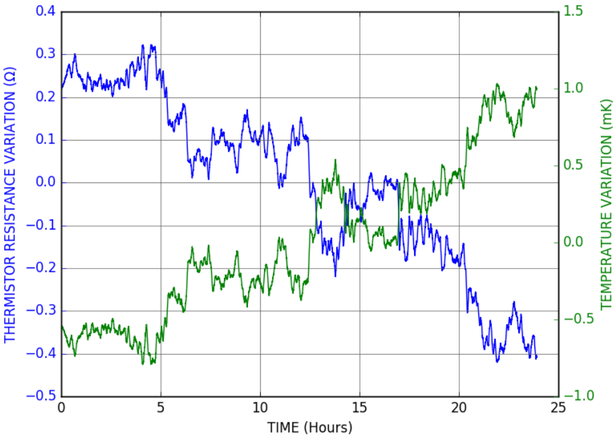

Because of the non-linear relationship between the temperature and the thermistor resistance, the temperature stability depends on the temperature setpoint.

Ordering codes

REFERENCE	ATTRIBUTE
TEC100L-50	

A.10 Appendix 10

Wirewound Resistors, Industrial, Precision Power, Silicone Coated, Axial Lead

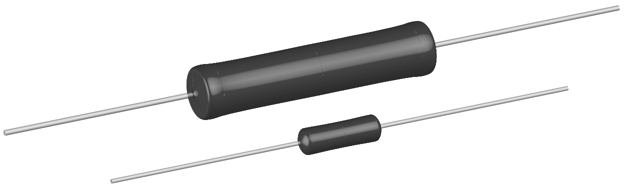

Note

* This datasheet provides information about parts that are RoHS-compliant and/or parts that are non-RoHS-compliant. For example, parts with lead (Pb) terminations are not RoHS-compliant. Please see the information/tables in this datasheet for details.

FEATURES

- High temperature coating (> 350 °C)
- Complete welded construction
- Meets applicable requirements of MIL-PRF-26
- Available in non-inductive styles (type NS) with Ayrton-Perry winding for lowest reactive components
- Excellent stability in operation (typical resistance shift < 0.5 %)
- MIL-PRF-26 qualified, type RW resistors can be found at: www.vishay.com/doc?30281
- Material categorization: For definitions of compliance please see www.vishay.com/doc?99912

Pb-free Available

e3

RoHS* Available

HALOGEN FREE Available

GREEN (5-2008) Available

STANDARD ELECTRICAL SPECIFICATIONS

GLOBAL MODEL	HIST. MODEL	POWER RATING (1) $P_{25\,°C}$ W U ± 0.05 % to ± 5 %	POWER RATING (1) $P_{25\,°C}$ W V ± 3 % to ± 10 %	RESISTANCE RANGE Ω ± 0.05 %	RESISTANCE RANGE Ω ± 0.1 %	RESISTANCE RANGE Ω ± 0.25 %	RESISTANCE RANGE Ω ± 0.5 %, ± 1 %	RESISTANCE RANGE Ω ± 3 %, ± 5 %, ± 10 %	WEIGHT (typical) g
RS1/4	RS-1/4	0.4	-	1 to 1K	0.499 to 1K	0.499 to 3.4K	0.1 to 3.4K	0.1 to 3.4K	0.21
RS1/2	RS-1/2	0.75	-	1 to 1.3K	0.499 to 1.3K	0.499 to 4.9K	0.1 to 4.9K	0.1 to 4.9K	0.23
RS01A	RS-1A	1.0	-	1 to 2.74K	0.499 to 2.74K	0.499 to 10.4K	0.1 to 10.4K	0.1 to 10.4K	0.34
RS01A...300	RS-1A-300	1.0	-	-	0.499 to 2.74K	0.499 to 10.4K	0.1 to 10.4K	-	0.34
RS01M	RS-1M	1.0	-	1 to 1.32K	0.499 to 1.67K	0.499 to 6.85K	0.1 to 6.85K	0.1 to 6.85K	0.30
RS002	RS-2	4.0	5.5	0.499 to 12.7K	0.499 to 12.7K	0.1 to 47.1K	0.1 to 47.1K	0.1 to 47.1K	2.10
RS02M	RS-2M	3.0	-	0.499 to 4.49K	0.499 to 4.49K	0.1 to 18.74K	0.1 to 18.74K	0.1 to 18.74K	0.65
RS02B	RS-2B	3.0	3.75	0.499 to 6.5K	0.499 to 6.5K	0.1 to 24.5K	0.1 to 24.5K	0.1 to 24.5K	0.70
RS02B...300	RS-2B-300	3.0	-	-	0.499 to 6.5K	0.1 to 24.5K	0.1 to 24.5K	-	0.70
RS02C	RS-2C	2.5	3.25	0.499 to 8.6K	0.499 to 8.6K	0.1 to 32.3K	0.1 to 32.3K	0.1 to 32.3K	1.6
RS02C...17	RS-2C-17	2.5	3.25	0.499 to 8.6K	0.499 to 8.6K	0.1 to 32.3K	0.1 to 32.3K	0.1 to 32.3K	1.6
RS02C...23	RS-2C-23	-	3.25	-	-	-	-	0.1 to 32.3K	1.6
RS005	RS-5	5.0	6.5	0.499 to 25.7K	0.499 to 25.7K	0.1 to 95.2K	0.1 to 95.2K	0.1 to 95.2K	4.2
RS005...69	RS-5-69	5.0	-	-	0.499 to 25.7K	0.1 to 95.2K	0.1 to 95.2K	0.1 to 95.2K	4.2
RS005...70	RS-5-70	-	6.5	-	-	-	-	0.1 to 95.2K	4.2
RS007	RS-7	7.0	9.0	0.499 to 41.4K	0.499 to 41.4K	0.1 to 154K	0.1 to 154K	0.1 to 154K	4.7
RS010	RS-10	10.0	13.0	0.499 to 73.4K	0.499 to 73.4K	0.1 to 273K	0.1 to 273K	0.1 to 273K	9.0
RS010...38	RS-10-38	10.0	-	-	0.499 to 73.4K	0.1 to 273K	0.1 to 273K	0.1 to 273K	9.0
RS010...39	RS-10-39	-	13.0	-	-	-	-	0.1 to 273K	9.0

Notes

- Models not available as lead (Pb)-free: RS01A...300, RS02B...300, RS02C...23, RS005...69, RS005...70, RS010...38, RS010...39
- Shaded area indicates most popular models

(1) Vishay Dale RS models have two power ratings depending on operation temperature and stability requirements. Models not available for characteristic V are: RS1/4, RS1/2, RS01A, RS01A…300, RS01M, RS02M, RS02B…300, RS005…69, and RS010…38

GLOBAL PART NUMBER INFORMATION

Global Part Numbering example: RS02C10K00FS7017

R	S	0	2	C	1	0	K	0	0	F	S	7	0	1	7	

GLOBAL MODEL (5 digits)	RESISTANCE VALUE (5 digits)	TOLERANCE CODE (1 digit)	PACKAGING (3 digits)	SPECIAL (up to 3 digits)
(See Standard Electrical Specifications Global Model column for options)	**R** = Decimal **K** = Thousand **15R00** = 15 Ω **10K00** = 10 kΩ	**A** = 0.05 % **B** = 0.1 % **C** = 0.25 % **D** = 0.5 % **F** = 1.0 % **H** = 3.0 % **J** = 5.0 % **K** = 10.0 %	**E70** = Lead (Pb)-free, tape/reel (smaller than RS005) **E73** = Lead (Pb)-free, tape/reel (RS005 and larger) **E12** = Lead (Pb)-free, bulk **S70** = Tin/lead, tape/reel (smaller than RS005) **S73** = Tin/lead, tape/reel (RS005 and larger) **B12** = Tin/lead, bulk	(Dash Number) From **1 to 999** as applicable

Historical Part Numbering example: RS-2C-17 10 kΩ 1 % S70

RS-2C-17	**10 kΩ**	**1 %**	**S70**
HISTORICAL MODEL	RESISTANCE VALUE	TOLERANCE CODE	PACKAGING

DIMENSIONS in inches [millimeters]

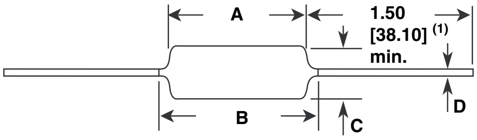

Note

(1) On some standard reel pack methods, the leads may be trimmed to a shorter length than shown

MATERIAL SPECIFICATIONS

Element: Copper-nickel alloy or nickel-chrome alloy, depending on resistance value

Core: Ceramic, steatite or alumina, depending on physical size

Coating: Special high temperature silicone

Standard Terminals: 100 % Sn, or 60/40 Sn/Pb coated Copperweld®

End Caps: Stainless steel

Part Marking: DALE, model, wattage (2), value, tolerance, date code

Note

(2) Wattage marked on part will be "U" characteristic

DERATING

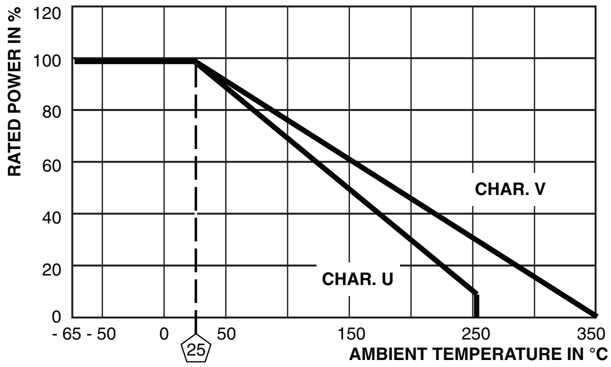

GLOBAL MODEL	DIMENSIONS in inches [millimeters]			
	A	B (3) (max.)	C	D
RS1/4	0.250 ± 0.031 [6.35 ± 0.787]	0.281 [7.14]	0.085 ± 0.020 [2.16 ± 0.508]	0.020 ± 0.002 [0.508 ± 0.051]
RS1/2	0.312 ± 0.016 [7.92 ± 0.406]	0.328 [8.33]	0.078 + 0.016 - 0.031 [1.98 + 0.406 - 0.787]	0.020 ± 0.002 [0.508 ± 0.051]
RS01A RS01A...300	0.406 ± 0.031 [10.31 ± 0.787]	0.437 [11.10]	0.094 ± 0.031 [2.39 ± 0.787]	0.020 ± 0.002 [0.508 ± 0.051]
RS01M	0.285 ± 0.025 [7.24 ± 0.635]	0.311 [7.90]	0.110 ± 0.015 [2.79 ± 0.381]	0.020 ± 0.002 [0.508 ± 0.051]
RS002	0.625 ± 0.062 [15.88 ± 1.57]	0.765 [19.43]	0.250 ± 0.031 [6.35 ± 0.787]	0.040 ± 0.002 [1.02 ± 0.051]
RS02M	0.500 ± 0.062 [12.70 ± 1.57]	0.562 [14.27]	0.185 ± 0.015 [4.70 ± 0.381]	0.032 ± 0.002 [0.813 ± 0.051]
RS02B RS02B...300	0.560 ± 0.062 [14.22 ± 1.57]	0.622 [15.80]	0.187 ± 0.031 [4.75 ± 0.787]	0.032 ± 0.002 [0.813 ± 0.051]
RS02C	0.500 ± 0.062 [12.70 ± 1.57]	0.593 [15.06]	0.218 ± 0.031 [5.54 ± 0.787]	0.040 ± 0.002 [1.02 ± 0.051]
RS02C...17 RS02C...23	0.500 ± 0.062 [12.70 ± 1.57]	0.593 [15.06]	0.218 ± 0.031 [5.54 ± 0.787]	0.032 ± 0.002 [0.813 ± 0.051]
RS005 RS005...69 RS005...70	0.875 ± 0.062 [22.23 ± 1.57]	1.0 [25.4]	0.312 ± 0.031 [7.92 ± 0.787]	0.040 ± 0.002 [1.02 ± 0.051]
RS007	1.22 ± 0.062 [30.99 ± 1.57]	1.28 [32.51]	0.312 ± 0.031 [7.92 ± 0.787]	0.040 ± 0.002 [1.02 ± 0.051]
RS010 RS010...39	1.78 ± 0.062 [45.21 ± 1.57]	1.87 [47.50]	0.375 ± 0.031 [9.53 ± 0.787]	0.040 ± 0.002 [1.02 ± 0.051]
RS010...38	1.78 ± 0.062 [45.21 ± 1.57]	1.84 [46.74]	0.375 ± 0.031 [9.53 ± 0.787]	0.040 ± 0.002 [1.02 ± 0.051]

Note

(3) B (max.) dimension is clean lead to clean lead

NS NON-INDUCTIVE

Models of equivalent physical and electrical specifications are available with non-inductive (Ayrton-Perry) winding. They are identified by substituting the letter N for R in the model number (NS005, for example).

Two conditions apply:

1. For NS models, divide maximum resistance values by two
2. Body O.D. on NS02C may exceed that of the RS02C by 0.010"

TECHNICAL SPECIFICATIONS

PARAMETER	UNIT	RS RESISTOR CHARACTERISTICS
Temperature Coefficient	ppm/°C	± 20 for 10 Ω and above, ± 50 for 1 Ω to 9.9 Ω, ± 90 for 0.5 Ω to 0.99 Ω
Maximum Working Voltage	V	$(P \times R)^{1/2}$
Insulation Resistance	Ω	1000 MΩ minimum dry, 100 MΩ minimum after moisture test
Operating Temperature Range	°C	Characterisitic U = - 65 to + 250, characteristic V = - 65 to + 350

PERFORMANCE

TEST	CONDITIONS OF TEST	TEST LIMITS	
		CHARACTERISTIC U	CHARACTERISTIC V
Thermal Shock	Rated power applied until thermally stable, then a minimum of 15 min at - 55 °C	± (0.2 % + 0.05 Ω) ΔR	± (2.0 % + 0.05 Ω) ΔR
Short Time Overload	5 x rated power (3.75 W and smaller), 10 x rated power (4 W and larger) for 5 s	± (0.2 % + 0.05 Ω) ΔR	± (2.0 % + 0.05 Ω) ΔR
Dielectric Withstanding Voltage	500 V_{RMS} min. for RS1/4 thru RS01A, 1000 V_{RMS} for all others, duration of 1 min	± (0.1 % + 0.05 Ω) ΔR	± (0.1 % + 0.05 Ω) ΔR
Low Temperature Storage	- 65 °C for 24 h	± (0.2 % + 0.05 Ω) ΔR	± (2.0 % + 0.05 Ω) ΔR
High Temperature Exposure	250 h at: U = + 250 °C, V = + 350 °C	± (0.5 % + 0.05 Ω) ΔR	± (2.0 % + 0.05 Ω) ΔR
Moisture Resistance	MIL-STD-202 Method 106, 7b not applicable	± (0.2 % + 0.05 Ω) ΔR	± (2.0 % + 0.05 Ω) ΔR
Shock, Specified Pulse	MIL-STD-202 Method 213, 100 *g*'s for 6 ms, 10 shocks	± (0.1 % + 0.05 Ω) ΔR	± (0.2 % + 0.05 Ω) ΔR
Vibration, High Frequency	Frequency varied 10 Hz to 2000 Hz, 20 *g* peak, 2 directions 6 h each	± (0.1 % + 0.05 Ω) ΔR	± (0.2 % + 0.05 Ω) ΔR
Load Life	2000 h at rated power, + 25 °C, 1.5 h "ON", 0.5 h "OFF"	± (0.5 % + 0.05 Ω) ΔR	± (3.0 % + 0.05 Ω) ΔR
Terminal Strength	Pull test 5 s to 10 s, 5 lb (RS1/4 thru RS01A), 10 lb for all others; torsion test - 3 alternating directions, 360° each	± (0.1 % + 0.05 Ω) ΔR	± (1.0 % + 0.05 Ω) ΔR

Disclaimer

ALL PRODUCT, PRODUCT SPECIFICATIONS AND DATA ARE SUBJECT TO CHANGE WITHOUT NOTICE TO IMPROVE RELIABILITY, FUNCTION OR DESIGN OR OTHERWISE.

Vishay Intertechnology, Inc., its affiliates, agents, and employees, and all persons acting on its or their behalf (collectively, “Vishay”), disclaim any and all liability for any errors, inaccuracies or incompleteness contained in any datasheet or in any other disclosure relating to any product.

Vishay makes no warranty, representation or guarantee regarding the suitability of the products for any particular purpose or the continuing production of any product. To the maximum extent permitted by applicable law, Vishay disclaims (i) any and all liability arising out of the application or use of any product, (ii) any and all liability, including without limitation special, consequential or incidental damages, and (iii) any and all implied warranties, including warranties of fitness for particular purpose, non-infringement and merchantability.

Statements regarding the suitability of products for certain types of applications are based on Vishay’s knowledge of typical requirements that are often placed on Vishay products in generic applications. Such statements are not binding statements about the suitability of products for a particular application. It is the customer’s responsibility to validate that a particular product with the properties described in the product specification is suitable for use in a particular application. Parameters provided in datasheets and/or specifications may vary in different applications and performance may vary over time. All operating parameters, including typical parameters, must be validated for each customer application by the customer’s technical experts. Product specifications do not expand or otherwise modify Vishay’s terms and conditions of purchase, including but not limited to the warranty expressed therein.

Except as expressly indicated in writing, Vishay products are not designed for use in medical, life-saving, or life-sustaining applications or for any other application in which the failure of the Vishay product could result in personal injury or death. Customers using or selling Vishay products not expressly indicated for use in such applications do so at their own risk. Please contact authorized Vishay personnel to obtain written terms and conditions regarding products designed for such applications.

No license, express or implied, by estoppel or otherwise, to any intellectual property rights is granted by this document or by any conduct of Vishay. Product names and markings noted herein may be trademarks of their respective owners.

Material Category Policy

Vishay Intertechnology, Inc. hereby certifies that all its products that are identified as RoHS-Compliant fulfill the definitions and restrictions defined under Directive 2011/65/EU of The European Parliament and of the Council of June 8, 2011 on the restriction of the use of certain hazardous substances in electrical and electronic equipment (EEE) - recast, unless otherwise specified as non-compliant.

Please note that some Vishay documentation may still make reference to RoHS Directive 2002/95/EC. We confirm that all the products identified as being compliant to Directive 2002/95/EC conform to Directive 2011/65/EU.

Vishay Intertechnology, Inc. hereby certifies that all its products that are identified as Halogen-Free follow Halogen-Free requirements as per JEDEC JS709A standards. Please note that some Vishay documentation may still make reference to the IEC 61249-2-21 definition. We confirm that all the products identified as being compliant to IEC 61249-2-21 conform to JEDEC JS709A standards.

A.11 Appendix 11

Power Metal Film Leaded Resistors

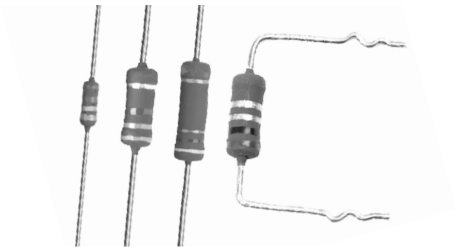

DESCRIPTION

A homogeneous film of metal alloy is deposited on a high grade ceramic body. After a helical groove has been cut in the resistive layer, tinned connecting wires of electrolytic copper or copper-clad iron are welded to the end-caps. The resistors are coated with a red, non-flammable lacquer which provides electrical, mechanical and climatic protection. This coating is not resistant to aggressive fluxes and cleaning solvents. The encapsulation is resistant to all cleaning solvents in accordance with IEC 60068-2-45.

FEATURES

- High power in small packages (1 W/0207 size to 3 W/0617 size)
- Different lead materials for different applications
- Defined interruption behaviour
- Technology: Metal film
- AEC-Q200 qualified (PR01 and PR02)
- Lead (Pb)-free solder contacts
- Pure tin plating provides compatibility with lead (Pb)-free and lead containing soldering processes
- Material categorization: For definitions of compliance please see www.vishay.com/doc?99912

Pb-free
RoHS
COMPLIANT

APPLICATIONS

- All general purpose power applications

TECHNICAL SPECIFICATIONS						
DESCRIPTION	**UNIT**	**PR01**	**PR02 Cu-lead**	**PR02 FeCu-lead**	**PR03 Cu-lead**	**PR03 FeCu-lead**
Resistance range [2]	Ω	0.22 to 1M	0.33 to 1M	1 to 1M	0.68 to 1M	1 to 1M
Resistance tolerance	%	± 1; ± 5	± 1; ± 5	± 1; ± 5	± 1; ± 5	± 1; ± 5
Resistance series		± 1 (E24, E96); ± 5 (E24 series) [1]				
Rated dissipation, P_{70} $1\ \Omega \le R$ $R < 1\ \Omega$	W	1 0.6	2 1.2	1.3 -	3 1.6	2.5 -
Thermal resistance (R_{th})	K/W	135	75	115	60	75
Temperature coefficient	ppm/K	≤ ± 250	≤ ± 250	≤ ± 250	≤ ± 250	≤ ± 250
Maximum permissible voltage ($U_{max.}$ AC/DC)	V	350	500	500	750	750
Basic specifications		IEC 60115-1				
Climatic category (IEC 60068-1)		55/155/56				
Stability after:						
Load (1000 h, P_{70})		ΔR max.: ± (5 % R + 0.1 Ω)				
Long term damp heat test (56 days)		ΔR max.: ± (3 % R + 0.1 Ω)				
Soldering (10 s, 260 °C)		ΔR max.: ± (1 % R + 0.05 Ω)				

Notes
- R value is measured with probe distance of 24 mm ± 1 mm using 4-terminal method.

(1) 1 % tolerance is available for R_n-range from 1 R upwards.
(2) Ohmic values (other than resistance range) are available on request.

PART NUMBER AND PRODUCT DESCRIPTION

Part Number: PR02000201001JA100

P	R	0	2	0	0	0	2	0	1	0	0	1	J	A	1	0	0

MODEL/SIZE	VARIANT	WIRE TYPES	TCR/MATERIAL	VALUE	TOLERANCE	PACKAGING (1)	SPECIAL
PR0100 **PR0200** **PR0300**	**0** = Neutral **Z** = Value overflow (Special)	**1** = Cu 0.6 **2** = Cu 0.8 **3** = FeCu 0.6 **4** = FeCu 0.8	**0** = Standard	**3 digit value** **1 digit multiplier** MULTIPLIER **7** = $*10^{-3}$ **2** = $*10^{2}$ **8** = $*10^{-2}$ **3** = $*10^{3}$ **9** = $*10^{-1}$ **4** = $*10^{4}$ **0** = $*10^{0}$ **5** = $*10^{5}$ **1** = $*10^{1}$	**F** = ± 1 % **J** = ± 5 %	**N4** **R2** **N3** **L1** **A5** **DC** **A1** **K1** **AC** **B1** **R5** **PC**	The 2 digits are used for all special parts. **00** = Standard

Product Description: PR02 5 % A1 1K0

PR02	5 %	A1	1K0
MODEL/SIZE	TOLERANCE	PACKAGING (1)	RESISTANCE VALUE
PR01 **PR02** **PR03**	± **1 %** ± **5 %**	**N4** **L1** **N3** **DC** **A5** **K1** **A1** **B1** **AC** **PC** **R5** **R2**	**1K0** = 1 kΩ **4K75** = 4.75 kΩ

Notes

- The PART NUMBER is shown to facilitate the introduction of a unified part numbering system for ordering products.

(1) Please refer to table PACKAGING for details.

PACKAGING

MODEL	TAPING	AMMO PACK		REEL		BULK, DOUBLE KINK		
		PIECES	CODE	PIECES	CODE	PITCH	PIECES	CODE
PR01	Axial, 52 mm Wire Cu 0.6 mm and FeCu 0.6 mm	5000	A5	5000	R5			
		1000	A1					
	Radial Wire Cu 0.6 mm	4000	N4			17.8 mm Wire Cu 0.6 mm or FeCu 0.6 mm	1000	L1
						12.5 mm Wire FeCu 0.6 mm	1000	K1
PR02	Axial, 52 mm Wire Cu 0.8 mm and FeCu 0.6 mm	1000	A1	5000 only with Cu 0.8 mm	R5			
	Radial Wire Cu 0.8 mm and FeCu 0.6 mm	3000 only with Cu 0.8 mm	N3	2000 only with Cu 0.8 mm	R2	17.8 mm Wire Cu 0.8 mm and FeCu 0.6 mm	1000	L1
						15.0 mm only with FeCu 0.8 mm Wire FeCu 0.6 mm	1000	B1
PR03	Axial, 63 mm Wire Cu 0.8 mm and FeCu 0.6 mm	500	AC					
	Radial Wire Cu 0.8 mm and FeCu 0.6 mm					25.4 mm Wire Cu 0.8 mm and FeCu 0.6 mm	500	DC
						20 mm Wire FeCu 0.8 mm	500	PC

DIMENSIONS

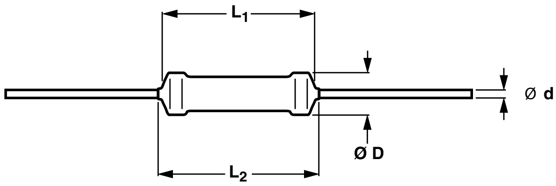

Type with straight leads

DIMENSIONS - Straight lead type and relevant physical dimensions; see straight leads outline					
TYPE	**Ø $D_{MAX.}$ (mm)**	**$L_{1\ MAX.}$ (mm)**	**$L_{2\ MAX.}$ (mm)**	**Ø d (mm)**	
				Cu	**FeCu**
PR01	2.5	6.5	8.0	0.58 ± 0.05	-
PR02	3.9	10.0	12.0	0.78 ± 0.05	0.58 ± 0.05
PR03	5.2	16.7	19.5	0.78 ± 0.05	0.58 ± 0.05

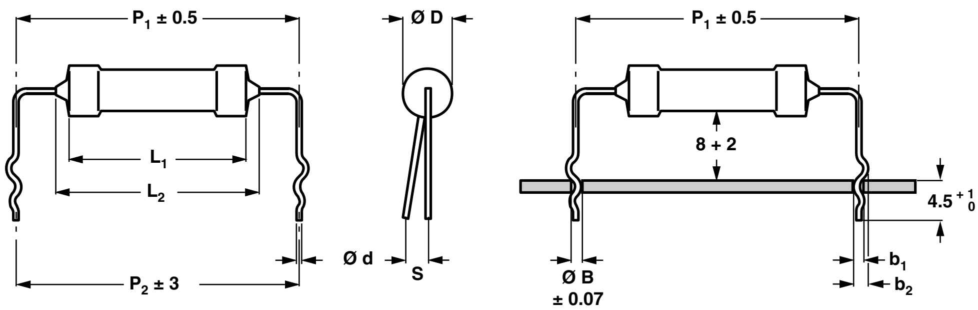

Type with double kink

Dimensions in millimeters

DIMENSIONS - Double kink lead type and relevant physical dimensions; see double kinked outline										
TYPE	**LEAD STYLE**	**Ø d (mm)**		**b_1 (mm)**	**b_2 (mm)**	**Ø $D_{MAX.}$ (mm)**	**P_1 (mm)**	**P_2 (mm)**	**$S_{MAX.}$ (mm)**	**Ø B (mm)**
		Cu	**FeCu**							
PR01	Double kink 17.8 mm pitch	0.58 ± 0.05	0.58 ± 0.05	1.10 + 0.25/- 0.20	1.45 + 0.25/- 0.20	2.5	17.8	17.8	2	0.8
	Double kink 12.5 mm pitch	-	0.58 ± 0.05	1.10 + 0.25/- 0.20	1.45 + 0.25/- 0.20		12.5	12.5	2	0.8
PR02	Double kink 17.8 mm pitch	0.78 ± 0.05	0.58 ± 0.05	1.10 + 0.25/- 0.20	1.45 + 0.25/- 0.20	3.9	17.8	17.8	2	0.8
	Double kink 12.5 mm pitch	-	0.78 ± 0.05	1.30 + 0.25/- 0.20	1.65 + 0.25/- 0.20		15.0	15.0	2	1.0
PR03	Double kink 17.8 mm pitch	0.78 ± 0.05	0.58 ± 0.05	1.10 + 0.25/- 0.20	1.65 + 0.25/- 0.20	5.2	25.4	25.4	2	1.0
	Double kink 12.5 mm pitch	-	0.78 ± 0.05	1.30 + 0.25/- 0.20	2.15 + 0.25/- 0.20		22.0	20.0	2	1.0

PRODUCTS WITH RADIAL LEADS (PR01, PR02)

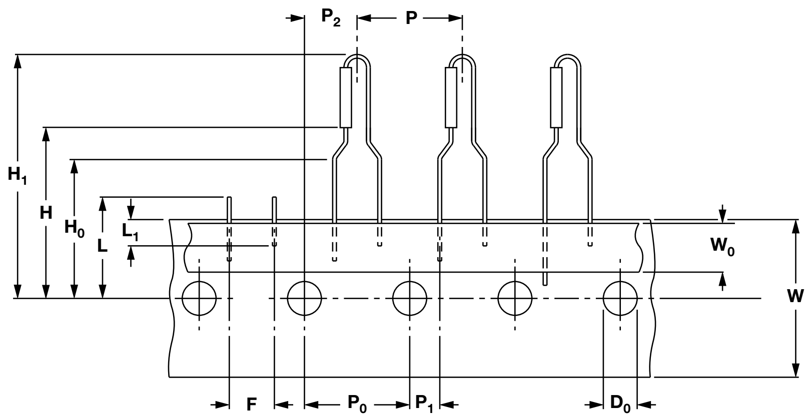

DIMENSIONS - Radial taping				
SYMBOL	**PARAMETER**	**VALUE**	**TOLERANCE**	**UNIT**
P	Pitch of components	12.7	± 1.0	mm
P_0	Feed-hole pitch	12.7	± 0.2	mm
P_1	Feed-hole centre to lead at topside at the tape	3.85	± 0.5	mm
P_2	Feed-hole center to body center	6.35	± 1.0	mm
F	Lead-to-lead distance	4.8	+ 0.7/- 0	mm
W	Tape width	18.0	± 0.5	mm
W_0	Minimum hold down tape width	5.5	-	mm
H1	Component height PR01	29	Max.	mm
	Component height PR02	29	± 3.0	
H_0	Lead wire clinch height	16.5	± 0.5	mm
H	Height of component from tape center	19.5	± 1	mm
D_0	Feed-hole diameter	4.0	± 0.2	mm
L	Maximum length of snipped lead	11.0	-	mm
L_1	Minimum lead wire (tape portion) shortest lead	2.5	-	mm

Note

- Please refer Packaging document (www.vishay.com/doc?28721) for more detail.

MASS PER UNIT	
TYPE	**MASS (mg)**
PR01 Cu 0.6 mm	212
PR01 FeCu 0.6 mm	207
PR02 Cu 0.8 mm	504
PR02 FeCu 0.6 mm	455
PR02 FeCu 0.8 mm	496
PR03 Cu 0.8 mm	1192
PR03 FeCu 0.6 mm	1079
PR03 FeCu 0.8 mm	1185

MARKING

The nominal resistance and tolerance are marked on the resistor using four or five colored bands in accordance with IEC 60062, marking codes for resistors and capacitors.

OUTLINES

The length of the body (L_1) is measured by inserting the leads into holes of two identical gauge plates and moving these plates parallel to each other until the resistor body is clamped without deformation (IEC 60294).

MOUNTING

The resistors are suitable for processing on automatic insertion equipment and cutting and bending machines.

MOUNTING PITCH			
TYPE	**LEAD STYLE**	**PITCH**	
		mm	**e**
PR01	Straight leads	12.5 (1)	5 (1)
	Radial taped	4.8	2
	Double kink large pitch	17.8	7
	Double kink small pitch	12.5	5
PR02	Straight leads	15.0 (1)	6 (1)
	Radial taped	4.8	2
	Double kink large pitch	17.8	7
	Double kink small pitch	15.0	6
PR03	Straight leads	23.0 (1)	9 (1)
	Double kink large pitch	25.4	10
	Double kink small pitch	20.0	8

Note

(1) Recommended minimum value.

FUNCTIONAL DESCRIPTION

PRODUCT CHARACTERIZATION

Standard values of nominal resistance are taken from the E96/E24 series for resistors with a tolerance of ± 1 % or ± 5 %. The values of the E96/E24 series are in accordance with IEC 60063.

FUNCTIONAL PERFORMANCE

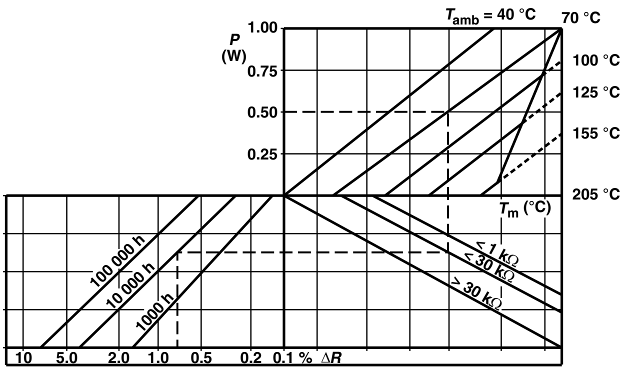

PR01 Drift nomogram

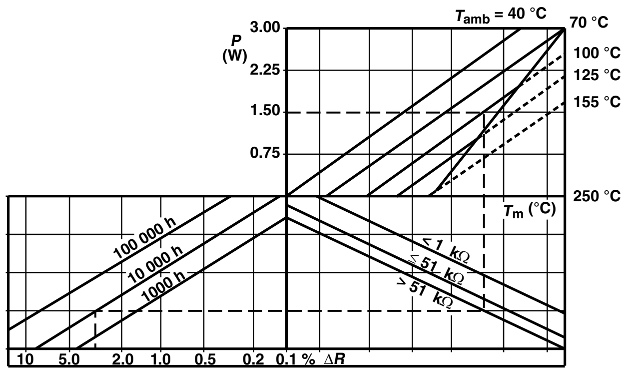

PR03 Drift nomogram

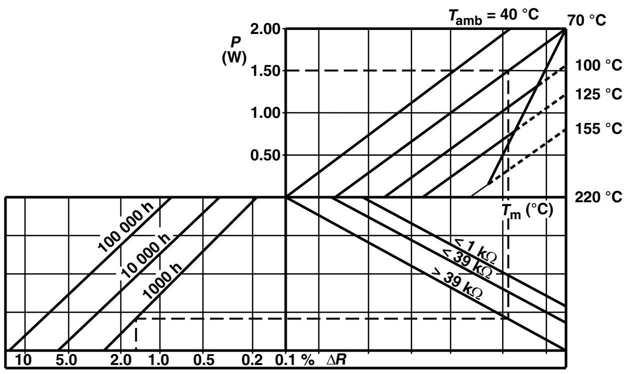

PR02 Drift nomogram

Note

- The maximum permissible hot-spot temperature is 205 °C for PR01, 220 °C for PR02 and 250 °C for PR03.

DERATING

The power that the resistor can dissipate depends on the operating temperature.

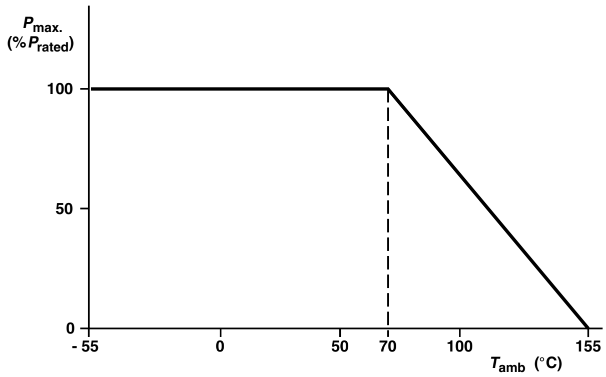

Maximum dissipation ($P_{max.}$) in percentage of rated power as a function of the ambient temperature (T_{amb})

PULSE LOADING CAPABILITIES

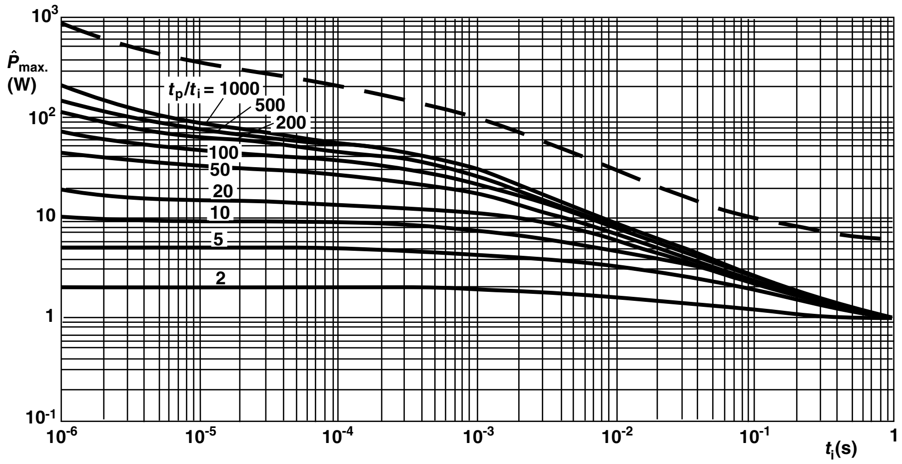

PR01 Pulse on a regular basis; maximum permissible peak pulse power ($\hat{P}_{max.}$) as a function of pulse duration (t_i)

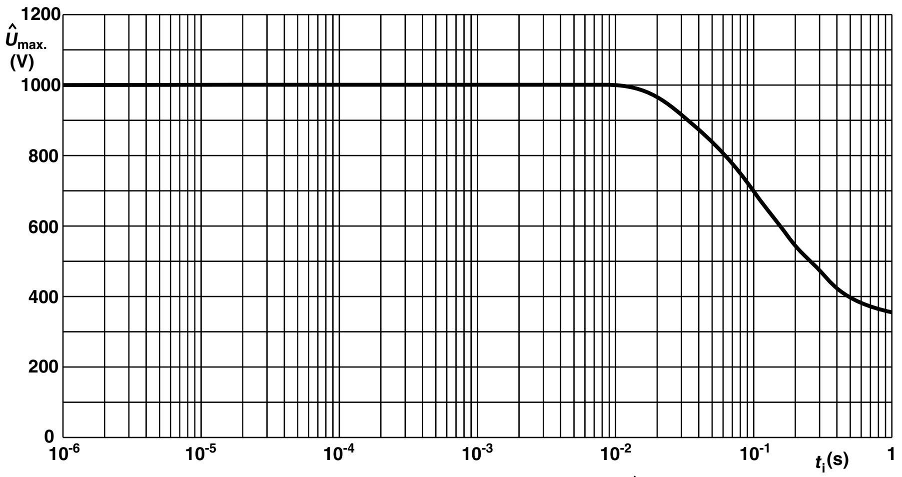

PR01 Pulse on a regular basis; maximum permissible peak pulse voltage ($\hat{U}_{max.}$) as a function of pulse duration (t_i)

PULSE LOADING CAPABILITIES

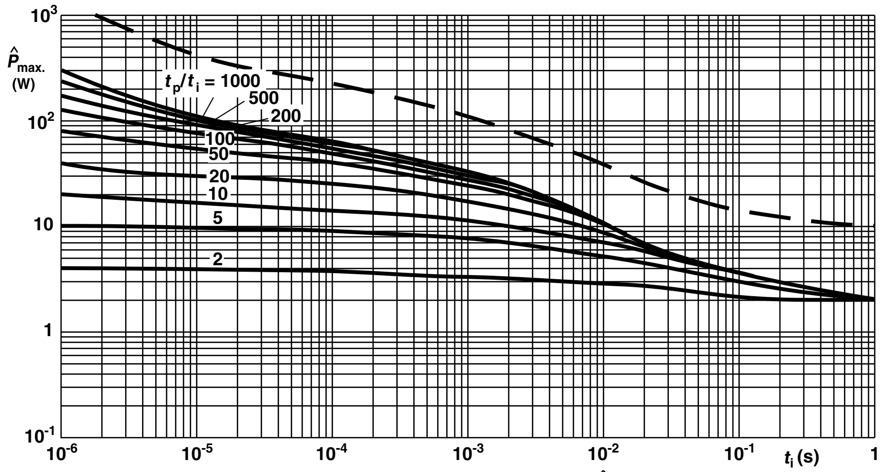

PR02 Pulse on a regular basis; maximum permissible peak pulse power ($\hat{P}_{max.}$) as a function of pulse duration (t_i)

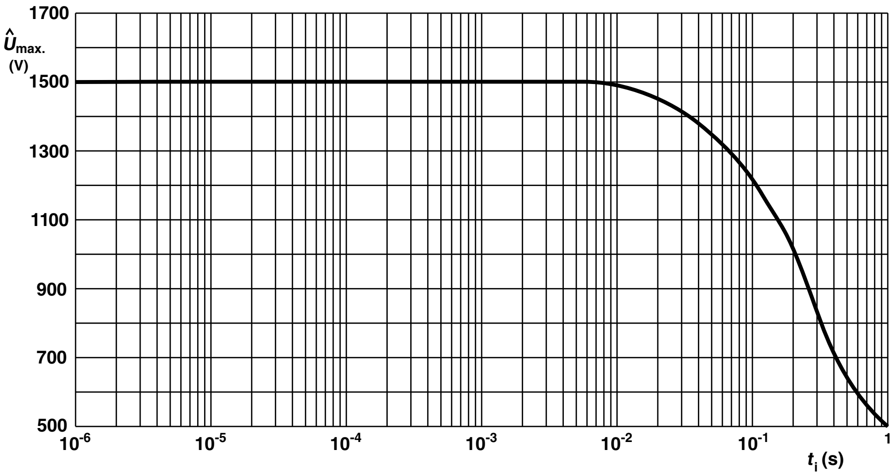

PR02 Pulse on a regular basis; maximum permissible peak pulse voltage ($\hat{U}_{max.}$) as a function of pulse duration (t_i)

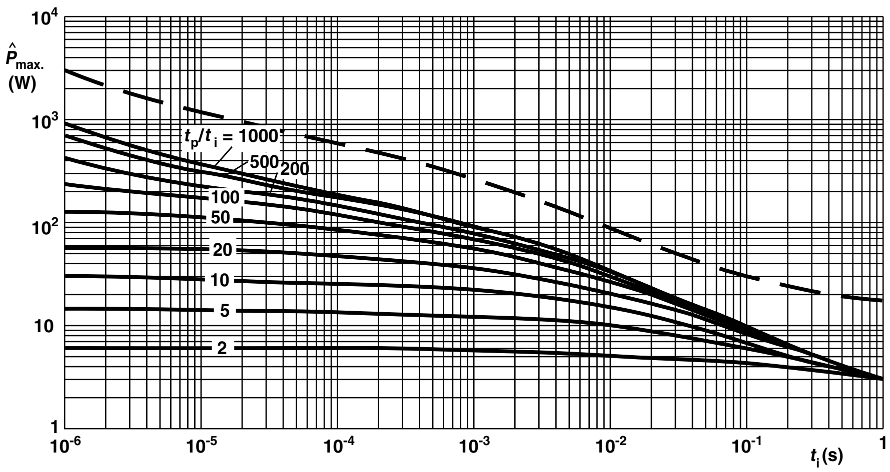

PR03 Pulse on a regular basis; maximum permissible peak pulse power ($\hat{P}_{max.}$) as a function of pulse duration (t_i)

PULSE LOADING CAPABILITIES

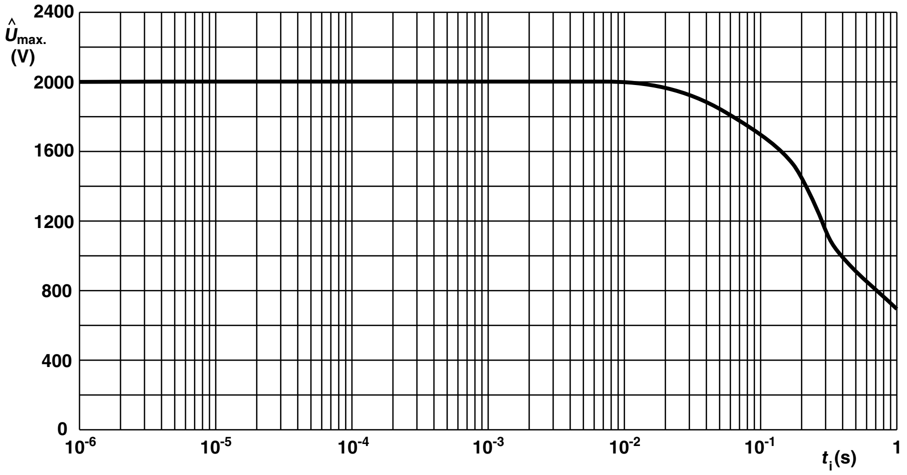

PR03 Pulse on a regular basis; maximum permissible peak pulse voltage ($\hat{U}_{max.}$) as a function of pulse duration (t_i)

INTERRUPTION CHARACTERISTICS

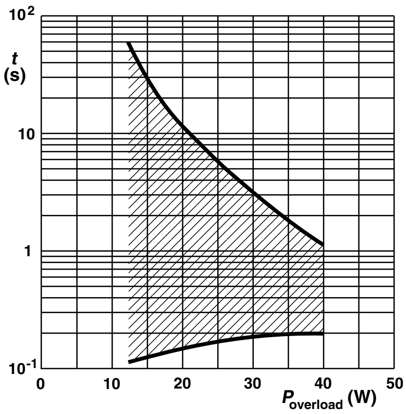

PR01 Time to interruption as a function of overload power
for range: 0 R 22 $\leq R_v <$ 1 R
This graph is based on measured data under constant voltage conditions; the data may deviate according to the applications.

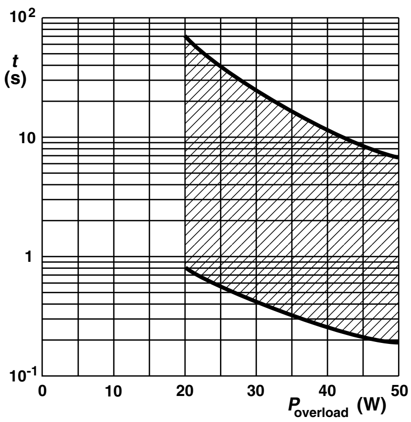

PR01 Time to interruption as a function of overload power
for range: 16 $R \leq R_n \leq$ 560 R
This graph is based on measured data under constant voltage conditions; the data may deviate according to the applications.

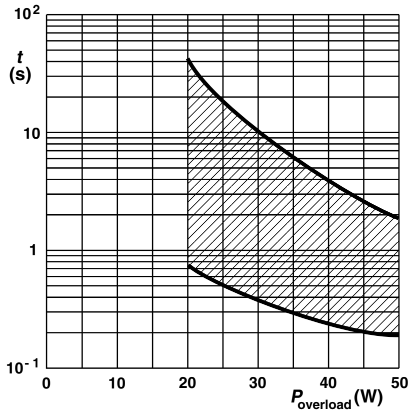

PR01 Time to interruption as a function of overload power
for range: 1 $R \leq R_n \leq$ 15 R
This graph is based on measured data under constant voltage conditions; the data may deviate according to the applications.

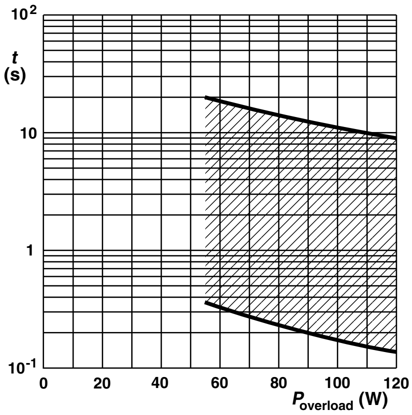

PR02 Time to interruption as a function of overload power
for range: 0.33 $R \leq R_n \leq$ 5 R
This graph is based on measured data under constant voltage conditions; the data may deviate according to the applications.

INTERRUPTION CHARACTERISTICS

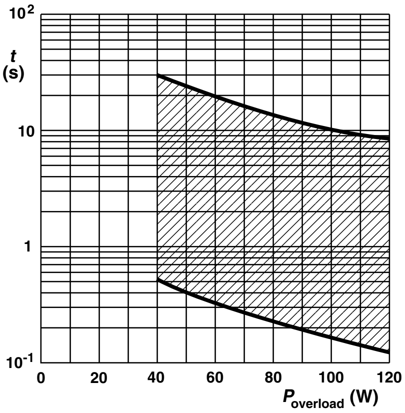

PR02 Time to interruption as a function of overload power for range: 5 $R \leq R_n \leq$ 68 R
This graph is based on measured data under constant voltage conditions; the data may deviate according to the applications.

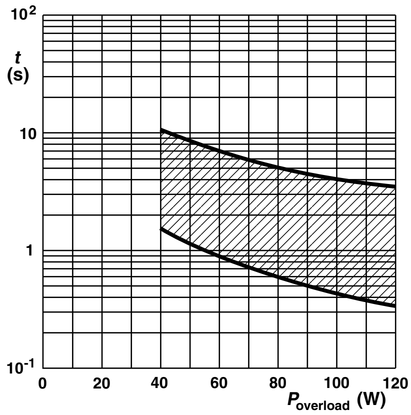

PR02 Time to interruption as a function of overload power for range: 68 $R \leq R_n \leq$ 560 R
This graph is based on measured data under constant voltage conditions; the data may deviate according to the applications.

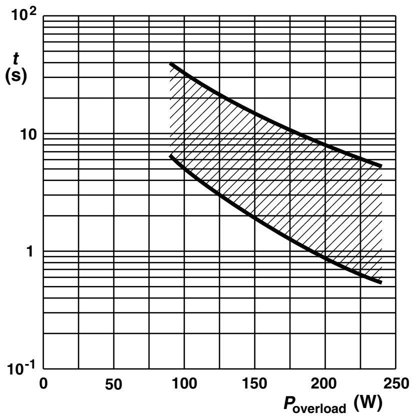

PR03 Time to interruption as a function of overload power for range: 0.68 $R \leq R_n \leq$ 560 R
This graph is based on measured data under constant voltage conditions; the data may deviate according to the applications.

APPLICATION INFORMATION

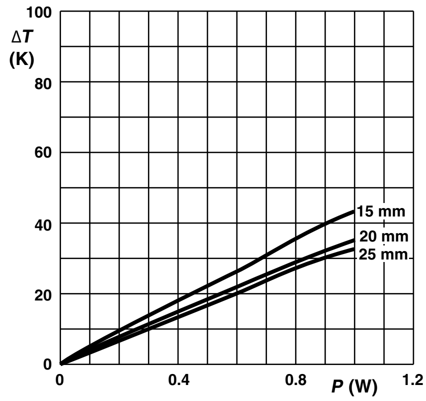

Ø 0.6 mm Cu-leads
Minimum distance from resistor body to PCB = 1 mm

PR01 Temperature rise (ΔT) at the lead end (soldering point) as a function of dissipated power at various lead lengths after mounting.

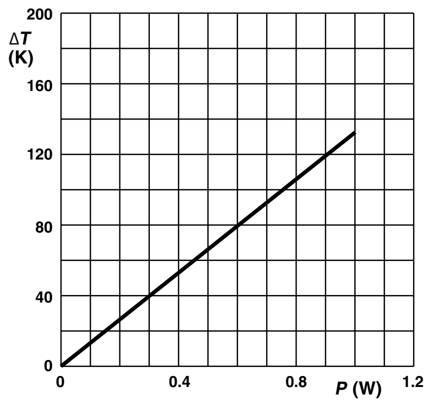

Ø 0.6 mm Cu-leads

PR01 Hot-spot temperature rise (ΔT) as a function of dissipated power.

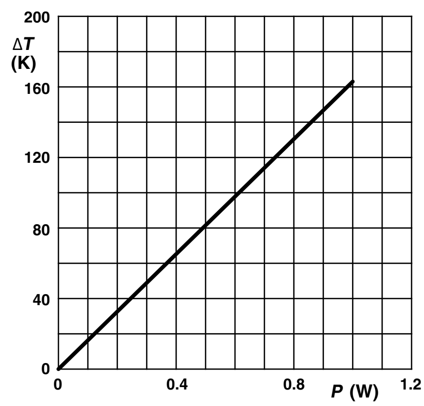

Ø 0.6 mm FeCu-leads

PR01 Hot-spot temperature rise (ΔT) as a function of dissipated power.

For technical questions, contact: filmresistorsleaded@vishay.com

APPLICATION INFORMATION

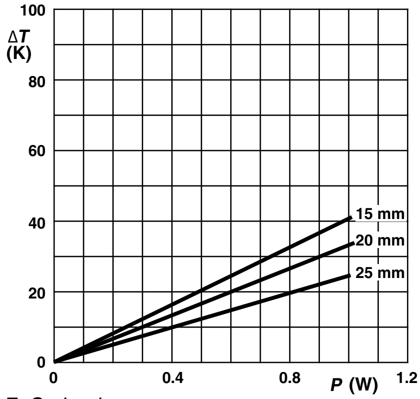

Ø 0.6 mm FeCu-leads
Minimum distance from resistor body to PCB = 1 mm

PR01 Temperature rise (Δ*T*) at the lead end (soldering point) as a function of dissipated power at various lead lengths after mounting.

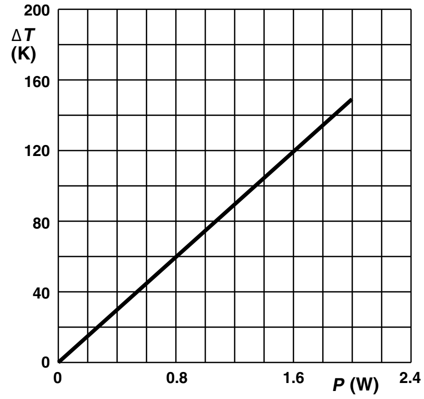

Ø 0.8 mm Cu-leads

PR02 Hot-spot temperature rise (Δ*T*) as a function of dissipated power.

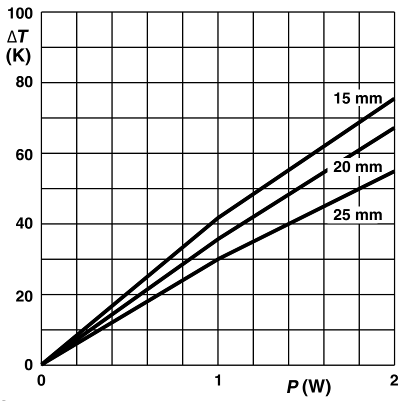

Ø 0.8 mm Cu-leads
Minimum distance from resistor body to PCB = 1 mm

PR02 Temperature rise (Δ*T*) at the lead end (soldering point) as a function of dissipated power at various lead lengths after mounting.

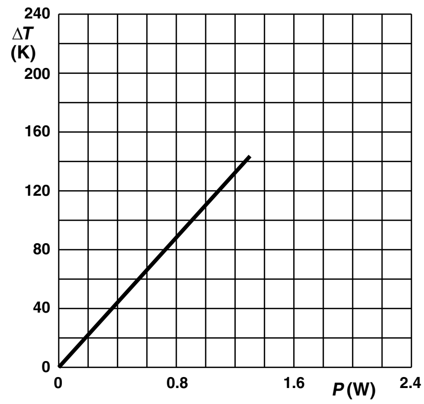

Ø 0.6 mm FeCu-leads

PR02 Hot-spot temperature rise (Δ*T*) as a function of dissipated power.

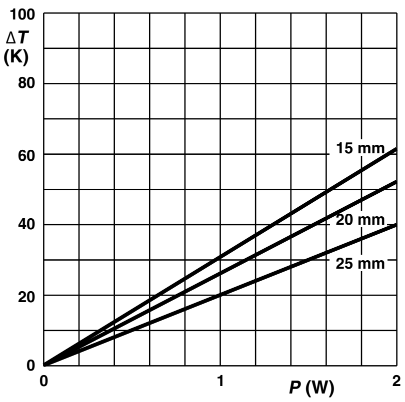

Ø 0.6 mm FeCu-leads
Minimum distance from resistor body to PCB = 1 mm

PR02 Temperature rise (Δ*T*) at the lead end (soldering point) as a function of dissipated power at various lead lengths after mounting.

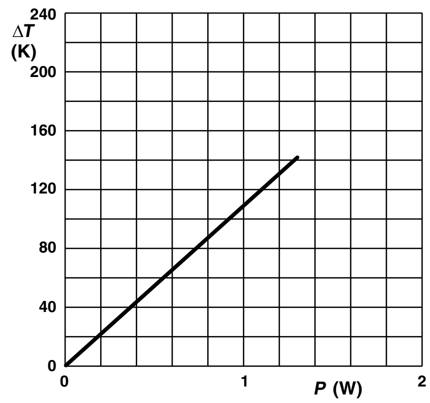

Ø 0.8 mm FeCu-leads

PR02 Hot-spot temperature rise (Δ*T*) as a function of dissipated power.

APPLICATION INFORMATION

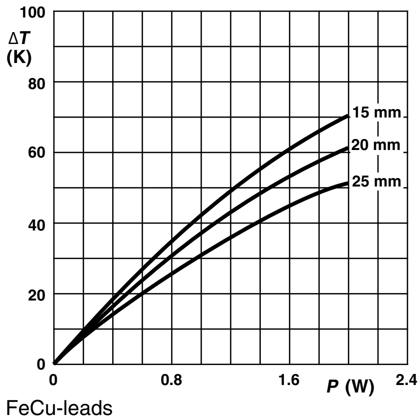

Ø 0.8 mm FeCu-leads
Minimum distance from resistor body to PCB = 1 mm

PR02 Temperature rise (Δ*T*) at the lead end (soldering point) as a function of dissipated power at various lead lengths after mounting.

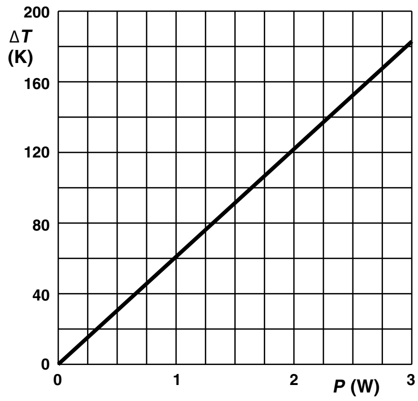

Ø 0.8 mm Cu-leads

PR03 Hot-spot temperature rise (Δ*T*) as a function of dissipated power.

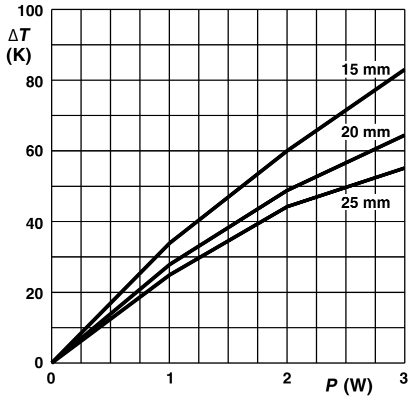

Ø 0.8 mm Cu-leads
Minimum distance from resistor body to PCB = 1 mm

PR03 Temperature rise (Δ*T*) at the lead end (soldering point) as a function of dissipated power at various lead lengths after mounting.

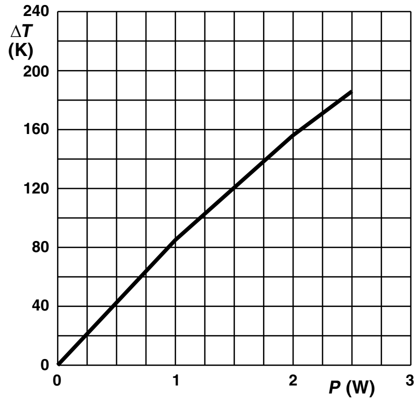

Ø 0.6 mm FeCu-leads

PR03 Hot-spot temperature rise (Δ*T*) as a function of dissipated power.

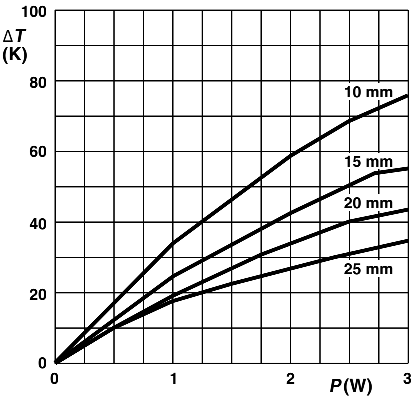

Ø 0.6 mm FeCu-leads
Minimum distance from resistor body to PCB = 1 mm

PR03 Temperature rise (Δ*T*) at the lead end (soldering point) as a function of dissipated power at various lead lengths after mounting.

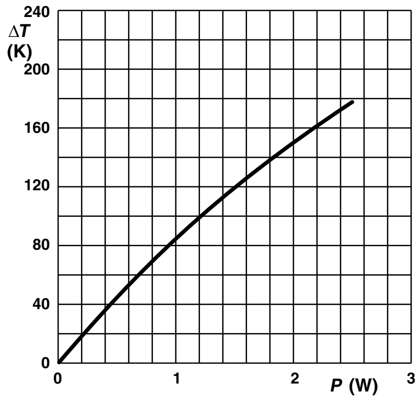

Ø 0.8 mm FeCu-leads

PR03 Hot-spot temperature rise (Δ*T*) as a function of dissipated power.

For technical questions, contact: filmresistorsleaded@vishay.com

APPLICATION INFORMATION

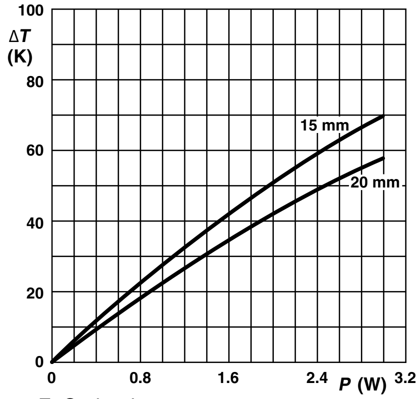

Ø 0.8 mm FeCu-leads
Minimum distance from resistor body to PCB = 1 mm

PR03 Temperature rise (Δ*T*) at the lead end (soldering point) as a function of dissipated power at various lead lengths after mounting.

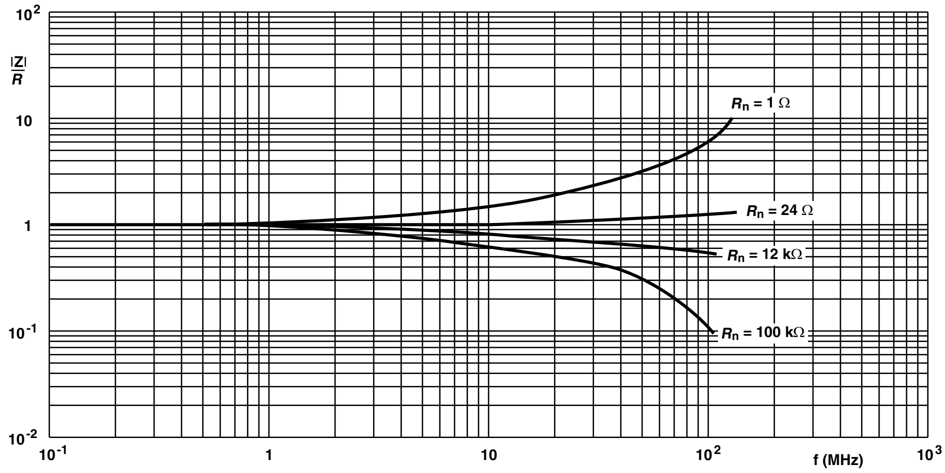

PR01 Impedance as a function of applied frequency

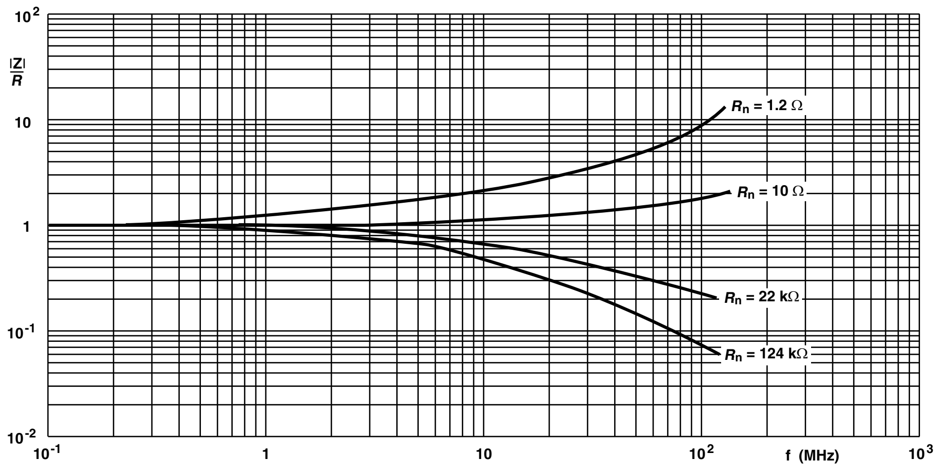

PR02 Impedance as a function of applied frequency

APPLICATION INFORMATION

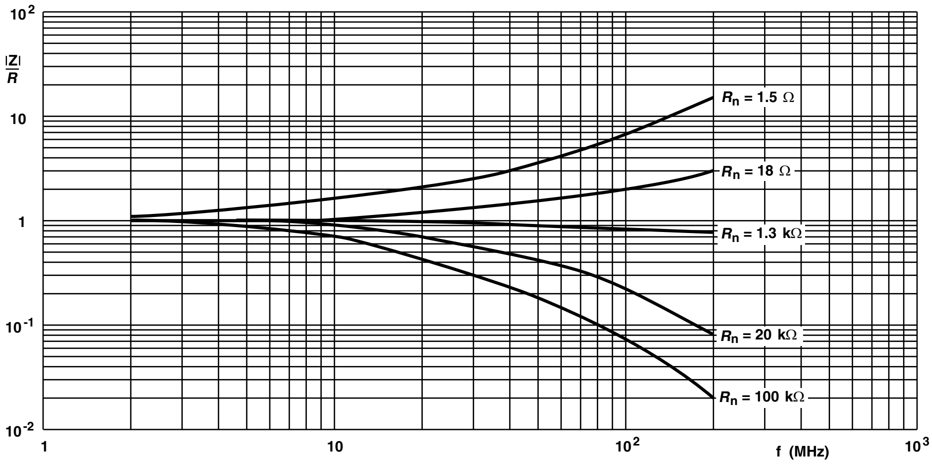

PR03 Impedance as a function of applied frequency

TESTS AND REQUIREMENTS

Essentially all tests are carried out in accordance with IEC 60115-1 specification, category LCT/UCT/56 (rated temperature range: Lower Category Temperature, Upper Category Temperature; damp heat, long term, 56 days).

The tests are carried out in accordance with IEC 60068-2-xx Test Method under standard atmospheric conditions according to IEC 60068-1, 5.3.

In the Test Procedures and Requirements table, tests and requirements are listed with reference to the relevant clauses of IEC 60115-1 and IEC 60068-2-xx test methods. A short description of the test procedure is also given. In some instances deviations from the IEC recommendations were necessary for our method of specifying.

All soldering tests are performed with mildly activated flux.

TEST PROCEDURES AND REQUIREMENTS				
IEC 60115-1 CLAUSE	**IEC 60068-2- TEST METHOD**	**TEST**	**PROCEDURE**	**REQUIREMENTS**
4.4.1		Visual examination		No holes; clean surface; no damage
4.4.2		Dimensions (outline)	Gauge (mm)	See Straight and Kinked Dimensions tables
4.5		Resistance (refer note on first page for measuring distance)	Applied voltage (+ 0 %/- 10 %): R< 10 Ω: 0.1 V 10 Ω ≤ R < 100 Ω: 0.3 V 100 Ω ≤ R < 1 kΩ: 1 V 1 kΩ ≤ R < 10 kΩ: 3 V 10 kΩ ≤ R < 100 kΩ: 10 V 100 kΩ ≤ R < 1 MΩ: 25 V R = 1 MΩ: 50 V	R - $R_{nom:}$ max. ± 5 %
4.18	20 (Tb)	Resistance to soldering heat	Thermal shock: 10 s; 260 °C; 3 mm from body	$\Delta R_{max.}$: ± (1 % R + 0.05 Ω)
4.29	45 (Xa)	Component solvent resistance	Isopropyl alcohol or H_2O followed by brushing	No visual damage
4.17	20 (Ta)	Solderability	2 s; 235 °C; Solder bath method; SnPb40 3 s; 245 °C; Solder bath method; SnAg3Cu0.5	Good tinning (≥ 95 % covered); no damage
		Solderability (after ageing)	8 h steam or 16 h 155 °C; leads immersed 6 mm: for 2 s at 235 °C; solder bath (SnPb40) for 3 s at 245 °C; solder bath (SnAg3Cu0.5)	Good tinning (≥ 95 % covered); no damage

TEST PROCEDURES AND REQUIREMENTS

IEC 60115-1 CLAUSE	IEC 60068-2-TEST METHOD	TEST	PROCEDURE	REQUIREMENTS
4.7		Voltage proof on insulation	Maximum voltage U_{RMS} = 500 V during 1 min; metal block method	No breakdown or flashover
4.16		Robustness of terminations:		
4.16.2	21 (Ua1)	Tensile all samples	Load 10 N; 10 s	Number of failures: < 1 x 10^{-6}
4.16.3	21 (Ub)	Bending half number of samples	Load 5 N; 4 x 90°	Number of failures: < 1 x 10^{-6}
4.16.4	21 (Uc)	Torsion other half of samples	3 x 360° in opposite directions	No damage $\Delta R_{max.}$: ± (0.5 % R + 0.05 Ω)
4.20	29 (Eb)	Bump	3 x 1500 bumps in three directions; 40 g	No damage $\Delta R_{max.}$: ± (0.5 % R + 0.05 Ω)
4.22	6 (Fc)	Vibration	Frequency 10 Hz to 500 Hz; displacement 1.5 mm or acceleration 10 *g*; three directions; total 6 h (3 x 2 h)	No damage $\Delta R_{max.}$: ± (0.5 % R + 0.05 Ω)
4.19	14 (Na)	Rapid change of temperature	30 min at LCT and 30 min at UCT; 5 cycles	No visual damage **PR01**: $\Delta R_{max.}$: ± (1 % R + 0.05 Ω **PR02**: $\Delta R_{max.}$: ± (1 % R + 0.05 Ω **PR03**: $\Delta R_{max.}$: ± (2 % R + 0.05 Ω
4.23		Climatic sequence:		
4.23.2	2 (Ba)	Dry heat	16 h; 155 °C	
4.23.3	30 (Db)	Damp heat (accelerated) 1st cycle	24 h; 55 °C; 90 % to 100 % RH	
4.23.4	1 (Aa)	Cold	2 h; - 55 °C	
4.23.5	13 (M)	Low air pressure	2 h; 8.5 kPa; 15 °C to 35 °C	
4.23.6	30 (Db)	Damp heat (accelerated) remaining cycles	5 days; 55 °C; 95 % to 100 % RH	$R_{ins\ min.}$: 10^3 MΩ $\Delta R_{max.}$: ± (1.5 % R + 0.1 Ω)
4.24	78 (Cab)	Damp heat (steady state)	56 days; 40 °C; 90 % to 95 % RH; loaded with 0.01 P_{70} (Steps: 0 V to 100 V)	$R_{ins\ min.}$: 1000 MΩ $\Delta R_{max.}$: ± (3 % R + 0.1 Ω)
4.25.1		Endurance (at 70 °C)	1000 h; loaded with P_{70} or $U_{max.}$; 1.5 h ON and 0.5 h OFF	$\Delta R_{max.}$: ± (5 % R + 0.1 Ω)
4.8		Temperature coefficient	Between - 55 °C and + 155 °C	≤ ± 250 ppm/K
4.6.1.1		Insulation resistance	Maximum voltage (DC) after 1 min; metal block method	$R_{ins\ min.}$: 10^4 MΩ

12NC INFORMATION FOR HISTORICAL CODING REFERENCE

The resistors have a 12-digit numeric code starting with 23

For 5 % tolerance:

- The next 7 digits indicate the resistor type and packing
- The remaining 3 digits indicate the resistance value:
  - The first 2 digits indicate the resistance value
  - The last digit indicates the resistance decade

For 1 % tolerance:

- The next 6 digits indicate the resistor type and packing
- The remaining 4 digits indicate the resistance value:
  - The first 3 digits indicate the resistance value
  - The last digit indicates the resistance decade

Last Digit of 12NC Indicating Resistance Decade

RESISTANCE DECADE	LAST DIGIT
0.22 Ω to 0.91 Ω	7
1 Ω to 9.76 Ω	8
10 Ω to 97.6 Ω	9
100 Ω to 976 Ω	1
1 Ω to 9.76 kΩ	2
10 Ω to 97.6 kΩ	3
100 Ω to 976 kΩ	4
1 MΩ	5

12NC Example

The 12NC for resistor type PR02 with Cu leads and a value of 750 Ω with 5 % tolerance, supplied on a bandolier of 1000 units in ammopack, is: 2306 198 53751.

12NC - Resistor Type and Packaging (1)

TYPE	LEAD Ø mm	TOL. (%)	23.. ... . (BANDOLIER)						
			AMMOPACK					REEL	
			RADIAL TAPED		STRAIGHT LEADS				RADIAL TAPED
					52 mm	52 mm	63 mm	52 mm	
			4000 UNITS	3000 UNITS	5000 UNITS	1000 UNITS	500 UNITS	5000 UNITS	2000 UNITS
PR01	Cu 0.6	1	-	-	**22 196 1....**	06 191 2....	-	06 191 5....	-
		5	06 197 03...	-	**22 193 14...**	06 197 53...	-	**06 197 23...**	-
PR02	Cu 0.8	1	-	22 197 2....	-	**22 197 1....**	-	06 192 5....	**2322 197 5....**
		5	-	06 198 03...	-	**06 198 53...**	-	**06 198 23...**	**2322 198 04...**
	FeCu 0.6	5	-	-	-	22 194 54...	-	-	-
PR03	Cu 0.8	5	-	-	-	-	**22 195 14...**	-	-
		1	-	-	-	-	**06 199 6...**	-	-
	FeCu 0.6	5	-	-	-	-	**22 195 54...**	-	-

Notes

- Preferred types in bold.

(1) Other packaging versions are available on request.

12NC - Resistor Type and Packaging

TYPE	LEAD Ø mm	TOL. (%)	23.. ... . (LOOSE IN BOX)			
			DOUBLE KINK			
			PITCH = 17.8 mm	PITCH = 25.4 mm	PITCH (2)(3)(4)	
			1000 UNITS	500 UNITS	1000 UNITS	500 UNITS
PR01	Cu 0.6	5	22 193 03...	-	-	-
	FeCu 0.6	5	22 193 43...	-	**22 193 53...** (2)	-
PR02	Cu 0.8	5	22 194 23...	-	-	-
	FeCu 0.6	5	22 194 83...	-	-	-
	FeCu 0.8	5	-	-	**22 194 63...** (3)	-
PR03	Cu 0.8	5	-	22 195 23...	-	-
	FeCu 0.6	5	-	22 195 83...	-	-
	FeCu 0.8	5	-	-	-	**22 195 63...** (4)

Notes

- Preferred types in bold.

(2) PR01 pitch 12.5 mm.

(3) PR02 pitch 15.0 mm.

(4) PR03 pitch 20.0 mm, with reversed kinking direction as opposed to the drawing for the type with double kink figure.

Disclaimer

ALL PRODUCT, PRODUCT SPECIFICATIONS AND DATA ARE SUBJECT TO CHANGE WITHOUT NOTICE TO IMPROVE RELIABILITY, FUNCTION OR DESIGN OR OTHERWISE.

Vishay Intertechnology, Inc., its affiliates, agents, and employees, and all persons acting on its or their behalf (collectively, "Vishay"), disclaim any and all liability for any errors, inaccuracies or incompleteness contained in any datasheet or in any other disclosure relating to any product.

Vishay makes no warranty, representation or guarantee regarding the suitability of the products for any particular purpose or the continuing production of any product. To the maximum extent permitted by applicable law, Vishay disclaims (i) any and all liability arising out of the application or use of any product, (ii) any and all liability, including without limitation special, consequential or incidental damages, and (iii) any and all implied warranties, including warranties of fitness for particular purpose, non-infringement and merchantability.

Statements regarding the suitability of products for certain types of applications are based on Vishay's knowledge of typical requirements that are often placed on Vishay products in generic applications. Such statements are not binding statements about the suitability of products for a particular application. It is the customer's responsibility to validate that a particular product with the properties described in the product specification is suitable for use in a particular application. Parameters provided in datasheets and/or specifications may vary in different applications and performance may vary over time. All operating parameters, including typical parameters, must be validated for each customer application by the customer's technical experts. Product specifications do not expand or otherwise modify Vishay's terms and conditions of purchase, including but not limited to the warranty expressed therein.

Except as expressly indicated in writing, Vishay products are not designed for use in medical, life-saving, or life-sustaining applications or for any other application in which the failure of the Vishay product could result in personal injury or death. Customers using or selling Vishay products not expressly indicated for use in such applications do so at their own risk. Please contact authorized Vishay personnel to obtain written terms and conditions regarding products designed for such applications.

No license, express or implied, by estoppel or otherwise, to any intellectual property rights is granted by this document or by any conduct of Vishay. Product names and markings noted herein may be trademarks of their respective owners.

Material Category Policy

Vishay Intertechnology, Inc. hereby certifies that all its products that are identified as RoHS-Compliant fulfill the definitions and restrictions defined under Directive 2011/65/EU of The European Parliament and of the Council of June 8, 2011 on the restriction of the use of certain hazardous substances in electrical and electronic equipment (EEE) - recast, unless otherwise specified as non-compliant.

Please note that some Vishay documentation may still make reference to RoHS Directive 2002/95/EC. We confirm that all the products identified as being compliant to Directive 2002/95/EC conform to Directive 2011/65/EU.

Vishay Intertechnology, Inc. hereby certifies that all its products that are identified as Halogen-Free follow Halogen-Free requirements as per JEDEC JS709A standards. Please note that some Vishay documentation may still make reference to the IEC 61249-2-21 definition. We confirm that all the products identified as being compliant to IEC 61249-2-21 conform to JEDEC JS709A standards.

Technical
University of
Denmark

Building 343, Ørsteds Pl.
2800 Kgs. Lyngby
Tlf. 45253800

www.electro.dtu.dk/